UNIVERSITA’ DEGLI STUDI DI PARMA

Dottorato di ricerca in Scienza e Tecnologia dei Materiali Innovativi

Ciclo XXVI

Growth and Characterization of ZnO and SiC Nanowires

Coordinatore:
Chiar.mo Prof. Enrico Dalcanale

Tutor:
Chiar.mo Prof. Giancarlo Salviati
Chiar.mo Prof. Andrea Zappettini

Dottorando: Sathish Chander Dhanabalan

This PhD Thesis work has been done within the European "NANOWIRING" Marie Curie Initial Training Network (ITN), which funded part of the research leading to these results by means of the European Union Seventh Framework Programme under grant agreement n° 265073.

The main objective of "NANOWIRING" Network is to embed a pool of postgraduates and young researchers in a multidisciplinary framework of research and development activities in the emerging field of science and applications based on the unique properties and opportunities offered by semiconductor nanowires. The main technological issues that the joint research programme intends to address within the project are the following: semiconductor nanowires for sensors, optoelectronic, nanoelectronic and energy harvesting applications.

Table of Contents

Chapter 1. Introduction 6

1.1 Nanotechnology and nanowires 6

1.2 Thesis description 14

References 18

Chapter 2. ZnO and SiC nanowires 21

2.1 Zinc oxide nanowires 21

2.1.1 Zinc oxide properties 21

2.1.1.1 *Basic properties and crystal structure* 22

2.1.1.2 *Physical properties* 24

2.1.1.3 *Electronic band structure* 25

2.1.1.4 *Piezoelectric properties* 27

2.1.1.5 *Optical properties* 27

2.1.1.6 *Mechanical properties* 28

2.1.2 Applications of zinc oxide nanostructures 29

2.1.2.1 *ZnO nanowires in energy harvesting applications* 31

2.1.2.2 *ZnO nanowires for gas sensing applications* 36

2.1.2.3 *ZnO nanowires for UV photodetectors* 42

2.1.2.4 *ZnO nanowires for biomedical applications* 43

2.1.2.5 *ZnO nanowires for piezoelectric humidity sensors* 45

2.1.2.6 *ZnO nanowires for pH measurement* 46

2.1.2.7 *ZnO nanowires for self-powered multifunctional devices* 46

2.2 Silicon Carbide nanowires 49

2.2.1 Silicon Carbide Properties 49

2.2.1.1 *Crystallographic Structures of SiC* 49

2.2.1.2 *Basic properties of bulk SiC* 51

2.2.1.3 *Wide range of properties of SiC focused towards applications* 52

2.2.1.4 *Properties of SiC Nanostructures* 54

2.2.2. Multidisciplinary applications of SiC nanostructures 57

2.2.2.1 *Biomedical applications* 58

2.2.2.2 *Sensor applications* 60

2.2.2.3 *Energy harvesting applications* 61

2.2.2.4 *Electronics MEMS/NEMS* 61

2.2.2.5 *Field emission devices* 64

2.2.2.6 *Other emerging areas* 67

References 69

Chapter 3. Experimental techniques 93

3.1 Growth mechanisms and techniques 93

3.1.1 Vapor-Solid growth mechanism 94

3.1.2 Vapor-Liquid-Solid growth mechanism 97

3.1.3 Chemical Vapor Deposition technique 103

3.1.3.1 *Gas/vapor dispensing system* 105

3.1.3.2 *Reactors* 107

3.1.3.3 *Single chamber evaporator and reactor* 108

3.1.4 Vapor Phase Epitaxy technique 109

3.1.4.1 *VPE system* 110

3.2 Characterization techniques 113
    3.2.1 Scanning Electron Microscopy 113
        3.2.1.1 *Working principle* 114
    3.2.2 Transmission Electron Microscopy 118
        3.2.2.1 *Working principle* 119
    3.2.3 X-ray Energy-Dispersive Spectroscopy 121
    3.2.4 Luminescence spectroscopy 122
        3.2.4.1 *Photoluminescence* 124
        3.2.4.2 *Cathodoluminescence* 126
    3.2.5 Raman Spectroscopy 127
References 132

Chapter 4. Results and Discussions 135

4.1. Vertically aligned ZnO nanowires 135
    4.1.1. Synthesis 139
        4.1.1.1 *TCO films* 142
        4.1.1.2 *Vapor-phase growth of vertically aligned nanowires* 144
    4.1.2. Characterization 147
        4.1.2.1 *Seeding films characterization* 147
        4.1.2.2. *ZnO nanostructures characterization* 150
4.2 Nanowires of ternary (In/Ga/Sn)ZnO oxides 156
    4.2.1 Synthesis 158
        4.2.1.1 *Growth Mechanism* 162
    4.2.2 Characterization 164
        4.2.2.1 *InZnO nanorods* 164
        4.2.2.2 *GaZnO and SnZnO nanorods* 170

4.3. 3C-SiC nanowires 173

4.3.1. Synthesis 173

4.3.2. Characterization 183

4.3.2.1 *Nickel assisted 3C-SiC nanowires* 184

4.3.2.2 *Iron assisted 3C-SiC nanowires* 193

4.4. SiC/SiO_2 core/shell nanostructure 199

4.4.1. Synthesis 202

4.4.2. Growth mechanism 206

4.4.3. Characterization 209

References 219

Chapter 5. Conclusions 235

5.1 Vertically aligned ZnO nanowires 236

5.2 Nanowires of ternary (In/Ga/Sn)ZnO oxides 237

5.3 3C-SiC nanowires 238

5.4 SiC/SiO_2 core/shell nanostructure 239

List of publications 240

Peer reviewed papers 240

Conferences presentations 241

Acknowledgement 243

Chapter 1

Introduction

1.1 Nanotechnology and nanowires

In 1999 chemist and Nobel Laureate Richard Smalley stated: "*Just wait, the next century is going to be incredible. We are about to be able to build things that work on the smallest possible length scales, atom by atom. These little nano things will revolutionize our industries and our lives*" [1].

Nanostructured materials also known as nanomaterials are materials which have relatively dimensions in nanometer length scales and exist in in the mesoscopic regime among isolated atoms or molecules and bulk matter. A nanometer, 10^{-9} m, is approximately ten times the size of smallest atoms, like hydrogen and carbon, although a micron is hardly greater than the wavelength of visible light and hence invisible to the human eye.

The foundation of nanoscience and nanotechnology is nothing but the nanoscale materials. They have become one of the most popular research topics in a very short period of time. The intense interest is fueled by the tremendous economical, technological and scientific impact foreseen in several areas:

- the capacity and speed of semiconducting chips exponentially grow form the key components that fundamentally assist all present technology and quickly approaching their limit of art and demands novel technology and innovative materials science in nanometer scale;
- new nanoscale materials and devices hold great potential in environmental, energy, biomedical and health sciences in the effective application of energy sources, efficient

environmental hazards treatment, precise detection and diagnosis of human diseases and better-quality treatment of those diseases;

- the reduction of material's dimension to nanoscale make significant change in its properties from the bulk material although the composition is more or less the same. Therefore, they are demonstrated to be a platform for great scientific findings and investigations [2].

The considerably diverse physical properties of the nanomaterials have been attributed to their specific structural features among the isolated atoms and the bulk materials [3]. Quantum confinement is the most popular term in the nano-world due to the changes in the atomic structure as a result of the direct influence of the ultra-small length scale on the energy band structure. These exceptional properties of the nanoscale materials may be attributed to the changes in the total energy and structure of the system [4, 5].

But even when quantum confinement is not obtained, nanostructured materials can show peculiar properties, once again in strong correlation with their size in nanometer scale and mainly due to the large influence of surfaces. Surface to volume ratio is, indeed, huge in these materials and generally it has extraordinary effects on their physical properties.

At nanoscale dimensions the normally collective electronic properties of the solid become severely distorted. The main implication of such confinement is the change in the system total energy; and hence the overall thermodynamic stability [4]. As the chemical reactivity is a function of system structure and occupation of outermost energy levels, it will be significantly affected at nanoscale leading to an equivalent change in their physical properties. While the increase in surface area and the surface free energy lead to a reduction in the interatomic distance for metals, the opposite was reported for the semiconductors and metal oxides. A major feature that discriminates various types of nanostructures is their dimensionality. Synthesis of size and shape controlled nanostructures, their self-assembly, properties and possible applications are under rigorous research. Realizing the importance of nanotechnology, state of the art technology centers with excellent processing, characterization and device fabrication facilities are being developed [4]. It is well understood that in order to realize the full potential, evolutional progress and revolutionary breakthrough of nanoscale materials are needed in the fabrication and synthesis of nanostructures, and in the understanding of the fundamental properties of such materials.

In past few decades, specifically since the nanotechnology initiative led by US, study of one dimensional (1D) nanostructured materials has become a principal concept in application oriented nanoscience and nanotechnology. The size reduction along with innovative electrical, chemical, mechanical and optical properties is widely supposed to be the outcome of surface and quantum confinement effects. Nanowire-like structures are the epitome system to understand the transport process in 1-D confined objects are of benefit not only in studying the vital phenomena in low dimensional structures, but also for emerging new group of nanodevices having extraordinary performance [6].

It is generally accepted that one dimensional nanostructures provide a good system to investigate the dependence of electrical and thermal transport or mechanical properties on dimensionality and size reduction. They are also expected to play an important role as both interconnects and functional units in fabricating electronics, optoelectronics, electrochemical, and electromechanical devices with nanoscale dimensions.

Initially the development in the field of one dimensional nanostructures with respect to quantum dots and wells was slow due to difficulties associated with the synthesis of one-dimensional nanostructures with controlled morphology, purity and chemical composition. There were several issues related to the fabrication of such one-dimensional nanostructures. Since past decade, a variety of synthesis methods have been used for the synthesis of such nanostructures [5].

Nanowires (NW) are hair-like, one-dimensional (1D) nanomaterials with diameters smaller than one hundred nanometers and lengths ranging from several hundreds of nm to as high as a few cm.

In this size range quantum confinement is often not achieved and in some case, to differentiate among nanowires with and without this property, the term “quasi-one-dimensional” (“quasi-1D” or “Q1D”) is used. Quasi-1D nanostructures are, hence, all those nanostructure like nanowires in which is not present any quantum confinement effects but unique properties, strongly different from those of the corresponding bulk materials, are strictly correlated with their size in the nanoscale.

The diameter of nanowires range from a single atom to a few hundreds of nanometers with the length varies from a few atoms to many microns. Depending on their aspect ratio, cross-section shape and other, the term “nanowire” generally resume a wider range of different names and nanostructures reported in literature such as whiskers, fibers, 1D structures ranging from several nanometers to several hundred microns, nanowires-wires with large aspect ratios (e.g. >20), nanorods-wires with small aspect ratios, nanocontacts-short wires bridged between two larger electrodes, nanobelts or nanoribbons with rectangular shape, vertically standing nanopillars, etc [5].

Their linear geometry on the nanometer scale provides an extremely high surface area with a nanoscale radius of curvature and great mechanical flexibility with near theoretical strength. These properties are advantageous in many chemical and mechanical applications. The geometry also provides anisotropic properties that should be interesting from the point of view of nanomaterials science and engineering. Their length, sometimes reaching as high values as the cm scale, makes them easy to be manipulated for device fabrication.

The physical and chemical conditions of nanowires govern their optical properties. The length, diameter and alignment of nanowires influence the emission and absorption properties. The critical factors in the emission and/or stimulated emission and absorption composition includes the impurity, doping level, defect concentration, crystal structure, growth direction, and nature of the facets.

Nanowires are also found to be favorable materials for progressive optoelectronics. The physical, chemical and mechanical properties play a major role in addition to the size of these materials comparable to visible light in wavelength from 400 to 650 nm. This suggests that nanowires could be employed to handle light on a nanometer scale and hence, might be used as constructing blocks in the field of advanced optoelectronics.

Semiconductor nanowires denote a significant and highly flexible nanometer-scale wire structure. Nanowire-based electronic devices find many applications and became a hot topic of research. With respect to nanotubes, semiconductor NWs could be predictably and reasonably grown in single-crystalline form and can be well-controlled during synthesis in chemical composition, diameter, length and doping/electronic properties [7].

Semiconductor nanowires (NWs) have been assembled into a series of electronic electronics devices such as crossed NW p-n diodes, crossed NW-FETs, nanoscale logic gates and computation circuits, optoelectronic devices, etc. More general applications of them include interconnects for nano-electronics, magnetic devices, biological labels, chemical and biological sensors. There are many reliable methods existing for their parallel assembly. It is also possible to combine distinct nanowire building blocks in ways not possible in conventional electronics. Hence, nanowires represent the best-defined class of nanoscale building blocks and this precise control over key variables has correspondingly enabled a wide range of devices and integration strategies to be pursued.

Different techniques have been developed in the synthesis and formation of 1-D nanostructured materials. Nanowires are a result of anisotropic, 1D crystal growth on a nanometer scale. Therefore, the key issue related to the growth of nanowires is how to induce 1D crystal growth in a controlled manner. Regarding this, many approaches have been studied and can be generally classified into four sections [8]:

- Spontaneous growth: Evaporation condensation, Dissolution condensation, Vapor-Liquid-Solid growth (VLS), Stress induced re-crystallization
- Template-based synthesis: Electrochemical deposition, Electrophoretic deposition, Colloid dispersion, melt, or solution filling, Conversion with chemical reaction
- Electro-spinning
- Lithography

The first three sections are considered as bottom-up approach while lithography is a top-down approach.

In the top-down approach, small features are patterned in bulk materials by a combination of lithography, etching and deposition, to form functional devices. The top-down approach has been unexpectedly successful in many venues, with microelectronics being perhaps the best example today. While the technique developments continue to push the resolution limits of the top-down approach, these improvements in resolution are associated with a near exponential increase in the costs associated with each new level of manufacturing facility. This economic limitation and other scientific problems with the top-down approach have motivated efforts worldwide to search for new strategies to meet demand for nanoscale structures.

The bottom-up approach represents a powerful alternative to conventional top-down methods. In the bottom-up approach functional electronic structures are assembled from chemically synthesized, well-defined nanoscale building blocks, much like the way nature uses proteins and other macromolecules to construct complex biological systems. So, in this approach lithography is substituted by nanometer-scale synthesis and assembly. This self-assembling approach is generally less expensive and more streamlined, in comparison with the top-down one, if the nanostructure complexity is not too high.

In bottom-up approach, the most important issue that one has to consider during the development of a synthetic method to grow nanostructures is the simultaneous control over morphology/shape, dimensions and monodispersity/uniformity.

In some cases the intrinsic anisotropy of a solid crystal structure or the right supersaturation parameters may be sufficient to accomplish a 1D vapor-solid (VS) or liquid-solid (LS) growth (Figure 1a) [9-11]. Otherwise, a liquid droplet of a catalytic element/compound may be used to strongly alter the growth symmetry by the introduction of a preferential direction in the vapor-liquid-solid (VLS) crystallization (Figure 2b) [12-16].

A different approach, instead, is to force and direct the formation of 1D-nanostrucure using various external templates [17-19]. Common templates employed in this techniques are, for example, the anodic alumina membranes (Figure 2c). Also carbon nanotubes have been used as templates to obtain small nanorods [20, 21]. A similar result may be also obtained using “capping reagents” (generally surfactant molecules) that, driven by hydrophilic/hydrophobic interactions and steric hindrance, organize themselves in tubular shapes (Figure 2d) [22, 23].

In both cases the crystallization takes place inside the available linear cavity and, at last, the templates or the “capping reagents” are chemically or physically removed. The major drawbacks of this method are: (i) the nanostructures generated using template method are often polycrystalline; (ii) the quality of structures that can be produced in each run of synthesis is relatively limited; (iii) grown nanostructures must be resistant to the physical or chemical methods used to remove the template.

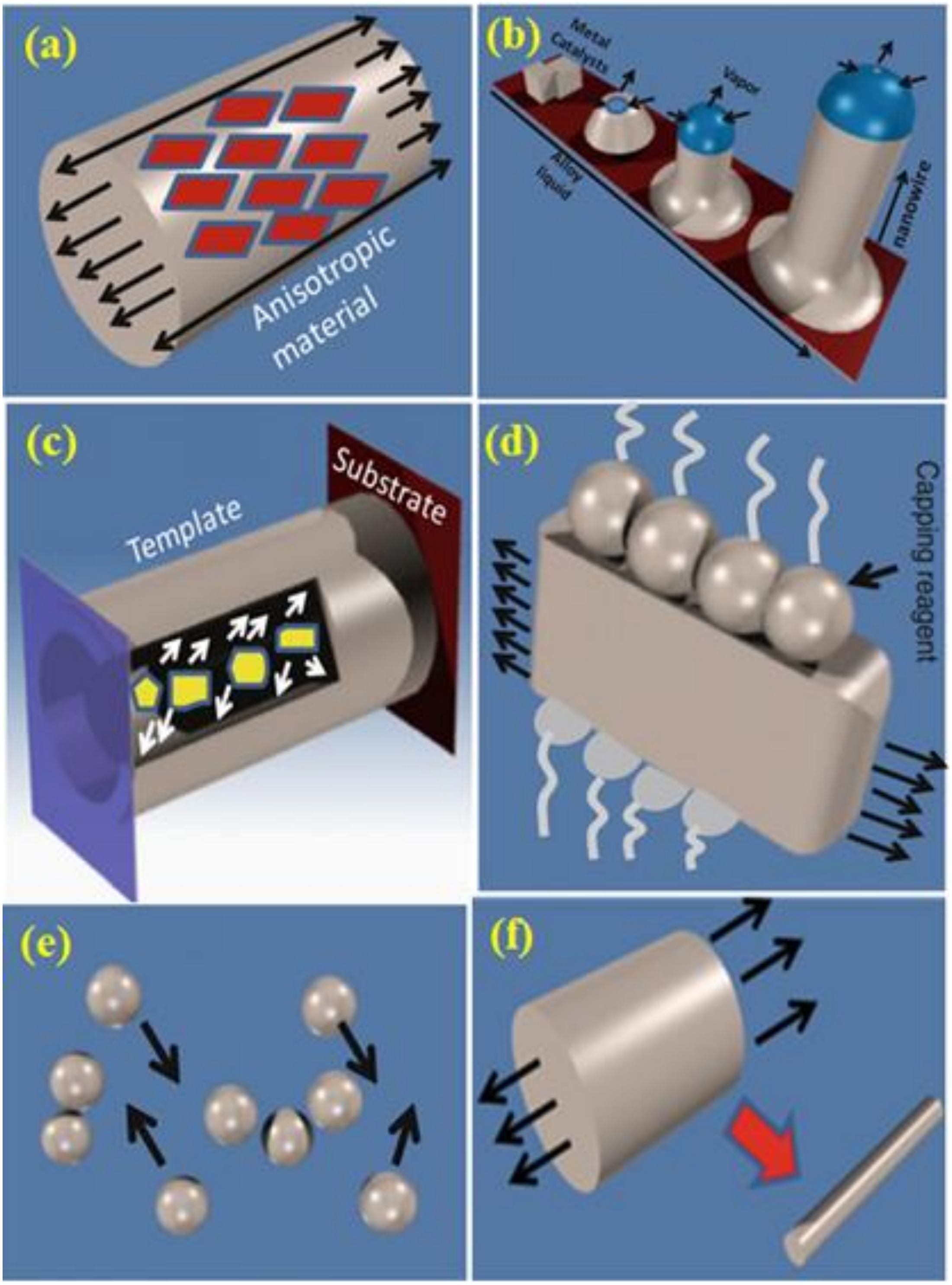

Figure1. Schematic illustrations of six different strategies to achieve 1D growth (a) dictation by anisotropic crystallographic structure of a solid, (b) confinement by a liquid droplet as in VLS growth, (c) template assisted growth, (d) kinetic control provided by a capping reagent, (e) self-assembly of 0D nanostructures and (f) size reduction of 1D microstructure (image from Ref. [5]).

Alternatively, for some materials it is possible to achieve a 1D-nanostructure by the self-assembly of zero-dimensional (0D) nanostructures, following a polymerization-like process (Figure 2e). Self-assembly has been extensively explored for generating complex nanostructures on various scales [24, 25].

Sometimes also techniques that combine bottom-up and top-down techniques are used, like anisotropic etching of a single crystal or near-field optical lithography with a phase shift mask (Figure 2f) to reduce the lateral dimension of one-dimensional structures from 1–10 μm to the regime ≤100 nm [26,27].

Among the above techniques, for this thesis work the attention has been focused on self-assembly vapor-solid growth mechanism and vapor-liquid-solid growth technique, which are widely used for zinc oxide and silicon carbide nanostructure.

1.2 Thesis description

Out of a short introduction about nanotechnology and nanowires, this Thesis is basically divided in three parts:

- ***Chapter 2*** is an overview chapter, describing the state of the art, the important properties of ZnO and SiC nanostructures and their main applications in different fields such as sensing, biomedical, opto-electronics, nano-electronics, energy harvesting and others possible applications;
- ***Chapter 3*** describes the exploited experimental methods, i.e. (i) growth mechanisms (more specifically vapor-solid and vapor-liquid-solid mechanism), (ii) vapor phase synthesis techniques (in particular Chemical Vapor Deposition and Vapor Phase Epitaxy), and (iii) characterization techniques for morphological, structural and optical study of the obtained nanostructured materials;
- ***Chapter 4*** resumes main experimental results and the related discussions for each of the four main growth topic faced during this Thesis work.

Finally in ***Chapter 5*** conclusions and future perspectives are provided.

More in details, this Thesis deals with the synthesis of semiconductor nanowires, which is today an important research topic and it is studied intensively worldwide for a wide spectrum of materials. Such low-dimensional nanostructures are indeed not only interesting for fundamental research, due to their unique structural and physical properties, but also for their fascinating potential in future concrete technological applications. So, deeper understanding and sufficient control of the growth of nanowires became one of the main goals for current research [28, 29]. The target of the Thesis work is the optimized synthesis of zinc oxide (ZnO) (Chapters 4.1 and 4.2) and silicon carbide (SiC) (Chapters 4.3 and 4.4) nanowires exploiting spontaneous growth process from vapor phase, such as vapor-solid (VS) and vapor–liquid–solid (VLS) techniques.

ZnO is one of the most interesting wide band-gap semiconductor material because of its physical and chemical properties [30]. MOreover, it is well known that high n-type conductivity can be achieved by alloying zinc oxide with group III elements (such as Al, In or Ga) in ternary or even quaternary oxide compounds, in order to obtain transparent conducting oxides (TCOs) [31]. The first part of experimental results concern the synthesis of vertically aligned ZnO nanowires (or “nanorods”) and the synthesis of ternary Zn(In,Ga,Sn)O oxide nanowires (or “nanorods”).

Chapter 4.1 describes the synthesis of vertically aligned ZnO nanowires. Synthesis of vertically aligned ZnO nanowires has been always very challenging for device fabrications. It was already suggested that control over the dimension, composition, position, orientation, reproducible and large-area growth processes of the ZnO nanostructures plays a very crucial role in the development of novel devices [32, 33]. Considering this challenge, solution-free and catalyst-free growth of vertically aligned ZnO nanorods using thermal CVD reactor at relatively low temperature (< 500 °C) have been systematically studied as a function of growth conditions (such as Zn evaporation, growth time, growth temperature, gas carrier flow, gas carrier to oxygen concentration, seeding film grain size, etc.). Different TCOs films such as Al-doped ZnO films deposited by PED, RF-sputtering techniques and ITO were considered for the growth as starting seeding-layers for the nanorods. The aim of the work was mainly focused to obtain a reproducible and large-area growth of vertically aligned nanorods on TCO substrates while controlling their thickness and length. The structural morphology of the different TCO substrates and that of the grown ZnO nanorods have been analyzed and correlated with the help of XRD, AFM and SEM investigations.

Chapter 4.2 describes the growth of nanowires of ternary (In/Ga/Sn)ZnO oxides. The introduction of a third element into ZnO nanostructures can give rise to dramatic changes in their morphologies and properties. In particular high n-type conductivity or other strong modifications of the conductivity properties can be achieved by alloying zinc oxide with group III, IV, V elements (such as Al, In, Ga, Sn or Sb) in ternary or even quaternary oxide compounds [34, 35]. For this reason, the synthesis of nanowires of ternary oxide compound based on ZnO have been taken into consideration. In this chapter of Thesis the achievements of the previous experiments on ZnO nanowires have been exploited and extended to grow indium zinc oxide (IZO) nanowires, with an indium concentration larger than 1% (that is the concentration required to get metallic behavior) at temperatures lower than 500°C. The growth of these ternary oxide nanostructures was obtained at relatively low temperature, starting from the corresponding metals, thanks to the direct deposition on the growth substrate of an In layer, which in its molten state and upon mixture with Zn acts as growth seed. Since the obtained indium concentration corresponds to the value required to get metallic behavior and make this ternary oxide a TCO (transparent conducting oxide), while the used temperature range makes it compatible also with commercial glass substrates. The possibility to use the same technique to growth nanowires of a wider family of ternary oxides such as GaZnO, SnZnO were also tested and discussed.

Among many kind of wide band-gap semiconductor, also SiC is very important, exhibiting excellent, unique physical and mechanical properties at nano-scale. All these properties give it a great potential for being used as building blocks in different applications in nano-electronics and nano-optoelectronics [36]. SiC biocompatibility and inertness can be also exploited for biomedical applications [37]. In this second part of results two types of SiC nanowires have been synthesized using vapour-liquid-solid growth technique: cubic (3C) SiC nanowires and SiC/SiO_2 core/shell nanowires.

Chapter 4.3 describes the growth of cubic (3C) SiC nanowires. Single crystalline 3C–SiC nanowires on a Si substrate have been shown to possess visible photoluminescence at room temperature and blue shift effect depending on the diameter of nanowires [38]. Moreover, 3C-SiC nanostructures are favorable candidate in biology and medicine as well, thanks to their excellent biocompatibility, especially blood compatibility, low density and high rigidity [39]. For all these reasons, the synthesis of cubic SiC nanowires have been considered. In the presented work, 3C-SiC nanowires were successfully grown using home-made induction-heated Vapor Phase Epitaxy (VPE) reactor using silane and propane as precursor through VLS growth mechanism on Si (100) and Si (111) substrate, using nickel (Ni) and iron (Fe) as a catalysts. The main aim of this work was the optimization of growth conditions to obtain SiC nanowires with Ni and Fe catalysts. The size and shape of the nanowires has been controlled by means of temperature and gas flow rate. The as grown samples were deeply characterized with morphologic and structural investigations.

Chapter 4.4 describes the growth of SiC/SiO_2 core/shell nanowires. Radial core-shell heterostructures offer the possibility to deeply change the physical and chemical properties of the core due to the presence of the shell [1]. In particular, semiconductor (SiC) nanowires coated with dielectric (SiO_2) layers form cable-like nanostructures in which the SiO_2 shell favors well established surface functionalization techniques for several potential applications in fields such as nano-electronics, opto-electronics, nano-medical etc. [36,37]. For this reason, growth of SiC/SiO_2 core/shell nanowires have been considered. In this work, the main focus was to synthetize self-assembled SiC core with coaxial SiO_2 shell nanowires by means of Ni and Fe catalyst assisted VLS growth in conventional CVD system. The growth conditions were optimized for both catalysts, studying the role of growth temperature, gas flow rate, and substrates in the growth mechanism. The grown nanowires are the basis for functionalized system for different nano-medical applications, such as targeted therapy against deep tumor cells.

The presented results are the outcome of a large and systematic experimental work I personally carried out at IMEM-CNR, especially from the synthesis point of view. The growth of ZnO nanowires has been developed under the supervision of Dr. Andrea Zappettini and Dr. Davide Calestani, while the growth of SiC nanowires has been developed under the supervision of Dr. Giancarlo Salviati and Dr. Giovanni Attolini.

The characterization of the obtained nanostructures has been performed thanks to the collaboration with colleagues of IMEM-CNR or members of the NANOWIRING Network. In particular SEM characterization has been done partially by myself and partially in collaboration with Dr. Davide Calestani, Dr. Filippo Fabbri. TEM and EDS characterizations were instead performed in collaboration with Dr. Laura Lazzarini and Dr. Francesca Rossi. Luminescence characterization has been done by means of different apparatus: photoluminescence spectra were collected in collaboration with Dr. Andrea Zappettini and Dr. Marco Villani, cathodoluminescence spectra in collaboration with Dr. Filippo Fabbri and, while PL on single nanostructures was performed at University of Valencia in collaboration with the Group of Dr. Nuria Garro. I personally spent one month in this Nanowiring Group in Valencia in order to have a deeper formation on Raman optical characterization collaborationg with the Nanowiring PhD student Albert Minj. TCO films used for the experiments were instead provided by Dr. Stefano Rampino, Dr. Francesco Pattini and Dr. Francesco Bissoli, from IMEM-CNR group of Dr. Edmondo Gilioli.

References

1. K. J. Klabunde, ed., Nanoscale materials in chemistry, Vol. 1035. New York: Wiley-Interscience, (2001).

2. J. Zhang, ed., Self-assembled nanostructures, Vol. 2, Springer, (2003).

3. C. Suryanarayana, Int . Mater., 40 (1995) 41.

4. S. V. N. T. Kuchibhatla, A. S. Karakoti, D. Bera and S. Seal, Progress in Materials Science, 52 (2007) 699–913.

5. Y. Xia, P. Yang, Y. Sun, Y. Wu, B. Mayers, B. Gates,Y. Yin, F. Kim and H. Yan, Advanced Materials, 15 (2003) 353-389.

6. Z. L. Wang, Journal of Physics: Condensed Matter., 16 (2004) R829-R858.

7. Y. Sun and J. A. Rogers, (Eds.), Semiconductor nanomaterials for flexible technologies: from photovoltaics and electronics to sensors and energy storage, William Andrew (2010).

8. G. Cao, Nanostructures and nanomaterials, Imperial college press (2004).

9. C. Lin and M. L. Povinelli, Opt. Express, 17 (2009) 19371–19381.

10. L. Hu and G. Chen, Nano Lett., 7 (2007) 3249–3252.

11. Z. Yu, A. Raman and S. Fan, Proc. Nat. Acad. Sci., 107 (2010) 17491–17496.

12. X.F. Duan and C. M. Lieber, J. Am. Chem. Soc., 122 (2000) 188-189.

13. Y. Zhang, Q. Zhang, N. Wang, Y. Yan, H. Zhou and J. Zhu, J. Cryst. Growth, 226 (2001) 185-191.

14. C. C. Chen, C. C. Yeh, C. H. Chen, M. Y. Yu, H. L. Liu, J. J. Wu, K. H. Chen, L. C. Chen, J. Y. Peng and Y. F. Chen, J. Am. Chem. Soc., 123 (2001) 2791-2798.

15. Y. Wang, L. Zhang, C. Liang, G. Wang and X. Peng, Chem. Phys. Lett., 357 (2002) 314-318.

16. M. H. Huang, Y. Wu, H. Feick, N. Tran, E. Weber and P. Yang, Adv. Mater., 13 (2000) 113-116.

17. T. Gao, G. Meng, J. Zhang, S. Sun and L. Zhang, Appl. Phys. A, 74 (2002) 403-406.

18. H. Q. Cao, Y. Xu, J. M. Hong, H. B. Liu, G. Yin, B. L. Li, C. Y. Tie and Z. Xu., Adv. Mater., 13 (2001) 1393.

19. Y. Li, G. W. Meng, L. D. Zhang and F. Phillipp, Appl. Phys. Lett., 76 (2000) 2011-2013.

20. Y. Yin,Y. Lu, Y. Sun and Y. Xia, Nano Lett., 2 (2002) 427-430.

21. Y. Zhang, N. W. Franklin, R. J. Chen and H. Dai, Chem. Phys. Lett., 331 (2000) 35-41.

22. S. Kwan, F. Kim, J. Akana and P. Yang, Chem. Commun., 5 (2001) 447-448.

23. Y. Y. Yu, S. S. Chang, C. L. Lee and C. C. Wang, J. Phys. Chem. B, 101 (1997) 6661-6664.

24. B. A. Korgel and D. Fitzmaurice, Adv. Mater., 10 (1998) 661-665.

25. D. Wyrwa, N. Beyer and G. Schmid, Nano Lett., 2 (2002) 419-421.

26. Taylor, G.F., Phys. Rev., 23 (1924) 655.

27. R. Penner, M. Heben, T. Longin and N. Lewis, Science, 250 (1990) 1118-1121.

28. H. J. Fan, P. Werner and M. Zacharias, SMALL, 2, 6, 700 – 717 (2006)

29. P. Yang, R. Yan and M. Fardy, Nano Lett., 10, 1529–1536 (2010)

30. Z. L. Wang, Ad. Funct. Mater 2008, 18, 3553.

31. H. Von Wenckstern, H. Schmidt, M. Brandt, A. Lajn, R. Pickenhain, M. Lorenz, M. Grundmann, D. M. Hofmann, A. Polity, B. K. Meyer, H. Saal, M. Binnewies, A. Börger, K. D. Becker, V. A. Tikhomirov and K. Jug, Prog. Solid State Ch., 37,153-172 (2009)

32. G. Wang, W. Lu, J. Li, J. Choi, Y. Jeong, S. Y. Choi, J. B. Park, M. K. Ryu, K. Lee, Small, 2, 1436 (2006)

33. G. Wang, Q. Wang, W. Lu, J. J. Li, Phys. Chem. B, 110, 22029 (2006)

34. M. Bazzani, A. Neroni, A. Calzolari, A. Catellani, Appl. Phys. Lett., 98, 121907 (2011)

35. H. J. Fan, A. S. Barnard and M. Zacharias, Appl. Phys. Lett. 90, 143116 (2007)

36. Special issue on silicon carbide devices and technology, IEEE Trans. Electron Dev. 55 1795–2065 (2008)

37. S. Saddow, Silicon Carbide Biotechnology: A Biocompatible Semiconductor for Advanced Biomedical Devices and Applications: Elsevier Science, (2011)

38. Y. Zhang, M. Nishitani-Gamo, C. Xiao and T. Ando, J. Appl. Phys. 91, 6066 (2002)

39. L. Nordsletten L, A. K. M. Høgåsen, Y. T. Konttinen, S. Santavirta, P. Aspenberg and A. O. Aasen, Biomaterials 17 1521 (1996)

Chapter 2

ZnO and SiC nanowires

2.1 Zinc oxide nanowires

2.1.1 Zinc oxide properties

Zinc oxide (ZnO) is a unique material that exhibits semiconducting as well as piezoelectric properties. It is an important semiconductor material because of its wide band-gap (3.37 eV at room temperature), large exciton biding energy (60 meV), and high optical gain. In addition, ZnO crystal cell has a lack of centrosymmetry, which results in a piezoelectric property, by which a mechanical stress/strain can be converted into electrical voltage, and vice versa, owing to the relative displacement of the cations and anions in the crystal [1]. ZnO is also an excellent material for sensor applications and, finally, it is a non-toxic, bio-safe and biocompatible material.

Then, this versatile functional material can be obtained in form of nanostructures with an exceptional variety of growth morphologies (Figure 1), such as nanowires, nanobelts, nanotetrapods, nanorods, nanocombs, nanorings, nanohelixes/nanosprings, nanocages, etc. [2]. Quite often, to simplify this chaotic and not always self-consistent nomenclature, the term *"nanowires"* is used to indicate any quasi-1D nanostructure such as wires, shorter rods, belts, etc.; the same will be done in this chapter. These different ZnO nanostructures can be easily synthesized by different growth techniques, some of which are cost-efficient and compatible with cheap substrates, such as glass and silicon.

The combination of all these properties and its availability in form of several nanostructures make ZnO one of the leading materials in today's nanotechnology research.

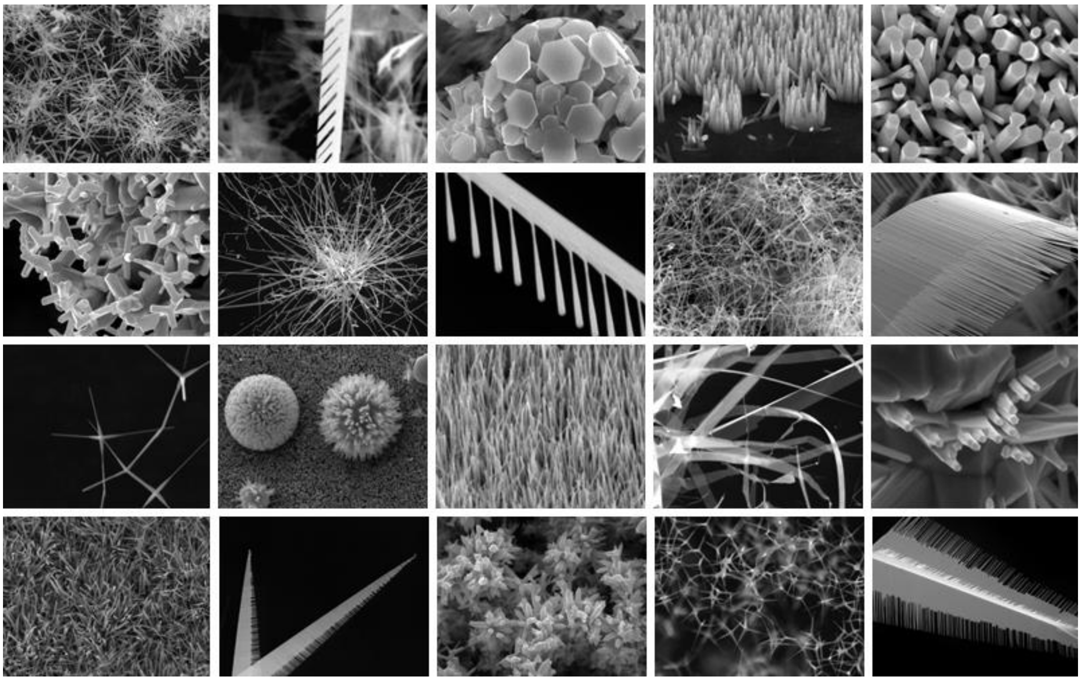

Figure 1. An example of different kinds of morphologies for ZnO nanostructures grown at IMEM-CNR laboratories.

2.1.1.1 Basic properties and crystal structure

ZnO is a II-VI group compound semiconductor with a wide array of distinctive properties. It is a n-type semiconductor, with a wide direct bandgap, a high exciton binding energy and large piezoelectric constant. It is transparent in visible region with strong absorption in the UV-Blue region of the electromagnetic spectrum. Most of the II–VI binary compound semiconductors crystallize in either cubic zinc blende or hexagonal wurtzite structure, where each anion is surrounded by four cations at the corners of a tetrahedron, and vice versa. This tetrahedral coordination is typical of sp^3 covalent bonding nature, but these materials also have a substantial ionic character that tends to increase the bandgap beyond the one expected from the covalent bonding.

Wurtzite zinc oxide has a hexagonal structure (space group C6mc) with lattice parameters a = 0.3296 and c = 0.5206 nm and it is the most stable phase for this material. The structure of

ZnO can be simply described as a number of alternating planes composed of tetrahedrally coordinated O^{2-} and Zn^{2+} ions, stacked alternately along the c-axis as shown in Figure 2. The tetrahedral coordination in ZnO results in non-centrosymmetric structure and consequently in piezoelectricity and pyroelectricity. Another important characteristic of ZnO are polar surfaces. The most common polar surface is the basal plane. The oppositely charged ions produce positively charged Zn-(0001) and negatively charged O-(000-1) surfaces, resulting in a normal dipole moment and spontaneous polarization along the c-axis as well as a divergence in surface energy. The other two most commonly observed facets for ZnO are {2-1-10} and {01-10}, which are non-polar surfaces and have lower energy than the {0001} facets [2].

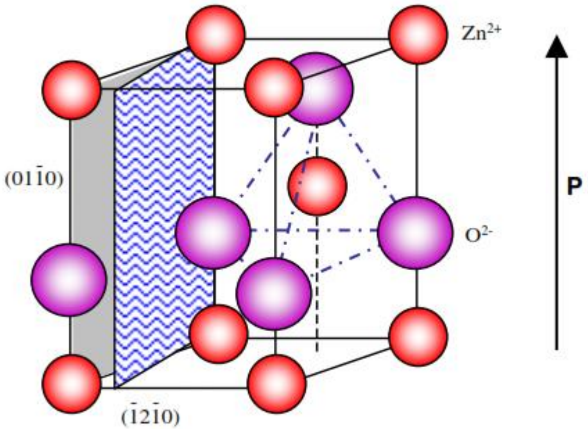

Figure 2. Wurtzite structure model of ZnO with the tetrahedral coordination of Zn-O [1]

In an ideal wurtzite crystal, the axial ratio c/a and the u parameter (which is a measure of the amount by which each atom is displaced with respect to the next along the c-axis) are correlated by the relationship $uc/a = (3/8)^{1/2}$, where $c/a = (8/3)^{1/2}$ and $u = 3/8$ for an ideal crystal. ZnO crystals deviate from this ideal arrangement by changing both of these values. This deviation occurs such that the tetrahedral distances are kept roughly constant in the lattice. Experimentally, for wurtzite ZnO, the real values of u and c/a were determined in the range u=0.3817–0.3856 and c/a =1.593–1.6035 [3-5]. Additional to the wurtzite phase, ZnO is also known to crystallize in the cubic zincblende and rocksalt (NaCl) structures. Zincblende ZnO is stable only by growth on cubic structures [6-8], whilst the rocksalt structure is a high-pressure metastable phase forming at ~10 GPa, and cannot be epitaxially stabilized [9]. Theoretical calculations indicate that a fourth phase, cubic cesium chloride, may be possible at extremely high temperatures, however, this phase has yet to be experimentally observed [10].

2.1.1.2 Physical properties

The basic physical properties of ZnO at 300 K are given in Table 1 [11-15]. There is some uncertainty in the values with respect to thermal conductivity variation caused by crystal defects [16] as well as uncertain values for hole mobility and effective mass because of the problems of producing robust and reproducible p-type doping of ZnO.

Properties	**Values**
Lattice constants at 300 K	a = 0.32495 nm, c = 0.52069 nm
Density	5.67526 g/cm^3
Molecular mass	81.389 g/mol
Melting point	2250 K
Electron effective mass	0.28 m_0
Hole effective mass	0.59 m_0
Static dielectric constant	8.656
Refractive index	2.008, 2.029
Bandgap energy at 300 K	3.37 eV
Exciton binding energy	60 meV
Thermal conductivity	0.6 – 1.16 W/Km
Specific heat	0.125 cal/g°C
Thermoelectric constant at 573 K	1200 mV/K
Electron mobility	~ 210 cm^2/Vs

Table 1. Basic physical properties of ZnO at 300 K [11-15].

These values are for bulk ZnO crystals. Any deviation induced on these values by the lower dimensionality of ZnO nanostructures can be, in principle, tuned by controlling the nanostructure size. This makes nanostructures an even more important tool for exploiting all the functional properties of this material at their best.

2.1.1.3 Electronic band structure

The band structure of a given semiconductor is pivotal in determining its potential utility. Consequently, an accurate knowledge of the band structure is critical if the semiconductor in question is to be incorporated in the family of materials considered for device applications. The electronic band structure of ZnO has been calculated by a number of groups and several theoretical methods have been employed to calculate the band structure of ZnO for its wurtzite, zinc-blende, and rocksalt polytypes [4, 10, 17]. Local density functional (LDA) and tight-binding methods were early used by considering the 3d states as core levels to simplify the calculation [17-20]. Despite the fact of achieving satisfactory agreements with qualitative valence-band dispersions, the quantitative disagreement with experimental results occurred and location of the Zn 3d states could not be predicted. More recently, researchers have started to include the effect of the Zn 3d level in their calculations and obtained reasonable match with the experimental data [21-24]. Vogel et al. [24] showed an alternative way to treat II-VI semiconductor compounds in which self-interaction corrections were added to the LDA. Figure 2 shows band structure calculations of ZnO both by LDA and self-corrected pseudopotential (SIC-PP) approaches included in LDA.

In Figure 3, it has been showed that valence band maxima and the lowest conduction band minima were obtained at Γ point k = 0, which proved that ZnO is a direct band gap semiconductor. The bands in the bottom of the right panel of Figure 3 represent Zn 3d levels. On the other hand, there is no band in the bottom of the left panel of Figure 3, which results from using conventional LDA method that does not include the effect of Zn 3d levels. The next 6 bands from -5 eV to 0 eV in the right panel of Figure 3 represent O 2p bonding states. In SIC-PP calculation, the bands are shifted down in energy considerably and the band gap is opened drastically. The band gap determined from this method is 3.77 eV, which is in better agreement with experiments.

There are several experimental methods to study the band structure of ZnO such as X-ray induced photoemission spectroscopy [25-27], UV photoemission measurements [28, 29], angle-resolved photoelectron spectroscopy [30, 31], and low-energy electron diffraction [32]. These experimental tools greatly facilitate the understanding and improvement of theoretical calculations. X-ray or UV reflection/absorption or emission techniques have conventionally been used to measure the electronic core levels in solids. These methods basically measure the energy difference by inducing transitions between electronic levels (e.g., transitions from the upper valence band states to the upper conduction band states and from the lower valence band states) or by exciting collective modes (e.g., the upper core states to the lower edge of the conduction band and to excitations of plasmons).

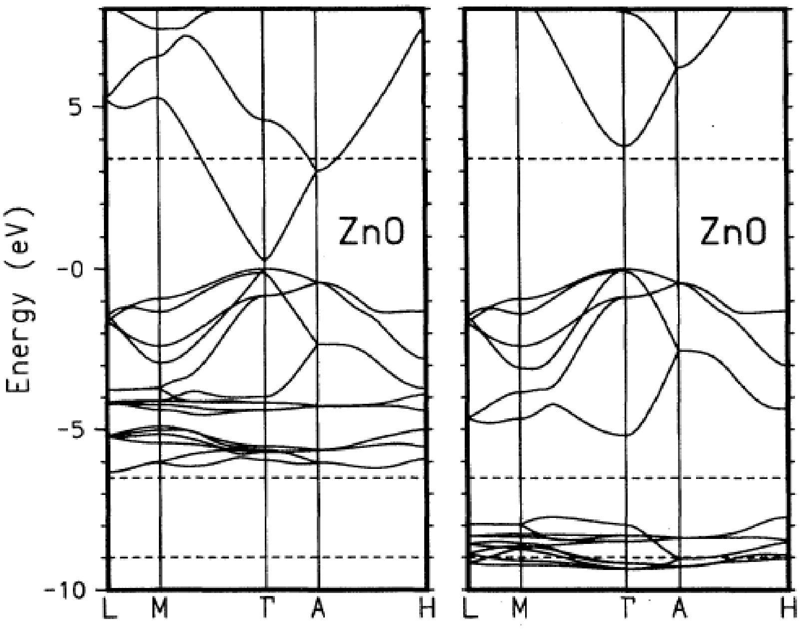

Figure 3. The band structure of bulk Wurtzite ZnO calculated by LDA method (left panel) and self-interaction corrected pseudopotential (SIC-PP) method [24].

Another important method for the investigation of the energy region is based on the photoelectric effect extended to the X-ray region, namely, photoelectron spectroscopy. The peaks in emission spectrum correspond to electron emission from a core level without inelastic scattering, which is usually accompanied by a far less intense tail region in the spectrum. Additionally, angle-resolved photoelectron spectroscopy technique together with synchrotron radiation excitation have been recognized as a powerful tool that enables the determination of experimental bulk and surface electronic band structures under the assumptions of k-conservation and single nearly free-electron-like final band [33].

On the other hand, the size of ZnO nanostructures generally reported in literature is much smaller than that of a bulk crystal. In these crystals at least one dimension is generally just a few nm wide. However they are not small enough to induce quantum confinement but at the same time surface-state induced band bending affects most of the nanocrystal, since Debye length (generally in the order of tens of nanometers) is comparable with their smaller radius [34].

Nanowires discussed in this thesis are generally called quasi-1D nanostructures to highlight that, even if they are not quantum structures, their size strongly affects their semiconducting properties.

2.1.1.4 Piezoelectric properties

ZnO has a wurtzite structure in which the Zn cations and O anions form a tetrahedral coordination. ZnO has two important characteristics. One is the presence of polar surfaces, such as Zn^{2+} -terminated (0001) and O^{2-}-terminated (0001). The interaction of the polar charges at the surface can lead to the growth of a wide range of unique nanostructures [35], such as nanobelts [36], nanosprings [37], nanorings [38] and nanohelixes [39]. But another significant characteristic is the lack of centrosymmetry, which results in a piezoelectric effect, by which a mechanical stress/strain can be converted into electrical voltage, and vice versa, owing to the relative displacement of the cations and anions in the crystal. It is important to point out that the polar surfaces are a surface effect, while piezoelectricity is an integrated volume effect. Previous studies have shown that ZnO nanowires and nanobelts exhibit piezoelectricity, and the piezoelectric coefficient is even larger than that of the bulk [40].

2.1.1.5 Optical properties

The wide bandgap (~3.37 eV at room temperature) makes ZnO also a promising material for photonic applications in the UV or blue spectral range, while the high exciton-binding energy (60 meV) [41] allows efficient excitonic emission even at room temperature.

There is a variety of experimental techniques available for the study of optical transitions in ZnO such as reflection, photoreflection, transmission, optical absorption, photoluminescence

[PL], cathodoluminescence, spectroscopic ellipsometry, and calorimetric spectroscopy. Room temperature PL spectra of ZnO typically consist of a UV emission band and a broad emission band in the green visible range, which is also called deep band emission (DBE). The UV emission band is related to a near band-edge (NBE) transition of ZnO, namely the recombination of the free excitons (FX) and bound exciton complexes (BXC), while the broad emission band between 420 and 700 nm is due to deep level emission (DLE). It is worth noting that this green luminescence band (GL, as other authors refer to it) is observed nearly in all samples regardless of growth conditions. The DLE is widely considered a defect emission band but there is still no agreement about its chemistry. Defects represent one of the controversial areas of semiconductors, and ZnO is no exception, as the measurement techniques are not able to correlate electrical or optical manifestation of defects to their origin precisely. The DLE band has been attributed to several defects in the crystal structure such as O–vacancy (V_O) [42-45], Zn–vacancy (V_{Zn}) [46-51], O–interstitial (O_i) [52], Zn–interstitial (Zn_i) [53] and O–antisite (O_{Zn}) [54].

Low temperature PL measurements of different ZnO nanostructures, such as nanowalls [55], nanosheets [56], nanowires [57, 58], nanorods [59-62], nanoparticles [63], nanowire/nanowall systems [64], nanoblades and nanoflowers [65] have been reported, and they are always characterized by these two component, although their relative weight can be very different from case to case.

2.1.1.6 Mechanical properties

Mechanical properties of different metal and semiconductor nanostructures have been studied by several groups using various analytical methods, which include atomic force microscopy (AFM), in-situ electron transmission electron microscopy (TEM), scanning electron microscopy (SEM), and nano-indentation. Mechanical properties such as reliability and stability include strength, stiffness, hardness, toughness, fatigue, buckling, Young’s and bulk moduli, piezoelectric constants, and yield strength. Nanostructures represent excellent model systems to investigate the size dependence of mechanical properties, particularly the ability to tune the dimension over continuous range to investigate mechanical properties as a function of shape and size [66].

In spite of the fact that ZnO has been considered one of the next generation material for use in nanoscale systems, its mechanical properties are not well studied. This is due to the challenges of material characterization at the nanoscale. Ji et al. [67] and Young et al. [68] found that the buckling load increased with increased diameter of the ZnO nanowires but that the Young's modulus increased with decreasing diameter. In addition, the Young's modulus for the nanowires was larger than for bulk ZnO. Kucheyev et al. [69] studied the deformation behavior of ZnO single crystals by a combination of spherical nanoindentation and AFM. They found multiple discontinuities in force-displacement curves during indentation loading. No discontinuities were observed on unloading. They found the slip was the major mode of plastic deformation in ZnO. The determined hardness and Young's modulus were 5.0±0.1 and 111.2±4.7 GPa, respectively.

Chen et al. [70] also reported the size dependence of Young's modulus in ZnO nanowires. They found that the measured modulus for nanowires with smaller diameter than 120 nm was increasing dramatically with the decreasing diameters. A core-shell composite nanowire model was proposed and assessed that the size-related elastic properties of GaN nanotubes can be explained by this model. On the other hand, Wen et al. [71] reported that in contrast to recent reports, Young's modulus was essentially independent of diameter and close to bulk value, whereas the ultimate strength increased for small diameter wires, and exhibits values up to 40 times that of the bulk.

2.1.2 Applications of zinc oxide nanostructures

From the 1960s, synthesis of ZnO thin films has been an active field because of their applications as sensors, transducers and catalysts. ZnO is a key technological material. The lack of a centre of symmetry in wurtzite, combined with large electromechanical coupling, results in strong piezoelectric and pyroelectric properties and the consequent use of ZnO in mechanical actuators and piezoelectric sensors. In addition, ZnO is a wide band-gap (3.37 eV) compound semiconductor that is suitable for short wavelength optoelectronic applications. The high exciton binding energy (60 meV) in ZnO crystal can ensure efficient excitonic emission at room temperature and room temperature ultraviolet luminescence has been reported in disordered nanoparticles and thin films. ZnO is transparent to visible light and can be made highly conductive by doping [1]. Because of these unique properties ZnO has attracted intensive research effort for different applications in transparent electronics, ultraviolet (UV) light emitters, piezoelectric devices, chemical sensors and spin electronics [72-81].

Invisible thin film transistors (TFTs) using ZnO as an active channel have achieved much higher field effect mobility than amorphous silicon TFTs [82-84]. These transistors can be widely used for display applications. ZnO has been proposed to be a more promising UV emitting phosphor than GaN because of its larger exciton binding energy of 60 meV. This leads to a reduced UV lasing threshold and yields higher UV emitting efficiency at room temperature [85].

Since it is transparent and it can be doped with a high concentration of trivalent atoms (e.g. Al, Ga or In) to increase the electrical conductivity, with minor effects on the crystal structure and transparency of the material [86-90], ZnO is also interesting for making transparent conductive oxide (TCO) films. Different deposition techniques are generally used to obtain high quality ZnO-based TCO layers, such as RF magnetron sputtering [91], chemical vapor deposition (CVD) [92] and pulsed laser deposition (PLD). In particular, doped-ZnO thin films grown by PLD exhibit high optical transparency [93], high conductive property and excellent crystalline quality [94].

Surface acoustic wave filters using ZnO films have already been used for video and radio frequency circuits. Piezoelectric ZnO thin film has been fabricated into ultrasonic transducer arrays operating at 100 MHz [95]. Bulk and thin films of ZnO have demonstrated high sensitivity for toxic gases [96-99] Furthermore, hole mediated ferromagnetic ordering in bulk ZnO by introducing Mn as dopant has been predicted theoretically [100] and reported recently [101]. Vanadium doped n-type ZnO films also demonstrate a Curie temperature above room temperature [102].

Based on these remarkable physical properties and the motivation of device miniaturization, large effort has been focused on the synthesis, characterization and device applications of ZnO nanostructures. ZnO has a very rich family of nanostructures and they all could find an application in such a wide range of research fields.

One-dimensional ZnO nanorods, nanowires, and nanotubes are of particular interest because of their large number of applications and in particular, the shape and size of the ZnO nanostructures play a key role for the performance of the devices. Thus, ZnO nanorods, nanowires, and nanotubes have found a variety of applications in the field of optoelectronics [103, 104], nanomechanics [105, 106], nanosensors [107-113], resonators [114], electric nanogenerator [115], and nanolasers [116]. Moreover ZnO nanostructures have piezoelectric property that can form the basis for electromechanically coupled sensors and transducers, but this property can also affect their growth, extending the range of possible morphologies to nanorings, nanobows, platelet circular structures, Y-shape split ribbons, and crossed ribbons, which originate when strong polar effects are present during the growth and that could be unique for many applications in nanotechnology [117].

ZnO nanostructures have been also frequently used for electrochemical and chemoresistive sensor purpose since the large surface-to-volume ratio property leads to an improved signal-to-noise ratio, faster response times, enhanced analytical performance, and increased sensitivity [118, 119]. In addition, ZnO nanostructures have unique biological advantages including non-toxicity, biosafety, bio-compatibility, and high electron communication features, which make them one of the most promising materials for biosensor applications.

In the next paragraphs, some of these applications for ZnO nanostructures will be presented more in detail.

2.1.2.1 ZnO nanowires in Energy Harvesting Applications

Photovoltaics, thermoelectricity, and electromagnetic induction are the most established technologies for energy harvesting. But today also the development in harvesting technologies for mechanical energy is of great interest [120]. Energy-harvesting methods applicable to the problem include systems that utilize light, random vibrations (e.g., vibrations near a roadway), temperature gradients (e.g., ground temperature is fairly constant at a point sufficiently below the surface), or any other phenomenon that could be exploited to provide energy.

ZnO nanostructures has been applied in the development of several and promising energy-harvesting devices, being piezoelectric, transparent to visible light and a made of semiconductor material that can be easily doped with ternary compounds to reach metal state.

Piezoelectric nanogenerators

As mentioned several times, ZnO is a piezoelectric material and in its nanostructured form can be easily bended or deformed even by small forces, hence producing large polarization in the nanocrystals. This potential difference between the two faces, in principle, can be used to generate power in an external circuit. This is the principle at the basis of nanogenerators (NG). Unfortunately the power generated by a single nanostructure is generally very low and methods to collect piezoelectric power from many nanostructures at once are required in order to produce a reasonable current flow.

Figure 4 shows a unique coupling of piezoelectric and semiconducting properties in the metal-semiconductor Schottky-barrier-governed transport process [121]. In this figure (a) and (b) represents the metal and semiconductor contacts between the AFM tip and the semiconductor ZnO NW at two reversed local contact potentials (positive and negative), showing reverse- and forward-biased Schottky rectifying behavior, respectively. The Schottky barrier is responsible for separating, accumulating, and later releasing the charges [122]. The schematic idea for replacing the role played by an ATM tip by an ‘‘inverted-V shaped’’ electrode is given in (c) and (d). The idea of introduction of a zigzag electrode to form hundreds of parallel tips, each acts like an AFM tip can be seen in (e).

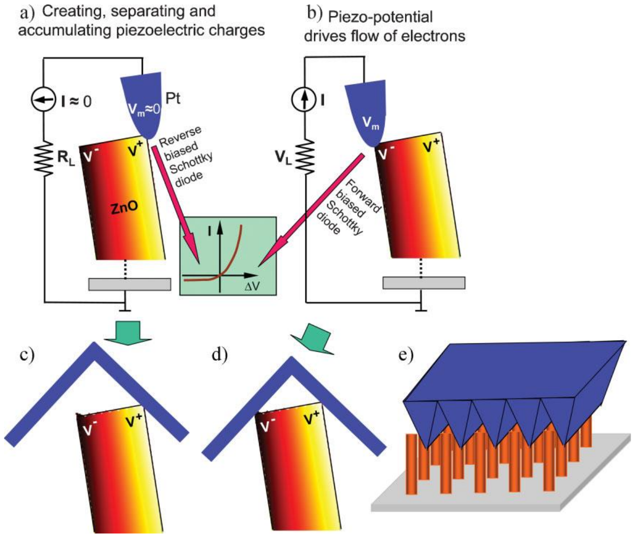

Figure 4. Physical principle of the observed power-generation process of a piezoelectric ZnO NW [121, 122]

The NG based on the ZnO NWs has the following experimental characteristics: i) The output potential is a sharp peak that is negative in reference to the grounded end of the NW. ii) No output current is received when the tip first touches the NW and pushes the NW; electrical output is observed only when the tip is about to leave the NW at the second half of the contact. iii) The power output occurs only when the tip touches the compressive side of the NW [123]. iv) An output signal is observed only for piezoelectric NWs. No electrical output is received if the NWs are tungsten oxide, carbon nanotubes, silicon, or metal. Friction or contact potential plays no role in the observed output power. v) The magnitude of the output signal is highly sensitive to the size of the NWs [124]. vi) To effectively output electricity, the contact between the tip and the NW is required to be Schottky in nature, and the contact between the NW and ground must be ohmic [120].

The nanowire-based energy-harvesting technology offers a few more advantages [121]:

- The NW/NB can be subjected to extremely large elastic deformation (ca. 90° bending) without plastic deformation or fracture.
- Due to their small diameter, NWs/NBs are most likely free of dislocations, and thus, expected to have a high resistance to fatigue, possibly extending the lifetime of the device.
- NWs/NBs can be bent under an extremely small applied force. This is unique for harvesting energy created by weak mechanical disturbance.
- The large surface area offered by NWs/NBs provides a unique opportunity for surface functionalization to improve physical and chemical properties and hence producing self-powered multifunctional devices
- ZnO NW arrays can be easily grown via chemical synthesis at 80 °C on any shaped substrate made of any material (crystalline or amorphous, hard or soft), it can be easily integrated with technologically important materials, such as silicon or polymers, at low cost.
- ZnO is a biocompatible, degradable, and nontoxic material [125] with a wide range of applications in medicine and cosmetics; thus, it has large potential also for implantable and flexible power sources.
- ZnO is an environmentally ‘‘green’’ material.

The ceramic or semiconductor substrates used for growing ZnO NWs are however usually hard, brittle, and cannot be used in areas that require a foldable or flexible power source, such as implantable biosensors in muscles or joints, and power generators built into walking shoes [126]. For these applications it is necessary to use conductive polymers, which are likely to be biocompatible and safe, as substrates. Two advantages are offered by this approach. One is the cost-effective, large-scale solution to grow ZnO NW arrays at a temperature below 80 °C. The other is the large degree of choice of flexible plastic substrates for growing aligned ZnO NW arrays, which could play an important role in flexible and portable electronics for harvesting low frequency (ca. 10 Hz) energy from the environment, such as from body movement (e.g., gestures, respiration, or locomotion). ZnO fiber based NGs have been recently demonstrated [127]. The design of the NG is generally based on the zigzag-electrode mechanism made by “rigid” silicon micro-machined substrates, but this could also be replaced by an array of metal wires. By brushing the metal NW arrays across the ZnO NW arrays, the metal wires act like an array of AFM tips that induce the mechanical deformation to the ZnO nanowires and collect the charges. Metal NW arrays were made by metal coating of ZnO nanowire arrays grown on Kevlar fibers. In practice, any fiber should work as long as it has good electrical conductivity. The NWs on the two fibers are ‘‘teeth-to-teeth’’, a relative deflection by a distance as short as one NW size is sufficient to generate electricity. A cycled relative sliding between the two fibers produces output voltage and current owing to the deflection and bending of the ZnO nanowires. This is the fiber-based NG [127], with potential for harvesting energy from body movement, muscle stretching, light wind, and vibration. It also establishes the basis for building a ‘‘power-shirt’’ to wear.

Nanostructured photoanodes for solar cell application

ZnO nanostructures are particularly interesting as n-type conductor (or TCO) in excitonic solar cells (XSC), e.g. in extremely thin absorber (ETA) and dye sensitized solar cells (DSSC). ZnO has recently emerged as a promising candidate due to its semiconducting properties which are very similar to the most used semiconductor oxide, TiO_2, but the possibility of obtaining ZnO nanostructures by easy and low-cost techniques renders ZnO a unique and even more interesting alternative [128]. In PV applications, TP employment is far less interesting than NR. TP “film” conduction is dominated by surface transport and hopping takes place, especially at the interface between different TP, thus limiting the mobility. On the other hand, NR are almost ideal structures in XSC. They have high surface / volume ratio, a “corrugated” surface that helps photon absorption and, above all, excellent electron transport properties confirmed by a mobility as high as 3000 cm^2/V·s (when not exposed to air, refer to [129] for details), higher than those of the state-of-the-art planar Si MOSFETs (less than 1000 cm^2/V·s).

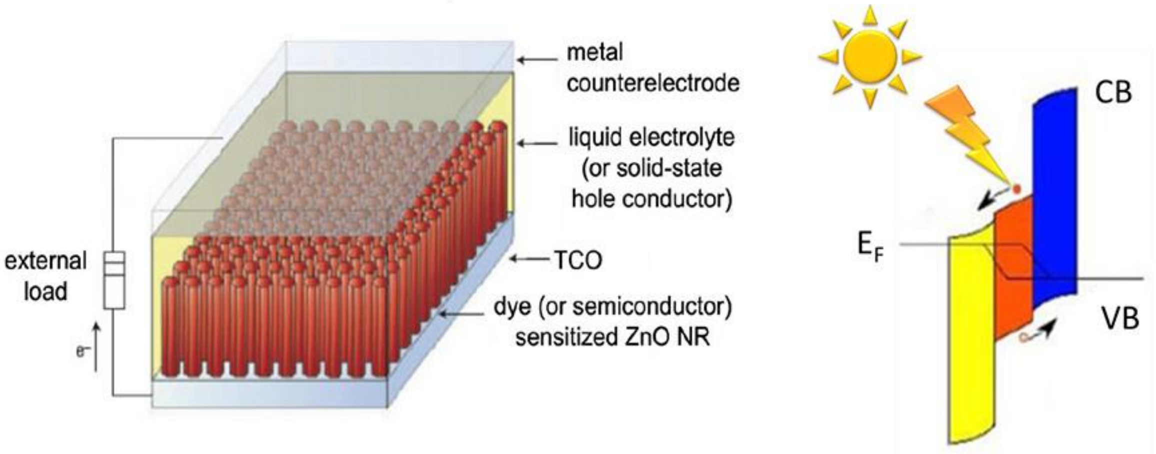

Figure 5. Different elements in a ZnO NR based XSC (left) adapted from [130]. Band gap alignment (right), adapted from [131].

A XSC consist typically of three active elements: a transparent n-type material, a thin absorbing layer (e.g. an organic dye in DSSC, a inorganic semiconductor in ETA) and a p-type material. Incident photons are absorbed inside the thin layer (orange in Figure 5, right) creating an exciton that diffuses to the interface and separates, transferring the electron to the CB of n-type material (blue in Figure 5, right) and then to the TCO; the hole is injected to the VB of p-type material (yellow in Figure 5, right), then collected to the metal counter electrode. A schematic view of a XSC based on ZnO NR and band alignment are reported in Figure 5.

Despite of the excellent electronic performance of ZnO nanostructures, the use in DSSC is still limited because of ZnO poor chemical stability in both acidic and alkaline environment (often needed to anchor the dye to semiconductor surface). The sensitization process follows the diffusion of the dye, adsorption on the ZnO surface, dissolution of Zn surface atoms and formation of [Dye–Zn^{2+}] complex [132]. Such complexes are thought to be responsible for the poor electron injection from the dye [133,134]. However, it must be noted that the issue of ZnO instability arises from the use of dyes previously developed and engineered specifically for TiO_2, which offers far better performances in aggressive environment. Research on ZnO

NR based DSSC is still an hot topic [135-137] albeit reported efficiencies are quite low (1-2% in most cases). Up to now, the best light-to-electricity conversion efficiency (η) of a DSSC based on ZnO nanostructures is found to be 6.06%, under 100 mW/cm^2 illumination [138].

Since the ETA-solar cell concept was proposed in 2000 by Konenkamp et al. [139], continuous and progressive improvements have been achieved. After some interesting reports on the integration of different materials in the ETA-solar cell architecture [140], Lévy-Clément et al. [141] demonstrated in 2005 the experimental feasibility of the concept for ZnO/CdSe/CuSCN solar cells (efficiency, η ~ 2.3% under 360 W/m^2 illumination) based on ZnO nanowire arrays. In 2008, Dittrich's group [142] also used ZnO nanowire arrays as building blocks for ZnO/In_2S_3/CuSCN ETA-solar devices, reaching conversion efficiencies up to 3.4%. Similar efficiencies were also reported in the last two years for devices based on nanocrystalline TiO_2 using Sb_2S_3 as a light absorber, keeping CuSCN as a hole collector [143-145]. Slightly higher conversion efficiencies (up to 5%) have been recently reported using TiO_2 with different hole conductor materials, such as spiro–OmeTAD [146] and P3HT [147]. As concerns ZnO, it is worth mentioning the study reported by Tak et al. who functionalized ZnO NR with CdS to extend light absorption in the visible region and produced a ZnO/CdS core-shell nanowire heterostructure array [148]: the cell has a high short-circuit photocurrent density of 7.23 mA/cm^2 with a power conversion efficiency of 3.53% under AM 1.5G illumination at 100 mW/cm^2. Finally, to my knowledge, the efficiency record, for a ZnO NR based ETA–solar cell, is currently reported by Krunks et al. with 4.2% for a ZnO/In_2S_3/$CuInS_2$ nanowire array [149].

2.1.2.2 ZnO nanowires for gas sensing applications

The issue of air quality is still a major concern in many countries. A clean air supply is essential to our health and the environment. The human nose serves as a highly advanced sensing system which may differentiate between hundreds of smells but fails if absolute gas concentrations or odorless gases need to be detected. The demand for detecting toxic and deleterious gases is accordingly urgent to support or replace human nose [150]. Sensing of poisonous gas is very important for saving human life and preserving industrial fields' safety. In order to further improve the sensitivity, selectivity, and chemical and thermal stability of the poisonous gas detectors, intensive efforts have been made in developing gas sensors based on nanostructured materials [151].

The response to different gases is related to a great extent to the surface state and morphology of the material. However, some critical limitations are difficult to overcome with the sensors with micrometer dimension. In such materials, limited surface-to-volume ratio determines a limited gas response to low concentration of tested gases and requires operation at elevated temperatures to reach a desired gas response. In order to overcome these limitations different types of nanostructured materials and approaches have been investigated for their gas response, selectivity and possible application in sensors with better characteristics [152]. ZnO has great potential for use in gas sensors due to its high electron mobility of conduction electrons and good chemical and thermal stability under the operating conditions of sensors [153, 154]. It is known that the sensing mechanism of ZnO belongs to the surface-controlled type [155], in which the grain sizes, defects, and oxygen-adsorption quantities play important roles in its gas sensitivity.

In several reports [156, 157], ZnO nanostructures have been demonstrated to have good sensitivity as sensing materials. However, the key contributing factors to its gas sensing, such as defects in ZnO nanowires, have not yet been thoroughly studied.

There has been significant recent interest in the use of surface-functionalized thin film and nanowire ZnO for sensing of gases, heavy metals, UV photons and biological molecules. For the detection of gases such as hydrogen, for example, ZnO is typically coated with a catalyst metal such as Pd or Pt to increase the detection sensitivity at room temperature. Functionalizing the surface with oxides, polymers and nitrides is also useful in enhancing the detection sensitivity for gases and ionic solutions. The use of enzymes or adsorbed antibody layers on the ZnO surface leads to highly specific detection of a broad range of antigens of interest in the medical and homeland security fields [158].

ZnO based gas sensors are mainly chemoresistive (Figure 6), which means that their electrical conductivity is dependent on the adsorption or redox reactions that take place on its surface and that generally involves an exchange of charge carriers. Several papers are reported in literature about the use of ZnO nanowires for gas sensing; here a few examples will be presented.

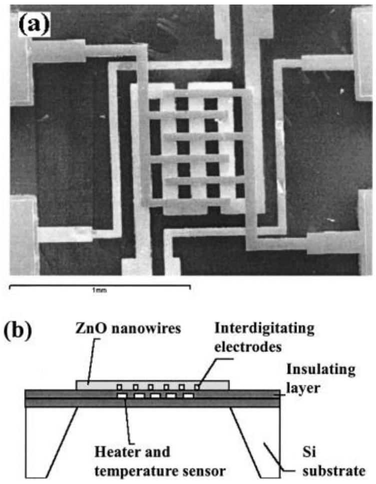

Figure 6. (a) Top-view SEM image of a substrate embedded with Pt interdigitating electrodes and Pt heater and (b) 3D schematic of a sensor structure typically used for chemoresistive oxide gas sensing [154].

Wan et al, for example, [202] investigated ZnO nanowires gas sensors were fabricated with microelectromechanical system technology and ethanol-sensing characteristics which is the first one of its kind. The sensor studied by them exhibited high sensitivity and fast response to ethanol gas at a work temperature of 300 °C and also demonstrated the potential application of those ZnO NWs for fabricating highly sensitive gas sensors. When ZnO nanowire sensor fabricated with the MEMS technology is exposed to air, an oxygen molecule adsorbs on the surface of the ZnO NWs and forms an O_2^- ion by capturing an electron from the conductance band. So ZnO NWs show a high resistance state in air ambient. When the ZnO nanowire sensor is exposed to a reductive gas at moderate temperature, the gas reacts with the surface oxygen species, which decreases the surface concentration of O_2^- ion and increases the electron concentration. This eventually increases the conductivity of the ZnO NWs. The sensitivity shows evidence of saturation when the ethanol concentration is up to 200 ppm. The sensitivity of the ZnO NW sensor at different working temperatures was also investigated with an ethanol concentration of 100 ppm. The sensitivity increased sharply as the temperature is raised from 200 to 300 °C. This is mainly because of the enhanced reaction between the ethanol and the absorbed oxygen at an elevated temperature. High sensitivity and fast response time were found at a working temperature of 300 °C. These results demonstrate that ZnO NWs can be used as the gas sensing material for fabricating highly sensitive gas sensors [159].

Gas sensor using a single ZnO nanowire as a sensing unit was reported by Liao et al [152]. This ZnO nanowire-based sensor has quick and high sensitive response to H_2S in air at room temperature. It has also been found that the gas sensitivity of the ZnO nanowires could be modulated and enhanced by He+ implantation at an appropriate dose. A possible explanation is given, based on the modulation model of the depletion layer. This new type of gas nanosensor is expected to find wide applications in various complicated moisture gases for quick detection of poisonous and inflammable gases [152]. Ahn et al [159] fabricated gas sensors by growing ZnO nanowires bridging the gap between two prepatterned Au catalysts. The sensor displayed fast response and recovery behavior with a maximum sensitivity to NO_2 gas at 225 °C. Gas sensitivity was found to be linearly proportional to the photoluminescence intensity of oxygen-vacancy-related defects in both as-fabricated and defect-controlled gas sensors by postannealing in Ar and H_2 atmosphere.

In recent years, hierarchically branched or porous ZnO nanostructure combining unique morphology and porous structure have attracted scientists' research interest because of their significantly enhanced surface-to-volume ratio and hence enhanced properties in gas sensor applications.

Shi et al [160] reported that a novel sensor assembled with ZnO nanowires joints was successfully demonstrated to show a high response and fast response/recovery to ethanol gas. For example, Zhang et al [161] have synthesized hierarchically porous ZnO nanosheets with ultrahigh ethanol response through hydrothermal process, followed by annealing of the zinc carbonate hydroxide hydrate precursor. Zhang et al, [162] have fabricated three-dimensional flower-like ZnO hierarchical nanostructures with good gas sensing properties through hydrothermal method, followed by annealing of 3D zinc hydroxide carbonate precursor.

Moreover Zhang et al [163] have reported a gas sensor based on hierarchically three-dimensional (3D) porous ZnO architectures with excellent sensing performances prepared by hydrothermal method combined with subsequent calcination of zinc carbonate hydroxide hydrate precursor. The results of Huang et al [164] showed that the responses to 100 ppm toluene, 2-propanol and acetone were 29.1, 53.7, and 57.2, respectively, at a working temperature of 300 °C, which is a very promising result for such porous ZnO nanowires consisting of nanocrystallites.

Zhang et al [165] also compared the sensing properties of brush-like hierarchical ZnO nanostructures to many different types of gases including 50 ppm ethanol, CH_4, C_6H_6, HCHO, NH_3, H_2, CO, Cl_2 and NO_2 gases with those of the straight ZnO nanowires [165]. They reported that the brush-like hierarchical ZnO nanostructures showed approximately 1.5 fold stronger responses to ethanol and C_6H_6 gases than straight ZnO nanowires, but the former showed more or less the same responses to the other gases compared to the latter. An et al [166] focused on the sensing properties of hierarchical ZnO nanostructures particularly toward NO_2 at very low concentrations because NO_2 is currently one of the most dangerous air pollutants. The multiple-networked branched ZnO nanowire sensors exhibited far superior NO_2 gas sensing properties than the unbranched nanowires.

Fabrication of ethanol gas sensor based on p-type ZnO nanoparticles (NPs) and n-type ZnO NWs on ZnO/glass substrate reported by Hsu et al [167] in which the gas responses of p-ZnO NPs/n-ZnO NWs are dominated by p-type sensing at 25 °C and n-type sensing above 200 °C. They showed that the reaction of ethanol with ionic oxygen species becomes stronger as the temperature is increased and produced more electrons at a higher temperature. These electrons increase the conductivity of n-type NW and reduce that of p-type NPs. The ease of nano-fabrication combined with the high compatibility with Si-based microelectronics afforded to semiconducting metal oxides makes ZnO a particularly interesting candidate for solid-state chemical gas sensing.

ZnO tetrapods-based, which are essentially a branched ZnO nanostructure made of four nanowires with a common core, were tested at IMEM-CNR as gas sensors (Figure 7) with different gases (CH_3CH_2OH, NO_2, CO and H_2S) and reported by Calestani et al [168]. Their response values have been measured as $S = 25$ and $S = 100$ towards 1 ppm and 5 ppm of hydrogen sulphide, respectively with no response drift (generally associated with sulphurization processes) in the sensor during exposition to H_2S.

This kind of tetrapod-based sensors showed also a very high sensitivity towards aldehydes [169]. Being toxic at low concentration for prolonged exposure time and in some cases even carcinogenic at high concentration, aldehyde detection is very important for monitoring environmental and domestic pollution, as well as food sophistication or contamination from packaging.

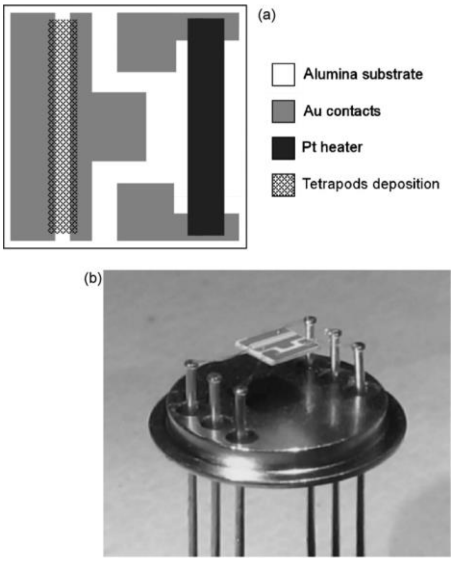

Figure 7. ZnO tetrapods-based sensor prototype [168] made at IMEM-CNR laboratories.

The use of catalyst metal coatings on ZnO NWs is found to greatly enhance, in particular, the detection sensitivity for hydrogen. The high surface-to-volume ratio of nanowires and the ability to use simple contact fabrication schemes make them attractive for hydrogen sensing applications functionalities [158]. For example, Tien et al [170] reported that Pt-coated ZnO nanorods are good potential candidates for detection of ppm concentrations of hydrogen at room temperature. Such a sensor has a rapid initial response to hydrogen exposure, while effective nanorod resistance continues to change for more than 15 min exposure. This suggests chemisorption of hydrogen to the metal/ZnO interface is the rate-limiting step in conductance changes to the ZnO. Recovery of initial resistance upon removal of hydrogen from the ambient was rapid. An activation energy of 12 kJ/mole was measured for the chemisorption of hydrogen onto the metal coating surface [170].

Also the monitoring of breath gases can potentially be used as disease-specific biomarkers. Acetone gas is indicative of diabetes [171], ammonia gas for renal disease [172], ethanol for hepatic steatosis [173] and trimethylamine for uremic patient [174]. Park et al [175] presented a technology to design and fabricate nanostructured gas sensors in fabric substrates, which is shown in Figure 8. Nanostructured gas sensors were fabricated by constructing ZnO nanorods on fabrics including polyester, cotton and polyimide for continuous monitoring of wearer's breath gas that can indicate health status. The developed fabric-based gas sensors demonstrated gas sensing by monitoring electrical resistance change upon exposure of acetone and ethanol gases. This study is an important cornerstone to develop wearable gas sensors for health monitoring in the conjunction of engineering and design disciplines.

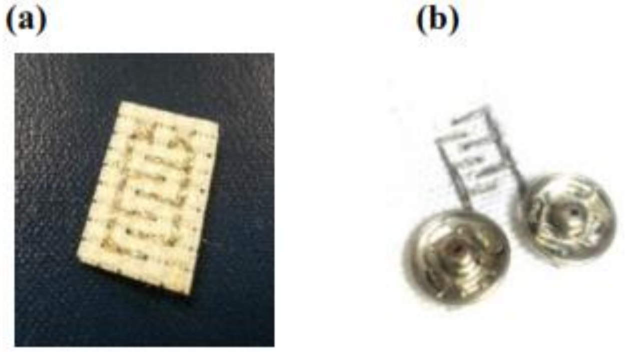

Figure 8. Design of embroidered electrode for wearable gas sensor based on ZnO nanorods, and (b) wearable gas sensor with snap buttons [175].

2.1.2.3 ZnO nanowires for UV photodetectors

The development of UV detectors in the spectral range shorter than λ~400 nm has attracted much interest recently because of potential applications in detection of biological materials and for the defense industry. In the former case, the UV photons are used to excite fluorescence at UV wavelengths from biological materials of interest and this is detected by the photodetectors. Wide bandgap detectors are very useful in bio-warfare agent detection because some pathogenic biological molecules fluoresce in the UV spectral region [176]. There is also interest in developing ZnO/ZnMgO nanowire UV detectors as a complementary technology for UV detection, with the following advantages relative to the nitrides [177-184]. ZnO-based materials offer similar band-gaps to the nitrides, but it has several advantages:

- ZnO nanowires can be grown at much lower-temperature on a wider range of substrates, including large area Si or cheap transparent materials such as glass.
- The nanowires can be transferred to any substrate for integration with other sensors and are compatible with low temperature materials such as polymers.

- The nanowire UV detectors operate at very low power levels compared to existing nitride UV detectors.
- The fabrication approach developed previously for ZnO nanowire gas sensors allows for a simple, low-cost, single-step approach to realizing robust UV detectors.
- ZnO nanowire UV detectors can be readily integrated with on-chip wireless circuits to provide data transmission to a central monitoring location. Thus, it is possible to have either single detectors or arrays of detectors that operate at very low-power levels and do not need constant monitoring by humans.
- The versatility of substrates also makes it possible to utilize 3D stacking technology developed for silicon substrates for data intensive applications. Devices stacked with overlying ZnO sensors would permit maximum sensor density and higher levels of integration with silicon or gallium arsenide electronics.

2.1.2.4. ZnO nanowires for biomedical applications

Thanks to their peculiar properties ZnO nanowires and other nanostructure have been used also in biomedical applications. Medical diagnostic, drug delivery and local cancer treatments are today some of the main targets for this nanomaterial, although most of the research in these fields is still under way. However some promising result is emerging, especially in the bio-sensing and diagnostic field. Here we describe some examples as a proof of concept.

In recent years, the need for high-performance glucose sensors has been increasing because the fast and precise detection of glucose is a decisive means to diagnose diabetes or tabolic disorders that are currently widespread around the globe. Accordingly, many forts have been made to develop glucose sensors with excellent glucose-detection capability based on electrochemistry, chemoluminescence, etc.

In particular, the enzyme-immobilized electrochemical glucose sensor based on ZnO nanorod is one of the most intensively investigated sensor types owing to its high selectivity, sensitive glucose detection, and relatively low-cost fabrication and is given in Figure 9 [185]. An important issue with this type of glucose sensor is that the materials should possess efficient enzyme loading characteristics and good biocompatibility. Zinc oxide (ZnO) has been used extensively as a support material for enzyme immobilization. In the literature, nanorods [186], nanocombs [187], and nanowires [188] of ZnO have been successfully used as materials for enzyme immobilization. In particular, aligned ZnO nanorod films directly grown on the indium tin oxide layer were successfully employed for immobilization of glucose oxidase, demonstrating their potential for the use of amperometric glucose biosensors [189].

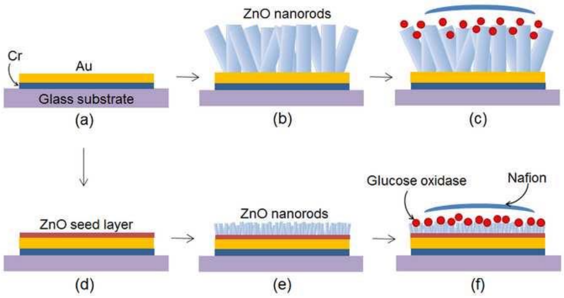

Figure 9. Fabrication of ZnO nanorod-based glucose sensors [185].

ZnO nanorods/Au hybrid nanocomposites were also used to entrap glucose oxidase, revealing reliable glucose-sensing capability [191]. Two review papers well describe the state-of-the-art use of ZnO materials for enzyme immobilization in electrochemical-based biosensors [191] and the surface functionalization of ZnO materials for biosensing [192]. The glucose-sensing capabilities were found to be proportional to the surface area of the nanorods, suggesting that densely packed, slim, and long ZnO nanorods are more favorable for obtaining superior ZnO nanorod-based glucose sensors [193-195].

AlGaN/GaN HEMTs with ZnO nanowires on the gate region can be used for measurements of pH in exhaled breath condensate (EBC) and glucose, through integration of the pH and glucose sensor onto a single chip and with additional integration of the sensors into a portable, wireless package for remote monitoring applications. The human pH value can vary significantly depending on the health condition. Since we cannot control the pH value of the EBC samples, we needed to measure the pH value while determine the glucose concentration in the EBC. With the fast response time and low volume of the EBC required for HEMT based sensor, a handheld and real-time glucose sensing technology can be realized as shown in Figure 10 [158].

Lactic acid can also be detected with ZnO nanorod-gated AlGaN/GaN HEMTs. Interest in developing improved methods for detecting lactic acid has been increasing due to its importance in areas such as clinical diagnostics, sports medicine, and food analysis. An accurate measurement of the concentration of lactic acid in blood is critical to patients that are in intensive care or undergoing surgical operations as abnormal concentrations may lead to shock, metabolic disorder, respiratory insufficiency, and heart failure.

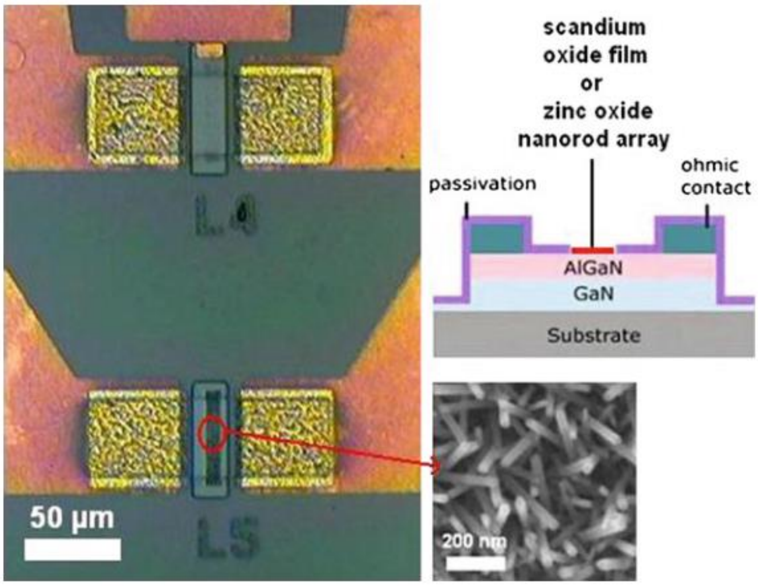

Figure 10. SEM image of an integrated pH and glucose sensor. The insets show a schematic cross-section of the pH sensor and also an SEM of the ZnO nanorods grown in the gate region of the glucose sensor [158].

Lactic acid concentration can also be used to monitor the physical condition of athletes or of patients with chronic diseases such as diabetes and chronic renal failure. In the food industry, lactate level can serve as an indicator of the freshness, stability and storage quality. For the reasons above, it is desirable to develop a sensor capable of simple and direct measurements, rapid response, high specificity, and low cost. The array of one-dimensional ZnO nanorods provided a large effective surface area with high surface-to-volume ratio and a favorable environment for the immobilization of Lox [158].

2.1.2.5 ZnO nanowires for piezoelectric humidity sensors

Piezoelectric humidity sensors have been demonstrated by the following experiments [196]. The devices were fabricated using a single ZnO nanobelt bridging two Au electrodes. Poly(Nisopropylacrylamide) (PNIPAM) and poly(diallyldimethylammonium chloride) (PDADMAC) were functionalized alternatively layer-by-layer on the top surface of the nanobelt. Measurement of a conducting channel that contained only multilayers of polymers also showed a drastic increase in conductivity a bent ZnO NB could produce a piezoelectric potential across the NB because of the strain-induced piezoelectric effect, which may trap and deplete the carriers in the nanobelt, analogous to the case of the PE-FET, resulting in a decrease of conductivity. This is a different detection mechanism in comparison to the sensors based on FETs.

2.1.2.6 ZnO nanowires for pH measurement

The measurement of pH is needed in many different applications, including medicine, biology, chemistry, food science, environmental science as well as oceanography. Solutions with a pH less than 7 are acidic and solutions with a pH greater than 7 are basic or alkaline. It has been found that ZnO nanorod surfaces respond electrically to variations of the pH in electrolyte solutions introduced via an integrated microchannel. The ion-induced changes in surface potential are readily measured as a change in conductance of the single ZnO nanorods and suggest that these structures are very promising for a wide variety of sensor applications [135, 166].

2.1.2.7 ZnO nanowires for self-powered multifunctional devices

A more complex device, or “system”, can be designed by couplying some of the previous devices in a single one, where for example ZnO nanostructures are both used for their sensing capabilities and for the energy harvesting that allows the device to be self-powered.

This kind of approach has been successfully applied mainly for silicon-based devices. Nanogenerators (NGs) based on the piezoelectric, triboelectric or pyroelectric effect, which can convert trace energy in the environment into electric energy, have performed as an efficient energy source for nanodevices and nanosystems. Self-powered nanosystems have been proved viable in self-powered pH sensors, UV sensors, self-charging power cells, small liquid crystal displays, commercial laser diodes, etc. Most recently, a new type of self-powered nanosystem, named as an active sensor, has been demonstrated by treating the output electric signal from NGs as either a power source or sensing signal in response to the change in environment, such as ambient wind velocity detectors, automobile speedometers and magnetic sensors [197]. Among various NG-based active sensors, ZnO nano/micro-wires have been intensively investigated because of their semiconducting and piezoelectric coupling properties [198, 199]. Taking a ZnO-based active photodetector as an example, ZnO nanowires generate different piezoelectric output under different intensities of UV illumination because the carrier density is significantly influenced by the intensity of UV illumination [200, 201].

Because of their semiconducting property, ZnO one-dimensional nanostructures are considered as extremely sensitive and fast responsive materials for gas sensing due to their large surface-to-volume ratio and surface adsorption activity [202-204]. If the gas sensing and piezoelectric properties of ZnO NWs NG can be coupled into a single physical process then a new type of self-powered active gas sensor can be realized through its surface-state-dependent piezoelectric output.

The output of a piezoelectric nanogenerator fabricated using ZnO nanowire arrays by Xue et al. [197] (Figure 11) is largely influenced by the density of the surface charge carriers at the nanowire surfaces.

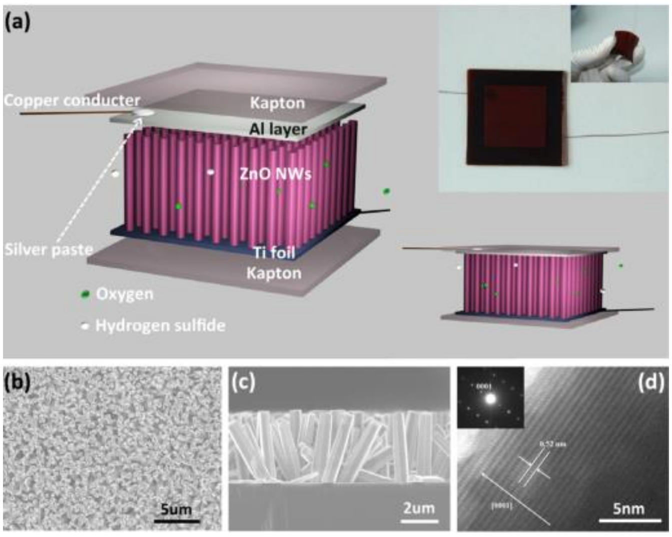

Figure 11. Structural design of nanogenerator using ZnO NW arrays [197]

Adsorption of gas molecules could modify the surface carrier density through a screening effect, thus, the output of the NG is sensitive to the gas concentration. Based on such a mechanism, they first studied the responses of an unpackaged NG to oxygen, H_2S and water vapor and demonstrated its sensitivity to H_2S to a level as low as 100 ppm. Therefore, the piezoelectric signal generated by a ZnO NWs NG can act not only as a power source, but also as a response signal to the gas, demonstrating a possible approach as a self-powered active gas sensor.

2.2 Silicon carbide nanowires

2.2.1 Silicon carbide properties

One-dimensional (1D) semiconductor nanostructures (wires, rods, belts, and tubes) have become the focus of intensive research, owing to their unique application in the fabrication of electronic, optoelectronic, and sensor devices on a nanometer scale. They possess novel properties intrinsically associated with low dimensionality and size confinement, which make “bottom-up” construction of nanodevices possible [205]. SiC has very unique properties, such as wide bandgap, excellent thermal conductivity, chemical inertness, high electron mobility, and biocompatibility, which promise well for applications in microelectronics and optoelectronics, and has thus attracted much interest from the materials and devices communities among the semiconductor nanowires [206-208]. In particular, SiC nanowires are used for the reinforcement of various nanocomposite materials or as nanocontacts in harsh environments, mainly due to their superior mechanical properties and high electrical conductance. Hence, research on 1D SiC nanowires is highlighted, both from the fundamental research standpoint and for potential application in nanodevices and nanocomposites. Various morphologies realized in SiC nanostructures are nanoneedles [209], flowers [210], beaded SiC nanochains [211], bamboo-like NWs [212], SiC hierarchial nanostructures [213, 214], ultralong NWs [215] and so on. Studies of controlling the shape of nanostructures become more attracting. Wu et al [216] changed the reaction temperature to obtain three different SiC NWs and Wang et al [217] varied the source species pressure to get control in the morphology.

2.2.1.1 Crystallographic structures of SiC

SiC is a IV–IV compound semiconductor, having a similar crystal structure to that of diamond with half of carbon atoms in diamond replaced by Si atoms to produce SiC. Crystal structure of 3C-SiC (cubic) and (b) 6H-SiC (hexagonal) polytypes is given in Figure 12. SiC is one of the most important materials for industrial applications and basic research, and has been applied in many areas, from cutting tools to nanoscale electrical devices. However, unlike diamond, SiC may exist in the form of numerous polytypes (different crystal structures). The crystalline structure of SiC can be considered to consist of the close-packed stacking of double layers of Si and C atoms. Each C or Si atom is surrounded by four Si or C atoms in strong tetrahedral sp^3 bonds. The distance between neighboring Si and C atoms is approximately 3.08 Å for all polytypes [218, 219]. There are more than 200 polytypes. The polytypes can be defined by the number of stacking layers in a unit cell. The atom arrangements of the most popular polytypes are 3C, 2H, 4H, and 6H. In polytype notation system, the first number denotes the periodicity and the following letters C or H refer to cubic and hexagonal structures, respectively. Though many polytypes of SiC are in existence, their molecular structure is identical. Except carbon atom covalently bonded with other four Si atom instead of carbon atoms, the entire configuration of unit cell of SiC is similar to diamond.

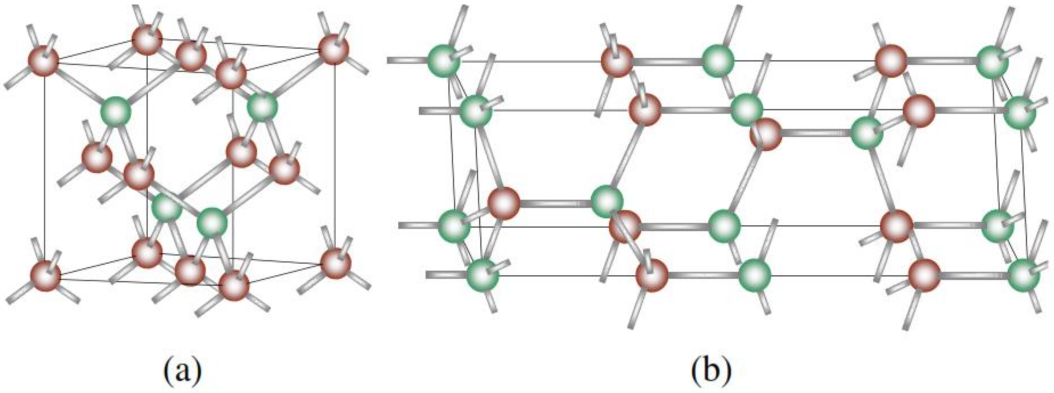

Figure 12. Crystal structure of (a) 3C-SiC (cubic) and (b) 6H-SiC (hexagonal) polytypes [218]

The 3C-SiC polytype is the only cubic polytype and it has a stacking sequence ABCABC. 4H-SiC consists of an equal number of cubic and hexagonal bonds with stacking sequences of ABCB. Two-thirds of 6H-SiC is composed of cubic bonds and one-third of hexagonal bonds, with stacking sequences of ABCACB. 4H- and 6H-SiC are called α-SiC, 3C-SiC is referred to as β-SiC because it is the only cubic SiC crystalline structure, and corresponds to the zinc-blende structure. As is obvious from the definition, cubic structure of 3C-SiC shows zero hexagonality. The band energy gap of SiC polytypes tends to increase with increasing the degree of hexagonality. In general, β-SiC, which often appears at low temperature, is easy to nucleate and grow. However, 4H-SiC and 6H-SiC are known as high-temperature stable polytypes, which need relatively high temperatures to grow (the 2H polytype is typically unstable because it can transform to a mixture of 3C and 6H polytypes above 400°C) [218].

2.2.1.2 Basic properties of bulk SiC

SiC materials are extremely hard, very inert, and have high thermal conductivity. Properties such as the breakdown electric field strength, the saturated drift velocity, and the impurity ionization energies are unique for the different polytypes [205]. β-SiC possesses the smallest bandgap (~2.3 eV) and has the highest electron carrier mobility compared with α-SiC, which makes it an important polytype in the microelectronics industry [220]. Because of these excellent properties, SiC is a perfect material in the electronics industry, with a wide application in the areas of high-temperature, high-power, high-frequency and optoelectronic devices, including rectifiers, power switches, RF, and microwave power devices [221, 222]. Besides, SiC, known for its high-temperature structure and reinforced composite material, can be also find application in the aerospace, car, machine, and petrochemical industries [222–227]. Typical properties of SiC polytypes are summarized in Table 2.

Parameters	**3C-SiC**	**4H-SiC**	**6H-SiC**
Lattice a (Å)	4.36	3.08	3.08
Lattice a (Å)	4.36	15.12	10.05
Bond length (Å)	1.89	1.89	1.89
Thermal expansion coefficient (10^{-6} K)	3.0	-	4.5
Density (g cm^{-3})	3.2	3.2	3.2
Thermal conductivity (W cm^{-1} K^{-1})	5	5	5
Melting point (°C)	2830	2830	2830
Mohs hardness	9	9	9
E_g (eV)	2.3	3.3	3.0
Electron mobility ($cm^2V^{-1}s^{-1}$, 300K)	≤ 1000	≤850	≤450
Hole mobility ($cm^2V^{-1}s^{-1}$, 300K)	≤40	≤120	≤100

Table 2. Typical properties of SiC polytypes [220, 228, 229]

2.2.1.3 Wide range of properties of SiC focused towards applications

The wide band gap of SiC (2.3 - 3.3 eV) opens up for SiC devices to be used at very high temperatures (in excess of 600 °C), because the thermal generation of electron-hole pair is low. Thanks to its wide bandgap, SiC material shows a higher than 10^{12} cm^{-3} intrinsic carrier concentration at over 1000 °C. SiC also possesses a very high breakdown field (3 - 5 M V cm^{-1}) due to wide band gap. The breakdown field of SiC is about ten times higher than the one of Si. The high electric breakdown field allows the fabrication of SiC devices with a theoretical power efficiency two orders of magnitude better than Si devices. High breakdown electric field of SiC enables to fabricate the device with small size, low-resistive and high power. The combination of high breakdown field and high saturated electron drift velocity values allowed also publication of high performance microwave PIN diodes [230]. SiC is also desirable for UV optical detection applications in consequence of insensitivity to longer wavelengths and very small dark current levels, even at elevated temperatures. Low dark current enables SiC photodiodes to exceed Si UV sensitivities by four orders of magnitude. The ruggedness of SiC is also an important advantage for UV detection, where hostile environments such as in-situ combustion monitoring and satellite-based missile plume detection are involved.

Generally speaking, the greater the wurtzite component, the larger is the band gap. 6H-SiC polytype is most easily prepared and best studied, while the 3C and 4H polytypes are attracting more attention due to their superior electronic properties. In addition, SiC has a large avalanche breakdown field, and an excellent thermal conductivity, all of which make it ideal for high-power operation. Despite of its indirect band gap, blue SiC LEDs are commercially available. The efficiency of these devices is less than 0.03%, but that is partly compensated by the ability to drive these LEDs at high currents. Moreover, large Si-C bonding energy allows use of elaborated yellow, green and blue emitting SiC LEDs in significant temperature and radiation fluence ranges [231].

SiC has nearly three times as high thermal conductivity (350 - 490 W m^{-1} K^{-1}) compared to Si and 7 times higher than GaAs, and is superior to Cu. Therefore, SiC based devices operate at extremely high power levels, since it can dissipate heat more efficiently. If this property is coupled with low thermal expansion, SiC devices could be used for specific applications, which require thermal shock resistant environment. Due to these properties of SiC mentioned above, SiC is expected to operate with the most advantageous benefits over conventional Si and GaAs electronics in high-power applications.

In addition, SiC is attractive for nonlinear optics applications. The optical damage threshold is an important characteristic of any nonlinear material because of the higher device efficiency with increasing power density. The performances of many materials are limited by modest damage thresholds. The extremely high melting point (T ~ 3100 K) and thermal conductivity of bulk SiC suggest the possibility of a high durability and threshold values. Large electro-optic coefficients are expected in SiC polytypes, which will make this compound an excellent candidate for electro-optical devices in the visible and near ultraviolet region [232]. SiC has very high etch resistance in most acid and alkaline solutions due to its chemical inertness. Therefore, SiC has attracted much attention as a possible material for microelectromechanical systems (MEMS) operating in harsh environments (aggressive and corrosive media). In addition, the native oxide is silicon dioxide, which makes SiC directly compatible with the usual Si technology.

SiC is one of the semiconducting materials that possess an excellent biocompatibility and great sensing potentiality compared to Si, which is widely used for fabrication of biological systems. According to our knowledge, several reports are found in the literature, which investigates crystalline SiC biocompatibility [233, 234]. Coletti and Saddow et al [233] have investigated the biocompatibility of SiC polytypes compared with Si by culturing mammalian cells directly on substrates. SiC in all its phases shows better proliferation than Si for all mammalian cell lines studied. There are no significant differences of the cell proliferation on different SiC polytypes. They suggest that two possible explanations could be the basis of the enhanced cell proliferation observed on SiC substrates. From the contact angle images, SiC surfaces are more hydrophilic than Si surfaces and mammalian cells preferentially adhere to hydrophilic surfaces. It is known that surfaces with a normal electrochemical potential close to the one of the cells are more biocompatible [233]. Since the electrochemical potential of carbon is comparable to that of living tissue, the higher carbon concentration of the SiC surfaces most likely justifies SiC greater biocompatibility. The results of this biocompatibility study show that SiC is indeed a better promising material for bio-applications than Si, whose cytotoxicity has been reported by several studies [233]. These results open up exciting perspectives for in a variety of medical applications [234] (e.g. implant coating material) and bio-electronic devices.

2.2.1.4 Properties of SiC Nanostructures

Field Emission of SiC Nanowires

Due to the small curvature of the tip radius, high ratio, chemical inertness, and electrical conductivity, SiC wide-bandgap semiconductors are considered to be promising for the next generation of large-area filed-emission flat panel displays (FEDs) [235-239]. A series of experiments have been carried out to investigate the field-emission characteristics of the 1D SiC nanostructures, which indicate that the SiC nanowires are characteristic of excellent emitting behavior for application in field-emission technology. The field-emission measurements were carried out in a vacuum chamber at a pressure of 3×10^{-5} Pa at room temperature. A platinum film coated on glass substrate with SiC nanowires was used as a cathode and a stainless steel plate with a diameter of 6 mm was used as an anode. Before testing the field emission, a 0.008 g SiC sample (HF-etched SiC fabricated by the high-frequency heating invented by us) was sonicated into a suspension in deionized water (DE) for 20 min and 20 drops of DE solution of SiC were dropped on the platinum film and dried at 50 °C. The distance (d) between the emitting surface and the plate was determined by first lowering the plate to the product until electric contact was observed, then lifting the plate to a certain value [240]. In other words, the field emission from SiC nanowires is a barrier tunneling, quantum mechanical process. Besides, the straight lines also show that the field emission is independent of the anode-sample separation, and only a function of the applied voltage.

Optical Properties of SiC nanowires

There have been some reports on the optical properties of SiC nanowires. Experiments showed that SiC nanowires have a significant redshift owing to the size confinement effect. The SiC nanowires have the typical Raman features at ∼784 and 938 cm^{-1} and both peaks have a marked redshift of 12 and 34 cm^{-1} compared to the TO and LO phonon modes of bulk SiC. SiC/SiO_2 nanocables were synthesized by the low-cost arc-discharge method in deionized water [241]. The SiC with 10 nm core diameter possesses two broad PL peaks at 317 and 368 nm. But two emission peaks of the SiC nanowires with 20 nm diameter are located at 312 and 393 nm. It is believed that the second peak results from the central β-SiC nanowire and the blueshift may be the result of the quantum size effects. The thinner the central SiC nanorod is, the higher the correspondent PL peak energy is.

Electrical properties of SiC nanowires

The electrical properties of SiC NW has not been investigated in much detail relative to that of Si NW. Up to now, only a few studies have been reported on the electrical properties of 3C-SiC NW. It might be due to very high structural defects density of SiC NW associated with a high level of n-type unintentional doping and weaker electrostatic gating effects of back gate configuration and poor-quality SiC NW-gate oxide interface. The n-type SiC NW FET shows high electric conductivity (2.2×10^{-2} Ω cm) for 0 V gate voltage due to highly n-type doping level [242]. The measured transconductance (g) has value of several 10^{-10} Ω^{-1}m [242, 243]. The estimated n-type doping concentration by fitting I-V curve with simulation program (Silvaco) was around 1×10^{19} cm^{-3} [243]. Best electron mobility value measured on SiC NWFET was around 15 cm^2 V^{-1} s^{-1} [244].

Rogdakis et al [243] have theoretically investigated the effect of doping concentration to explain poor performance of SiC NWs FETs. Their simulation results show that the device could have a good gating effect with high mobility (> 80 cm^2 V^{-1} s^{-1}) at a doping level of 10^{17} cm^{-3} with an ideal interface (that is to say, without interface scattering). Chen et al [245] have reported for the first time the fabrication of p-type SiC NW FET using a Al-doped 3C SiC NW. But, one again p-type FETs based on an individual Al-doped 3C-SiC NW exhibits a low mobility 6.4 cm^2 V^{-1} s^{-1}. The estimated hole carrier density from I-V curve was determined to be 1.7×10^{17} cm^{-3}. To exploit excellent electrical property of SiC NWs, many efforts need to be put forth, in particular, to minimize the structural defects (SFs) and unintentional doping. The devices with either ideal ohmic or Schottky barrier contacts are an important parameter to determine the device operating modes. And it is also strongly crucial to investigate about reliable and reproducible of complementary doping (p-type) of SiC NWs.

Mechanical Properties of SiC nanowires

The mechanical properties of nanostructures have aroused considerable interest due to possible stronger property than their bulk counterparts. This might be attributed to a reduction in the number of defects per unit length (compared with larger structures), which leads to mechanical failure. For the practical applications of SiC NWs, it is important not only to understand its mechanical properties, such as toughness and hardness, but also to investigate mechanical response, such as elastic-plastic response and brittle-ductile transition, in the nano-domain [246]. Researchers have investigated the mechanical properties of various nanowire systems with different approaches, such as nano-indentation [247], atomic force microscopy (AFM) [248] and mechanical resonance by in situ TEM [249].

Two main approaches have been developed to characterize the mechanical properties of various NWs. The first one has measured the strength of SiC nanorods with AFM by physical bending of the SiC nanostructure, which was pinned at one end to molybdenum disulfide surfaces [248]. The bending force was measured versus displacement along free-end lengths. The measured bending strength and Young’s modulus of SiC nanostructures were 53.4 and 660 GPa, respectively. Young’s modulus of SiC nanostructure shows were substantially greater than those found previously for any type SiC structures (SiC whiskers and fibers), and they approaches theoretically predicted value (600 GPa) for [111] oriented bulk SiC [248].

The second method used electric-field-induced resonance for measuring the mechanical properties by the field emission microscopy (FEM) [250] and in situ TEM [249]. One end of the NW is pinned on the tip, and an oscillating voltage is applied across the ball and its counter electrode. Mechanical resonance occurs when the applied frequency matches the natural resonance frequency of NWs. Wang et al [249] have measured the mechanical property of biaxial SiC-SiO_x NWs by in situ TEM. They have proved that the effective Young’s modulus (E_{eff}) of biaxial structured SiC–SiO_x NWs is the combination from SiC and SiO_x. The Young’s modulus determined by FEM yielded a high Young’s modulus value (Y =750 GPa) [250], which is corresponding to the highest value reported in the literature for a bulk single crystal of 748 GPa.

Han et al [251] have directly observed the mechanical behavior of SiC NWs in situ TEM measurement by bending individual NWs. Instead of a crystalline fracture (or any cracks) under deformation, the SiC NW has transformed from crystalline to amorphous at the mostly strained region. Large strain plasticity of SiC NWs at temperatures close to room temperature has been observed for the first time in this study. From their experimental results, the plastic deformation process of SiC NWs is typically regarded as three stages, dislocation initiation, dislocation propagation and amorphization. Zhang et al [246] have investigated the plastic deformation and fracture behavior of individual SiC NWs by in situ stretching equipment in a SEM. The plastically deformed region shows identical size and morphology without any necking appearance, indicating a super-plastic deformation.

Super-Plasticity of β-SiC NWs at low temperature was reported by Yufei et al [252]. Super-plasticity is the ability of a material to exhibit an exceptionally large strain deformation rate during extensile deformation process [253]. Ceramics and semiconductors, at room temperature, or more specifically below a transition temperature, behave as nearly ideal brittle solids that fail due to fracture without evidence of plastic deformation [254, 255]. SiC, as a reinforcing material behave with high hardness, high strength and high stiffness but brittleness. Bulk SiC ceramic material can transform to be ductile above 1000 °C [256, 257]. As a wide bandgap semiconductor material, SiC nanowires (SiCNWs) are very attractive for applications in nanoelectronics that are able to be operated at high temperatures, high powers, high frequencies, and in harsh environments [258-260]. For the practical use of SiC NWs, it is fundamentally important not only to investigate electronic properties, but also to understand mechanical properties, such as elastic-plastic response, brittle-ductile transition (BDT) [261]. The mechanical properties of semiconductor nanowires can be rather different from those of bulk materials. Making a complete elucidation of these properties would be especially important [262, 263]. Atomistic molecular dynamics (MD) simulations can provide detailed information about dislocation motion, crack branching, fracture, and BDT of nanowires [264-266]. Super-plasticity of single-crystal beta-SiC [111] nanowires for > 200 % elongation was observed by in situ axial-tensile experiments in a scanning electron microscope. The SiC nanowires were characterized by a bamboo-like structure appearing as the 3C structured segments intergrowth along the nanowire. The axial localized plasticity and super-plasticity are suggested to result only from the 3C segments, through dislocation generation, propagation and amorphization in contrast to the highly defected structural segments that conduct elastic-deformation only, owing to the lack of slip systems. These results provide key information for understanding the mechanical behavior of SiC nanowires.

2.2.2 Multidisciplinary applications of SiC nanostructures

The great interest that SiC has gathered in latest years is due the possibility to combine in one single material good semiconducting and chemical properties, biocompatibility and sensing potentiality. SiC chemical inertness, wide bandgap, tribological properties and hemocompatibility make it a very promising candidate for biosensors, interface with biological tissues and lab-on-chip medical devices. Moreover, the possibility to realize nanostructures opens the possibility to assembly novel nanoscale devices and arrays by the bottom-up approach, and to enhance the sensing capabilities of the material thanks to the high surface/volume ratio. Low dimensional SiC may exhibit distinctive electronic, optical, thermal and chemical properties, as well as carrier quantum confinement. Many one-dimensional structures have proven to exhibit better properties than the same material with bulk size, and this would permit to combine appropriate building blocks to obtain unique functions, or combinations of functions, in integrated nanosystems.

Only few of the most notable applications of nano-SiC will be cited here. Range of application and issues arising in case of SiC nanowires (NWs) were discussed recently by Zekentes et al [267]. The study of mechanical, thermoelectric and hydrophobic properties of SiC NWs is limited and additional work is necessary towards their complete description, which is necessary for evaluating their potential for related applications. Moreover, there is a series of quality criteria with different weight factors for each application. There are still theoretical and experimental works to be conducted on nano-SiC to fully realize their potential for the manufacture of stable light emitters and for nonlinear optics, while biocompatibility and hydrophilicity of the bulk material make SiC nanostructures an ideal candidate for application in biology and medicine.

2.2.2.1 Biomedical applications

SiC has been proposed as a suitable material for bio-related in vivo and in vitro applications due to its biocompatibility and chemical inertness [268]. For in vivo applications, SiC is expected to be a promising coating material of implantable parts, such as total hip replacement, because it possess biocompatibility, chemical inertness and superior tribological properties compare to common orthopedic metals [269]. Traditional orthopedic materials (such as titanium and stainless steel) are biocompatible for use in joint replacement. However, it is a relatively soft metal and wears easily, which leads to component loosening. Therefore, mechanically stable and biocompatible SiC material is expected to be an excellent coating material for in vivo applications [269]. But, there is no report for in vivo applications based on SiC NWs up to now. SiC NWs are potentially applicable as coating materials or fillers of traditional orthopedic materials to increase the biocompatibility and mechanical properties.

Cancer treatment

Quantum dots (QDs) can be useful tool for monitoring cancerous cells and for providing a mean to better understand its evolution for in vitro analysis due to its excellent luminescent property. Novel implementation of 3C-SiC NPs has been reported recently by Mognetti et al [270]. The authors claim about the selective influence of SiC NPs on viability and proliferation on oral squamous carcinoma (AT-84 and HSC) and immortalized cell lines (S-G). More importantly, reported cytotoxicity was higher for cancer than for immortalized cells. Since one of the limitations of classical antineoplastic drugs is their lack of selectivity, these results open a new way in the search for antiproliferative drugs.

Bio-labelling applications

SiC QDs do not need a protective shell to avoid the cytotoxicity owing to its biocompatibility. Despite of excellent biocompatibility of SiC NWs, to the best of our knowledge, there has been no report of the bio-sensor based on SiC NWs. Two groups have reported application of SiC quantum dots (QDs) for cell imaging applications [271, 272]. For in vitro application, 3C-SiC quantum dots (QDs) with no protective shells have been used for fluorescence imaging of biological living cells [232]. Botsoa et al [272], highlighted high penetration, accumulation, and heterogeneous distribution of the bare QDs in the intracellular environment. The main advantage of the elaborated 3C-SiC QDs, over conventionally used QDs based on II-VI semiconductors is the non-cytotoxicity for in vitro analysis and their potential biocompatibility for in vivo studies. Under the UV/violet excitation, the cells marked by the QDs were very bright while the autofluorescence of unmarked cells was not visible at all. Comparison between the fluorescence micrographs and the microscope photos obtained under white light demonstrates that the fluorescing QDs are strongly localized inside the cells. Indeed, one can easily notice a heterogeneous distribution of the fluorescence intensity inside the cell. Since the highest intensities correspond to the position of the nuclei, it means that the QDs penetrated into the cells and preferentially concentrated at the nuclei. However, authors left the question whether the QDs entered the nucleus or were just concentrated on the outside of the nucleus membrane.

Nanoporous filtration membranes

Rosenbloom et al [273] have fabricated free-standing SiC nanoporous membranes obtained by electrochemical etching in both p-type and n-type material. Authors showed that these membranes permit the diffusion of proteins up to 29000 Daltons (1Da=$1.660538921\times10^{-27}$ kg), while those of 45000 Da and higher were excluded. The size range of proteins able to cross the membranes includes many important cell signalling molecules, which tend to be small. This suggests that the material may be suitable for biosensor and other applications where permeability of small molecules and small proteins and exclusion of larger molecules is desirable. It was confirmed that porous SiC has very low protein adsorption and comparable to the best commercially available polymer nanoporous membrane.

2.2.2.2 Sensor applications

Over the past decade, there has been an increased interest in the fabrication of chemiresistive-type biosensors that have the ability to selectively detect the binding of label-free biomolecules through a mechanism in which device resistivity changes upon bioconjugation [274-279]. Surface functionalized nanowires (NWs) are ideal active elements for such biosensors due to their high surface-to-volume ratio [278, 279]. In terms of materials systems, silicon (Si) and silicon carbide (SiC) are attractive semiconductors for inclusion in biosensing devices due to their electronic properties [274, 275, 279, 280], biocompatibility and ability for selective functionalization toward specific analytes [274-277, 281, 282]. For developing semiconductor NW-based devices that directly sense the binding of biomolecules through resistivity changes, an analyte-specific functionalization of the NW surface is necessary. An understanding of the mechanisms by which the functional and analyte molecules bind to the surface is essential for device fabrication and usage. A solution-based sequential layer functionalization method for streptavidin protein immobilization on Si and SiC NWs was reported by Williams et al [283] which enables the assembly of multifunctionalized NWarrays on a single biosensing chip. Si and SiC NW surfaces functionalised with 3-aminopropyltriethoxysilane/biotin present selective and specific streptavidin conjugation, making both of these semiconductors suitable for NW-based sensing platforms for the multiplexed electrical detection of bioanalytes.

Generally, NWs FET regarded as a basic component and structure for sensing devices. Conventional SiC NWs FET shows poor performance in terms of low mobility and weak gate owing to high density of SFs associated with a high level of non-unintentional doping. Therefore, SiC NWs based sensor, which modified or functionalized the channel of SiC NWs FET with molecular receptors, could not guarantee a sensitive and selective operation due to poor electrical properties of SiC NWs FET. Thus, the growth of defect-free SiC NWs with controlled doping is strongly needed to realize the excellent performance of bio-sensor based on SiC NWs.

2.2.2.3 Energy harvesting applications

SiC is known to be a material highly suitable for fabricating devices able to operate in harsh environment [284] and this work is the first step towards the fabrication of a high temperature micro-supercapacitor. Supercapacitors have attracted much attention for energy storage applications, owing to their long cycle life and high power densities. Their specific capacitance has been studied as a function of their morphology (size, diameter) and the optimal growth conditions have led to a capacitance comparable to the state of the art. They exhibit an exceptional stability, with a lifetime exceeding 10^6 charge/discharge cycles. An excellent thermal stability is expected for SiC NWs, opening the way to the fabrication of high temperature micro-supercapacitors. The measured capacitance of the NWs sample is 26 times higher than the SiC thin film alone and 7 times higher than the SiC thin film covered with annealed Ni. As expected, SiC NWs, thanks to their high aspect ratio, exhibit a high specific capacitance around 400 $\mu F/cm^2$ [285].

2.2.2.4 Electronics MEMS/NEMS

SiC is an excellent structural material for MEMS and NEMS applications due to its outstanding mechanical, chemical, and electrical properties combined with its compatibility with Si micromachining techniques. Nanoscale electromechanical devices and systems (NEMS), with their ultrasmall sizes, ultralow operating power levels, high operating speeds and low energy losses, offer interesting perspectives for technological applications such as resonant sensing, RF signal processing and nanomechanical computing. It has been reported that suspended structures that are active elements in NEMS/MEMS devices can be made by depositing or directly growing nanomaterials on a substrate [286-288]. The principles of MEMS can be scaled down to nanoscale dimensions of NEMS for increased sensitive to external perturbations.

The controlled assembly of nanomaterials onto the specified positions is challenging because the synthesis of nanomaterial relies on stochastic process from vapor phase chemicals. An advantage of using a synthesized nanomaterial is that its dimensional parameter, i.e., the diameter for an one-dimensional nanowire or the thickness for a two-dimensional sheet or film, can be reduced to an atomic level. This characteristic is useful for minimizing devices. The high aspect ratio structure can enhance the sensitivity to molecular adsorption and the mechanical flexibility to external forces. However, it is challenging to integrate these nanometer scale materials into reliable devices. In contrast, the material of relatively large scale is more stable and more easily handled for fabrication. A stable contact between the nanomaterials and electrodes still remains a critical challenge for nanoscale devices [289]. Jung et al [289] used commercially available β-SiC nanowires having few hundred nanometers diameter and 1 to 100 µm in length for fabricating a suspended device structure. SiC based NEMS show substantially higher frequencies than other materials due to high values of parameters related to the nano-resonator itself, such as Young’s modulus and quality factor, which describes the strength of the damping of its oscillations relative to its center frequency.

Among the smallest and most sensitive NEMS are resonators based on very thin NWs [290, 291]. Such NWs (e.g., sub-100 nm and even sub-50 nm in width), however, have been made by bottom-up chemical synthesis or growth [291]. In a top-down lithographical approach and at large scale, it is particularly challenging to make such thin NWs with good control, and incorporate them into functional devices and complex systems. SiC NWs are attractive for making robust and reliable NEMS switches; future engineering of SiC materials and explorations of nanoscale contacts would further advance the performance and reliability of such devices [292]. Feng et al [293] demonstrated a top-down SiC NW-based NEMS using a 50 nm SiC epilayer grown on Si substrate. They have made SiC NWs with cross sections as small as 20X50 nm by employing top-down processes consisting of lithography and nanomachining. Those SiC NWs can be designed and engineered to make very high frequency NEMS resonators with remarkable performance (e.g., resonance frequency f_0 ~100

MHz, and quality factor Q>1000) at room temperature, as well as devices with multiple functions enabled by novel, flexible design and patterning of in-plane complex structures. Radio-frequency characterization of these resonators was achieved by engineering efficient magnetomotive signal transduction into a new compact apparatus, and by enhancing capacitive detection with impedance-matching circuits.

For nanoelectronic applications, the carrier concentration and mobility should be accurately controlled along the NW. The first experiments on 3C–SiC based NWFETs [294] revealed that the carrier concentration is too high, due to unintentional doping, resulting in very low electron mobility. Possible causes for these high residual doping values are impurities contamination and/or large number of extended defects. It seemed difficult to obtain monocrystalline SiC NWs without extended defects like staking faults and low residual doping with the low cost ‘chemistry-driven’ methods used up to now. Figure 13 shows the SEM images of a suspended SiC NW device with point-contact and other complementary gate electrodes where (a) represents the top-view of a 9 µm-long, 100 nm-wide, 50 nm-thick device. Close-in view at one clamped end of the device, demonstrating a well-controlled undercut from dry etch release is given in (b). In the vicinity of the point-contact gate, typically achieved small gaps are ~ 10−40 nm for the point contact and ~ 40−70 nm for the 8 µm-wide, large flat gate (opposite to the point-contact gate) and is explained in (c).

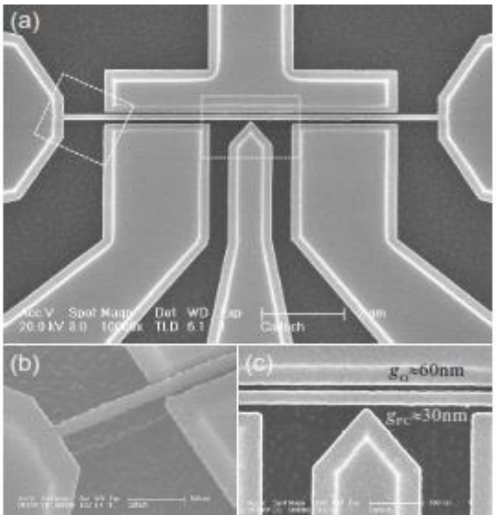

Figure 13. SEM images of a suspended SiC NW device with point-contact and other complementary gate electrodes [89].

2.2.2.5 Field emission devices

Nanostructures are offering intrinsic advantages for the fabrication of field emitters (FE). In general, for FE applications, a high aspect ratio is highly desirable to obtain a low threshold voltage for emission. In the case of NWs, this aspect ratio is considerably increased compared with bulk materials. Apart from the geometry of the material, another important parameter is the low electron affinity that permits the emission of electrons for lower applied electric fields and leads to higher emission current density. Moreover, the superior chemical and physical stability of SiC would result in a longer lifetime of the device by minimizing emission instabilities. SiC NWs were found to be very promising for FE applications, for example in field emission diodes (FED) and other nanoelectronic devices [295].

SiC NWs are expected to show reliable emission property even at high temperature due to its inherent properties as excellent thermal stability. Extraordinary properties of SiC NWs, such as chemical inertness and excellent mechanical property, result in long life expectancy (100 h) with stable emission property even under a severe environment, such as high electric field and high temperature. Thus, SiC NWs are expected to have great potential applications in the areas of X-ray sources for medical imaging, UV light-emitting diodes and UV photodiodes. SiC 1D nanostructure has been considered as one of the most promising candidates with excellent properties for field emitters, not only because of its outstanding mechanical properties, high thermal conductivity and chemical stabilities, and electron affinity [296, 297] but also because of its intrinsic properties of high aspect ratio and high field enhancement factor [297, 298]. Up to date, many efforts have been devoted to the investigation of fieldemission (FE) properties related to various SiC nanostructures.

The reported turn-on fields (E_{to},defined to be the electric field required to generate a current density of 10 $\mu A/cm^2$) of SiC nanowires were ranged in 3.33-20 $V\mu m^{-1}$[299], and that of SiC nanorods and nanobelts exhibited to 13-17 $V\mu m^{-1}$ [300], and 3.2 $V\mu m^{-1}$ [301], respectively; the FE properties could be further enhanced up to 0.7-2.9 $V\mu m^{-1}$ by using aligned SiC nanowires as the emitters [298, 302]; to and the remarkable increase of emission current to the decrease of work function induced by the raise of temperatures.

Most recently, Zhang et al have obtained E_{to} of quasi-aligned β-SiC nanowires as low as to 0.55-1.54 $V\mu m^{-1}$ [303]. To improve the FE properties of SiC nanostructures, one of the effective strategies is to reduce the tip size of nanostructures, namely, to obtain a needlelike nanostructures [304], which could favor a high electron emission current density due to the strong local electric field at the tips and the unique emission direction owing to their geometries of small curvature radius [305].

Even much progress has been made to the FE properties of SiC 1D nanostructures during the past decades as mentioned above, most of the reported works have been carried out just at RT. A study of field emission from nanostructures at higher temperatures is very interesting for many reasons [306, 307]: i) can disclose the changes of the electron emission characteristics under various conditions and provide additional insight into the physical properties of nanostructures; ii) for investigation of direct thermal electric conversion; iii) benefit to obtaining a high emission current densities required for many unique applications for example electron microscopes.

SiC NWs exhibit good field-emitting properties [308]. Until now, a variety of 1D and quasi-1D functional nanostructures of SiC have been successfully fabricated, including nanowires, nanotubes, nanoboxes, hollow nanospheres and nanocables, as the promise that nanostructures may dramatically improve the desired properties for many applications has stimulated great interest [309-317]. Shen et al [316] studied the field emission of bamboo-like SiC nanowires which showed a turn-on field of 10.1 $V\mu m^{-1}$. These NWs have a very high aspect ratio, which also contributes to the geometry enhancement factor and greatly enhances the electron emission and are good candidates for low-cost, large-area electron emitters. The FE studies on β-SiC nanoarchitectures showed turn-on field of ~12 V/µm [317]. Two linear behaviors were observed within measurement range might be due to current saturation, attributed to possible adsorbents on nanostructure appearing under higher electric field or caused by space charge effect. This kind of new hierarchical SiC nanoarchitectures may find applications in flat-panel displays or nanodevices.

Perisanu et al [250] have measured high Young’s modulus of SiC NW during the field emission, which shows more mechanical robustness than CNTs. The excellent properties of SiC NWs make these materials particularly interesting candidates for robust field emitter with life expectancy and stable field emission. The research for field emission of 1D structure could be divided into mainly three categories to improve the field emission property, reducing the tip size, doping or coating of the tip, and increasing the emitter sites density [303].

Field emission ability of nanostructures have typically been characterized by two properties, electron emission turn-on field (E_{on}) and threshold field (E_{th}), which defined as the electric fields required to produce a current density of 10 µA cm^{-2} (minimum current level for field emission) and 10 mA cm^{-2}, (current level for realistic application) respectively. Some applications of field emission need the additional information, such as maximum current density, emission stability and life time. Their best values measured on SiC NWs emitters with a needle shape show low turn-on field (0.55 - 1.54 V μm^{-1}) and threshold field (1.88 V μm^{-1}) [303]. It is believed that needle shape of SiC NW provides higher density of electron emitting sites than typical cylinder shape. In addition, Al doping also might be contributed to this field emission enhancement.

Temperature dependent FE properties of 3C-SiC nanoneedles (NN) was reported by Wei et al [318]. FE of as-synthesized SiC NNs are of the order of 1.30 to 0.66 V/µm with the temperature increased from RT to 500°C. The significant reduction of E_{to} and the remarkable increase of emission current to the decrease of work function induced by the increase of temperature and these NNs was suggested that it could be an excellent candidate for field emitters.

In recent years, researchers focused on the study of 1D SiC nanomaterials with different morphologies. Wu et al [319] prepared needle-shaped SiC NWs with a turn-on field of 5 V/µm. Yang et al [320] grew highly oriented SiC porous nanowire arrays with excellent FE performances. But they did not give any explanation concerning the FE properties of their products. Deng et al [321] found that the diameter and length of the SiC NWs had a strong effect on its FE performance. Shen et al [322] attributed the FE properties to stacking faults existing in the knot parts and the special bamboo-like morphology. To date, many valuable data have been reported on FE properties of 1D SiC nanomaterials, but it is still an extremely challenging work to establish a universal mechanism to clarify the influence of morphologies on FE properties of SiC NWs. Morphology dependent Field Emission characteristics of felted, curly and straight β-SiC NWs was studied by Li et al [323]. Linearity of J-E curves implies that FE from SiC NWs follows Fowler-Nordheim (FN) theory. FE properties strongly depend on their morphologies was elucidated. Magnetic field shield effect (MFSE) has great effect on moving electrons along the felted NWs and curly NWs but has negligible effect on those along straight NWs which are well separated from each other. Physical significance and process of FE is clearly explained by the authors.

2.2.2.6 Other emerging areas

Photocatalysis

Large-scale SiC NWs coated with a trace of amorphous silicon oxide layer were synthesized by high-frequency induction heating of SiO powders [324]. Typically, a single nanowire has an average core of 8–20 nm in diameter. The photocatalytic activity of the obtained SiC NWs was evaluated by the photocatalytic decomposition of gaseous acetaldehyde accompanied by the generation of CO_2. The result shows that the SiC NW exhibits the characteristic of an excellent photocatalyst. Furthermore, it is found that the as synthesized amorphous SiO_2 coated SiC manifests higher photocatalytic activity than the bare SiC NWs, resulting from their stronger absorption of gaseous acetaldehyde and higher probability of trapping of an excited electron in the conductive band of SiC coated by SiO_2 while holes remain in the SiC valence band.

Biomimetics- Superhydrophobicity of SiC NWs

SiC-NWs are hydrophilic due to the existence of a native oxide. Initiated by the “lotus leaf” effect in nature, various artificial super-hydrophobic coatings with self-cleaning function have been being identified. However, when the size of a material is reduced to the nanoscale, the property of SiC could be changed into hydrophobic due to the high-energy barrier between a solid and liquid interface. Niu et al [325] have demonstrated high super hydrophobicity by laterally aligning SiC NWs during the growth. Aligned SiC NWs show excellent super hydrophobic property with a high water contact angle more than 156 ± 2°, compared to random oriented NWs (147 ± 2°) and pure Si wafers (101 ± 2°). Even after exposing the samples in air for one week, it shows little variation (less than 5°). Aligned SiC NWs show the better super hydrophobicity with surface fictionalization with CF_2/CF_3 groups. Wang et al [326] have modulated the surface properties of SiC NWs by a coating of C. The measured water contact angles of SiC NWs and C-sheathed SiC NWs are 68° and 112°, respectively. The surface modifications of C coating tailored SiC surface property from hydrophilic to hydrophobic, which could maintain excellent electrical property of SiC NWs even in a humid atmosphere.

Self-cleaning coating exhibiting super-hydrophobic nature has been realized from SiC NWs by Niu and Wang [327]. The authors have fabricated the coating material by dropping the SiC

NWs into a mixture of tetraethyl orthosilicate (TEOS), ethanol and hydrochloric acid. The mixture could be coated on glass and a possible on any substrate other substrates. This exhibited high water contact angle (~160°), low sliding angle (~5°) and high roughness (1928.9 nm). The interesting phenomenon was the high chemical stability obtained from them even after immersing in water for 14 days. When water droplets rolled off from the SiC NWs coated glass, it also takes a dust with them. Based on the above mentioned experimental results, super hydrophobic property of SiC NWs may open new possibilities to apply it into various self-cleaning fields, such as in fields of various coatings, textiles, on windows in high-rise buildings and on car windscreens. But, it is still required to further improve the stability of the coating and against damage to use in practical applications.

SiC can be used as a heterogeneous catalyst support and a potential material in order to replace traditional industrial catalytic support because it exhibit high resistance towards oxidation, chemical inertness, high mechanical strength and high thermal conductivity [328, 329]. The very low surface area of the commercial SiC catalytic support material could be improved by the use of nanostructured SiC.

Reinforcement coatings

In mechanical reinforcing, the issues of mobility and residual doping are not so critical. Instead of high-quality-crystal production, a high growth method throughput and large length-to-diameter ratio are demanded. The first results related to the use of SiC NWs as reinforcing material are very promising showing a realistic industrial perspective especially for operation at high temperature and/or oxidizing environments [330, 331].

References

1. Z. L. Wang, Ad. Funct. Mater 2008, 18, 3553.

2. Z. L. Wang, Journal of Physics: Condensed Matter, 16 (2004) R829-R858.

3. E. H. Kisi and M. M. Elcombe, Acta Cryst., C45 (1989) 1867.

4. J. E. Jaffe and A. C. Hess, Phys. Rev. B, 48 (1993) 7903.

5. L. Gerward and J. S. Olsen, J. Synchrotron Radiat., 2 (1995) 233.

6. T. Kogure and Y. Bando, J. Electron Microsc., 47 (1993) 7903.

7. A. B. M. A. Ashrafi, A. Ueta, A. Avramescu, H. Kumano, I. Suemune, Y. W. Ok and T. Y. Seong, Appl. Phys. Lett., 76 (2000) 550.

8. S. K. Kim, S. Y. Seong and C. R. Cho, Appl. Phys. Lett., 82 (2003) 562.

9. C. H. Bates, W. B. White and R. Roy, Science, 137 (1962) 993.

10. J. E. Jaffe, J. A. Snyder, Z. Lin and A. C. Hess, Phys. Rev. B, 62 (2000) 1660.

11. D. R. Lide (Ed.), CRC Handbook of Chemistry and Physics, 73rd Edition, CRC Press,

New York, 1992.

12. C. Jagadish and S. J. Pearton (eds.), Zinc Oxide Bulk, Thin Films, and Nanostructures (Elsevier, Amsterdam, 2006), p. 1.

13. Ü. Özgür, Ya. L. Alivov, C. Liu, A. Teke, M. Reshchikov, S. Dogan, V. Avrutin, S.J. Cho and H. Morkoc, J. Appl. Phys., 98 (2005) 041301.

14. D. C. Look, Mater. Sci. Eng., 80 (2001) 383.

15. T. Olorunyolemi, A. Birnoim, Y. Carmel, O. Wilson, I. Lioyd, S. Smith and R. Campbell, J. Am. Cera. Soc., 85 (2002) 1249.

16. D. I. Florescu, L. G. Mourokh, F. H. Pollak, D. C. Look, G. Cantwell and X.Li, J. Appl. Phys., 91 (2002) 890.

17. S. Bloom and I. Ortenburger, Phys. Stat. Sol B, 58 (1973) 561.
18. J. R. Chelikowsky, Solid. State. Commun, 22 (1977) 351.
19. I. Ivanov and J. Pollmann, Phys. Rev. B, 24 (1981) 7275.
20. D. H. Lee and J. D. Joannopoulos, Phys. Rev. B, 24 (1981) 6899.
21. P. Schröer, P. Krüger and J. Pollmann. Phys. Rev. B, 47 (1993) 6971.
22. S. Massidda, R. Resta, M. Posterna and A. Baldereschi, Phys. Rev. B, 52 (1995) R16977.
23. P. Schröer, P. Krüger and J. Pollmann. Phys. Rev. B, 49 (1994) 17092.
24. D. Vogel, P. Krüger and J. Pollmann. Phys. Rev. B, 52 (1995) R14316.
25. D. W. Langer and C. J. Vesely, Phys. Rev. B, 2 (1970) 4885.
26. L. Ley, R. A. Pollak, F. R. McFeely, S. P. Kowalezyk and D. A. Shirley, Phys. Rev. B, 9 (1974) 600.
27. C. J. Vesely, R. L. Hengehold, and D. W. Langer, Phys. Rev. B, 5 (1972) 2296.
28. P. A. Powell, W. E. Spicer and J. C. McMenamin, Phys. Rev. Lett, 27 (1971) 97.
29. R. A. Powell, W. E. Spicer and J. C. McMenamin, Phys. Rev. B, 6 (1972) 3056.
30. R. T. Girard, O. Tjernberg, G. Ghiana, S. Söderholm, U. O. Karlsson, C. Wigren, H. Nylen and I. Lindau, Surf. Sci., 373 (1997) 409.
31. K. Ozawa, K. Sawada, Y. Shirotori, K. Edamoto and M. Nakatake, Phys. Rev. B, 68 (2003) 125417.
32. C. B. Duke, A. R. Lubinsky, S. C. Chang, B. W. Lee, and P. Mark, Phsy. Rev. B, 15 (1977) 4865.
33. Himpsel, F.J. Advances in Physics, 32 (1983) 1.
34. E. Comini, V. Guidi, C. Malagu`, G. Martinelli, Z. Pan, G. Sberveglieri and Z. L. Wang, J. Phys. Chem. B, 108 (2004) 1882.

35. Z. L. Wang, X. Y. Kong, Y. Ding, P. X. Gao, W. L. Hughes, R. S. Yang and Y. Zhang, Adv. Funct. Mater., 14 (2004) 944.

36. Z. W. Pan, Z. R. Dai and Z. L. Wang, Science, 209 (2001) 1947.

37. X. Y. Kong and Z. L. Wang, Nano Lett., 3 (2003) 1625.

38. X. Y. Kong, Y. Ding, R. S. Yang and Z. L. Wang, Science, 303 (2004) 1348.

39. P. X. Gao, Y. Ding, W. J. Mai, W. L. Hughes, C. S. Lao and Z. L. Wang, Science, 309 (2005) 1700.

40. M. H. Zhao, Z. L. Wang and S. X. X. Mao, Nano Lett., 4 (2004) 587.

41. D. Ozgur, Ya. I. Alivov, C. Liu, A. Teke, M. A. Reshchikov, S. Dogan, V. Avrutin, S.-J. Cho and H. Morkoc, J. Appl. Phys., 98 (2005) 041301.

42. R. Djelloul, A. Rabadanov, Turk J Phys, 2004, 28, 309.

43. P. H. Kasai, Phys. Rev., 1963, 130, 989

44. K: Vanheusden, W. L. Warren, C. H. Seager, D. R. Tallant, J. A. Voigt, and B. E. Gnade, J. Appl. Phys., 1996, 79, 7983

45. S. Yamauchi, Y. Goto, and T. Hariu, J. Cryst. Growth, 2004, 260, 1

46. A. Janotti and C.G. Van de Walle, Appl. Phys. Lett., 2005, 87, 122102

47. A. Janotti and C.G. Van de Walle, Phys. Rev. B, 2007, 76, 165202

48. M. Liu, A.H. Kitai, P. Mascher, J. Lumin. 1992, 54, 35

49. E. G. Bylander, J. Appl. Phys., 1978, 49, 1188

50. G. Yang, X. Du, J. Wang, B. Wang, Y. Liu, D. Zhang, D. Liu, H. Liu, S. Yang, J. Cryst. Growth, 2003, 252, 275

51. O. D. Jayakumar, V. Sudarsan, C. Sudakar, R. Naik, R. K. Vatsa, A. K. Tyagi, Scripta Materialia, 2010, 62, 662

52. J. Zhong, A.H. Kitai, P. Mascher, W. Puff, J. Electrochem. Soc., 1993, 140, 3644

53. R. Bahskar, et.al., Indian Journal of Pure and Applied Physics, 2009, 47, 772

54. B. Lin and Z. Fu, Appl. Phys. Lett., 2001, 79 (7), 943

55. X. H. Zhang, Y. C. Liu, X. H. Wang, S. J. Chen, G. R. Wang, J. Y. Zhang, Y. M. Lu, D. Z. Shen and X. W. Fan, J. Phys. Condens. Matter, 17 (2005) 3035.

56. S. Chen, Y. Liu, C. Shao, R. Mu, Y. Lu, J. Zhang, D. Shen and X. Fan, Adv. Mater., 17 (2005) 586.

57. H. C. Hsu and W. F. Hsieh, Solid State Commun., 131 (2004) 371.

58. S. Ozaki, T. Tsuchiya, Y. Inokuchi and S. Adachi, Phys. Stat. Sol. A, 202 (2005) 1325.

59. B. P. Zhang, N. T. Binh, Y. Segawa, K. Wakatsuki and N. Usami, Appl. Phys. Lett, 83 (2003) 1635.

60. W. I. Park, Y. H. Jun, S. W. Jung and G. C. Yi, Appl. Phys. Lett, 82 (2003) 964.

61. J. Jie, G. Wang, Y. Chen, X. Han, Q. Wang, B. Xu, J. G. Hou, Appl. Phys. Lett, 86 (2005) 031909.

62. L. E. Greene, M. Law, J. Goldberger, F. Kim, J. C. Johnson, Y. Zhang, R. J. Saykally and P. Yang, Angew. Chem., 115 (2003) 3030; Angew. Chem. Int. Ed, 42 (2003) 3031.

63. Y. H. Tong, Y. C. Liu, S. X. Lu, L. Dong, S. J. Chen and Z. Y. Xiao, J. Sol-Gel Sci. Technol, 30 (2004) 157.

64. J. Grabowska, A. Meaney, K. K. Nanda, J. P. Mosnier, M. O. Henry, J. R. Duclere and E. McGlynn, Phys. Rev. B, 71 (2005) 115439.

65. H. W. Suh, G. Y. Kim, Y. S. Jung, W. K. Choi and D. Byun, J. Appl. Phys, 97 (2005) 044305.

66. J. E. Shigley et al. Mech. Eng. Desig (7th ed.) 2004, McGraw-Hill.

67. L. W. Ji, S. J. Young, T. H. Fang and C. H. Liu, Appl. Phys. Lett, 90 (2007) 033109.

68. S. J. Young, L. W. Ji, S. J. Chang, T. H. Fang, T. J. Hsueh, T. H. Meen and I. C. Chen, Nanotechnology, 18 (2007) 225603.

69. S. O. Kucheyev, J. E. Bradly, J. S. Williams, C. Jagadish and M. V. Swain, Appl. Phys. Lett., 80 (2002) 956.

70. C. Q. Chen, Y. Shi, Y. S. Zhang, J. Zhu and Y. J. Yan, Phys. Rev. Lett., 96 (2006) 075505.

71. B. M. Wen, J. E. Sader and J. J. Boland, Phys. Rev. Lett., 101 (2008) 175502.

72. K. Nomura, H. Ohta, K. Ueda, T. Kamiya, M. Hirano, and H. Hosono, Science, 300 (2003) 1269.

73. T. Nakada, Y. Hirabayashi, T. Tokado, D. Ohmori, and T. Mise, Sol. Energy 77 (2004) 739.

74. S. Y. Lee, E. S. Shim, H. S. Kang, S. S. Pang, and J. S. Kang, Thin Solid Films, 437 (2005) 31.

75. R. Könenkamp, R. C. Word, and C. Schlegel, Appl. Phys. Lett., 85 (2004) 6004.

76. S. T. Mckinstry, and P. Muralt, J. Electroceram., 12 (2004) 7.

77. Z. L. Wang, X. Y. Kong, Y. Ding, P. Gao, W. L. Hughes, R. Yang, and Y. Zhang, Adv. Funct. Mater., 14 (2004) 943.

78. M. S. Wagh, L. A. Patil, T. Seth, and D. P. Amalnerkar, Mater. Chem. Phys., 84 (2004) 228.

79. Y. Ushio, M. Miyayama, and H. Yanagida, Sensor Actuat. B, 17 (1994) 221.

80. H. Harima, J. Phys.: Condens. Matter., 16 (2004) S5653.

81. S. J. Pearton, W. H. Heo, M. Ivill, D. P. Norton, and T. Steiner, Semicond. Sci. Technol., 19 (2004) R59.

82. J. Nishii, F.M. Hossain, S. Takagi, T. Aita, K. Saikusa, Y. Ohmaki, I. Ohkubo, S. Kishimoto, A. Ohtomo, T. Fukumura, F. Matsukura, Y. Ohno, H. Koinuma, H. Ohno, and M. Kawasaki, Jpn. J. Appl. Phys., 42 (2003) L347.

83. F. M. Hossain, J. Nishii, S. Takagi, T. Sugihara, A. Ohtomo, T. Fukumura, H. Koinuma, H. Ohno, M. Kawasaki, Physica E, 21 (2004) 911.

84. B. J. Norris, J. Anderson, J. F. Wager, D. A. Kszler, J. Phys. D: Appl. Phys., 36 (2003) L105.

85. P. Yang, H. Yan, S. Mao, R. Russo, J. Johnson, R. Saykally, N. Morris, J. Pham, R. He, H. -J. Choi, Adv. Mater., 12 (2002) 323.

86. C. Klingshrin, ChemPhysChem 8 (2007) 782.

87. A. I. Hochbaum and P. D. Yang, Chem. Rev. 110 (2010) 527.

88. C. Agashe, O. Kluth, G. Schope, H. Siekmann, J. Hupkes and B. Rech, Thin Solid Films 442 (2003) 167.

89. M. Law, L. E. Greene, J. C. Johnson, R. Saykally and P. D. Yang, Nature Mater. 4 (2005) 455.

90. I. Gonzalez-Valls and M. Lira-Cantu, Energy Environ. Sci. 2 (2009) 19.

91. W. J. Jeong, S. K. Kim and G. C. Park, Thin Solid Films 506/507 (2006) 180.

92. M. Purica, E. Budianu, E. Rusu, M. Danila and R. Gavrila, Thin Solid Films 403/404 (2002) 485.

93. B. L. Zhu, X. H. Sun, X. Z. Zhao, F. H. Su, G. H. Li, X. G. Wu, J. Wu, R. Wu and J. Liu, Vacuum 82 (2008) 495.

94. E. Bellingeri, D. Marré, I. Pallecchi, L. Pellegrino, G. Canu and A. S. Siri, Thin Solid Films 486 (2005) 186.

95. Y. Ito, K. Kushida, K. Sugawara, and H. Takeuchi, IEEE Trans. Ultrasonics, Ferroelectrics, and Frequency Control, 42 (1995) 316.

96. H. -W. Ryu, B. -S. Park, S. A. Akbar, W. -S. Lee, K. -J. Hong, Y. -Jin Seo, D. -C. Shin, J. -S. Park, G. -P. Choi, Sens. Actuator B, 96 (2003) 717.

97. G. Sberveglieri, Sens. Actuator B, 23 (1995) 103.

98. G. S. Trivikrama Rao, D. Tarakarama Rao, Sens. Actuator B, 55 (1999) 166.

99. X. L. Cheng, H. Zhao, L. H. Huo, S. Gao, J. G. Zhao, Sens. Actuator B, 102 (2004) 248.

100. T. Di et l , Semicond. Sci. Technol., 17 (2002) 377.

101. P. Sharma, A. Gupta, K. V. Rao, F. J. Owens, R. Sharma, R. Ahuja, J. M. Osorio, B. Johansson, G. A. Gehring, Nat. Mater., 2, (2003) 673.

102. H. Saeki, H. Tabata, T. Kawai, Solid State Commun. 120 (2001) 439.

103. A. Wadeasa, O. Nur, and M. Willander, Nanotechnology, 20 (2009) 065710.

104. M. Willander, Y. E. Lozovik, Q. X. Zhao, O. Nur, Q.H. Hu, and P. Klason, Proc. SPIE, 6486 (2007) 648614.

105. M. Riaz, A. Fulati, Q. X. Zhao, O. Nur, M. Willander, and P. Klason, Nanotechnology, 19 (2008) 415708.

106. M. Riaz, A. Fulati, L. L. Yang, O. Nur, M. Willander, and P. Klason, J. Appl. Phys., 104 (2008) 104306.

107. J. P. Liu, C. X. Guo, C. M. Li, Y. Y. Li, Q. B. Chi, X. T. Huang, L. Liao, T. Yu, Electrochem. Commun, 11 (2009) 202.

108. O. Lupan, G. Y. Chai, L. Chow, Microelectron. Eng, 85 (2008) 2220.

109. A. Umar, M. M. Rahman, A. Al-Hajry, Y. B. Hahn, Talanta, 78 (2009) 284.

110. A. Umar, M. M. Rahman, M. Vaseem, Y. B. Hahn, Electrochem. Commun., 11, (2009) 118.

111. A. Umar, M. M. Rahman, Y. B. Hahn, J. Nanosci. Nanotechnol., 9 (2009) 4686.

112. A. Umar, M. M. Rahman, Y. B. Hahn, Talanta, 77 (2009) 1376.

113. A. Umar, M. M. Rahman, S. H. Kim, Y. B. Hahn, Chem. Commun, 2 (2008) 166.

114. X. D. Bai, P. X. Gao, Z. L. Wang, and E. G. Wang, Appl. Phys. Lett., 82 (2003) 4806.

115. Z. L. Wang, and J. H. Song, Science, 312 (2007) 242.

116. Q. X. Zhao, P. Klason, M. Willander, P. J. Bergman, W. L. Jiang and J. H. Yang, Phys. Scr., T126 (2006) 13; H. J. Zhou, M. Wissinger, J. Fallert, R. Hauschild, F. Stelzl, C. Klingshirn and H. O. Kalt, Appl. Phys. Lett., 91 (2007) 181112.

117. P.X. Gao and Z.L. Wang, J. Appl. Phys., 97 (2005) 044304.

118. P. D. Batista and M. Mulato, Appl. Phys. Lett., 87 (2005) 143508.

119. B. S. Kang, F. Ren, Y. W. Heo, L. C. Tien, D. P. Norton and S. J. Pearton, Appl. Phys. Lett., 86 (2005) 112105.

120. Z. L. Wang, Adv. Funct. Mater., 18 (2008) 1.

121. X. D. Wang, J. H. Song, J. Liu and Z. L. Wang, Science, 316 (2007) 102.

122. Z. L. Wang and J. H. Song, Science, 312 (2006) 242.

123. J. H. Song, J. Zhou and Z. L. Wang, Nano Letters, 6 (2006) 1656.

124. P. X. Gao, J. H. Song, J. Liu and Z. L. Wang, Adv. Mater., 19 (2007) 67.

125. J. Zhou, N. S. Xu and Z. L. Wang, Adv. Mater., 18 (2006) 2432.

126. P. X. Gao, J. H. Song, J. Liu and Z. L. Wang, Adv. Mater., 19 (2006) 67.

127. Y. Qin, X. D. Wang and Z. L. Wang, Nature, 451 (2008) 809.

128. L. E. Greene, M. Law, J. Goldberger, F. Kim, J. C. Johnson, Y. Zhang, R. J. Saykally, P. Yang, Angew. Chem., Int. Ed., 2003, 42 (26), 3031

129. W. Park, J. S. Kim, G. C. Yi, M. H. Bae, and H.J. Lee, Appl. Phys. Lett. 2004, 85, 5052

130. L. E. Greene, J.C. Johnson, R. Saykally, P.D. Yang, Nat. Mater. 2005, 4, 455

131. R. Tena-Zaera, A. Katty, S. Bastide, C. Lévy-Clément, B. O'Regan and V. Muñoz-Sanjosé. Thin Solid Films, 2005, 483, 372

132. I. Gonzalez-Valls and M. Lira-Cantu, Energy Environ. Sci., 2009, 2, 19–34

133. K. Keis, C. Bauer, G. Boschloo, A. Hagfeldt, K. Westermark, H. Rensmo, H. Siegbahn, J. Photochem. Photobiol., A, 2002, 148, 57

134. M. Quintana, T. Edvinsson, A. Hagfeld and G. Boschloo, J. Phys. Chem. C, 2007, 111, 1035

135. S. H. Ko et al., Nano Lett., 2011, 11, 666

136. S. Chu, Dongdong Li, P.-C. Chang, and J. G. Lu, Nanoscale Res Lett., 2011, 6 (1), 38

137. E. Guillen, E. Azaceta, L. M. Peter, A. Zukal, R. Tena-Zaera and J. A. Anta, Energy Environ. Sci., 2011, 4, 3400

138. C. Y. Lin, Y.H. Lai, H. W. Chen, J. G. Chen, C. W. Kung, R. Vittala, K. C. Ho, Energy Environ. Sci., 2011, 4, 3448

139. K. Ernst, M.C. Lux-Steiner, R. Konenkamp, 16th European Photovoltaic Solar Energy N46. Conference, 2000, 63–66

140. K. Ernst, A. Belaidi and R. Könenkamp, Semicond. Sci. Technol., 2003, 18, 475

141. C. Lévy-Clément, R. Tena-Zaera, M. A. Ryan, A. Katty and G. Hodes, Adv. Mater., 2005, 17, 1512–1515

142. A. Belaidi, T. Dittrich, D. Kieven, J. Tornow, K. Schwarzburg and M. Lux-Steiner, Phys. Status Solidi RRL, 2008, 2, 172

143. Y. Itzhaik, O. Niitsoo, M. Page and G. Hodes, J. Phys. Chem. C, 2009, 113, 4254

144. C. Choné and G. Larramona, French Patent 2899385, (05 October, 2007)

145. S. Nezu, G. Larramona, C. Chon, A. Jacob, B. Delatouche, D. Péré and C. Moisan, J. Phys. Chem. C, 2010, 114, 6854

146. S. J. Moon, Y. Itzhaik, J.-H. Yum, S. M. Zakeeruddin, G. Hodes and M. Grätzel, J. Phys. Chem. Lett., 2010, 1, 1524

147. J. A. Chang, J.H. Rhee, S.H. Im, Y.H. Lee, H.J. Kim, S.I. Seok, M.K. Nazeeruddin and M. Grätzel, Nano Lett., 2010, 10, 2609

148. Y. Tak, S.J. Hong, J.S. Lee and K. Yong, J. Mater. Chem., 2009, 19, 5945

149. I. Mora-Seró, S. Giménez, F. Fabregat-Santiago, E. Azaceta, R. Tena-Zaera and J. Bisquert, Phys. Chem. Chem. Phys., 2011, 13, 7162

150. Y.-F. Sun, S.-B. Liu, F.-L. Meng, J.-Y. Liu, Z. Jin , L.-T. Kong and J.-H. Liu, Sensors, 12 (2012) 2610.

151. L. Liao, H. B. Lu, J. C. Li, C. Liu, D. J. Fu and Y. L. Liu, Appl. Phys. Lett., 91 (2007) 173110.

152. O. Lupan, V. V. Ursaki, G. Chai, L. Chow, G. A. Emelchenko, I. M. Tiginyanu, A. N. Gruzintsev and A.N. Redkin, Sensors and Actuators B, 144 (2010) 56.

153. M. H. Huang, S. Mao, H. Feick, H. Q. Yan, Y. Y. Wu, H. Kind, E. Weber, R. Russo and P. D. Yang, Science, 292 (2001) 1897.

154. Q. Wan, Q. H. Li, Y. J. Chen, T. H. Wang, X. L. He, J. P. Li and C. L. Lin, Appl. Phys. Lett., 84 (2004) 3654.

155. Z. Gergintschew, H. Forster, J. Kositza and D. Shipanski, Sens. Actuators B, 26–27 (1995) 170.

156. L. Liao, H. B. Lu, J. C. Li, H. He, D. F. Wang, D. J. Fu, C. Liu and W. F. Zhang, J. Phys. Chem. C., 111 (2007) 1900.

157. M. Law, H. Kind, B. Messer, F. Kim and P. D. Yang, Angew. Chem., Int. Ed., 41 (2002) 2405.

158. S. J. Pearton, D. P. Norton and F. Ren, Chapter 10, 321-343, Metal Oxide Nanomaterials for Chemical Sensors, Springer, Ed. M. A. Carpenter, S. Mathur and A. Kolmakov, Springer (2013).

159. M. W. Ahn, K. S. Park, J. H. Heo, J. G. Park, D. W. Kim, K. J. Choi, J. H. Lee and S. H. Hong, Appl. Phys. Lett., 93 (2008) 263103.

160. Y. H. Shi, M. Q. Wang, C. Hong, Z. Yang, J. P. Deng, X. H. Song, L. L. Wang, J. Y. Shao, H. Z. Liu and Y. C. Ding, Sensors and Actuators B, 177 (2013) 1027.

161. L. X. Zhang, J. H. Zhao, H. Q. Lu, L. Li, J. F. Zheng, H. Li and Z. P. Zhu, Sensors and Actuators B, 161 (2012) 209.

162. H. J. Zhang, R. F. Wu, Z. W. Chen, G. Liu, Z. N. Zhang and Z. Jiao, Cryst. Eng. Comm., 14 (2012) 1775.

163. J. Zhang, S. R. Wang, M. J. Xu, Y. Wang, B. L. Zhu, S. M. Zhang, W. P. Huang and S. H. Wu, Crystal Growth and Design, 9 (2009) 3532.

164. J. Huang, H. Ren, P. Sun, C. Gu, Y. Sun and J. Liu, Sensors and Actuators B, 188 (2013) 249.

165. Y. Zhang, J. Xu, X. Jiang, H. Li, Q. Pan and P. Xu, J. Phys. Chem. C, 113 (2009) 3430.

166. S. An, S. Park, H. Ko, C. Jin W. I. Lee and C. Lee, Thin Solid Films, 547 (2013) 241.

167. C. -L. Hsu, K.-C. Chen, T.-Y. Tsai and T. -J. Hsueh, Sensors and Actuators B, 182 (2013) 190.

168. D. Calestani, M. Zha, R. Mosca, A. Zappettini, M. C. Carotta, V. Di Natale and L. Zanotti, Sensors and Actuators B, 144 (2010) 472.

169. D. Calestani, R. Mosca, M. Zanichelli, M. Villani and Andrea Zappettini, J. Mater. Chem., 2011, 21, 15532.

170. L. C. Tien, H. T. Wang, B. S. Kang, F. Ren, P. W. Sadik, D. P. Norton, S. J. Pearton and J. Lin, Electrochem. Solid-State Lett., 8 (2005) G239.

171. Q. Zhang, P. Wang, J. Li and X. Gao, Biosensors and Bioelectronics, 15 (2000) 249.

172. K. T. Moorhead, D. Lee, J. G. Chase, A. R. Moot, K. M. Ledingham, J. Scotter, R. A. Allardyce, S. T. Senthilmohan and Z. Endre, Computer Methods and Programs in Biomedicine, 89 (2008) 226.

173. B. P. J. d. L Costello, R. J. Ewen, N. M. Ratcliffe and M. Richards, Journal of Breath Research, 2 (2008) 037017.

174. S. Tjoa and P. Fennessey, Analytical Biochemistry, 197 (1991) 77.

175. H. Park, H. Ahn, D. J. Kim and H. Koo, ISWC’13, September 9–12, Zurich, Switzerland (2013)

176. G. A. Shi, M. Saboktakin, M. Stavola and S. J. Pearton, Appl. Phys. Lett., 85 (2004) 5601.

177. B. S. Kang, Y. W. Heo, L. C. Tien, D. P. Norton, F. Ren, B. P. Gila and S. J. Pearton, Appl. Phys. A, 80 (2005) 1029.

178. B. S. Kang, F. Ren, Y. W. Heo, L. C. Tien, D. P. Norton and S. J. Pearton, Appl. Phys. Lett., 86 (2005) 112105.

179. Y. W. Heo, B. S. Kang, L. C. Tien, D. P. Norton, F. Ren, J. R. LaRoche and S. J. Pearton, Appl. Phys. A, 80 (2005) 497.

180. P. W. Sadik, S. J. Pearton, D. P. Norton, E. Lambers and F. Ren, J. Appl. Phys., 101 (2007) 104514.

181. S. J Pearton, F. Ren, Y. -L. Wang, B. H. Chu, K. H. Chen, C. Y. Chang, W. Lim, J. Lin and D. P. Norton, Progress in Materials Science, 55 (2010) 1.

182. J. X. Wang, X. W. Sun, A. Wei, Y. Lei, X. P. Cai, C. M. Li and Z. L. Dong, Appl. Phys. Lett., 88 (2006) 233106.

183. A. Wei, X. W. Sun, J. X. Wang, Y. Lei, X. P. Cai, C. M. Li, Z. L. Dong and W. Huang, Appl. Phys. Lett., 89 (2006) 123902.

184. J. Wright, W. Lim, D. P. Norton, F. Ren, S. J. Pearton, J. Johnson and A. Ural, Semicond. Sci. Technol., 25 (2010) 024002.

185. J. Y. Kim, S. -Y. Jo, G. -J. Sun, A. Katoch, S. -W. Choi and S. S. Kim, Sensors and Actuators B: Chemical, (2013).

186. A. Wei, X. W. Sun, J. X. Wang, Y. Lei, X. P. Cai, C. M. Li, Z. L. Dong and W. Huang, Appl. Phys. Lett., 89 (2006) 123902.

187. J. X. Wang, X. W. Sun, A. Wei, Y. Lei, X. P. Cai, C. M. Li and Z. L. Dong, Appl. Phys. Lett., 88 (2006) 233106.

188. J. Zang, C. M. Li, X. Cui, J. Wang, X. Sun, H. Dong and C. Q. Sun, Electroanalysis, 19 (2007) 1008.

189. X. Liu, Q. Hu, Q. Wu, W. Zhang, Z. Fang and Q. Xie, Colloid. Surface. B, 74 (2009) 154.

190. Y. Wei, Y. Li, X. Liu, Y. Xian, G. Shi and L. Jin, Biosens. Bioelectron., 26 (2010) 275.

191. Z. Zhao, W. Lei, X. Zhang, B. Wang and H. Jiang, Sensors, 10 (2010) 1216.

192. R. Yakimova, L. Selegård, V. Khranovskyy, R. Pearce, A. L. Spetz and K. Uvdal, Frontiers in Bioscience, 4 (2012) 254.

193. J. X. Wang, X. W. Sun, A. Wei, Y. Lei, X. P. Cai, C. M. Li and Z. L. Dong, Appl. Phys. Lett., 88 (2006) 233106.

194. A. Wei, X. W. Sun, J. X. Wang, Y. Lei, X. P. Cai, C. M. Li, Z. L. Dong and W. Huang, Appl. Phys. Lett., 89 (2006) 123902.

195. J. Y. Kim, S. -Y. Jo, G. -J. Sun, A. Katoch, S. -W. Choi and S. S. Kim, Sensors and Actuators B: Chemical, (2013).

196. C. S. Lao, Q. Kuang, Z. L. Wang, M.-C. Park and Y. L. Deng, Appl. Phys. Lett., 90 (2007) 107.

197. X. Xue, Y. Nie, B. He, L. Xing, Y. Zhang and Z. L. Wang, Nanotechnology, 24 (2013) 225501.

198. S. Bai, Q. Xu, L. Gu, F. Ma, Y. Qin and Z. L. Wang, Nano Energy, 1 (2012) 789.

199. Y. Yang, S. Wang, Y. Zhang and Z. L. Wang, Nano Lett., 12 (2012) 6408.

200. Y. S. Zhou, R. Hinchet, Y. Yang, G. Ardila, R. Songmuang, F. Zhang, Y. Zhang, W. Han, K. Pradel, L. Montès, M. Mouis and Z. L. Wang, Adv. Mater., 25 (2013) 883.

201. Y. Hu, Y. Zhang, L. Lin, Y. Ding, G. Zhu and Z. L. Wang, Nano Lett., 12 (2013) 3851.

202. Q. Wan, Q. H. Li, Y. J. Chen, T. H. Wang, X. L. He, J. P. Li and C. L. Lin, Appl. Phys. Lett., 84 (2004) 3654.

203. J. X. Wang, X. W. Sun, Y. Yang, H. Huang, Y. C. Lee, O. K. Tan and L. Vayssieres, Nanotechnology, 17 (2006) 4995.

204. Q. H. Li, Y. X. Liang, Q. Wan and T. H. Wang, Appl. Phys. Lett., 85 (2004) 6389.

205. W. Zhou, Y. Zhang, X. Niu and G. Min, One-Dimensional SiC Nanostructures: Synthesis and Properties (pp. 17-59). Springer New York (2008).

206. Ruff M, Mitlehner H, Helbig R (1994) SiC devices: Physics and numerical simulation. IEEE Trans. Electron. Devices 41:1040–1054

207. Morkoc H, Strite S, Gao GB, Lin ME, Sverdlov B, Burns M J., Appl. Phys. 76 (1994)1363–1398

208. Cicero G, Catellani A, Galli G (2004) Phys. Rev. Lett. 93:016102–016105

209. Z. J. Li, W. P. Ren and A. L. Meng, Appl. Phys. Lett., 97 (2010) 263117.

210. G. W. Ho, A. S. W. Wong, D. J. Kang and M. E. Welland, Nanotechnology, 15 (2004) 996.

211. Y. J. Hao, J. B. Wagner, D. S. Su, G. Q. Jin and X. Y. Guo, Nanotechnology, 17 (2006) 2870.

212. G. Z. Shen, Y. Bando, C. H. Ye, B. D. Liu and D. Golberg, Nanotechnology, 17 (2006) 3468.

213. G. Z. Shen, Y. Bando and D. Golberg, Cryst. Growth Des., 7 (2007) 35.

214. J. Z. Guo, Y. Zuo, Z. J. Li, W. D. Gao and J. L. Zhang, Physica E, 39 (2007) 262.

215. J. J. Chen, Q. Shi, L. H. Gao and H. L. Zhu, Phys. Status Solidi A, 207 (2010) 2483.

216. R. B. Wu, B. S. Li, M. X. Gao, J. J. Chen, Q. M. Zhu and Y. Pan, Nanotechnology, 19 (2008) 335602.

217. H. T. Wang, Z. P. Xie, W. Y. Yang, J. Y. Fang and L. N. An, Cryst. Growth Des., 8 (2008) 3893.

218. Harris GL (1995) Properties of Silicon Carbide. INSPEC, the Institution of Electrical Engineers, London

219. Zetterling CM (2002) Process Technology for Silicon Carbide Devices. EMIS Processing Series, no. 2. INSPEC, IEE, UK

220. Casady JB, Johnson RW (1996) States of silicon carbide (SiC) as a wide-bandgap semiconductor for high-temperature applications: A review. Solid State Electron. 39:1409–1422.

221. Baliga BJ (1996) Power Semiconductor Devices. PWS-Kent, Boston, MA

222. Treu M, Rupp R, Blaschitz P (2006) Commercial SiC device processing: Status and requirements with respect to SiC based power devices. Superlattice Microstruct. 40:380–387

223. Sha JJ, Park JS, Hinoki T, Kohyama A (2007) Bend stress relaxation of advanced SiC-based fibers and its prediction to tensile creep. Mech. Mater. 39:175–182

224. Mehregany M, Zorman CA (1999) SiC MEMS: Opportunities and challenges for applications in harsh environments. Thin Solid Films 355–356:518–524

225. Djenkal D, Goeuriot D, Thevenot F (2000) SiC-reinforcement of an Al2O3–γ AlON composite. J. Eur. Ceram. Soc. 20:2585–2590

226. Muller G, Krotz G, Niemann E (1994) SiC for sensors and high-temperature electronics. Sens. Actuators A: Phys. 43:259–268

227. Dimitrijev S, Jamet P (2003) Advances in SiC power MOSFET technology. Microelectron. Reliab. 43:225–233

228. Andrievski R.A. Synthesis, structure and properties of nanosized silicon carbide. Reviews on Advanced Materials Science, 2009, vol. 22, p.1–20.

229. Goldber Y., Levinshtein M.E., Rumyantsev S.L. Properties of Advanced Semiconductor Materials GaN, AlN, SiC, BN, SiC, SiGe. New York: John Wiley & Sons Inc., 2001, p. 93-148.

230. K. Zekentes, N. Camara, G. Konstantinidis, L. P. Romanov, A. V. Kirillov, and M. S. Boltovets, “Microwave p-i-n diodes and switches based on 4H-SiC”, in Microwave Conference, 2006. 36th European, 2006, pp. 99-102.

231. Svechnikov G.S., Rizikov I.V., Ivanov A.I. Multicolour, radiation-resistant SiC light-emitting diodes. Diamond and Related Materials, 1994, vol. 3, p.1045–1047.

232. Niedermeier S., Schillinger H., Sauerbrey R., R., Adolph, B., & Bechstedt, F. Second-harmonic generation in silicon carbide polytypes. Applied Physics Letters, 1999, vol. 75, no. 5, p.618–620.

233. S. Saddow, Silicon Carbide Biotechnology: A Biocompatible Semiconductor for Advanced Biomedical Devices and Applications: Elsevier Science, 2011.

234. S. Santavirta, M. Takagi, L. Nordsletten, A. Anttila, R. Lappalainen, and Konttinen Y.T., "Biocompatibility of silicon carbide in colony formation test in vitro - A promising new ceramic THR implant coating material," Arch. Orthop. Traum. Su, vol. 118, pp. 89-91, 1998.

235. Wu ZS, Deng SZ, Xu NS, Chen J, Zhou J, Chen J (2002) Needle-shaped silicon carbide nanowires: Synthesis and filed electron emission properties. 80:3829–3831

236. Wong KW, Zhou XT, Au CK, Lai HL, Lee CS, Lee ST (1999) Filed-emission characteristics of SiC nanowires prepared by chemical-vapor deposition. Appl. Phys. Lett. 75:2918–2920

237. Lo HC, Hwang JS, Chen KH, Hsu CH, Chen CF, Chen LC (2003) SiC-capped nanotip arrays for field emission with ultralow turn-on filed. Appl. Phys. Lett. 83:1420–1422

238. Feng DH, Jia TQ, Li XX, Xu ZZ, Chen J, Deng SZ (2003) Catalytic synthesis and photoluminescence of needle-shaped 3C-SiC nanowires. Solid State Commun. 128:295–297

239. Deng SZ, Li ZB, Wang WL, Xu NS, Zhou J, Zheng XG, Xu HT, Chen J, She JC (2006) Field emission study of SiC nanowires/nanorods directly grown on SiC ceramic surface. Appl. Phys. Lett. 89:023118–023200

240. Zhou WM, Wu YJ, Kong ESW, Zhu F, Hou ZY, Zhang YF (2006) Field emission from nonaligned SiC nanowires. Appl. Surf. Sci. 253:2056–2058

241. Liu XM, Yao KF (2005) Large-scale synthesis and photoluminescence properties of SiC/SiO_x nanocables. Nanotechnology 16:2932–2935

242. H.-K. Seong, H.-J. Choi, S.-K. Lee, Lee. J.-I., and D.-J. Choi, "Optical and electrical transport properties in silicon carbide nanowires," Applied Physics Letters, vol. 85, pp. 1256-1258, 2004.

243. K. Rogdakis, S.-Y. Lee, M. Bescond, S.-K. Lee, E. Bano, and K. Zekentes, "3C-Silicon Carbide Nanowire FET: An Experimental and Theoretical Approach," Electron Devices, IEEE Transactions on, vol. 55, pp. 1970-1976, 2008.

244. W. M. Zhou, F. Fang, Z. Y. Hou, L. J. Yan, and Y. F. Zhang, "Field-effect transistor based on β-SiC nanowire," Electron Device Letters, IEEE, vol. 27, pp. 463-465, 2006.

245. Y. Chen, X. Zhang, Q. Zhao, L. He, C. Huang, and Z. Xie, "P-type 3C-SiC nanowires and their optical and electrical transport properties," Chemical Communications, vol. 47, pp. 6398-6400, 2011.

246. Y. Zhang, X. Han, K. Zheng, Z. Zhang, X. Zhang, J. Fu, Y. Ji, Y. Hao, X. Guo, and Z. L. Wang, "Direct Observation of Super-Plasticity of Beta-SiC Nanowires at Low Temperature," Advanced Functional Materials, vol. 17, pp. 3435-3440, 2007.

247. X. Li, X. Wang, Q. Xiong, and P. C. Eklund, "Mechanical Properties of ZnS Nanobelts," Nano Letters, vol. 5, pp. 1982-1986, 2005.

248. Eric W. Wong, Paul E. Sheehan, and Charles M. Lieber, "Nanobeam Mechanics: Elasticity, Strength, and Toughness of Nanorods and Nanotubes," Science, vol. 277, pp. 1971-1975, 1997.

249. Z. L. Wang, Z. R. Dai, R. P. Gao, Z. G. Bai, and J. L. Gole, "Side-by-side silicon carbide--silica biaxial nanowires: Synthesis, structure, and mechanical properties," Applied Physics Letters, vol. 77, pp. 33493351, 2000.

250. S. Perisanu, V. Gouttenoire, P. Vincent, A. Ayari, M. Choueib, M. Bechelany, D. Cornu, and S. T. Purcell, "Mechanical properties of SiC nanowires determined by scanning electron and field emission microscopies," Physical Review B, vol. 77, p. 165434, 2008.

251. X. D. Han, Y. F. Zhang, K. Zheng, X. N. Zhang, Z. Zhang, Y. J. Hao, X. Y. Guo, J. Yuan, and Z. L. Wang, "Low-Temperature in Situ Large Strain Plasticity of Ceramic

SiC Nanowires and Its Atomic-Scale Mechanism," Nano Letters, vol. 7, pp. 452-457, 2006.

252. Yuefei Z, Xiaodong H, Kun Z, Ze Z, Xiaona Z, Jingyong F, Yuan J, Yajuan H, Xiangyun G and Zhonglin W, Adv. Funct. Mater. 17 (2007) 3435.

253. O. D. Sherby, J. Wadsworth, Deformation, Processing and Structure (Eds: G.Krauss), ASM Int., Metals Park, OH 1984.

254. C. J. Shih, M. A. Meyers, V. F. Nesterenko, S. J. Chen, Acta Mater. 2000, 48, 2399.

255. D. J.Green, An Introduction to the Mechanical Properties of Ceramics, Cambridge University Press, Cambridge 1998.

256. P. Pirouz, M.Zhang, J. L. Demenet, H. M. Hobgood, J. Phys. Condens. Matter 2002, 14, 12929.

257. P. B. Hirsch, S. G. Roberts, Acta Mater. 1996, 44, 2361.

258. H. K. Seong, H. J. Choi, S. K. Lee, J. I. Lee, D. J. Choi. Appl. Phys. Lett. 2004, 85, 1256.

259. Z. W. Pan, H. L. Lai, F. C. K. Au, X. F. Duan, W. Y. Zhou, W. S. Shi, N. Wang, C. S. Lee, N. B. Wong, S. T. Lee, S. S. Xie, Adv. Mater. 2000, 12, 1186.

260. X. H. Sun, C. P. Li, W. K. Wong, N. B. Wong, C. S. Lee, S. T. Lee, B. K. Teo, J. Am. Chem. Soc. 2002, 124, 14 464.

261. A. M. Leach, M. McDowell, K. Gall, Adv. Funct. Mater. 2007, 17, 43.

262. P. X. Gao, W. Mai, Z. L. Wang, Nano Lett. 2006, 6, 2536.

263. R. He, P. Yang, Nat. Nanotechnol. 2006, 1, 42.

264. J. Li, J. K. V. Vliet, T. Zhu, S. Yip, S. Suresh, Nature 2002, 418,307.

265. K. S. Cheung, S. Yip, Phys. Rev. Lett. 1990, 65, 2804.

266. Z. Wang, X. Zu, F. Gao, W. J. Weber, Appl. Phys. Lett. 2006, 89, 243, 123.

267. Zekentes K. and Rogdakis K. SiC nanowires: material and devices. Journal of Physics D: Applied Physics, 2011, vol. 44, no. 133001.

268. S. Saddow, Silicon Carbide Biotechnology: A Biocompatible Semiconductor for Advanced Biomedical Devices and Applications: Elsevier Science, 2011.

269. S. Santavirta, M. Takagi, L. Nordsletten, A. Anttila, R. Lappalainen, and Konttinen Y.T., "Biocompatibility of silicon carbide in colony formation test in vitro - A promising new ceramic THR implant coating material. ," Arch. Orthop. Traum. Su, vol. 118, pp. 89-91, 1998.

270. Mognetti B., Barberis A., Marino S., Di Carlo, F., Lysenko, V., Marty, O., & Geloen, A. Preferential Killing of Cancer Cells Using Silicon Carbide Quantum Dots. Journal of Nanoscience and Nanotechnology, 2010, vol. 10, no. 12, p.7971–7975.

271. Fan J., Li H., Jiang J., So, L. K., Lam, Y. W., & Chu, P. K. 3C-SiC nanocrystals as fluorescent biological labels. Small, 2008, vol. 4, no. 8, p.1058–1062.

272. Botsoa J., Lysenko V., Geloen A., Marty, O., Bluet, J. M., & Guillot, G. Application of 3C-SiC quantum dots for living cell imaging. Applied Physics Letters, 2008, vol. 92, no. 173902.

273. Rosenbloom A.J., Sipe D.M., Shishkin Y., Ke, Y., Devaty, R. P., & Choyke, W. J. Nanoporous SiC: A Candidate Semi-Permeable Material for Biomedical Applications. Biomedical Microdevices, 2004, vol. 6, no. 4, p.261–267.

274. Y. Cui, Q. Wei, H. Park, and C.M. Lieber: Nanowire nanosensors for highly sensitive and selective detection of biological and chemical species. Science 293, 1289 (2001).

275. F. Patolsky, G. Zheng, and C.M. Lieber: Nanowire-based biosensors. Anal. Chem. 78,4261(2006).

276. Z. Li, Y. Chen, X. Li, T.I. Kamins, K. Nauka, and R.S. Williams: Sequence-specific label-free DNA sensors based on silicon nanowires. Nano Lett. 4, 245 (2004).

277. J. Kim, M. Junkin, D.H. Kim, S. Kwon, Y.S. Shin, P.K. Wong, and B.K. Gale: Applications, techniques, and microfluidic interfacing for nanoscale biosensing. Microfluid. Nanofluid. 7, 149 (2009).

278. M. Shao, D.D.D. Ma, and S.T. Lee: Silicon nanowires- synthesis, properties, and application. Eur. J. Inorg. Chem. 27, 4264 (2010).

279. C.M. Lieber: Semiconductor nanowires: A platform for nanoscience and nanotechnology. MRS Bull. 36, 1052 (2011).

280. R. Yakimova, R.M. Petoral, G.R. Yazdi, C. Vahlberg, A. Lloyd Spetz, and K. Uvdal: Surface functionalization and biomedical applications based on SiC. J. Phys. D: Appl. Phys. 40, 6435 (2007).

281. R.M. Petoral, Jr., G.R. Yazdi, A. Lloyd Spetz, R. Yakimova, and K. Uvdal: Organosilane-functionalized wide-band-gap semiconductor surfaces. Appl. Phys. Lett. 99, 223904 (2007).

282. E.H. Williams, A.V. Davydov, A. Motayed, S.G. Sundaresan, P. Bocchini, L.J. Richter, G. Stan, K. Steffens, R. Zangmeister, J.A. Schreifels, and M.V. Rao: Immobilization of streptavidin on 4H-SiC for biosensor development. Appl. Surf. Sci. 16,6056(2012).

283. Williams, EH., John AS, Mulpuri VR, Albert VD, Vladimir PO, Nancy JL, Kristen LS, Sergiy K, Kris AB, Amy KM and Yaroslav K, Journal of Materials Research 28, no. 01 (2013): 68-77

284. R. Cheung, Silicon Carbide Micro Electromechanical Systems for Harsh Environments, Imperial College Press, 2006.

285. Vincent, M., Kim, M. S., Carraro, C. and Maboudian, R. (2012, January). Silicon carbide nanowires as an electrode material for high temperature supercapacitors. In Micro Electro Mechanical Systems (MEMS), 2012 IEEE 25th International Conference on (pp. 39-42). IEEE

286. J. S. Bunch, A. M. van der Zande, S. S. Verbridge, I. W. Frank, D. M. Tanenbaum, J. M. Parpia, H. G. Craighead and P. L. McEuen, Science 315, 490 (2007).

287. A. A. Balandin, S. Ghosh, W. Z. Bao, I. Calizo, D. Teweldebrhan, F. Miao and C. N. Lau, Nano Lett. 8, 902 (2008).

288. I. W. Frank, D. M. Tanenbaum, A. M. Van der Zande and P. L. McEuen, J. Vac. Sci. Technol. B 25, 2558 (2007).

289. I Jung, J. -H. Chung, R. Piner, J. W. Suk and R. S. Ruoff, NANO: Brief Reports and Reviews Vol. 4, 351 (2009).

290. X.L. Feng, R.R. He, P.D. Yang, M.L. Roukes, "Very High Frequency Silicon Nanowire Electromechanical Resonators", Nano Lett., vol. 7, pp. 1953-1959, 2007.

291. R.R. He, X.L. Feng, M.L. Roukes, P.D. Yang, "Self-Transducing Silicon Nanowire Electromechanical Systems at Room Temperature", Nano Lett., vol. 8, pp. 1756-1761, 2007.

292. Feng XL, Matheny MH, Zorman CA, Mehregany M and Roukes ML. "Low voltage nanoelectromechanical switches based on silicon carbide nanowires", Nano Lett Vol. 10, (2010) 2891–2896

293. Feng XL, Matheny MH, Karabalin RB, Zorman CA, Mehregany M and Roukes ML, Solid-State Sensors, Actuators and Microsystems Conference, IEEE, Transducers (2009) 2246-2249

294. Rogdakis K., Lee S.-Y., Bescond M., Lee, S. K., Bano, E. And Zekentes, K. 3C-Silicon Carbide Nanowire FET: An Experimental and Theoretical Approach. IEEE Transactions on Electron Devices, 2008, vol. 55, no. 8, p.1970–1976.

295. Kim D.-W., Choi Y.-J., Choi K.J., Park, J. G., Park, J. H., Pimenov, S. M., Frolov, V.D., Abanshin, N.P., Gorfinkel, B. I., Rossukanyi, N. M. and Rukovishnikov, A.I. Stable field emission performance of SiC nanowire-based cathodes. Nanotechnology, 2008, vol. 19, no. 225706.

296. (a) Casady, J.; Johnson, R. Solid-State Electron. 1996, 39, 1409. (b) Wong, E.; Sheehan, P.; Lieber, C. Science 1997, 277, 1971. (c) Fan, J.; Wu, X.; Chu, P. Prog. Mater. Sci. 2006, 51, 983.

297. Fang, X. S.; Bando, Y.; Gautam, U. K.; Ye, C.; Golberg, D. J. Mater. Chem. 2008, 18, 509.

298. Pan, Z. W.; Lai, H. L.; Au, F. C. K.; Duan, X. F.; Zhou, W. Y.; Shi, W. S.; Wang, N.; Lee, C. S.; Wong, N. B.; Lee, S. T.; Xie, S. S. Adv. Mater. 2000, 12, 1186.

299. (a) Wong, K. W.; Zhou, X. T.; Au, F. C. K.; Lai, H. L.; Lee, C. S.; Lee, S. T. Appl. Phys. Lett. 1999, 75, 2918. (b) Shen, G. Z.; Bando, Y.; Ye, C. H.; Liu, B. D.; Golberg, D. Nanotechnology 2006, 17, 3468. (c) Wu, Z. S.; Deng, S. Z.; Xu, N. S.; Chen, J.; Zhou, J.; Chen, J. Appl. Phys. Lett. 2002, 80, 3829. (d) Deng, S. Z.; Li, Z. B.; Wang, W. L.; Xu, N. S.; Jun, Z.; Zheng, X. G.; Xu, H. T.; Jun, C.; She, J. C. Appl. Phys. Lett. 2006, 23118. (e) Ryu, Y.; Park, B.; Song, Y.; Yong, K. J. J. Cryst. Growth 2004, 271, 99. (f) Tang, C. C.; Bando, Y. Appl. Phys. Lett. 2003, 83, 659.

300. Zhou, X. T.; Lai, H. L.; Peng, H. Y.; Au, F. C. K.; Liao, L. S.; Wang, N.; Bello, I.; Lee, C. S.; Lee, S. T. Chem. Phys. Lett. 2000, 318, 58.

301. Wei, G.; Qin, W.; Kim, R.; Sun, J.; Zhu, P.; Wang, G.; Wang, L.; Zhang, D.; Zheng, K. Chem. Phys. Lett. 2008, 461, 242.

302. Yang, Y. J.; Meng, G. W.; Liu, X. Y.; Zhang, L. D.; Hu, Z.; He, C. Y.; Hu, Y. M. J. Phys. Chem. C 2008, 112, 20126.

303. Zhang, X.; Chen, Y.; Xie, Z.; Yang, W. J. Phys. Chem. C 2010, 114, 8251.

304. Tang, Y.; Cong, H.; Chen, Z.; Cheng, H. Appl. Phys. Lett. 2005, 86, 233104.

305. Liu, C.; Hu, Z.; Wu, Q.; Wang, X. Z.; Chen, Y.; Sang, H.; Zhu, J. M.; Deng, S. Z.; Xu, N. S. J. Am. Chem. Soc. 2005, 127, 1318.

306. (a) Klein, R.; Leder, L. B. Phys. Rev. 1961, 124, 1046. (b) Shin, S.; Fisher, T.; Walker, D.; Strauss, A.; Kang, W.; Davidson, J. J. Vac. Sci. Technol. B 2003, 21, 587. (c) Wan, C. S.; Li, Z. H.; Fan, K. N.; Zheng, X.; Chen, G. H. Phys. Rev. B 2006, 73, 165422. (d) Liao, L.; Zhang, W.; Lu, H.; Li, J.; Wang, D.; Liu, C.; Fu, D. Nanotechnology 2007, 18, 225703. (e) Zhang, Q. Y.; Xu, J. Q.; Zhao, Y. M.; Ji, X. H.; Lau, S. P. Adv. Funct. Mater. 2009, 19, 742.

307. Zhu, H.; Masarapu, C.; Wei, J.; Wang, K.; Wu, D.; Wei, B. Phys. E 2009, 41, 1277.

308. Zhou X T, Lai H L, Peng H Y, Au F C K, Liao L S, Wang N, Bello I, Lee C S and Lee S T 2000 Chem. Phys. Lett. 318 58

309. Liang C H, Meng G W, Zhang L D, Wu Y C and Cui Z 2000 Chem. Phys. Lett. 329 323

310. Sun X H, Li C P, Wong W K, Wong N B, Lee C S, Lee S T and TeoBK2002 J. Am. Chem. Soc. 124 14464

311. Tang C C, Bando Y, Sato T and Kurashima K 2002 Adv. Mater14 1046

312. Liu J W, Zhong D Y, Xie F Q, Sun M, Wang E G and Liu W X 2001 Chem. Phys. Lett. 348 357

313. Hu J Q, Lu Q,TangKB,Deng B, Jiang R R, Qian Y T, Yu WC,Zhou G E, Liu X M and Wu J X 2000 J. Phys. Chem. B 104 5251

314. Rao C N R, Gundiah G, Deepak F L, Govindaraj A and Cheetham A K 2004 J. Mater. Chem. 14 440

315. Zhang Y, Ichihashi T, Landree E, Nihey F and Iijima S 1999 Science 285 1719

316. Shen GZ, Bando Y, Ye CH, Liu BD and Golberg D, Vol. 17, (2006) 3468–3472

317. Shen GZ, Bando Y and Golberg D, Cryst. Growth Des., Vol. 7, (2007) 35–38

318. Wei G, Liu HY, Shi CK, Gao FM, Zheng JJ, Wei GD and Yang WY, "Temperature-Dependent Field Emission Properties of 3 C-SiC Nanoneedles", J. Phys. Chem. C, Vol. 115, (2011) 13063–13068

319. Z. S. Wu, S. Z. Deng, N. S. Xu, J. Jian, C. Zhou, and J. Chen, Appl. Phys. Lett. 80, 3829 (2002).

320. Y. J. Yang, G. W. Meng, X. Y. Liu, L. D. Zhang, Z. Hu, C. Y. He, and Y. M. Hu, J. Phys. Chem. C 112, 20126 (2008).

321. S. Z. Deng, Z. B. Li, W. L. Wang, N. S. Xu, J. Zhou, X. G. Zheng, H. T. Xu, J. Chen, and J. C. She, Appl. Phys. Lett. 89, 023118 (2006).

322. G. Shen, Y. Bando, C. Ye, B. Liu, and D. Golberg, Nanotechnology 17, 3468 (2006).

323. Li ZJ, Ren WP and Meng AL. "Morphology-dependent field emission characteristics of SiC nanowires", Appl. Phys. Lett., Vol. 97, (2010) 263117

324. Zhou W., Yan L., Wang Y., & Zhang, Y. SiC nanowires: A photocatalytic nanomaterial. Applied Physics Letters, 2006, vol. 89, no. 013105.

325. J. J. Niu, J. N. Wang, Q. F. Xu, Langmuir, 24 (2008) 6918-6923

326. X. Wang, B. Tang, F. Gao, J. Zheng, G. Wei, and W. Yang, Journal of Physics D: Applied Physics, vol. 44, p. 245404, 2011.

327. J. J. Niu and J. N. Wang, J. Phys. Chem. B, 113 (2009) 2909.

328. M. J. Ledoux and C. Pham-Huu, Cattech, 5(4) (2001) 226.

329. J. M. Nhut, R. Vieira, L. Pesant, J. P. Tessonnier, N. Keller, G. Ehret, C. Pham-Huu and M. J. Ledoux, Catalysis Today, 76 (2002) 11.

330. H. -J. Song and Z. -Z. Zhang, Materials Science and Engineering: A, 2006, 426, p.59–65.

331. Shin J.-H., Kumar B.V.M., Kim J.-H. and Hong, S. H., Journal of the American Ceramic Society, 2011, vol. 94, no. 11, p.3683–3685.

Chapter 3

Experimental techniques

3.1 Growth mechanisms and techniques

Nanowires have been obtained so far by a huge number of synthesis methods, depending on the material to be grown, on the undesired impurity level tolerance, on the substrate requirements, on the target application. However, whenever the need of high purity, precise and uniform thickness control, low misfit dislocations, excellent homogeneity, sharp epitaxial layer/substrate and layer/layer interfaces, is required, vapor phase growth techniques are generally preferred.

Among them we can enumerate Chemical and Physical Vapor Phase Deposition (CVD/PVD), a more controllable Vapor Phase Epitaxy (VPE) and Metal-Organic Vapor Phase Epitaxy (MOVPE), Molecular Beam Epitaxy (MBE), Atomic Layer Epitaxy (ALE), Low Energy Plasma Enhanced Chemical Vapor Deposition (LEPECVD), Metal-Organic Molecular Beam Epitaxy (MOMBE) and Migration Enhanced Epitaxy (MEE).

In the present thesis work the attention has been focused on self-assembly Vapor-Solid (VS) growth mechanism and Vapor-Liquid-Solid (VLS) growth mechanism, which are widely used for both zinc oxide and silicon carbide nanostructures. Both these mechanisms can be exploited in synthesis processes from vapor phase. Different Chemical Vapor Deposition (CVD) and Vapor Phase Epitaxy (VPE) growth systems have been employed for the growth of nanowires of these two materials.

3.1.1 Vapor-Solid growth mechanism

Vapor-Solid (VS) growth mechanism, otherwise called "evaporation-condensation method", is the mechanism by which gaseous reagents produce a supersaturated vapor of a solid species that then condenses, if possible on a solid surface that is usually the substrate or the growing crystal. The fundamental steps of this kind of growth can be resumed as shown in Figure 1, taken from Ref. [1]:

1) diffusion of the growth species to the growing surface (this usually is rapid and hence it is not a limiting factor)

2) adsorption and desorption of the growth species onto and from the growing surface (this is a process that can be rate limited when the concentration of the growth species is low)

3) surface diffusion of the adsorbed growth species where the growth species can be incorporated into a growth site and contribute to the crystal growth or escape from the surface

4) surface growth by irreversible incorporation the absorbed growth species in the crystal

5) if byproduct of a chemical reaction are produced, they desorbs from the surface.

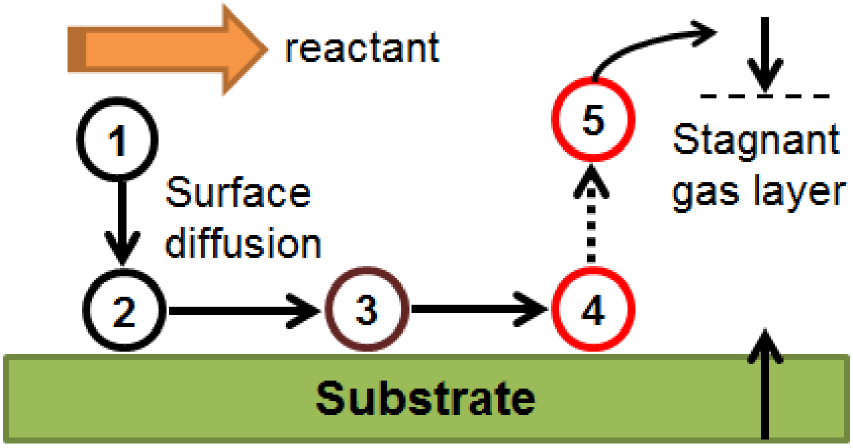

Figure 1. Schematic of the different steps in a VS mechanism [1].

In most crystal growth process, the rate limiting step is either step 2 or step 4 [1]. When step 2 is the rate limiting process, the growth rate is determined by condensation rate given by the factor J (atoms cm^{-2} s^{-1})

$$J = \frac{\alpha\sigma P_0}{\sqrt{2\Pi mkT}} \tag{1}$$

where α is the accommodation coefficient, $\sigma = (P-P_0)/P_0$ is the supersaturation of the growth species, P_0 is the equilibrium vapor at temperature T, m is the mass of the growth species and k is the Boltzmann constant. The growth rate increases linearly with the growth species concentration. Further increase in this concentration would result in a change from an adsorption limited to a surface limited process. When the surface becomes the limiting factor the growth rate becomes independent of the concentration.

An impinging growth species onto the growth surface can be described in terms of the residence time and/or the diffusion distance before escaping back to the vapor phase. The residence time on the surface is described by

$$\tau_s = \frac{1}{v}\exp\left(\frac{E_{des}}{kT}\right) \tag{2}$$

where v is the vibrational frequency of the adatom, (typically 10^{12} s^{-1}) and E_{des} is the desorption energy required for the growth species escaping back to the vapor. While residing in the surface, the growth species will diffuse in the surface with coefficient D_s given by:

$$D_s = \frac{1}{2}a_0 v \exp\left(-\frac{E_s}{kT}\right) \tag{3}$$

E_s is the activation energy for surface diffusion and a_0 is the size of the growth species. So the mean diffusion distance X for a growth species from the site of incidence is

$$X = \sqrt{2}D_s\tau_s = a_0 \exp\left(\frac{E_{des}-E_s}{kT}\right) \tag{4}$$

In a crystal surface, if the mean diffusion distance is much larger than the distance between growth centers, all adsorbed growth species will be incorporated in the crystal structure. In this case the accommodation coefficient will be 1. On the other hand, if the diffusion distance X is much smaller than the distance between growth sites, the growth species will return to the vapor and the accommodation coefficient will be zero. The accommodation coefficient is dependent on the desorption energy, the activation energy of surface diffusion and on the density of growth sites. The growth sites can be understood as the number of broken or dangling bonds of the atoms in the surface. The broken bonds will be the sites where the growing species will be incorporated to the surface for a crystal growth.

All crystal facets can be characterized in three categories [1] depending on the number of dangling periodic bond chains in a facet. These categories are flat surface, stepped surface and kinked surface. The number of periodic broken bonds chains can be understood as the number of broken bonds per atom on a given facet. To exemplify the process let us imagine that we have a simple cubic crystal. Each atom will have a coordination number of 6 (this is 6 chemical bonds). If an atom is adsorbed in the surface it will diffuse randomly with a characteristic diffusion distance *X* defined above. If it is adsorbed in a flat (terrace) surface, it would for one chemical bond. Such atom is called an “adatom”. This atom will for one bond with the surface and it is considered a unfavorable energy state. Under this condition it will diffuse in the surface. If the adatom does not find a growth site (this is a more energetically favorable location in the surface) it will return to the bulk solution/vapor phase (Figure 2a). If in its diffusion path the adatom finds a ledge or a ledge-kink in the surface it can form a double (ledge) of a triple (ledge-kink) chemical bond. In this situation the energy configuration is more favorable and the atom is incorporated to the crystal (Figure 2b).

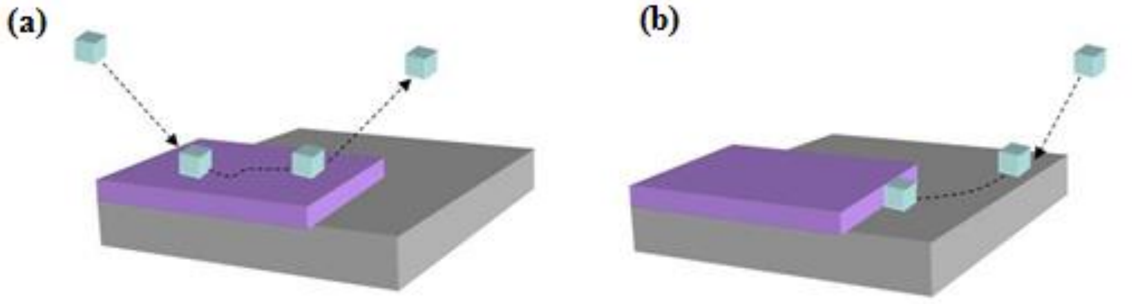

Figure 2. Illustration of adatom desorption (a) or incorporation (b) on the growing crystal surface [1]

The growth of a flat surface is due to the advancement of the steps (or ledges). For a given crystal facets and given growth condition, the growth rate will be dependent on the step density. A misorientation will result in an increased density of steps and consequently will lead to a high growth rate. An increased step density would favor the irreversible incorporation of adatoms by reducing the surface diffusion distance between the impinging site and the growth site, before adatoms escape back to the vapor phase.

The formation of nanowires or nanorods by VS mechanism requires that an anisotropic growth is triggered. In ideal growth conditions, on flat surfaces this is generally rather difficult because some conditions that break the substrate planar uniformity is required. But when one or more of the following circumstances is realized, an anisotropic nanowire-like growth may be obtained:

1) Different facets in a crystal having strongly different growth rate.

2) Presence of imperfections (e.g. screw dislocation) in specific crystal directions.

3) Preferential accumulation of or poisoning by impurities on specific facets.

4) Discontinuous stress release or substrate roughness on the growth surface.

Size and shape of the obtained nanowires is in this case correlated to these conditions and the growth parameters.

3.1.2 Vapor-Liquid-Solid growth mechanism

Vapor-Liquid-Solid (VLS) mechanism is the most widely used to grow nanowires of controlled dimension, thanks to its simplicity and versatility when applied in many semiconductor systems. The VLS mechanism is a 1D crystal growth mechanism that is assisted by a metal catalyst. It results in the creation of whiskers, rods, and wires. 1D crystal growth was initially developed nearly 50 years ago in the Si industry and the mechanism was suggested for wider use by Wagner in 1964 [2,3]. Figure 3 shows a schematic of the VLS mechanism.

As described in Ref [2], in this mechanism, the metal catalyst forms liquid alloy droplets at a high temperature by adsorbing vapor components. For some reason, e.g., temperature or vapor pressure fluctuation, the alloy is further supersaturated. It then drives the precipitation of the component at the liquid–solid interface to achieve minimum free energy of the alloy system. Accordingly, the 1D crystal growth begins, and it continues as long as the vapor components are supplied. Because Vapor (carries solid components), Liquid (catalyst alloy), and Solid (precipitated one-dimensional structures) phases are involved, it is known as the VLS mechanism. The main advantage of this technique is that size and position of the catalyst are related to the diameter and position of the 1D structures, as the liquid phase is confined to the area of the precipitated solid phase. A possible issue, on the contrary, may arise from the presence of a residual metal droplet on the tip of the grown 1D crystals.

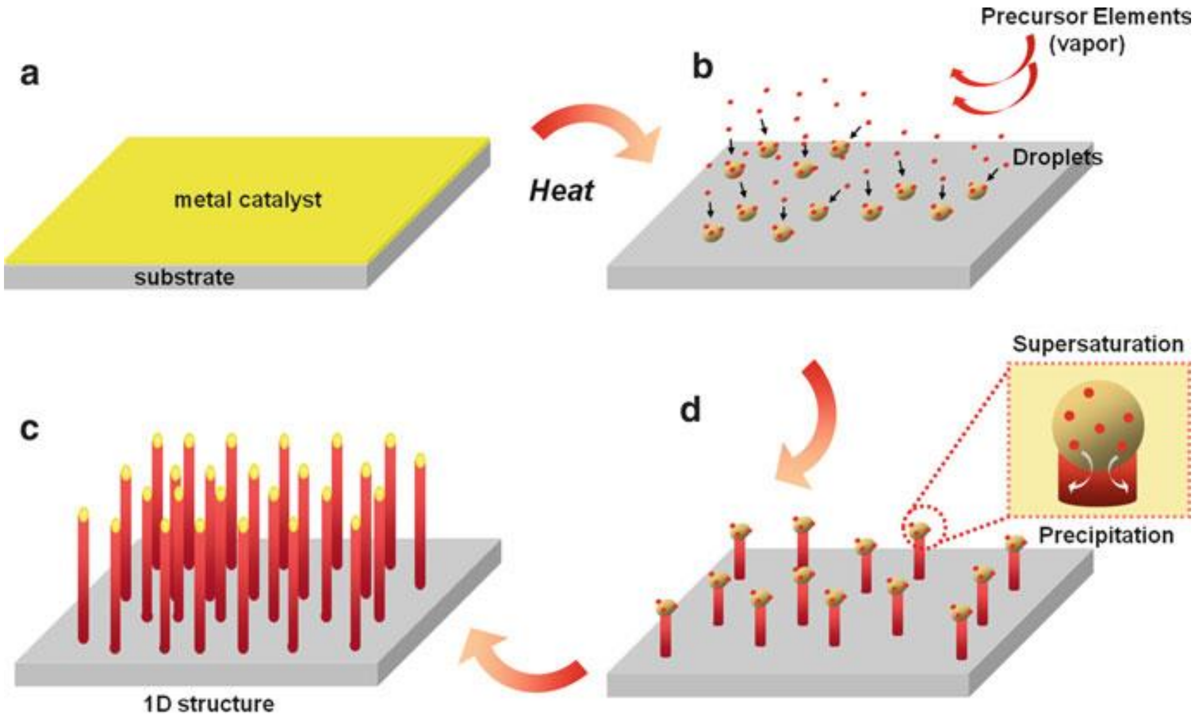

Figure 3. Growth of 1D structures by VLS mechanism [2]

The mechanism works at a high temperature, so that the metal catalyst can form a liquid alloy. Therefore, chemical processes that occur at high temperatures, such as chemical vapor deposition (CVD), molecular beam epitaxy (MBE), laser ablation (LA) and carbothermal reduction (CR), are generally used in conjunction with the mechanism. Occasionally, metal catalysts sometimes work in a solid state in a vapor or liquid phase environment in a process termed the VSS (vapor–solid–solid) or LSS (liquid–solid–solid) mechanism. Since the 1970s, the mechanism has been used to grow various types of whiskers on the micrometer or mm scale. A typical example is SiC whiskers, which are excellent reinforcements for high-strength, high-toughness ceramic or metal composites [4].

The mechanism was then noted for the growth of 1D structures on a nanometer scale, i.e., nanowires, in the 1990s, and the feasibility of this was demonstrated by several groups, including the Lieber group at Harvard University, the Yang group at the University of

California Berkeley, and the Samuelson group at Lund University. As this mechanism was slated to become a core method for the growth of semiconductor nanowires, unambiguous experimental evidence of this mechanism was required for further study. Regarding this, Yu directly observed the growth of Ge nanowires by using an in situ high-temperature transmission electron microscope [5]. The findings of Yu's study showed that there are three well-defined stages in the VLS mechanism: alloying (note that the catalyst in Figure 4a-c becomes larger as the Ge component dissolves and becomes alloyed with Au), precipitation of Ge (the bright area in c and d), and axial growth (extended structures in e and f).

Other observations regarding the growth of Si nanowires on the substrate further confirmed the working of the VLS mechanism with the assistance of a liquid catalyst [6]. The brief history of the VLS mechanism implies that it can be generally used for the growth of many 1D structures, from the nm to even the mm scale. It also shows the rising of new technology from old technology as a good example of the progress of science and technology from previous studies. In fact, previous studies have established some fundamental aspects, as discussed below, which are essential for growing 1D structures using a catalyst.

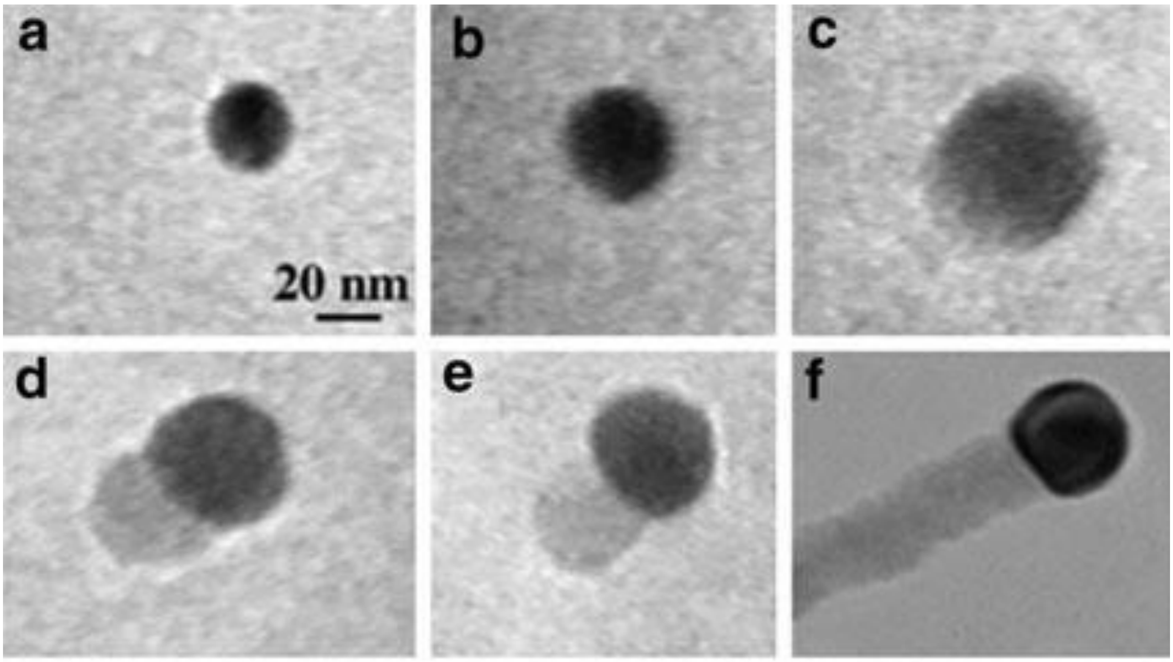

Figure 4. Direct observation of growth of 1D Ge structures by VLS mechanism using Au as catalyst [5]

Three phases (gas, liquid, and solid) and two interfaces (gas/solid and liquid/solid) are involved in the VLS mechanism. As resumed in Ref [2], in these complex system, the kinetics of the VLS mechanism consists of four steps (Figure 5) [7–10]:

1) mass transport in the gas phase

2) chemical reaction at the vapor–liquid interface

3) diffusion in the liquid phase

4) incorporation of atoms in a crystal lattice

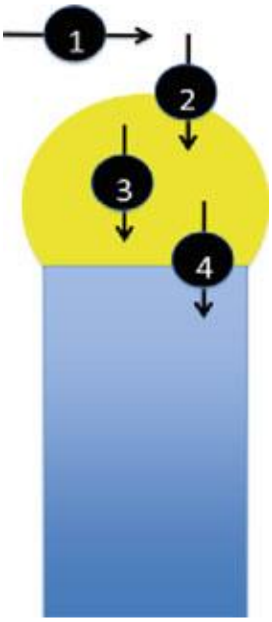

Figure 5. Kinetic steps in VLS mechanism: (1) mass transport in the gas phase; (2) chemical reaction on the vapor–liquid interface; (3) diffusion in the liquid phase; and (4) incorporation of atoms in a crystal lattice [2]

Identification of the rate-determining step among these is important to control the overall kinetics of the VLS mechanism. However, this is complicated, as three phases, two interfaces, and chemical reactions are involved [7]. Nevertheless, it may be possible to draw some insight based on the experimental results. As an example, the rate-determining step for the growth of 1D Si structures with an Au catalyst could be postulated as follows: Among the steps, step (3) can be excluded, because atoms diffuse in liquid metals very quickly [8] and thick nanowires or whiskers do not grow more slowly than those that are thinner, while the shape of the liquid droplet is maintained as nearly hemispherical and thus retains a longer diffusion length [7]. Step (1) can also be excluded because the diffusion coefficient in the gaseous phase usually follows the following power law [7, 8]:

$$D = D_0 (T/T_0)^n (P/P_0), \qquad n = 1.5 \sim 2$$

Hence, the growth rate should follow the power law. However, this is not the case in many cases [7–10]. The primary evidence for regarding step (2) as the rate-limiting step is that the growth rate is proportional to the partial pressure of the reactant gas. However, this does not fully support the argument given that the growth process consists of two activated steps in series [7]. The dependence of the growth rate on the reactant vapor concentration is not in itself evidence that any of the steps is the rate-determining step. Rather, it simply reflects the dependence of the growth rate on supersaturation. Therefore, the rate-determining step would be step (4), the incorporation of atoms in a crystal lattice. It should be noted that the rate-determining step can be changed by the materials involved in the kinetics and by the processing conditions. Therefore, it should be carefully postulated by as many experimental results and data as possible [2].

In the VLS growth, a second phase material, commonly referred as either impurity or catalyst is purposely introduced to direct and confine the crystal growth. A catalyst forms a liquid droplet by itself or by alloying with growth material during the growth, which acts as a trap of growth species. Enriched growth species in the catalyst droplets subsequently precipitates at the growth surface resulting in one-directional growth. Requirements for VLS growth are [2]:

- The catalyst or impurity must form a liquid solution with the crystalline material to be grown at the deposition temperature.
- The distribution coefficient of the catalyst or impurity must be less than unity at the deposition temperature.
- The equilibrium vapor pressure of the catalyst or impurity over the liquid droplet must be very small to avoid (or minimize) evaporation of the catalyst in the droplet.
- The catalyst or impurity must be chemically inert.
- The interfacial energy plays an important role; the wetting characteristics influence the diameter of the nanowire for a given volume of the droplet , a small wetting angle results in a large growth area and a large diameter nanowire .

- For a compound nanowire growth, one of the constituents can serve as the catalyst.
- For a controlled unidirectional growth the solid-liquid interface must be well defined crystallographically.

The size of nanowires grown by VLS method is solely determined by the size of the liquid catalyst droplets. To grow thinner nanowires, one can simply reduce the size of the liquid droplets. Typical method used to form small liquid catalyst droplets is to coat a thin layer of catalyst on the growth substrate and to anneal at elevated temperatures. During annealing, catalyst reacts with the substrate to form a eutectic liquid and further lead to reduction in the overall surface energy. Nanowires can be grown using a nanometer-sized metal catalyst because the diameter of a 1D structure is confined by the size of the catalyst. Indeed, the bulk of previous studies demonstrated the growth of nanowires using nanofilms (that convert to nanoliquid droplets at a high temperature due to surface tension) or nanoparticles. However, it is difficult to decrease the size of the catalyst and in turn the diameter of nanowires in an unlimited manner. Thermodynamically, the minimum radius R_m of a liquid metal droplet is given as [11],

$$R_m = \frac{2V_l}{RT\ln(s)}\sigma_{lv} \qquad (5)$$

where V_l is the molar volume of the droplet, σ_{lv} is the liquid–vapor surface energy, and s is the degree of supersaturation of the vapor. According to this equation, using a smaller catalyst requires a higher degree of supersaturation. However, the chemical potential of the component in the metal–alloy catalyst becomes high as the size of the catalyst decreases due to the Gibbs–Thompson effect:

$$\Delta\mu = \frac{2\gamma}{r} \qquad (6)$$

Here, $\Delta\mu$ is the chemical potential difference of the component species in the liquid droplet, γ is the surface energy, and r is the radius of curvature of the droplet. Therefore, dissolving a vapor component into a liquid alloy becomes increasingly difficult as the size decreases, making it difficult to reach supersaturation states that sufficiently induce the growth of nanowires. Indeed, it is known that the growth of 1D structures with diameters of several tenths of nm is feasible; however, ensuring a smaller diameter (e.g., sub-10 nm) is difficult due to the thermodynamic limitations associated with the use of a nano-catalyst. An additional difficulty that arises when downsizing a catalyst comes from the manipulation of metal nanoparticles or droplets. It is well known that nanoparticles have strong van der Waals attractive forces and thus agglomerate into larger particles. Furthermore, Ostwald ripening occurs between nanoparticles at high temperature.

Ostwald ripening is a spontaneous process that occurs because larger particles are more energetically favorable. Accordingly, nanoparticles tend to transform into large particles to attain a lower energy state if the temperature is high enough to induce diffusion of the metal component. Because the van der Waals attractive forces and Ostwald ripening lead to the formation of larger droplets, larger diameter 1D structures are often grown from a nano metal catalyst [2]. Thus, metal nanoparticles have to be carefully separated from each other in the course of the preparation, positioning on the substrate, and heating for the growth of 1D structures.

3.1.3 Chemical Vapor Deposition technique

Chemical Vapor Deposition (CVD) is a process whereby a solid material is deposited from a vapor by a chemical reaction occurring on or in the vicinity of a normally heated substrate surface. The solid material is obtained as a coating, a powder, or as single crystals. By varying the experimental conditions, such as substrate material, substrate temperature, composition of the reaction gas mixture, total pressure gas flows, etc., materials with different properties can be grown. CVD is a technique operating at in wide temperature range, typically between 200°C and 1600°C, from inorganic or organic precursors in a flow of inert and/or reactive carrier gases [12].

A characteristic feature of the CVD technique is its excellent throwing power, enabling the production of coatings of uniform thickness and properties with a low porosity even on substrates of complicated shape. Another characteristic feature is the possibility of localized, or selective deposition, on patterned substrates. CVD is employed in many thin film applications [13]. It is, for instance, used in the microelectronics industry to make films serving as dielectrics, conductors, passivation layers, oxidation barriers, and epitaxial layers. Other CVD applications are the preparation of high temperature materials (tungsten, ceramics, etc.) and the production of solar cells, of high temperature fiber composites, and of particles of well-defined sizes [14]. CVD is used also in the field of ceramic superconductors because oxygen activity in the vapor can be precisely controlled during the deposition and no annealing in oxygen is needed after the growth to achieve superconductivity.

In a standard CVD process, near or on a heated substrate surface, a chemical reaction of the following type occurs:

gaseous reactants → solid material (+ gaseous sub-products)

In the case also gaseous sub-products are generated by the reaction, these are generally evacuated as exhaust gases by the carrier gas flow. There exist several types of CVD processes. In thermally activated CVD (TACVD), the deposition is initiated and maintained simply by heat. However also photons, electrons, and ions, as well as a combination of these (plasma activated CVD), may induce and maintain CVD reactions [15, 16]. In CVD, gaseous reactants are admitted into a reactor (see Figure 6) where product deposition takes place.

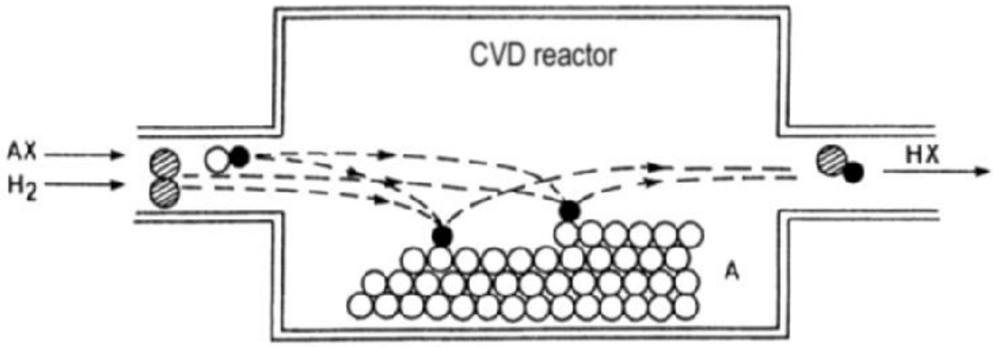

Figure 6. Example of CVD process (adapted from Ref. [14])

Even though several rate-limiting steps can be identified in a CVD process, only five main categories of control are normally discussed [14]:

1) Thermodynamic control. Thermodynamic control means that the deposition rate is equal to the mass input rate into the reactor (corrected for the yield of the process). This occurs at extreme deposition conditions (very low flow rates, high temperatures, etc.). The temperature dependence of the deposition rate is obtained from thermodynamic calculations.

2) Surface kinetics control. If the deposition rate is lower than the mass input rate into the reactor and the mass transport rate in the vapor in the reactor to or from the substrate, a surface kinetics control or nucleation control exist. The surface kinetics control is favorable for obtaining coatings of uniform thicknesses on more complicated shaped substrates.

3) Mass transport control. A process may also be controlled by the mass transport in the vapor in the reactor to or from the substrate surface. This occurs frequently at high pressures and high temperatures.

4) Nucleation control. At low supersaturation the deposition rate may be controlled by the nucleation.

5) Homogeneous reaction control. In some processes the formation rate of key species in the vapor may control the deposition rate.

The choice of the CVD system is affected by a number of factors: the reactants used in the process, the maximum acceptable leak rate for air into the system, purity of the deposited material, size and shape of the substrate, process economy, etc. [17]. A CVD system is advantageously constructed in three modules:

1) the carrier gas and reactive gas/vapor dispensing system
2) the reactor, including components for defining the gas flows
3) the exhaust system containing a total pressure controller, vacuum pump, scrubber and/or reactant recycle system.

3.1.3.1 Gas/vapor dispensing system

Reactants, which are gases at room temperature, are stored in gas bottles. After pressure regulation, their flows are usually measured with mass flow meters. Use of mass flow meters yields high accuracy and allows electronic control of gas flows. Those reactants that are liquids or solids at room temperature, on the contrary have to be fed to the system in other ways. They can be admitted to the system by simply heating them above the melting (evaporation), boiling (gas phase transition) or sublimation (dissociation, decomposition, atomization, etc.) point. The evaporation rate can be varied by varying the source temperature and/or the dimensions of the transport channels from the sources. Another way of introducing these substances is to use an evaporator or sublimator together with a carrier gas. The latter is used when evaporation process is slow or vapor amount of the source substance is too small to be transported in an efficient way. For example the carrier gas can be bubbled through the liquid to be evaporated or flowed above its surface. Carrier gas pushes vapors of the liquid substance, transporting it into the reactor. In this case the evaporation rate depends on the temperature of the liquid, the liquid level in the container, and the flow rate of the carrier gas. For the highest reproducibility it is important to have a nearly constant level of the liquid in the container. However, some alternatives to these evaporators exist which use carrier gases and are independent of the liquid level. In one alternative, the use of saturated vapor pressure is exploited: the liquid is evaporated from a vessel, cooled and condensed in a cooler, leaving a carrier gas saturated with a well-known concentration of the substance vapor at the temperature of the cooler. If two or more reactant liquids have to be used in the process, it is seldom possible to vaporize them in the same evaporator while maintaining the predetermined molar ratio since they normally have different vapor pressures.

The principle of the sublimator is similar to that of the evaporator. In a sublimator the substance is transferred to the vapor by sublimation (solid →gas) and then transported to the reactor by the carrier gas. The use of a carrier gas is generally mandatory because evaporation rate during a sublimation process are often low. Direct metering of liquids/solids followed by immediate vaporization in a vessel can also be used.

For speeding up the vaporization it is also possible to use a flash vaporizer [18], a vessel containing pieces of porcelain of high temperature.

Many CVD processes are strongly affected by contaminants in the vapor. The contaminants originate from the reactants themselves, the reaction sub-products and from various undesired chemical reactions between the gases and the materials in the gas dispensing system (in the tubes, evaporators, sublimators). Most frequently impurities come from air leakage that can bring strongly reactive oxygen, water vapors or nitrogen in the reactor. The contamination level can be reduced by:

- Purifying the reactants (for example hydrogen and argon can be purified to a level of 1 ppm in commercially available purifiers)
- Having a low leak rate (good sealing in the whole used pressure and temperature ranges, use of degassed O-rings where they are used for vacuum seals)

- Using carrier gases which are non-reactive with the materials to be vaporized (in evaporators and sublimators)
- Using materials in the tubes, vaporizers, reactors, etc., which are compatible with the used gases/vapors
- Installing purge line, which is important when reactive gases, e.g., halides, are used Finally, in CVD, explosive, flammable and toxic gases (hydrogen, silane, phosphine, arsine) are frequently employed.

Correct handling of the gases is, therefore, necessary. Every precaution should be taken. Effective ventilation systems and gas detectors (commercially available) should be used.

3.1.3.2 Reactors

The process selected, as well as the size, shape, and number of substrates, define the type of reactor and its geometry [17]. Two main reactor types can be distinguished:

1. HOT WALL REACTOR

In the hot wall reactor [19], the reactor tube is surrounded by a furnace. This means that the substrates and the wall of the reactor have nearly the same temperature. In addition to the film growth occurring on the substrates, film growth might thus take place on the inner side of the reactor walls. When thick films are formed on the reactor walls, there is a reasonable risk that particles will break loose from reactor walls, fall down on the surface of the growing film, and introduce pinholes or other imperfections in it. There might also be a source of contamination in this reactor type because of the reaction between the material of the reactor wall and the vapor. In the hot wall reactor, homogeneous nucleations and reactions may take place in the vapor, affecting the deposition on the substrate and hence the structure of the films. Moreover, as the reactants are transported through the reactor, there is a progressive reduction in their concentration, which may yield to different deposition conditions within the reactor. On the other hand many substrates can be deposited simultaneously in a hot wall reactor.

2. COLD WALL REACTOR

In the cold wall reactor [20], the walls of the reactor are cold and only the substrate is heated if necessary. In this system usually no deposition occurs on the walls, eliminating the risk of particles breaking loose from the walls. Furthermore, a low wall-temperature reduces the risk of contaminating vapor/wall reactions. In the cold wall reactor, the homogenous nucleations and reactions in the vapor are suppressed and surface reactions become dominant. The steep temperature gradients near the substrate surface may introduce severe natural convection resulting in a non-uniform film thickness and microstructure. However, with the higher flexibility of the cold wall reactor, high cleanliness, high deposition rates (yielding high wafer throughput), high cooling rates combined with the needs of thickness uniformity, automatic wafer handling and use of increasing wafer diameter, there is tendency to more frequently use cold wall reactors in the microelectronics. Finally the cold wall reactor is not compatible with that processes in which wall temperature is cold enough to condensate reactants or sub-products vapors, which can accumulate and give rise once again to particles breaking loose issues.

3.1.3.3 Single chamber evaporator and reactor

In some case, the source material/substance evaporation is performed in the same reactor chamber where deposition is performed. This simplified version of a CVD system exploits different regions of a single furnace where temperature gradients are well known and controllable. In most of cases, these single chamber systems are hot wall reactors.

A typical example of this kind of CVD systems are linear furnaces, like tubular furnaces, where the main reactor chamber is a single tube through which a carrier gas can flow and that is placed inside a furnace with one or more heating elements that can produce the proper thermal gradient. Evaporation/sublimation temperature and substrate temperature are controlled separately by their position in the furnace and the temperature profile (Figure 7).

In this system, if no carrier gas is used, temperature gradient determines the reagents vapors flow directions and in this case it could be difficult to control them. For this reason in most of case a carrier (inert or reactive) gas is used. In this case the source to be evaporated is placed upstream and substrate downstream. Temperature profiles can be further tuned to promote or limit reagents and sub-products diffusion in the reactor.

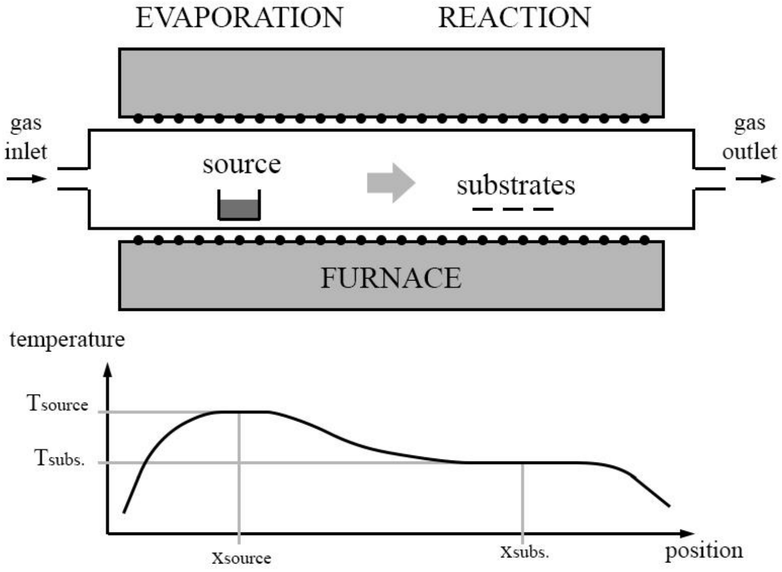

Figure 7. Scheme of a single chamber CVD evaporator and reactor

Unfortunately, this system is usually unsuitable for co-evaporation of multiple sources.

3.1.4 Vapor Phase Epitaxy technique

Vapor phase epitaxy (VPE) involves precipitation from a supersaturated vapor phase (Figure 8). This vapor may contain pure elemental material, but more often involves chemical precursors for the desired substance [17] (e.g. MOVPE).

The main difference with CVD technique is that in VPE reactions the involved vapor pressures are generally lower so that a slower but more controllable and nearly layer-by-layer growth can be achieved. The term epitaxy, more precisely, refers to the possibility of growing the new material layers accordingly to the substrate crystal structure and hence affecting its crystal growth orientation.

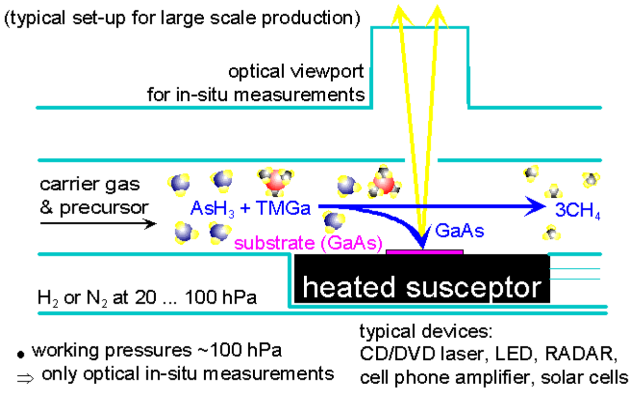

Figure 8 Example of a VPE process [17]

Indeed VPE is itself a subset of CVD, which is not necessarily epitaxial.

A huge range of vapor-phase precursors can be found, making this technique extremely versatile [21]. Moreover, the vapor can be continuously replenished in a controllable way, allowing for much greater control over growth of complex structures than can be achieved with other techniques. This technique is today one of the most common ones for growing semiconductor device structures, and it also plays an important role in the growth of nanostructures. The major limitation is that both reactants and operation are considerably more expensive than other techniques.

3.1.4.1 VPE system

As described in Ref. [21], the major parts of a typical VPE system are:

1) gas handling system

2) reactor chamber

3) heating system for pyrolysis temperature

4) exhaust system

5) safety apparatus

The reactor chamber is generally a quartz tube or a stainless steel chamber containing a substrate placed on a heated susceptor where the source materials and radicals are introduced in order to achieve the compound semiconductor growth. The hot susceptor has a catalytic effect on the decomposition of the gaseous products and the growth takes place primarily at the hot surface. The vapor flow is controlled by the carrier gas flow, possibly diluted with a dilution gas and stabilized by keeping the pressure in the bubbler at a constant level. The chemical reaction in this technique takes place at a heated substrate surface of gas molecules having the material to be grown. The carrier gas transports the liquid vapors to the growth chamber [21].

The general carrier gas used in VPE growth process is palladium purified hydrogen (H_2) to dilute the reactants and also to transport the reactants to the growth zone. When the metal organics and hydrides are thermally cracked on a hot substrate, deposition takes place. These chemicals are transported by a carrier flow and reach the substrate surface by diffusing through a stagnant carrier gas boundary layer above the substrate.

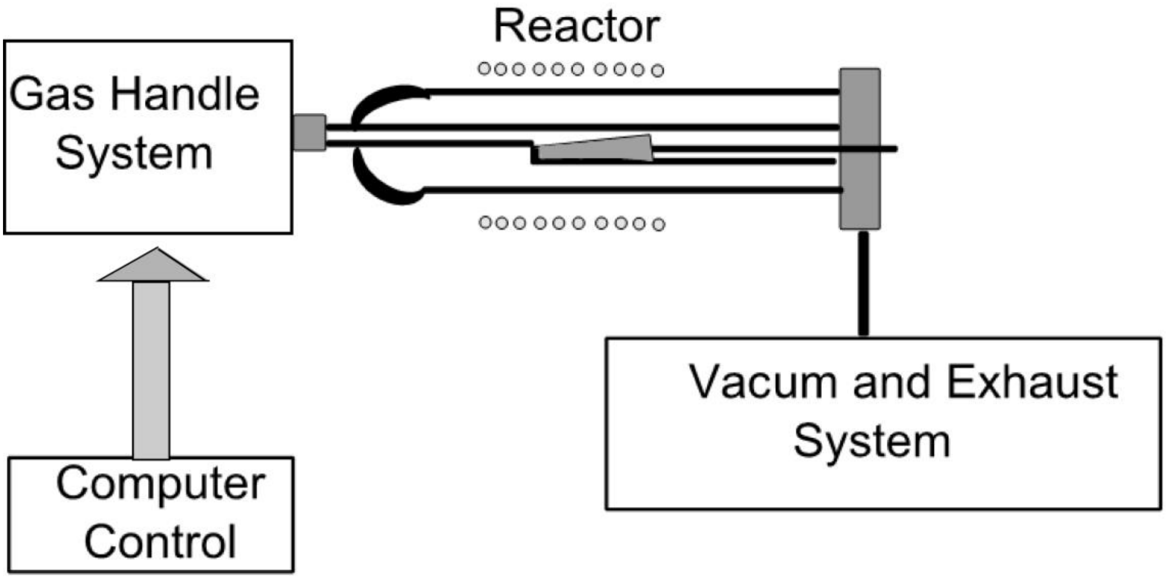

Figure 9. Block diagram of a VPE reactor [23]

The VPE deposition process takes place in a growth chamber in which, under constant pressure and temperature conditions, several chemical reactions occur. The precursors that have been transported into the chamber undergo heterogeneous reactions in the vapor phase and homogeneous reactions with the substrate [22]. The block diagram of the VPE reactor is shown in Figure 9.

The gas handling system includes source like alkyls, hydrides, valves, pumping and instruments necessary in controlling the gas flows mixtures. The gas-handling system has to be maintained to grow high quality layers. Stainless steel tubes are used in the transport of alkyls from the source to the reactor chamber [23]. The electronic mass flow controllers and thermal bath system supply precisely controlled amounts of gas to the reactor chamber.

The purity of the starting materials is one of the major issues in semiconducting device technology and hence much care is taken in purifying every material used in the VPE reactor to avoid any kind of contamination. The main impurities present in H_2 gas are O_2 and H_2O. Any improper gas cylinder or gas system component change can also introduce contamination. In the growth of VPE, selection of tubes, fittings and valves form the essential criteria for high purity of films [24]. Electronic mass flow controllers (MFC) are able to control the exact amount of carrier gas flowing through the bubbler by maintaining a constant source vapor pressure. Hence, the amount of the source material transported to the reactor is controlled. MFCs are reliable and accurate in the measurement and control of the mass flow rate of the gases.

3.2 Characterization Techniques

Different techniques have been used for this thesis work, mainly to identify and study the morphology, the composition, the crystal structure and finally the optical and electronic properties of the grown nanostructures.

Considering that the main aim of this thesis is the growth of nanowires, the theoretical background of electron microscopy-based techniques is briefly resumed. As a consequence, the scanning and transmission electron microscopy basic principles are taken from well-known text books and manuals. The scanning electron microscopy (SEM) was used as a first and immediate technique for checking morphology, size and distribution of the grown nanostructures onto the substrates after each synthesis parameter change. This feed-back process was fundamental to optimize the nanostructure properties.

Then other techniques were used on selected samples for a deeper study of the chemical and physical properties of the grown nanowires. Transmission electron microscopy (TEM) was mainly used to determine the crystal structure and orientation of the nanocrystals, while in some case X-ray energy-dispersive spectroscopy (EDS) was used to evaluate the chemical composition of the nanowires as well as the presence of core-shell structures.

The optical characterization was then used to check the crystal phase and to have information about the electronic properties and on the presence of defects/impurities inside the nanostructures. Photoluminescence, cathodoluminescence and Raman spectroscopy were employed on selected emblematic samples in order to obtain complementary data.

3.2.1 Scanning Electron Microscopy

The first scanning electron microscope (SEM) was built by von Ardenne in 1938, while the first commercial SEM was developed in England in 1965 [25]. The SEM is primarily used as a non-destructive technique for investigating the surface morphology of materials at the nanoscale.

Electron microscopes make use of an electron beam to investigate samples beyond the typical resolution limits of an optical microscopes [26]. Indeed, the Abbe's equation defines a maximum theoretical resolution d for an optical microscope as:

$$d = (0.612\ \lambda) / (n \sin\alpha)$$

where λ is the wavelength of imaging radiation and ($n \sin\alpha$) is the numerical aperture (n is the refraction index of the medium between point source and lens, relative to free space, and α is half the angle of the cone of light from specimen plane accepted by the objective in radians). This means that the maximum resolution for an optical microscope with ideally perfect lenses is about 300 nm. For electrons, instead, following De Broglie equation:

$$\lambda = h / m\ v \approx 1.23\ \text{nm} / V^{1/2}$$

where h is Planck's constant, m is mass of the particle, v is velocity of the particle and V is the accelerating voltage. This means that electrons have a resolution limit around 0.05-0.01 nm, although in real applications the lower "perfection grade" of magnetic lenses respect to optical ones and other constrains generally strongly affect this value and hence SEM maximum resolution is typically close to 1 nm. This is however close to atomic resolution and makes electron microscope a perfect tool for nanostructures investigation.

Beside this, the use of a high energy electron beam (usually accelerated up to 40KV) also generate a lot of different signals (electrons and photons in different energy ranges) from the sample, each of which contains complementary information not only about morphology (or topography) but also about its composition, crystalline structure and other physical properties.

Different scanning electron microscopes have been used for the characterization of the grown samples: a Philips 515 SEM with tungsten filament operating at 25KV and a JEOL 6400F FEG-SEM, as well as a FEI Quanta FEG-ESEM operating at 30KV for selected samples.

3.2.1.1 Working principle

The electron column (figure 10) is where the electron beam is generated under vacuum, focused to a small diameter, and scanned across the surface of a specimen by electromagnetic deflection coils. The lower portion of the column is called the specimen chamber. The secondary electron detector is located above the sample stage inside the specimen chamber. Specimens are mounted and secured onto the stage which is controlled by a goniometer. The manual stage controls are found on the front side of the specimen chamber and allow for x-y-z movement, 360° rotation and 90° tilt however only the tilt cannot be controlled through the computer system thus there is no need to use all of the manual controls manipulate the orientation of the sample inside the sample chamber.

The quality and resolution of SEM images are function of three major parameters: (i) instrument performance, (ii) selection of imaging parameters (e.g. operator control), and (iii) nature of the specimen. All three aspects operate concurrently and neither of them should or can be ignored or overemphasized [27, 28].

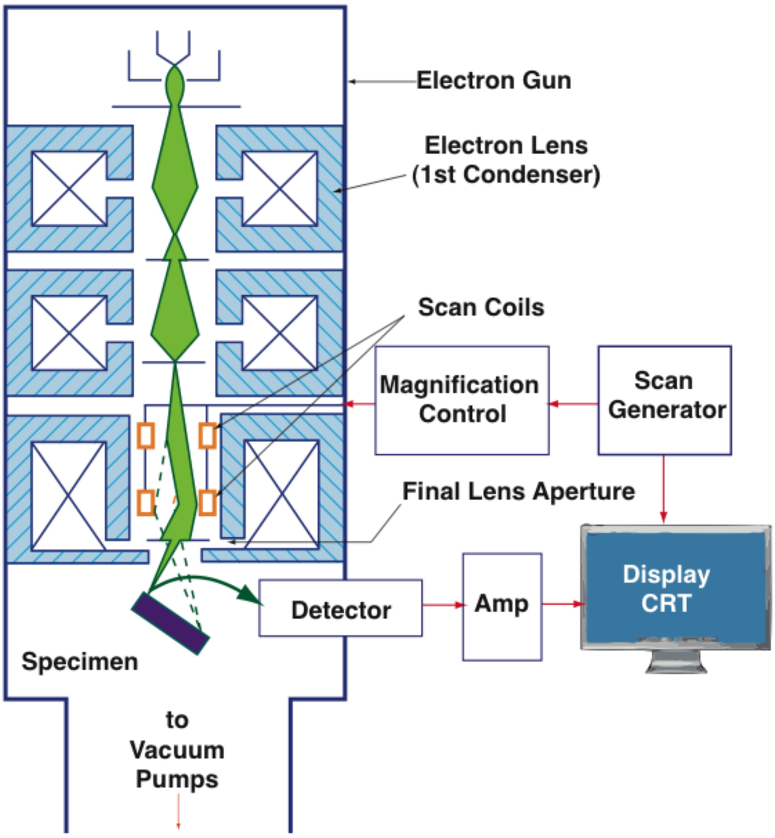

Figure 10. Scanning electron microscope column [29]

Each point on the specimen that is struck by the accelerated electrons emits signal in the form of electromagnetic radiation. Selected portions of this radiation, usually secondary (SE) and/or backscattered electrons (BSE), are collected by a detector and the resulting signal is amplified and displayed on a TV screen or computer monitor. The resulting image is generally straightforward to interpret, at least for topographic imaging of objects at low magnifications. The electron beam interacts with the specimen to depth on both beam energy and specimen atomic number. Complex interactions of the beam electrons with the atoms of the specimen produce wide variety of radiation that can be collected in different way to study different properties of the sample.

In detail, main components of the electron column are:

1) Electron gun: located at the top of the column where free electrons are generated. by thermionic emission from a filament cathode. Tungsten was originally the most used filament type in thermionic electron guns because it has the highest melting point and lowest vapor pressure of all metals, thereby allowing it to be heated for electron emission, and because of its low cost. Other types of electron emitters include lanthanum hexaboride (LaB_6) cathodes, which can be used in a standard tungsten filament SEM if the vacuum system is upgraded and field emission gun (FEG), which may be of the cold-cathode type using tungsten single crystal emitters or the thermally assisted Schottky type, using emitters of zirconium oxide. Emitted electrons are primarily accelerated toward an anode that is adjustable from 200V to 30 kV (1kV=1000V).

2) Condenser lenses: after the beam passes the anode it is influenced by two condenser lenses that cause the beam to converge and pass through a focal point. What occurs is that the electron beam is essentially focused down to 1000 times its original size. In conjunction with the selected accelerating voltage the condenser lenses are primarily responsible for determining the intensity of the electron beam when it strikes the specimen [27].

3) Apertures: depending on the microscope one or more apertures may be found in the electron column. The function of these apertures is to reduce and exclude extraneous electrons in the lenses. The final lens aperture located below the scanning coils determines the diameter or spot size of the beam at the specimen. The spot size on the specimen will in part determine the resolution and depth of field. Decreasing the spot size will allow for an increase in resolution and depth of field with a loss of brightness [27].

4) Scanning system: images are formed by rastering the electron beam across the specimen using deflection coils inside the objective lens. The stigmator or astigmatism corrector is located in the objective lens and uses a magnetic field in order to reduce aberrations of the

electron beam. The electron beam should have a circular cross section when it strikes the specimen however it is usually elliptical thus the stigmator acts to control this problem [27, 29].

5) Specimen chamber: at the lower portion of the column the specimen stage and controls are located. The secondary electrons from the specimen are attracted to the detector by a positive charge.

The types of signals produced by a SEM include secondary electrons (SE), back-scattered electrons (BSE), characteristic X-rays, light (cathodoluminescence) (CL), specimen current, transmitted electrons, etc. (Figure 11). . The signals result from interactions of the electron beam with atoms at or near the surface of the sample. Also transmitted electrons can be collected as a product of the electron-specimen interaction (see e.g. the electron beam induced current imaging cross sectional mode-EBIC)

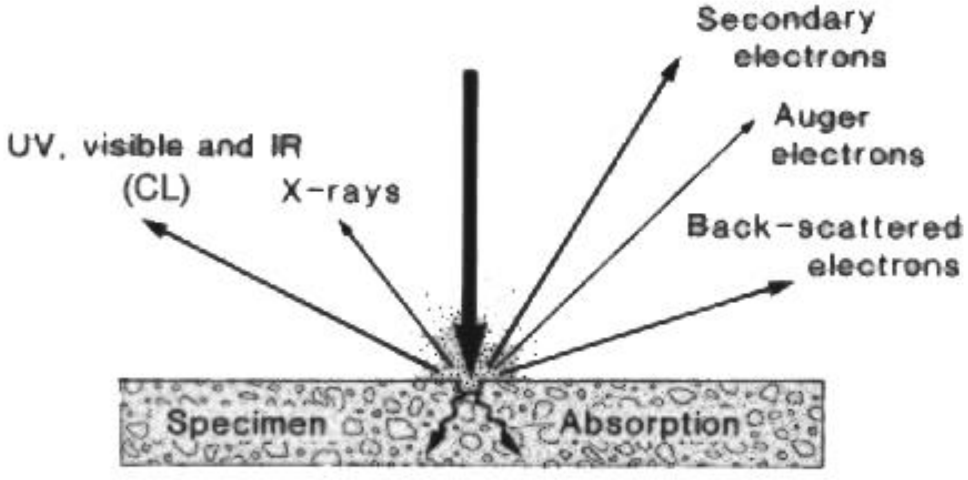

Figure 11. Schematic representation of different processes induced by keV electrons.

In the most common or standard detection mode, low-energy (<50 eV) secondary electrons, which are ejected from the k-shell of the specimen atoms by inelastic scattering interactions with beam electrons, are collected by a positive voltage to reconstruct an image of the sample surface morphology. Using the signal of secondary electrons, image resolution less than 0.5 nm is namely possible.

Backscattered electrons (BSE), on the contrary, consist of high-energy electrons originating in the electron beam, that are reflected or back-scattered out of the specimen interaction volume by elastic scattering interactions with specimen atoms. Since heavy elements (high atomic number) backscatter electrons more strongly than light elements (low atomic number) BSE are used to generate images in which the contrast between areas is dependent on different chemical compositions.

Also photons with different energies can be collected from the sample during the beam irradiation to obtain other kind of information. This is the case, for example, of energy-dispersive spectroscopy and cathodoluminescence that will be discussed separately in this chapter.

3.2.2 Transmission Electron Microscopy

Transmission Electron Microscopy (TEM) is a well-established technique for the study of defects and crystal structure at atomic resolution in semiconductor materials [30, 31]. TEM is a microscopy technique in which a beam of electrons is transmitted through an ultra-thin specimen by interacting with the specimen as it passes through. The microscope image is formed by the electrons transmitted through the specimen after their interaction with the specimen atoms. This image is then magnified and focused onto an imaging device, such as a fluorescent screen, on a layer of photographic film or to be detected by a sensor such as a Charge Coupled Device (CCD) camera. As opposite to conventional microscopy, HRTEM does not use absorption by the sample for image formation (except than for organic specimens), but in case of crystal samples, the contrast arises from the interference in the image plane of the electron wave with itself. TEM is capable of imaging at a significantly higher resolution than light microscopes owing to the small de Broglie wavelength of electrons [21].

There are two main kind of information that can be used to form a TEM image: contrast and diffraction. Contrast formation in TEM depends greatly on the operation mode. Complex imaging techniques that utilize the unique ability to change lens strength or to deactivate a lens, allow for many operating modes (Bright field, Diffraction contrast, Electron energy loss, Phase contrast, etc.). These modes may be used to discern information that is of particular interest to the investigator. On the other hand, by adjusting the magnetic lenses such that the back focal plane of the lens rather than the imaging plane is placed on the imaging apparatus, a diffraction pattern can be generated. For thin crystalline samples, this produces an image that consists of a pattern of dots in the case of a single crystal, or a series of rings in the case of a polycrystalline material. In particular, for the single crystal case the diffraction pattern is dependent upon the orientation of the specimen and the structure of the sample illuminated by the electron beam. This image provides the investigator with information about the space group symmetries in the crystal and the crystal's orientation to the beam path.

A Jeol 2200FS field emission TEM, working at 200KV and equipped with HAADF, EELS and EDX has been used for the characterization of the grown ZnO and SiC samples.

3.2.2.1 Working principle

The four main components of TEM are electron optical column, vacuum system, the necessary electronics with the lens supplies for focusing and deflecting the beam and the high voltage generator for the electron source and control software. A modern TEM typically comprises of an operating console surmounted by a vertical column and containing the vacuum system and control panels conveniently placed for the operator. The microscope may be fully enclosed to reduce interference from environmental sources. It may even be operated remotely, removing the operator from the instrument environment to the benefit of both the operator and the instrument.

Like in a SEM, in a TEM an electron beam is generated from a filament and the accelerated at high voltage (e.g. up to 200-300KV) through the column to reach the sample. But, in the case of TEM, image is generated below the sample from those electrons that penetrated and interacted with the sample (Figure 12). Each imaging electron interacts independently with sample. As a result of the interaction with the sample, the electron wave passes through the imaging system of the microscope where it undergoes further phase change and interferes as the image wave in the imaging plane. It is important to realize that the recorded image is not a direct representation of the crystallographic structure of sample.

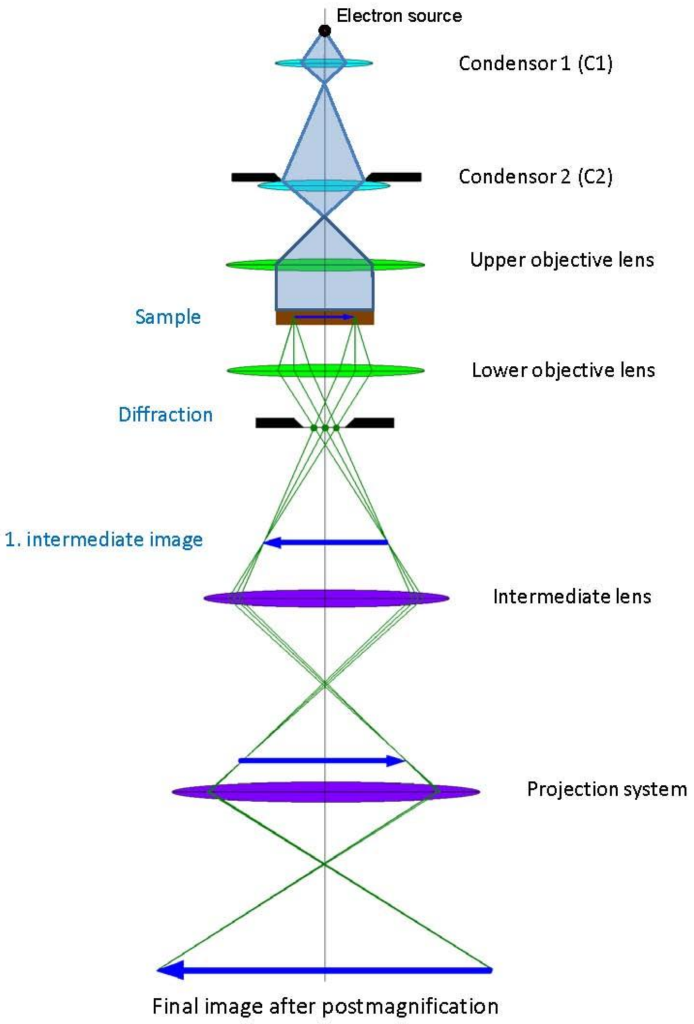

Figure 12. Main setup of a TEM [30].

After the electron source we have a system of condenser lenses. These lenses are used in order to form the electron beam. By changing the focal distance of condenser lenses we can create parallel or convergent illumination. The parallel beam is usually used in traditional TEM. The convergent beam is typical for STEM mode (Scanning TEM), because one needs to illuminate the sample point-by-point.

Objective lenses of the microscope are used for image formation. After propagating through objective lens all electron beams from the sample are focused at the image plane. Here one uses objective apertures in order to exclude electrons at high scattering angles. In HRTEM mode usually no objective apertures are used. The objective lenses define the quality of imaging and in that way the resolution of microscope.

The projection system of microscope consists of intermediate lens and projection lenses. By changing the strength (i.e. the focal distance) of intermediate lens it's possible to switch between diffraction and imaging modes. If the back focal plane of objective lenses correspond to the object plane of intermediate lens we can obtain diffraction on the viewing screen. In imaging mode we readjust the intermediate lens so that its object plane is the image plane of objective lens. The projection lenses are used for post-magnification of the image. By HRTEM the highest magnification can be 10^6 or even higher. The final image is generally recorded with a CCD.

3.2.3 X-ray energy-dispersive spectroscopy

In Figure 11, among the different signals emerging from a sample that is irradiated with a high energy electron beam we can find also X-rays. The incident beam, indeed, may excite an electron in an inner shell of an atom in the sample, ejecting it from the shell while creating an hole. When electron from an outer shell fills the hole, the difference in energy between the higher-energy shell and the lower energy shell may be released in the form of an X-ray. As the energy of the X-rays are characteristic of the difference in energy between the two shells and of the atomic structure of the element from which they were emitted, this allows to correlate the X-ray photon to a specific element [26].

This is the principle of X-ray Energy Dispersive Spectroscopy (EDS), or X-ray microanalysis. The number and energy of the X-rays emitted from a specimen can be indeed measured by an energy-dispersive spectrometer and the elemental composition of the portion of sample that is hit by the beam ca be calculated.

EDS is available both for SEM and TEM. The main difference between these two is spatial resolution because the spatial distribution of the electron-hole pairs generated by the electron beam, commonly called generation volume or interaction volume, is different in a bulk SEM sample and in a very thin TEM sample. The size of this volume directly affects EDS resolution because X-rays can be generate by any atom in that volume. So, in the case of a “bulky” SEM sample a pear-shaped generation volume, that is dependent mainly on beam acceleration voltage and sample’s average atomic number, is formed and its size generally range from 100 nm up to 5 μm. On the contrary, generation volume in a thin TEM sample is limited by the higher beam voltage (which make the volume-shape narrower near the surface) and by the small sample thickness.

Thanks to sophisticated modelling tools it is possible to make a quantitative (or semi-quantitative) chemical compositional analysis out of the EDS measured spectra. Usually the minimum error associated with this quantitative evaluation ranges between 0.1% and 1%, (or more) depending on the several experimental conditions [26].

At the same time, making a point-by-point analysis during the SEM or STEM scanning it is also possible to create elemental maps of the observed sample. Mapping resolution is strictly correlated with the spatial EDS resolution.

For this thesis work the EDS microanalysis tool on Jeol 2200 FS Field Emission TEM was used.

3.2.4 Luminescence Spectroscopy

The “luminescence” phenomena may be subdivided in two different stages: in the first one the system is excited from its current energetic state to an excited one, while in the second stage it returns to the fundamental state by the emission of a photon. The energy of the emitted photon is equivalent to the energy difference between the excited and the fundamental state.

So, luminescence is the spontaneous emission of light from an “excited” material. Depending on the nature of the excitation, it is possible to define different kind of luminescence [33]:

- Photoluminescence (PL): excitation by light;
- Cathodoluminescence (CL): excitation by an electron beam;
- Electroluminescence: excitation by an electric field;

- Triboluminescence: mechanical excitation (stress, friction, brake…)
- Chemiluminescence: excitation by a chemical reaction.

For example, when a semiconductor with an energy gap Eg is excited by a radiative energy hν>Eg, the photons are adsorbed and electron-hole pairs are generated. After a certain time Δt electrons and holes recombine to return in their fundamental states. The recombination may occur through a non-radiative process, transferring the energy to the crystal lattice by phonons, or through a radiative process, in which a photon is emitted.

Since the energy of the emitted photons is equivalent to the energy difference between the excited and the fundamental state, they represent an important information source about the energy band structure of the material. Especially, with these luminescence investigations it is possible to investigate the existence of energy levels that are inside the band gap, due to defects or impurities.

Defect and impurities generally plays an important role in the optical properties of a semiconducting material. Impurities may give rise to luminescence processes, but the same effect may originate from structural defects in the crystal lattice, as vacancies, interstitials, color center (e.g. Frenkel defects) or substitutionals. These defects are generally called “luminescence centers”.

Beside these, other energetic levels can indirectly influence the luminescence process. For example, in a crystal some “trap” level may exist, which can be reached by excited charge-carriers. An extra “activation energy” is needed to let the electrons or holes exit this metastable state and escape from these levels. The position of the “trap” levels inside the band gap influences the time delay of the luminescence process after the end of the excitation. Alternatively, as mentioned before, also non-radiative recombination centers can exist inside the crystal and, in this case, the energy may be transferred to the crystal lattice in the form of thermal energy (phonons).

For all these reasons luminescence spectroscopy is a very sensitive tool for investigating intrinsic and extrinsic transitions in semiconductors. In this thesis work two kinds of luminescence spectroscopy has been used: photoluminescence (PL) and cathodoluminescence

(CL) spectroscopies. Spectra obtained with these two techniques are essentially very similar but there are some fundamental differences:

- the spatial resolution is different in PL and CL: in fact, a PL measurement collects the light emitted from the portion of the sample that is lighted by the laser spot, while, thanks to the SEM capability to focus its electron beam, CL can be measured on a region of a few hundreds nm^2. In the case of nanostructures this means that while PL generally produces spectra averaged from the signal of many nanostructures at once, CL can be focused on a single nanostructure
- CL excitation source is much more energetic (orders of magnitude higher than the band gap energy) than that of a PL measurement. The high energy employed in CL measurement implies that also the transitions that are generally not favored may be observed, giving rise to some small alteration to the spectra. Moreover the high energy generally heats the sample.

3.2.4.1 Photoluminescence

Photoluminescence spectroscopy is a contactless, non-destructive method of probing the electronic structure of materials. It is mainly used as a diagnostic tool for semiconductors [33].

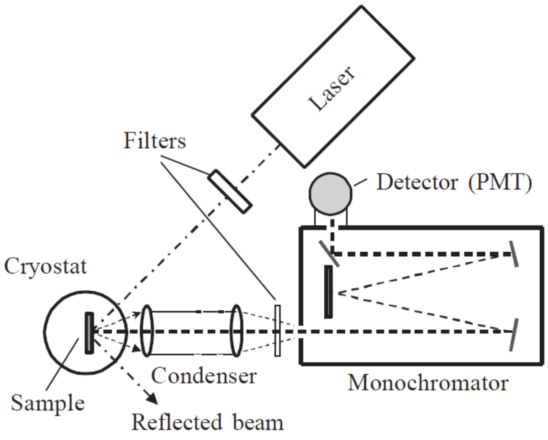

Figure 13. Schematic representation of the PL setup.

Photoluminescence is a result of incident-photon absorption that generates electron-hole pairs (photoexcitation) and produces emission of a photon at different wavelength. The incident photons, when absorbed, excite electrons usually from the valence band into the conduction band through momentum-conserving processes because the photon momentum can be considered negligible. The electrons and holes thermalize to the lowest energy state of their respective bands via phonon emission before recombining across the fundamental bandgap or the defect levels within the bandgap and emitting photons of the corresponding energies.

The used PL setup is schematized in Figure 13. Exciting laser is a 325 nm He-Cd produced by Kimmon Electronics and rated for 200 mW. Laser beam passes through a mechanical chopper (32 Hz frequency) controlled by a power supply allowing precise adjustments of the chopper frequency. The periodic interruptions of the light was required in order to provide the reference signal for the lock-in amplifier, which operates on the base of a phase-locked loop (PLL) device. Two optical mirrors set the beam height and a convergent lens focuses the spot on the sample mounted on the cryostat. Luminescence light is collected through two condenser lenses and focused on monochromator's input slits. PMT is used as photon to electron conversion element, the signal is amplified by a lock-in amplifier (Princeton Applied Research mod. 5209) and a RS-232 pc based interface (SPEX 1702/04) is used to program the spectrum acquirement. User-defined parameters are: wavelength range (330 ÷ 800 nm), scanning speed (0.1 ÷ 15 Å/s), and integration time (3 ms ÷ 3 s).

The low temperature setup is made by a rotary pump (10^{-3} mbar), a compressor and the cryostat. Rotary pump is used to make vacuum inside the cryostat chamber, while the compressor employs a closed loop circulation of helium gas, used for sample cooling. The gas flows from the compressor to the refrigerator cryostat through a stainless steel high pressure hoses. Helium is heated when cooling the cryostat cold head, that is thermally coupled to the cold finger where the sample in mounted on. Two diodes control the temperature: one just above the cold head and the other is mounted on the cold finger itself, 5 mm away from the sample.

Micro-PL on single nanowires have instead performed on selected samples by means of a different system, described further on in this chapter together with Raman Spectroscopy characterization (Chapter 3.2.5).

3.2.4.2 Cathodoluminescence

Cathodoluminescence imaging and spectroscopy is used in a wide range of research fields. CL process can be defined as the emission of light as the result of electron ("cathode ray") bombardment [34]. A very well known example of cathodoluminescence is the cathode ray tube, used in television screens, where luminescing phosphors are irradiated with an electron beam. The typical diameter of an electron beam in an a field emission electron microscope is in the order of nanometers and the interaction volume diameter of such a beam is in the order of 100-300 nm, which is at least one order of magnitude smaller than the spot of a typical laser beam used in PL measurements. By varying the beam energy one can also obtain depth resolved information, as the range of the electrons is directly proportional to the beam energy. CL is an important tool in material science because it can be used to locally characterize the optical emission of the material and because its high resolution makes it an ideal tool in nanosciences, to investigate the properties of single nanostructures [35, 36].

A CL system is an extension to either a TEM or SEM. A parabolic mirror with a 1 mm diameter hole in the top allowing the electron beam to pass through is a vital component in the CL-SEM apparatus and is placed between sample stage and pole pieces (Figure 14).

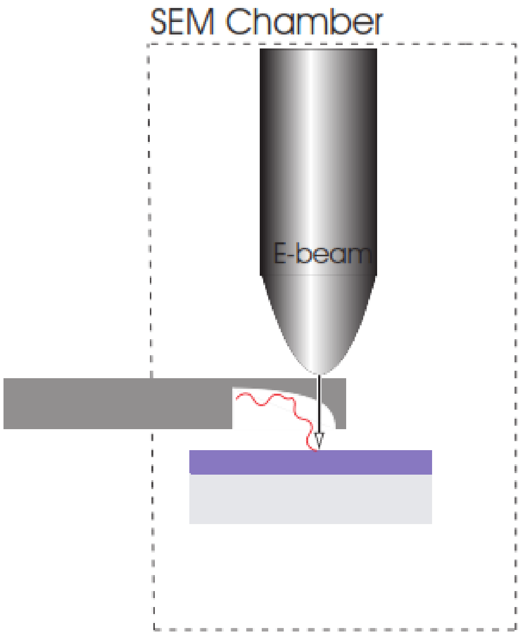

Figure 14. Schematic representation of the detection of light with the parabolic mirror from the CL system [34].

Through a hole in the mirror, the sample is irradiated with electrons and the luminescence is collected. The incident electrons excite luminescence and while some of the photons will escape back up the hole the collection efficiency of the mirror is typically quite high ~ 75%. For the most efficient collection, the sample must be in the focal point of the mirror. Because of the parabolic shape, the mirror reflects the light as a parallel beam into a waveguide. A light guide is used to keep the mirror in place under the pole pieces and the retractable system allows the light guide to be moved back from under the pole pieces when not in use to avoid collision with other detectors, large samples and the stage.

In a CL measurement the detection of the light can occur in two modes. In the panchromatic mode, all the emitted light is collected by the detector, while in the monochromatic mode the light is led through a monochromator which allows one to take a spectrum, or make an image at one particular wavelength. Two mirrors are used for switching between these modes. The photons collected are transferred via highly reflecting mirrors to the monochromator for the luminescence examination. Moreover, by exploiting the microscope scan capabilities, it is possible to make CL maps in both these two ways.

The formation of cathodoluminescence radiation occurs in three fundamental processes resulting in the emission of CL radiation are (1) the generation, (2) motion and (3) recombination of excess charge carriers. The factors which ultimately determine the resolution obtainable in CL-SEM includes probe diameter, generation volume and minority carrier diffusion length.

The used CL setup is mounted on a Cambridge 360 Stereoscan SEM, with a commercial Gatan MonoCL2 monochromator/detector system with and alkali halide photomultiplier.

3.2.5 Raman Spectroscopy

Raman spectroscopy is a spectroscopic technique based on inelastic scattering of monochromatic light, usually from a laser source [37]. Inelastic scattering means that the frequency of photons in monochromatic light changes upon interaction with a sample. Photons of the laser light are absorbed by the sample and then reemitted. Frequency of the reemitted photons is shifted up or down in comparison with original monochromatic frequency, which is called the Raman effect. This shift provides information about vibrational, rotational and other low frequency transitions in molecules [38-42]. Raman spectroscopy can be used to study solid, liquid and gaseous samples.

A Raman system typically consists of four major components: Excitation source (Laser), sample illumination system and light collection optics, wavelength selector (filter or Spectrophotometer) and detector (photodiode array, CCD or PMT). A sample is normally illuminated with a laser beam in the ultraviolet, visible or near infrared range. Scattered light is collected with a lens and is sent through interference filter or spectrophotometer to obtain Raman spectrum of a sample. Since spontaneous Raman scattering is very weak the main difficulty of Raman spectroscopy is separating it from the intense Rayleigh scattering. More precisely, the major problem here is not the Rayleigh scattering itself, but the fact that the intensity of stray light from the Rayleigh scattering may greatly exceed the intensity of the useful Raman signal in the close proximity to the laser wavelength.

In many cases the problem is resolved by simply cutting off the spectral range close to the laser line where the stray light has the most prominent effect. People use commercially available interference (notch) filters which cut-off spectral range of ± 80-120 cm^{-1} from the laser line. This method is efficient in stray light elimination but it does not allow detection of low-frequency Raman modes in the range below 100 cm^{-1}. Stray light is generated in the spectrometer mainly upon light dispersion on gratings and strongly depends on grating quality. Raman spectrometers typically use holographic gratings which normally have much less manufacturing defects in their structure then the ruled once. Stray light produced by holographic gratings is about an order of magnitude less intense then from ruled gratings of the same groove density.

Using multiple dispersion stages is another way of stray light reduction. Double and triple spectrometers allow taking Raman spectra without use of notch filters. In such systems Raman-active modes with frequencies as low as 3-5 cm^{-1} can be efficiently detected. In earlier times people primarily used single-point detectors such as photon-counting Photomultiplier Tubes (PMT). However, a single Raman spectrum obtained with a PMT detector in wavenumber scanning mode was taking substantial period of time, slowing down any research or industrial activity based on Raman analytical technique. Nowadays, more and more often researchers use multi-channel detectors like Photodiode Arrays (PDA) or, more commonly, a Charge-Coupled Devices (CCD) to detect the Raman scattered light. Sensitivity and performance of modern CCD detectors are rapidly improving. In many cases CCD is becoming the detector of choice for Raman spectroscopy.

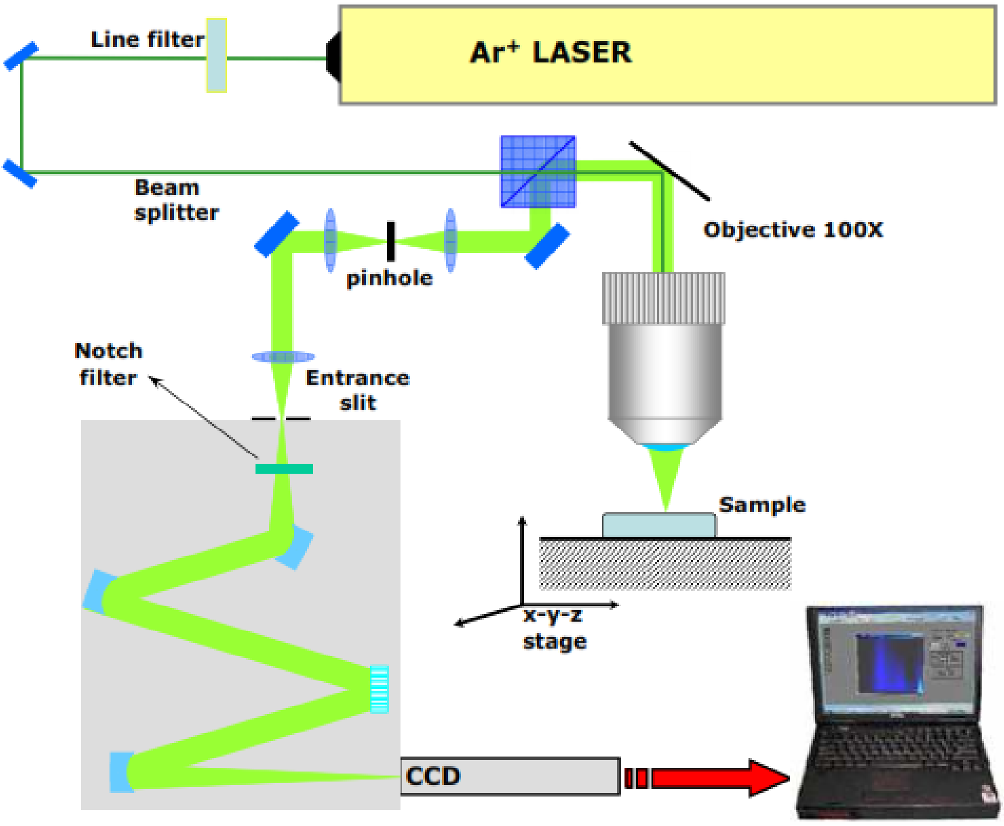

Figure 15. Raman spectroscopy setup used in our measurements

Figure 15 shows a simplified diagram of the setup employed in the Raman dispersion measurements of this work. In this work as in most of the typical Raman spectroscopy setups, a laser was used as a photon source because its highly monochromatic, collimated, polarized and intense light, all of them desired characteristics in the excitation. The laser beam passes through a holographic filter specific for each line, in order to remove any unwanted sidebands and/or plasma spontaneous emission lines. In such cases of lines without commercial available filters, a prism monochromator was used. The output power was adjusted to the desired value by mean of current control of the laser power supply or the use of neutral filters.

Excitation and collection of the dispersed light was done by mean of optical microscope coupled to the T64000 system, as observed in Figure 16. This have a 100X objective with a numerical aperture of 0.95. The spot of the laser using this objective is around 1 µm in the visible region. In this optical arrangement, a confocal setup was included in the path of the dispersed light. The confocal setup means that the sample is illuminated with diffraction limited spot and the illuminating spot is imaged on an ideally point-like detector. Practically, the point-like detector is realized with an adjustable pinhole in front of the real detector. By using a confocal optical system the signal from each layer of a layered sample can be separated from the signal coming from the surrounding area. A real confocal configuration requires a very accurate optical alignment and a high degree of stability and reproducibility of the mechanical and optical alignment. After to pass through the confocal setup, the light collected in a back-scattering configuration is focused on the entrance slit of the spectrometer by a lens. This lens is positioned to match the numerical aperture of that.

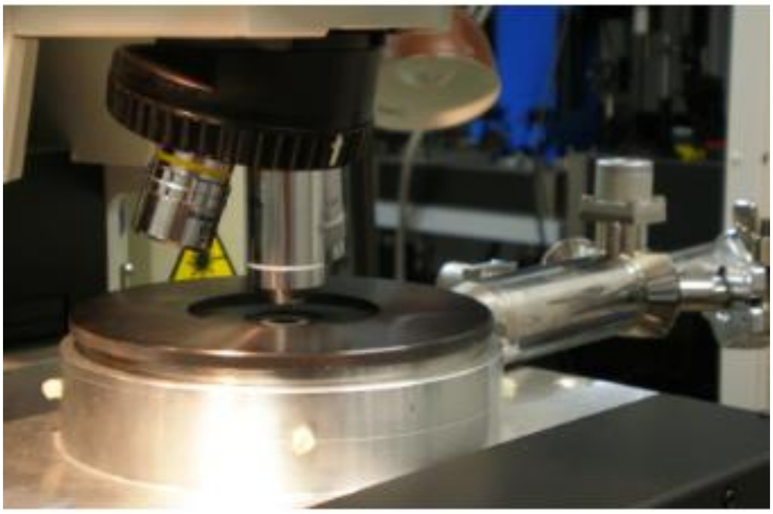

Figure 16. Picture of the microscope arrangement coupled to the T64000 in order to develop micro-PL and also possible micro-Raman measurements.

The spectrometer T64000 spectrometer from Jobin-Yvon$^{@}$ was used in our experiments. The focal distance of this is 0.75 m and an 1800 grooves/mm grating dispersed the incoming light.

The dispersed signal was detected using a charge coupled device (CCD) having 1024 x 256 pixels, cooled by using liquid nitrogen. This kind of detector has a high sensitivity and a low dark current, allowing to accumulated charge for a longer time. The spectral resolution of the whole system around 500 nm is about 1 cm. This same setup has been employed also for low temperature micro-PL measurements (Figure 16). For these, a microstatHe cryostat model from Oxford instruments was used to cool the sample. This model is a vacuum loading continuous flow cryostat. The advantages of this cryostat include a short and adjustable work distance for its use with high magnification - large work distance microscope objectives. In this case, a 100x objective with a free work distance of 4.7 mm and a numerical aperture of 0.75. Liquid-nitrogen instead than the originally designated liquid-helium was used because. This allows to reach sample temperatures as low as 90K, which is enough to our requirements.

References

1. Y. Sun and J. A. Rogers, (Eds.), Semiconductor nanomaterials for flexible technologies: from photovoltaics and electronics to sensors and energy storage, William Andrew (2010).

2. G. C. Yi, (Ed.). Semiconductor nanostructures for optoelectronic devices. Springer. Chicago (2012).

3. S. Wagner and W.C. Ellis, Appl. Phys. Lett., 4 (1964) 89; in Whisker Technology. ed. by A.P. Levitt (John Wiley and Sons, Inc., New York, 1970).

4. H.-J. Choi and J.-G. Lee, J. Mat. Sci., 30 (1995) 1982.

5. Y. Wu and P. Yang, J. Am. Chem. Soc., 123 (2001) 3165.

6. F.M. Ross, J. Tersoff and M.C. Reuter, Phys. Rev. Lett., 95 (2005) 146104.

7. E.I. Givargozov, J. Cryst. Growth, 31 (1975) 20.

8. T.I. Kamins, R.S. Williams, D.P. Basile, T. Hesjedal and J.S. Harris, J. Appl. Phys., 89

(2001) 1008.

9. K. Lew and J.M. Redwing, J. Cryst. Growth, 254 (2003) 14.

10. J. Kikkawa, Y. Ohno and S. Takeda, Appl. Phys. Lett., 86 (2005) 123109–1.

11. M.H. Huang, Y.Wu, H. Feick, N. Tran, E. Weber and P. Yang, Adv. Mat., 13 (2001) 113.

12. K. L. Choy, Progress in materials science, 48 (2003) 57.

13. A. Sherman, Chemical vapor deposition for microelectronics: principles, technology, and applications. (1987) US.

14. J. O. Carlsson, Thin solid films, 130 (1985) 261.

15. U. Jansson, J. O. Carlsson, B. Stridh, S. Söderberg and M. Olsson, Thin Solid Films, 172 (1989) 81.

16. W. A. P. Claassen and J. Bloem, J. Cryst. Growth, 51 (1981) 443.

17. Rees Jr and S. William, Ed., CVD of Nonmetals, (2008) John Wiley & Sons.

18. C. F. Powell, J. H. Oxley, J. M. Blocher and J. Klerer, Vapor Deposition, Journal of The Electrochemical Society, 113 (1966) 266C.

19. K. J. Hüttinger, Chemical Vapor Deposition, 4 (1998) 151.

20. D. L. Brors and R. C. Cook, Method and apparatus for cold wall chemical vapor deposition, U.S. Patent No. 5,551,985. 3 Sep. (1996).

21. G. B. Stringfellow, Organometallic Vapour Phase Epitaxy: Theory and Practice, (1989) Academic Press, Boston.

22. J. J. Coleman, Proc. IEEE, 85 (1997) 1715.

23. M. J. Ludowise, J. Appl. Phys., 58 (1985) R31.

24. K. Seshan, Handbook of Thin Film Deposition, 3rd Edition, (2012) Elsevier, UK.

25. D. McMullan, Scanning, 17 (1995) 175.

26. J. Goldstein, D. Newbury, D. Joy, C. Lyman, P. Chlin, E. Lifshin, L. Sawyer, and J. Michael, Scanning Electron Microscopy and X-Ray Microanalysis, 2007, Springer, New York, USA

27. M. T. Postek, K. S. Howard, A. H. Johnson and K. L. McMichael, Scanning Electron Microscopy: A Student's Handbook, Ladd Research Ind., Inc., (1980) Williston, VT.

28. C. E. Lyman, D. E. Newbury, J. I. Goldstein, D. B. Williams, A. D. Romig, J. T. Armstrong, P. Echlin, C. E. Fiori, D. C. Joy, E. Lifshin and K. –R. Peters, Scanning Electron Microscopy, X-Ray Microanalysis and Analytical Electron Microscopy: A Laboratory Workbook, (1990) Plenum Press. New York, N.Y.

29. I. M. Watt, The Principles and Practice of Electron Microscopy, (1985) Cambridge Univ. Press. Cambridge, England.

30. P. J. Goodhew and F. J. Humphreys, Electron microscopy and analysis. 2nd edition, (1988) Taylor & Francis.

31. D. B Williams and C. B. Carter, Transmission Electron Microscopy: A Textbook for Materials Science, Part 1, (2009) Springer, New York, USA.

32. I. M. Watt, The principles and practice of electron microscope, (1997) Cambridge University Press.

33. C. Klingshirn, Semiconductor Optics, 2007, Springer, Heidelberg, Berlin

34. B. G. Yacobi and D. B. Holt, J. Appl. Phys., 59 (1986) R1.

35. H. J. Fan, F. Bertram, A. Dadgar, J. Christen, A. Krost and M. Zacharias, Nanotech., 15 (2004) 1401.

36. L. Lazzarini, G.Salviati, F. Fabbri, M. Zha, D. Calestani, A. Zappettini, T. Sekiguchi and B Dierre, ACS Nano, 3 (2009) 3158.

37. B. Schrader, Ed., Infrared and Raman Spectroscopy: Methods and Applications, (1995) John Wiley & Sons: Chichester.

38. J. R. Ferraro, Introductory Raman Spectroscopy, (1994) Academic Press: New York.

38. G. Turrell and F. J. Corset, Eds., The Raman Effect, (1996) Academic Press: New York.

40. J. G. Grasselli and B. J. Bulkin, Eds., Analytical Raman Spectroscopy, (1991) John Wiley & Sons: Chichester.

41. J. J. Laserna, Modern Techniques in Raman Spectroscopy, (1996) John Wiley & Sons: Chichester.

42. K. Kneipp, H. Kneipp, I. Itzkan, R. R. Dasari and M. S. Feld, Chemical Reviews, 99 (1999) 2957.

Chapter 4

Results and Discussion

4.1 Vertically aligned ZnO nanowires

Arrays of one dimensional aligned nanostructures offer the concurrence of high efficiencies of charge carrier transport with large interface areas for charge separation and/or transfer with the surrounding species, material or electrolyte. So that nanowires (NWs) and nanotube based electrodes are broadly used to improve the efficiency of a plenty of applications where both charge carrier transport and separation, transfer are fundamental [1]. More specifically, vertical aligned ZnO nanowires hold promise to drive the revolution in different applications such as dye-sensitized solar cells (DSSCs) [2,3], piezoelectric energy harvesting [4,5], light-emitting diodes [6,-8], water splitting [9−11] sensor arrays, field electron emitter arrays, and vertical field-effect transistors [12], etc. Synthesis of vertically aligned ZnO nanowires has been always very challenging for device fabrications. It was already suggested that control over the dimension, composition, position, orientation, reproducible and large-area growth processes of the ZnO nanostructures plays a very crucial role in the development of novel devices [14, 15]. Among all of the other ZnO nanostructures, vertically aligned ZnO nanorods would offer the unique opportunity to control the device properties by changing the aspect ratio and hence the nanostructure properties. Aspect ratio of vertically aligned ZnO nanorods plays a major role, for example, in the energy harvesting applications such as dye sensitized solar cells (DSSC) and nanogenerators.

ZnO-based DSSC technology is alternative to TiO_2 is considered as one of the most promising materials for solar cells. ZnO possesses energy band structure and physical properties similar to those of TiO_2, but its electron mobility is higher by 2-3 orders of magnitude. Therefore, ZnO is expected to exhibit faster electron transport with reduced recombination loss. Although the conversion efficiencies (0.4-5.8%) obtained for ZnO are much lower than the maximum reported 11% for TiO_2 [47]. ZnO is still considered the most promising alternative to TiO_2 due to its ease of crystallization and anisotropic growth. ZnO nanowire arrays were first used in DSSCs shown in Figure 1a with the intention of replacing the traditional nanoparticle film with a consideration of increasing the electron diffusion length [48, 49].

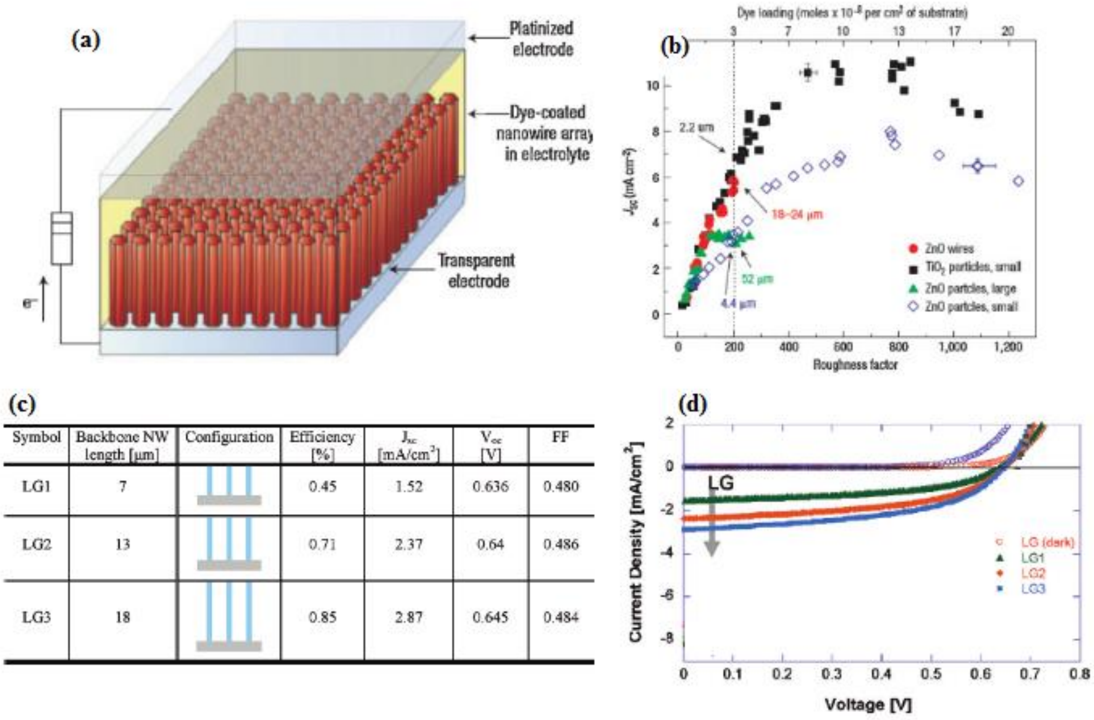

Symbol	Backbone NW length [μm]	Configuration	Efficiency [%]	J_{sc} [mA/cm²]	V_{oc} [V]	FF
LG1	7		0.45	1.52	0.636	0.480
LG2	13		0.71	2.37	0.64	0.486
LG3	18		0.85	2.87	0.645	0.484

Figure 1. ZnO-nanowire based dye-sensitized solar cells (DSSC) [48 - 51]. (a) Schematic diagram of the cell with a photoelectrode comprised of the ZnO-nanowire array [48, 50]. b) Comparative performance of nanowire and nanoparticle cells (c,d) Characteristics table and J-V curve of DSSC with ZnO nanorods [51].

The superiority of ZnO nanowires as a direct pathway for electron transport is illustrated by Figure 1b, in which the short-circuit current densities as a function of the internal roughness factor are compared for cells with ZnO nanowires, TiO_2 nanoparticles, and ZnO nanoparticles. This confirms that the transport efficiency of nanoparticle films falls off above a certain film thickness due to critical recombination. In addition, the nanowire cells generate considerably higher current densities than the ZnO nanoparticle cells over the accessible range of roughness factors. This is also a confirmation that the nanowires offer better electron transport when compared to nanoparticles [48, 50].

Besides the one-dimensional structure of nanowires/nanorods, the feature of nanowire/nanorods arrays with vertically aligned growth on the TCOs (FTO, ITO, AZO) substrate is also addressed as one of important aspects that provide the direct pathway for electron transport in DSCs. This has been demonstrated convincingly in previous research.

For example, one study found that a ZnO nanorods array led to a ten-fold increase in the photovoltaic efficiency when compared to a randomly oriented nanorods film [55]. Also, the short circuit current density (J) and the overall light conversion efficiency increased as the length of the ZnO NW increased due to effective surface area increase (Figure1c-d) and dense network of crystalline ZnO NWs can increase the electron diffusion length and electron collection, because the NW morphology provides more direct conduction paths for electron transport from the point of injection to the collection electrode [51]. However, the insufficient surface area of nanowire/nanorod arrays seems to be the primary factor that limits the amount of dye adsorption as well as the conversion efficiency of the cells. Many attempts have been made to solve this problem. One such approach is to reduce the diameter size of the nanowires/nanorods, thus increasing the density of the array [52, 53, 54].

Wang's group [56] demonstrated an approach to convert mechanical energy into electric power with the use of aligned zinc oxide (ZnO) nanowires (NWs). The mechanism of the power generator relies on the coupling of piezoelectric and semiconducting properties of ZnO as well as the formation of a Schottky barrier between the metal and ZnO contacts [56]. Experimental design for converting nanoscale mechanical energy into electrical energy by a vertical piezoelectric ZnO nanorods as shown in Figure 2a-c. It was observed that the performance of the nanogenerators was not dependent on the substrates but mainly depends on the crystal quality, effective length, diameter and density of the nanowires across the substrates. It was observed that the calculated output electrical potential was increasing for lengths of 600 to 4000 nm and then it decreases upon any further increase of the length. As the length is increased the aspect ratio also increases and the deflection of the nanowire increases. This leads to an increase in the output electrical potentials up to an aspect ratio of 80 (at a length of 4000 nm and a fixed diameter of 50 nm). Upon further increase in the length (increase of the aspect ratio) the output voltage signal starts to decrease. The decrease in the output electrical potential was due to the excessive deflection in the nanowire in both the lateral and the vertical directions.

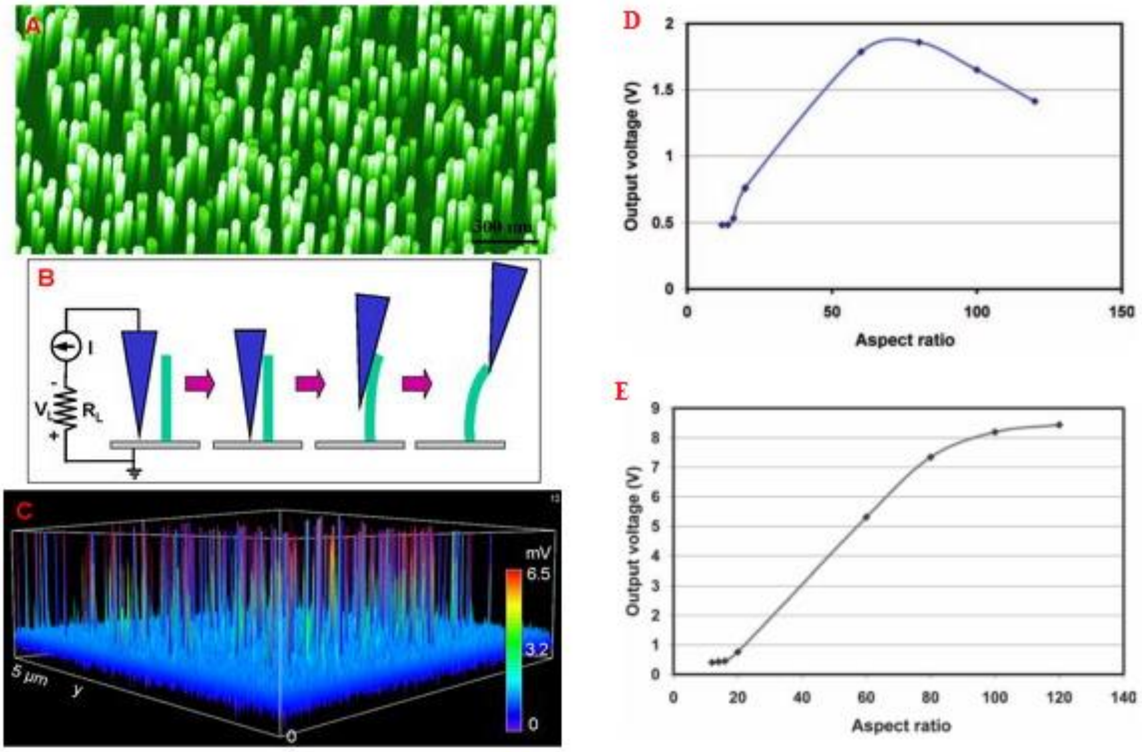

Figure 2. Experimental design for converting nanoscale mechanical energy into electrical energy by a vertical piezoelectric ZnO nanorods. Right: (a) SEM of ZnO nanorods, (b) Experimental setup and procedures for generating electricity by deforming a PZ NW with a conductive AFM tip, (c) output voltage image of the NW arrays [56] Left: Output electrical potential SEM images of merged ZnO nanorods on different grain size AZO film deposited by RF-sputtering Vs aspect ratio of ZnO nanowires (d) controlled at constant diameter of 50 nm and changing the nanowire length from 600 nm to 6000 nm (e) controlled at constant length of 1000 nm and changing the nanowire diameter from 8 nm to 83 nm [57].

This excessive deflection in the nanowire might cause a screening of the charge carriers on the outer surfaces of the nanowires resulting in a decrease of the electrical potential. It is shown that the output electrical potential is increasing with decreasing the diameter of the nanowires and become less effective below a diameter of 12.5 nm. As the diameter is decreasing the aspect ratio is increasing and the deflection of the nanowire increases yielding an increase in the output electrical potentials up to a diameter of 12.5 nm. With further increase in the aspect ratio no effect on the output voltage signal was observed. During all these calculations the lateral force was kept constant i.e., 80 nN [57].

It can be observed that the aspect ratio of ZnO nanorods plays an important role in the above mentioned applications and it seems that the results are quite dependent on the experimental conditions, specifically on the synthesis method, substrate treatment, growth parameters, geometrical structure of the nanowires and array (pattern, diameter, length, density, etc.), and the measuring method (sensitization process, electrolyte composition, light-source intensity, and active area of photo electrode film, etc.).

This means that if vertically aligned nanowires or nanorods have to be synthesized for device preparation, the chosen growth technique must grant, as much as possible, cost-efficiency, good physical properties (not affected by undesired defects, impurities or dopants) and control of nanostructure size, shape and density.

4.1.1 Synthesis

There are different techniques that have been used to synthesize aligned ZnO nanowires, such as catalyzed vapor transport techniques [16–20], metal–organic vapor-phase epitaxy (MOVPE) [21] and chemical vapor deposition (MOCVD) [22,23], solution processes [24–28], carbothermal reactions [29–31], pulsed laser deposition [32–34], hydrothermal growth [35,36], electrochemical deposition [37], template deposition [38,39], sputtering [40,41], thermal evaporation [42–44], spray pyrolysis [45] and continuous-spray pyrolysis (CoSP) [46], etc.

Each of the above methods are characterized by pros and cons and, generally, the choice is determined by the priority requirements of final application (cost, purity, perfection, size, compatibility with other materials or techniques, etc.). Among them thermal CVD reactor have been consider for the growth of aligned ZnO nanorods due to following criteria.

Solution based growths of ZnO–NRs are generally the most suitable techniques for cheap and large scale productions, even on flexible substrates, but not always they can be matched easily with the other deposition processes for each component of the device, as for example a photovoltaic cell. Moreover, in those devices where ZnO-NRs have an active role in the light adsorption and/or exciton separation, the intrinsic doping from solution inclusions may degrade the device performance. On the contrary, vapor-phase growths are generally less controllable and more expensive, especially when metal-organic precursors or metal catalyst are used in order to improve the synthesis reproducibility.

Although wet chemical methods are those that usually grant the cheapest and largest productions, also a catalyst-free thermal evaporation could be considered a low-cost technology for the growth of metal oxide nanostructures, since it makes use of a rather simple and low-cost setup and it does not require expensive precursors or catalysts. Moreover, if only metal and oxygen are used to obtain the desired oxide, material purity is usually expected to be very high, with minimum contributions from undesired impurities. On the other hand, in thermal CVD process the required temperatures are sometimes not compatible with all the possible device substrates. For example, with this technique it is generally not possible to obtain aligned ZnO nanorods at a temperature that is lower than 550 °C [30, 43], which is instead required when glass substrates are employed. This temperature is in fact close to the melting point of Zn and the supersaturation obtained by direct evaporation of a Zn source is usually not high enough to nucleate a vapor–solid (VS) growth of these aligned nanocrystals, even if a seeding film (mainly ZnO, but also sapphire, GaN, etc.) is used [30, 42, 44]. Nevertheless a higher Zn vapor pressure is also required to sustain the formation and condensation of liquid zinc droplets during the whole growth of the nanostructures by a self-catalyzed vapor–liquid–solid (VLS) mechanism [42].

The growth of vertically oriented ZnO nanorods on ZnO films and Al-doped ZnO (or simply "AZO") TCO by simple thermal evaporation at comparably low temperature (< 500 °C) was previously reported by our group at IMEM-CNR [57, 58]. It is an alternative solution-free and catalyst-free synthesis method and it has been explored for the realization of 3D nanostructured ZnO-based TCOs. Previous reports concluded that small Zn nanoclusters on the polar surface of a (001)-oriented ZnO film can generate preferential, energetically favored and oriented nucleation sites for the growth of homogeneous arrays of aligned nanorods. A growth setup that promotes the formation of such nanoclusters has been defined and thin aligned ZnO nanorods have been obtained at 480 °C, over an area of a few square centimeters (laboratory-scale reactor) of undoped and Al-doped ZnO films.

In this thesis work, the growth of vertically aligned ZnO nanorods have been systematically studied as a function of growth conditions (such as Zn evaporation, growth time, growth temperature, gas carrier flow, gas carrier to oxygen concentration, seeding film grain size, etc.) and compared for different TCO substrates. The aim of the work is mainly focused to obtain a reproducible and large over area growth of vertically aligned nanorods on TCO substrates and to control the thickness and length of the nanorods. The structural morphology of the different TCO substrates and also the grown ZnO nanorods have been analyzed with the help of XRD, AFM and SEM.

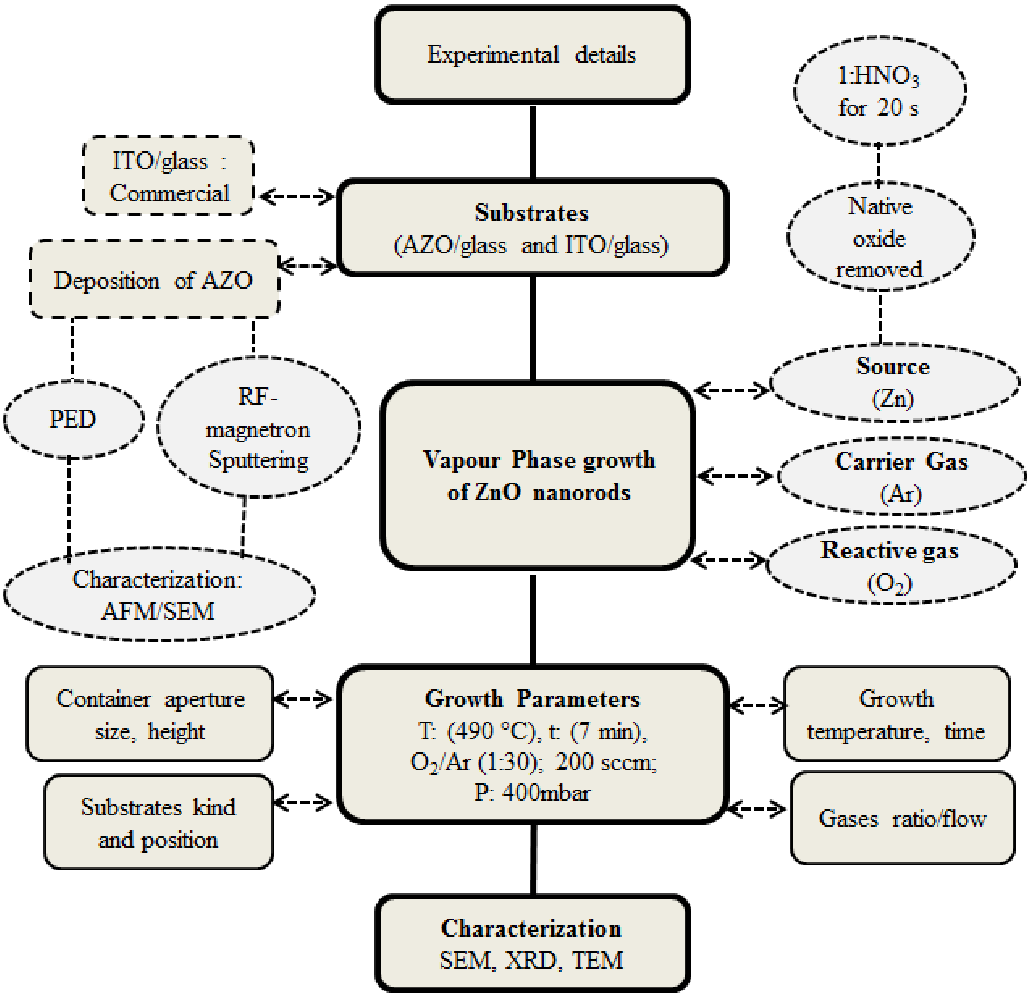

Figure 3. Flowchart of experimental scheme

Vertically aligned ZnO nanorods have been grown using home-made CVD reactor. The experimental details are resumed in the flowchart given in Figure 3.

4.1.1.1 TCO films

The present study is aimed to the growth of vertically aligned ZnO nanorods over two different Al-doped (2%) ZnO (AZO) and indium tin oxide (ITO) substrates. These substrates serve the purpose of the seeding layer for nanorods growth. Pulsed electron deposition (PED) and RF magnetron sputtering techniques were employed to obtain AZO substrates. ITO substrates used for the growth was commercially purchased.

AZO film by PED

AZO were deposited on soda-lime glass substrates by PED technique in which a pulsed high power electron beam penetrates in to the target (~ 1 µm) resulting in a quick evaporation of target material. In order to focus the deposition in the preferred area of the substrate by means of mechanical masking. The aim of depositing AZO films on glass substrates by PED are generally characterized by low roughness, high transparency, preferential grain orientation with the c-axis perpendicular to the substrate and good electrical conductivity.

Commercial ZnO (Sigma Aldrich, 4N) powder and Al_2O_3 (2 wt%, Sigma Aldrich, 5N) powder mixtures were used as target for AZO deposition. Free-standing 40 mm diameter pellets were prepared with these powders by pressing at 280 bar for 5 min, after a fine grinding in a ball mill with iso-propanol for 30 minutes. The obtained targets were then sintered at 1000 °C for 12 h in order to increase their toughness while maintaining a sufficient porosity and finally polished to obtain a smooth and uniform surface. After high vacuum pumping, the deposition chamber pressure was set to 1:5–2:5 10^3 mbar in Ar to optimize the PED plume, while the substrate temperature was set to 200 °C. These conditions were chosen in order to deposit a film with the best transparency and conductivity characteristics [57].

A commercial PED source (supplied by Neocera Inc., USA) was used to ablate the target. The acceleration voltage of the incident pulsed electron beam was fixed to 14 kV for both pure ZnO and AZO, with a pulse repetition rate of 10 Hz. In these conditions the electron beam impacts on a 4 mm^2 target area with a pulse energy of about 12 J cm^2. The substrates were finally cooled to room temperature while keeping the same base pressure value. No post-growth annealing treatments were performed.

AZO substrates by RF magnetron sputtering

RF magnetron sputtering is one of the most widely used methods in semiconductor processes due to the advantages such as high deposition rate and simple implementation. AZO were deposited on soda-lime glass substrates in which powerful magnets are used to ionized the target. In this process 2 inch Al doped ZnO target were user for deposition of AZO film.

The base pressure of the chamber was maintained at a pressure below 1 x 10-6 mbar, deposition rate of 0.46 nm/min depending on the RF power. Ar was used as reaction gas for film deposition and pressure during deposition inside the chamber was maintained at 5 x 10-3 mbar. The distance between the target and substrate was fixed as (60 mm).

A RF source (13.5 MHz) was used to sputter the target. The experiment was performed at room temperature with RF power values of 60 W. After the deposition the shutter were closed and the sample were kept in the base pressure of 10-3 mbar. No post-growth annealing treatments were performed.

The morphology of the AZO films was studied by atomic force microscopy (AFM Digital Instruments NANOSCOPE IIIA). The electrical properties of the AZO films used were measured by a four-probe Van der Pauw setup. The crystal structure and orientation were investigated by x-ray diffraction (XRD) spectra and rocking-curves (Siemens D-500 diffractometer with a Cu Kα source—λ 1.540 A), and photoluminescence (325 nm excitation by He–Cd laser) measurements.

Commercial ITO substrates

In_2O_3:SnO_2 (ITO) films are widely used as reference TCO materials for many photovoltaic applications. In particular, they are widely used in the test and production of DSSC. Solaronix, which is one of the leading companies in this field, furnished 1”x1” substrates with ITO coating film with about 5 μm thickness and ~ 7 Ohm/square resistivity.

4.1.1.2 Vapor Phase growth of vertically aligned ZnO nanorods

An home-made thermal CVD reactor was used for the growth of ZnO nanorods. The fine grains of pure zinc (Zn) metallic powders (5 N purity, 300 mg) was chosen as Zn source. It is very important to remove the native oxides present on the surface of the zinc prior to growth because it helps to enhance Zn evaporation. To remove native oxide, Zn powders were etched with diluted nitric acid (1%) for 20 to 30 seconds. The remaining nitric acid was removed by continuous rinsing with deionized water and the collected powders were dried at room temperature. Zn powder was placed inside an alumina boat (Zn source container – see Figure 4) and it was partially covered for allowing the generated vapor to exit only through a small window.

A large number of experiments have been performed, systematically changing the growth parameters in order to see their effects on the nanostructures growth. Although the growth system is rather simple, a large number of variable have to be taken into account:

- source temperature
- substrate temperature and distance from source
- source container size, exit windows size (w), Zn amount in the container and volume of the empty buffer above it (proportional to h value)
- carrier gas flow
- carrier gas / oxygen ratio
- system pressure
- evaporation time, reaction time, heating/cooling rates

Zn evaporation, which is not favored below 500°C because this value is just above its melting point, turned out to be the fundamental process to control the growth of ZnO nanowires. This is unfortunately affected, directly or indirectly, by most of the mentioned parameters. The experiments main result is that the simplest way to control this process is through the modulation of the Zn evaporation buffer in the source container, by varying the height of filling (h). So all the other parameters were fixed at optimal values and just h values was used to control the growth of nanowires.

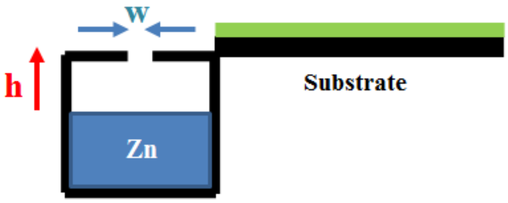

Figure 4. Schematic diagram positioning of source container and substrate

The substrates with different seeding films were placed beside the Zn source container in downstream position and were loaded in the center of the tubular furnace of the reactor's growth chamber given in Figure 5.

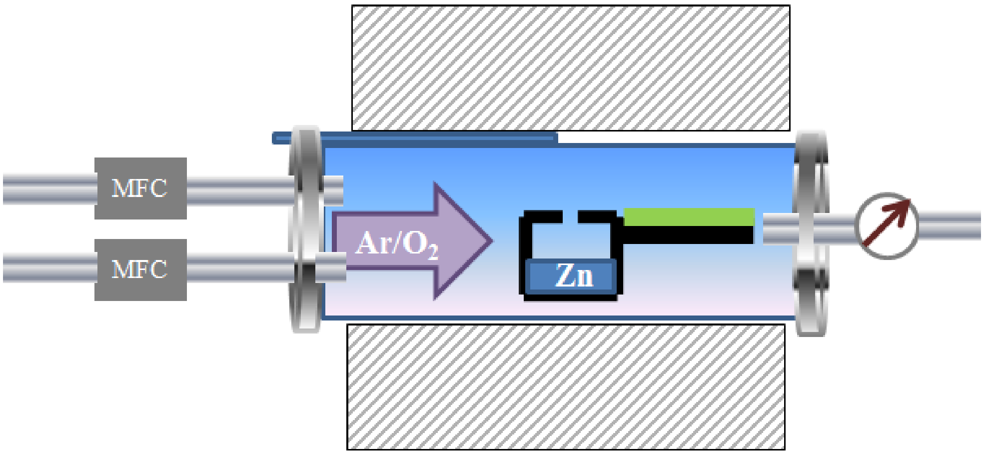

Figure 5. Schematic diagram of thermal CVD reactor

The reactor was evacuated at the beginning of the process so that the oxygen present in the chamber and among Zn powder grains can be completely removed. Oxygen (O_2) and Argon (Ar) were used as reactive and carrier gases respectively. The temperature was gradually increased to 490 °C with 50 sccm Ar flow. When temperature reaches the maximum of 490 °C, Ar flow was stopped and Ar/O_2 mixture (30:1 mass ratio, 200 sccm total flow, 400 mbar) was introduced. After 7 minutes, Ar/O_2 flow was replaced by Ar only flow and the furnace cooling process takes place. Substrates were removed once the furnace reached room temperature.

At a first look the described growth system looks similar to others reported in the literature, but in this procedure some peculiar and fundamental key-points are present. In fact, both source material partial coverage and the used gas flows are specifically configured in order to promote the formation of Zn clusters at a certain stage of the growth process. More in detail, we can subdivide the growth process into three main steps, which are illustrated in Figure 6.

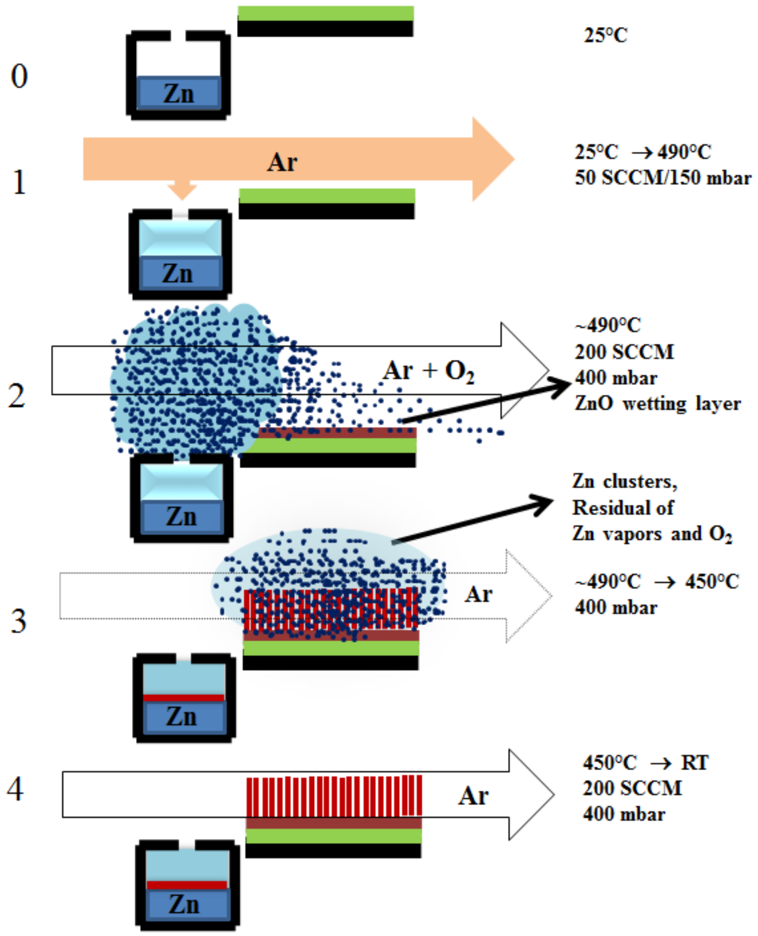

Figure 6. Schematic diagram of growth process of vertically aligned ZnO nanorods.

The first step is devoted to the accumulation of Zn vapors in the source material container (source container) and takes place during heating and the 7 min temperature plateau at 490 °C. During this first step, oxygen is mixed with Ar in the gas flowing at the top of the source container and, in that position, Zn vapors escaping from the small container window are locally oxidized, preventing any premature growth on the substrate. At the same time, the small window size prevents any strong oxidation of source material that, by continuous evaporation, fills the empty container volume with a pressure that approaches the equilibrium value for Zn vapor at this temperature.

The second step is very fast and allows Zn nanoclusters to form. It starts when the Ar/O_2 mixture is substituted by a larger Ar flow. The decrease in oxygen content in the reactor let Zn vapor spread in the reactor from the container window, where it gets in contact with the colder Ar flow. Indeed, the used inert gas flow is so large that gas never completely thermalizes inside the reactor. The sudden temperature gradient promotes the formation of Zn clusters that are brought by the flow in the nearby substrate region. This second step takes place in less than 1 min and then stops because further Zn condensation is rapidly inhibited by the decrease in Zn vapor pressure, since vapor accumulation is no more active and evaporation rate decreases because reactor cooling starts.

The third and last step, then, takes place during the first minutes of cooling (generally from 490 °C to 450 °C), during which Zn nanoclusters on the substrate oxidize and act as nuclei and preferential growth sites for nanorods. It is indeed the synthesis step in which ZnO nanorods nucleate and grow on the substrate. ZnO nanorods grow rapidly (and nearly contemporary) by consuming most of the neighboring residual Zn vapor and O_2.

Using this model and predicted growth mechanism, several experiment has been carried out to control and reproduce the growth of vertically aligned ZnO nanorods.

The as-grown samples were characterized to study their morphology using Scanning Electron Microscopy (Philips 515 SEM and FEI Quanta FEG-ESEM). The crystal structure and orientation were investigated by X-ray diffraction (Thermo ARL X-ray diffractometer with a solid state detector). The optical properties were characterized using photoluminescence (325 nm excitation by He–Cd laser) measurements.

4.1.2 Characterization

4.1.2.1 Seeding films characterization

The morphology of AZO film deposited by PED and RF-sputtering were studied using SEM and AFM techniques. Figure 7a shows the SEM image of the AZO film deposited by PED in which the surface seems to be homogeneous and also uniform deposition was observed. There were only few droplet like structures seen on the surface attributed to the PED deposition. SEM images of this film was used to get rough idea of the surface roughness and the grains where not so clear to visible. The roughness of the film has been estimated by AFM analysis and the image is shown in the Figure 7c. The average roughness was found to be ~10 nm (RMS value). This kind of flat surface contributes to the uniform growth of ZnO nanorods over large area.

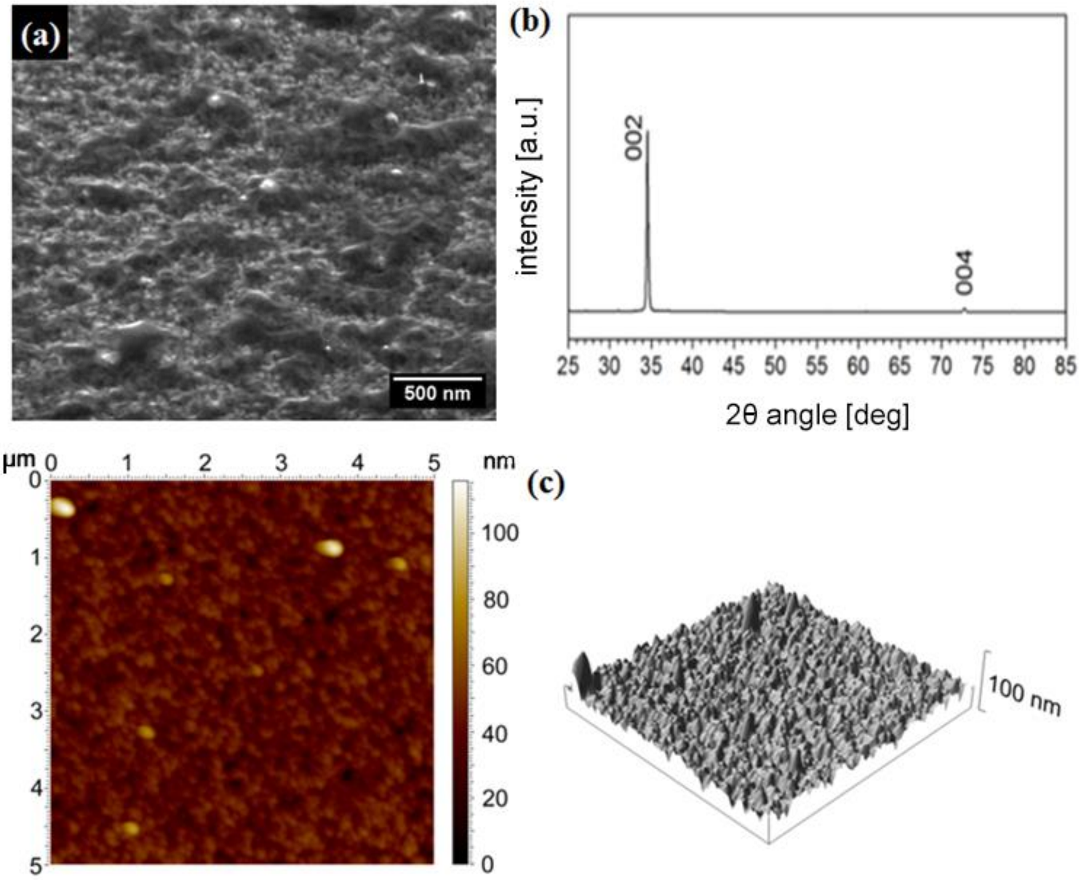

Figure 7. Morphology and structural analysis of AZO film deposited by PED and used as seeding film the growth of ZnO nanowires: (a) SEM image (b) XRD and (c) AFM

The different growth conditions of sputtering technique, on the contrary, produced AZO films with larger grains. In Figure 8a a SEM image of the AZO film deposited by RF-sputtering is reported and a typical AFM characterization is instead shown in Figure 8c. It can be clearly observed that the grains are in this case in a 100-500 nm range and, hence, nearly one order of magnitude larger than in the previous case.

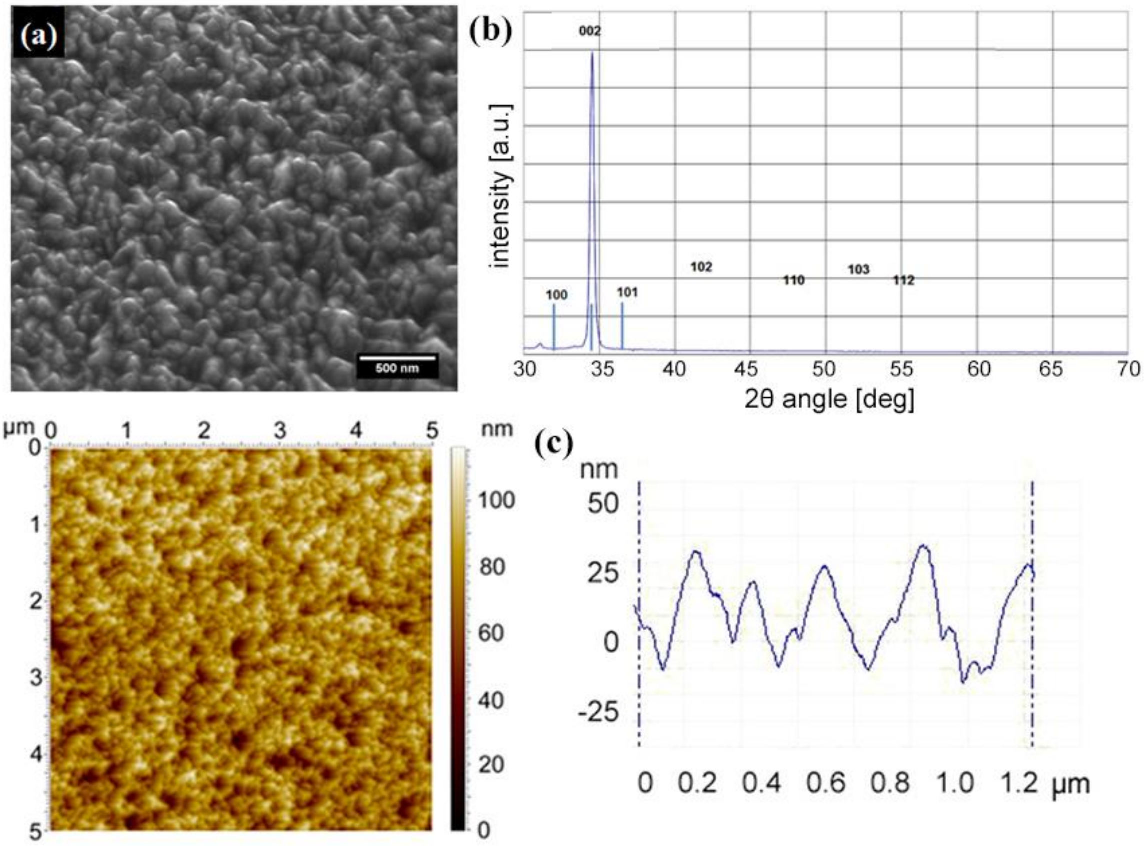

Figure 8. Morphology of AZO film deposited by RF magnetron sputtering and used as seeding film the growth of ZnO nanowires: (a) SEM image (b) XRD and (c) AFM

In both sputtering and PED AZO films, independently on grain size, a common orientation in the film with c axis (the polar axis of wurtzite structure) perpendicular to the glass substrate is clearly visible (Figure 7b and 8b), so that all grain polar surfaces are exposed. It should be pointed out here that this kind of orientation in ZnO films is not surprising, since very often these polycrystalline films, grown with different techniques (PED, PLD, sputtering, etc.), self-arrange in such an ordered structure, probably for energy minimization between crystals polar faces.

Also commercial ITO films are characterized by grains with an average size similar to that of sputtered AZO films.

4.1.2.2 ZnO nanostructures characterization

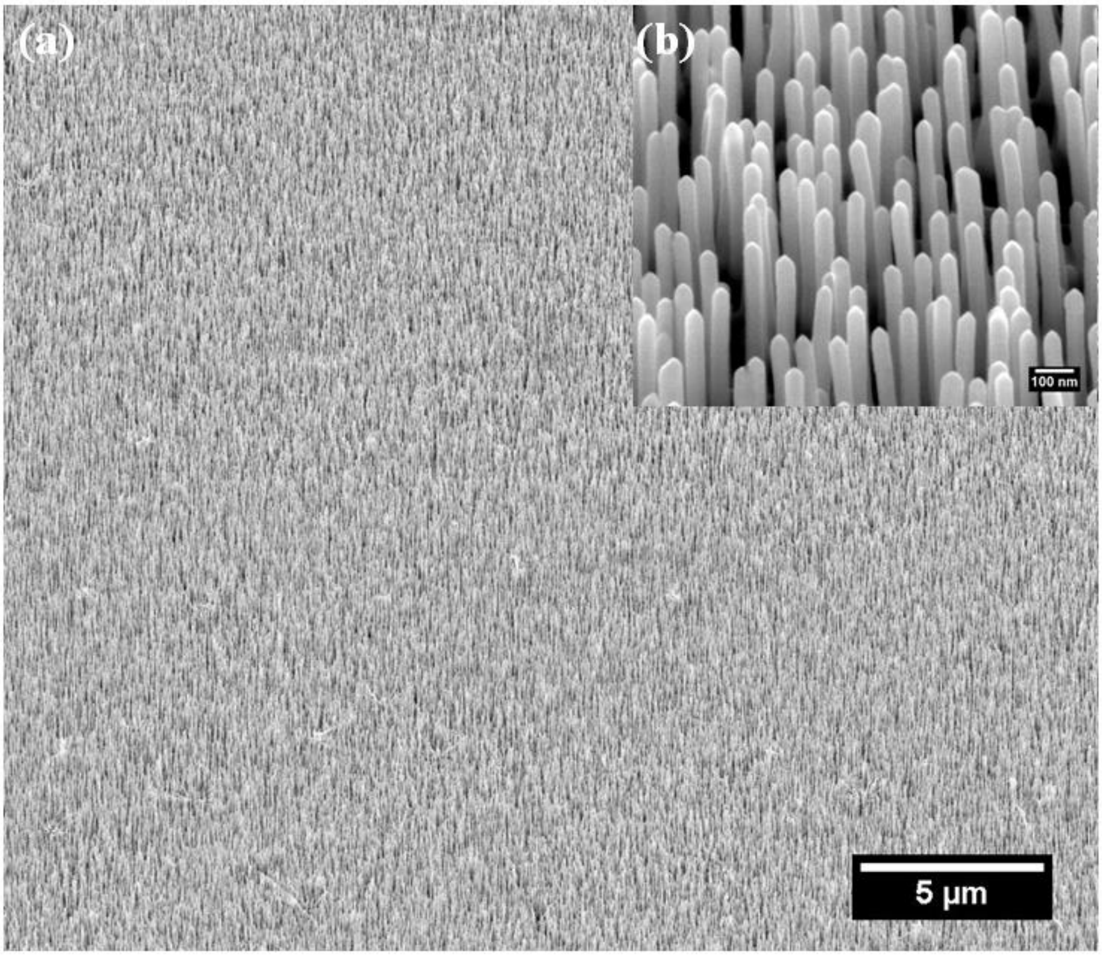

Figure 9. SEM image of ZnO-NRs grown on AZO film deposited by PED. (a) Homogeneous distribution of ZnO NRs on a larger area and magnified (tilted view) (b) magnified view of ZnO-NRs (tilted view).

At first, vertically aligned ZnO nanorods were grown on AZO substrate deposited by PED, using different conditions such as growth temperature, evaporation and reaction time, Ar/O_2 mixture ratio and flow rate, gap size (w) of the window in source container and the height of the empty buffer space (h).

The nanorods obtained were of homogeneous with 30–50 nm diameter and 0.3–3 µm length depending on the growth conditions. A homogeneous distribution of thin nanorods (Figure 9) has been observed over a 2 square centimeters area (the whole substrate size).

A thin inner-layer (ZnO wetting layer), whose thickness depends on the growth conditions, can be revealed in cross section SEM images between nanorods and the seeding films (left side of Figure 10). The better growth alignment has been obtained on AZO films deposited by PED with low surface roughness (<100 nm). XRD measurements (right side of Figure 10) clearly show a preferential orientation along the [001] direction, since only the (002) peak is essentially present. This means that nanorods grew with the same orientation of the seeding films.

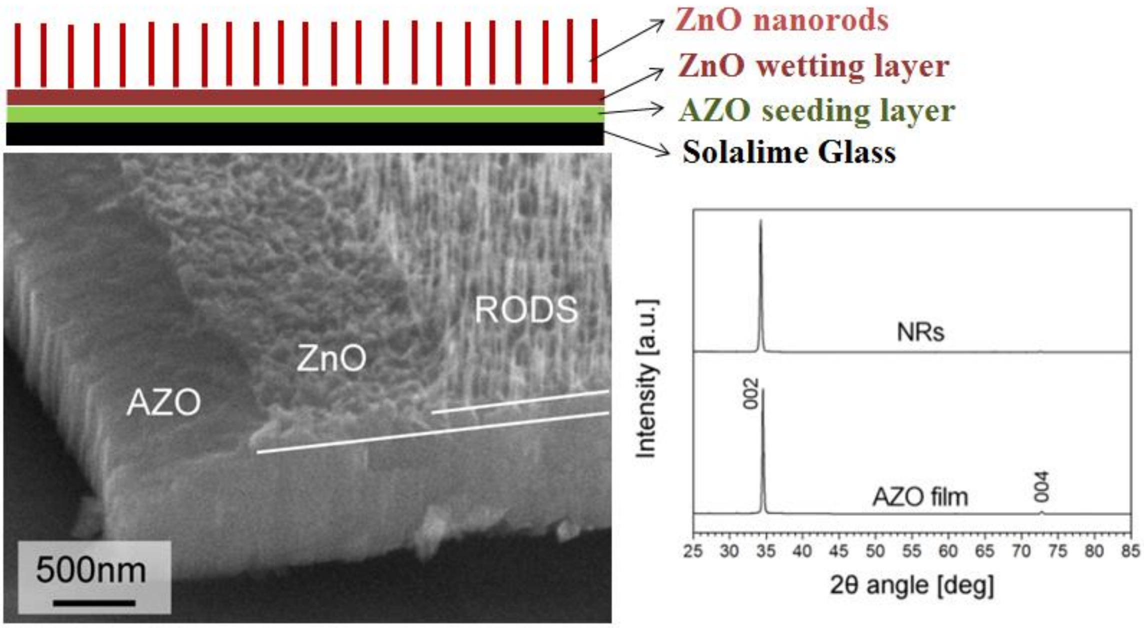

Figure 10. SEM image and XRD spectra of AZO/ZnO-layer/ZnO nanorods on commercial glass with seeding AZO film deposited by PED.

As described in the previous paragraph, the following experiments were performed by keeping constant most of the growth parameters, such as growth temperature, growth time, gas flow, and growth pressure, substrate distance from the source and aperture window size. The growth were performed only by varying the h value, proportional to the empty buffer size in the container, from 0.5 to 2 cm.

The grown nanorods were then examined by SEM analysis (Figure 11). If the empty space volume in source container is larger ("h" value of about 2 cm), only a minimum amount of Zn vapor exits from the source container windows and only for a limited time (empty volume has to be filled before Zn vapor exit from the window with a sufficient pressure). Therefore, supersaturation in the substrate region is not enough to start nucleation of nanorods and only a rough ZnO polycrystalline film was formed (Figure 11a).

If more Zn is put in the container and hence empty volume is reduced (“h” between 1 to 2 cm), Zn vapor that exits from the container is enough to form Zn clusters on the substrates and it is provided on the substrate for a time which is long enough to promote the growth of nanorods (Figure 11b-c). In this way, it is also possible to tune the length of nanorods from 100 nm to 1.5 µm by varying the value of “h” (the lower is “h” value, the longer are nanorods).

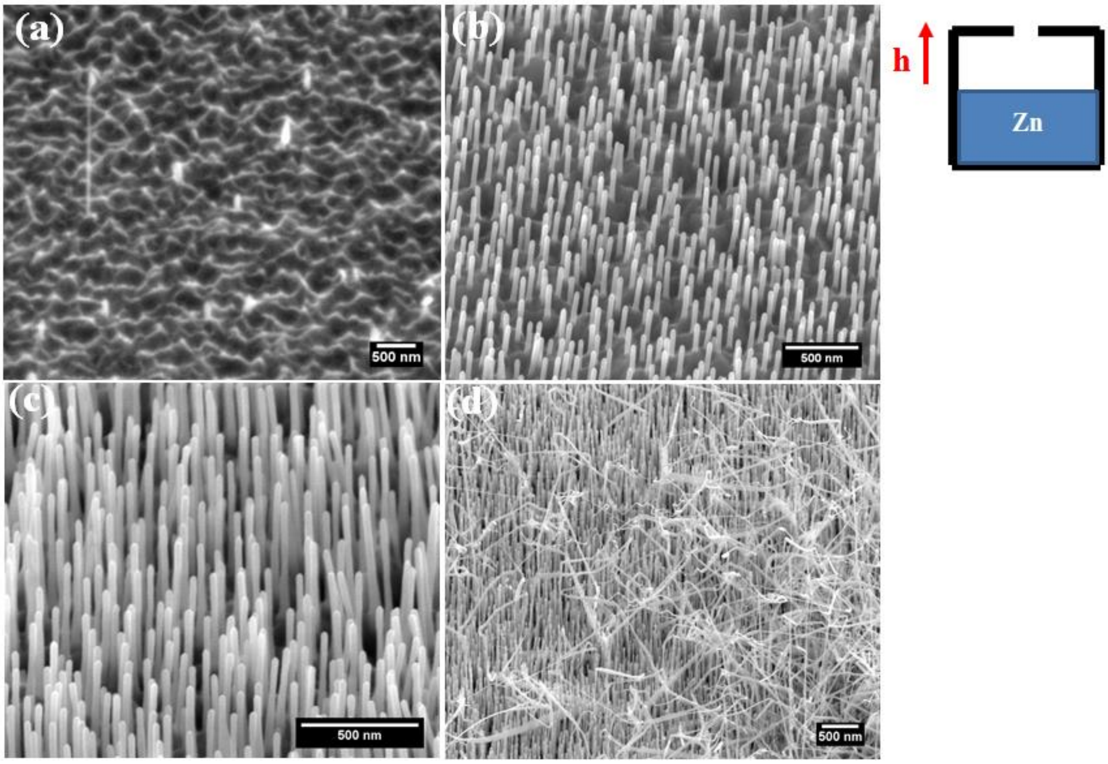

Figure 11. SEM images of different ZnO nanorods growths, obtained by changing the height of the height of Zn in source container.

However, when the volume of the empty space is decreased even more inside the source container (“h” < 1 cm) additional ZnO nanostructures were found on vertically aligned nanorods, as shown in Figure 11d. This is because the large excess in Zn vapor favors the further nucleation of additional nanostructures after the growth of nanorods.

Also the correct modulation of the source container window (w) was studied in depth and a maximum and minimum aperture value were found: within these limits, it was observed that it is possible to affect cluster/nanorod size and distribution by changing the window gap size and the gas flows (Figure 12). Larger w values and smaller flows generally favor the growth of high-density nanowires (Figure 12a), while opposite conditions favor lower densities (Figure 12b). However this kind of control is much more difficult and less reproducible than that obtained on nanowires length by h.

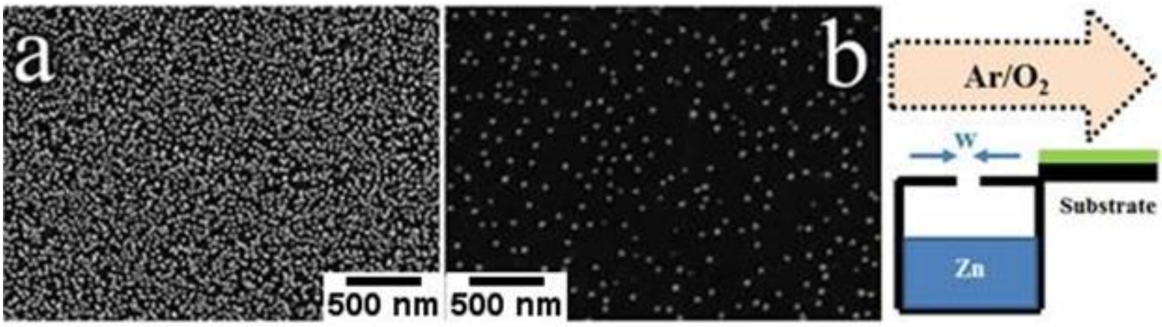

Figure 12. Top view SEM images of different ZnO nanorods growths, obtained by modulating the size of window "w" in source container: (a) large window, (b) small window.

Nanowires nucleation and distribution on the substrate seems to be more affected by the seeding layer and the deposition of very small clusters on its surface during the first part of the growth. In Figure 13 it is shown what happens when one of these two conditions are not the right ones.

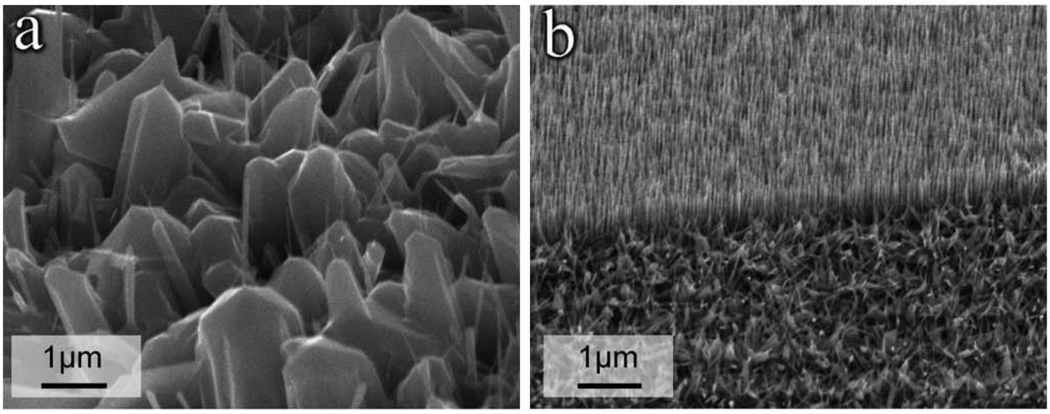

Figure 13. Tilted-view SEM images of: (a) large non-oriented crystals obtained when larger droplets are condensed on the seeding film; (b) boundary between the two regions of a Si substrate where ZnO seeding film is present (top) and not present (bottom)

The preferential orientation of seeding film grains clearly plays a fundamental role in the alignment of the grown nanowires. But also the grain size of AZO films plays an important role to control the diameter in the growth of vertically aligned ZnO nanorods. The grain size of the seeding layer affects the thickness and shape of the nanorods as shown in Figure 14. AZO films deposited by RF-sputteringhas indeed larger grain size (Figure 14c). The presence of larger but still oriented grains at the beginning of the vapour phase process promote the growth of nearly aligned rods with similarely larger dimeter, i.e. 100-500 nm (Figure 14d). The obtained nanorods, indeed, were found to have an average thickness of 250 nm

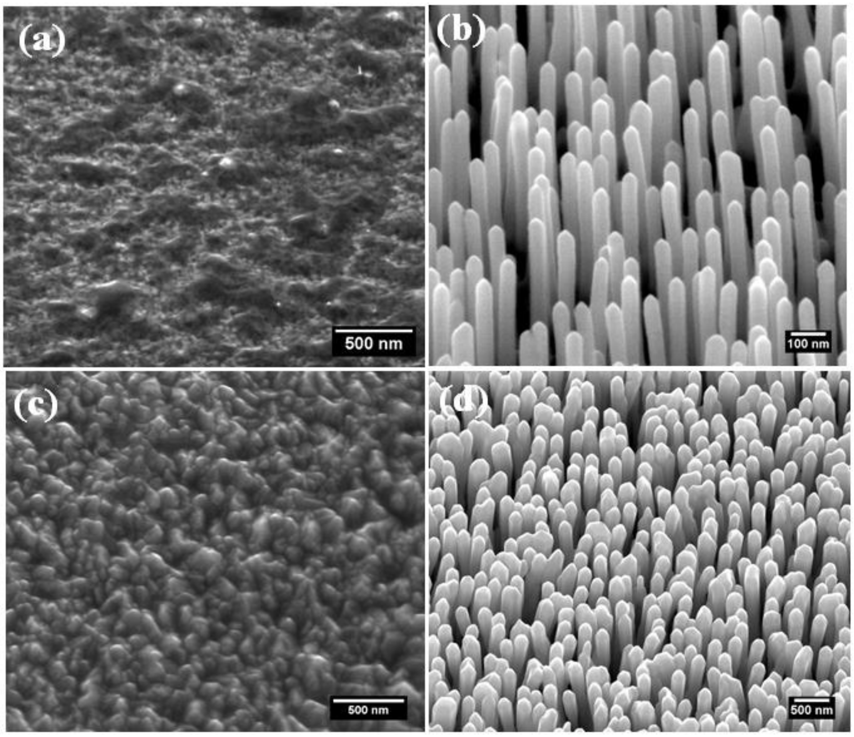

Figure 14. SEM images of AZO film deposited by (a) PED, (c) RF-sputtering and (b, d) corresponding ZnO nanorods on growth on the substrate.

But If the grain size is larger than 500 nm, it was observed that the transition from the continuous film to thin and sharp nanorods is more difficult, so a structure with large and often merged crystals (Figure 15) is observed.

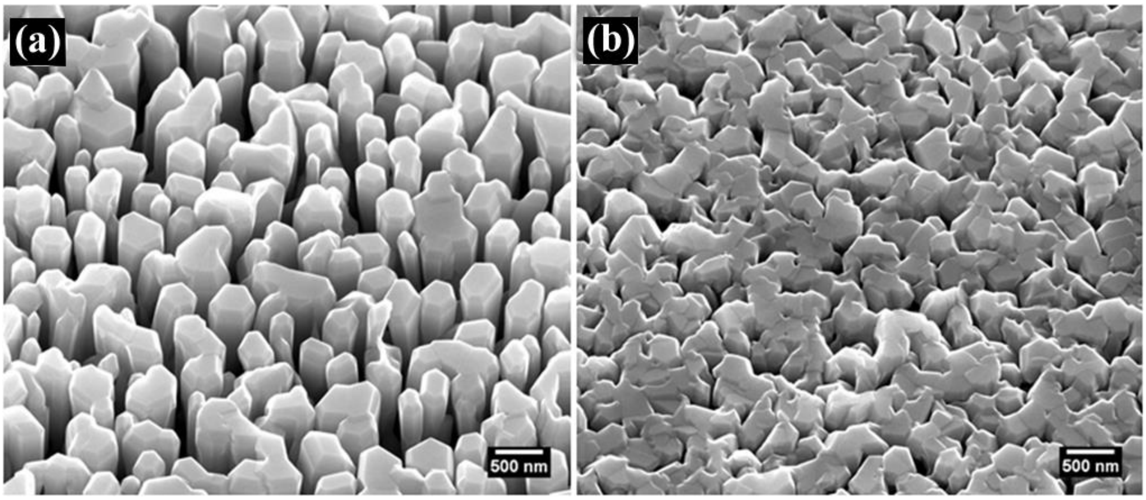

Figure 15. SEM images of merged ZnO nanorods on different grain size AZO film deposited by RF-sputtering.

On the other side, as said before the alignment of the nanorods at this temperature is influenced by the presence of common orientation of the polar axis in seeding layer grains. So, while AZO "oriented" seeding layer helps to grow aligned ZnO nanorods, a seeding layer with a different crystal structure and no polarization, as in the case of a commercial ITO films, leaded to the growth of randomly oriented rods/wires as shown in Figure 16.

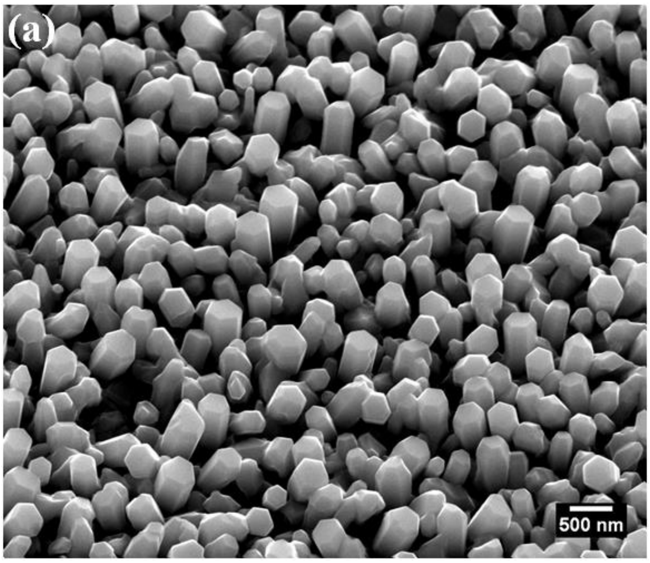

Figure 16. SEM images of ZnO nanorods on commercial ITO substrates

4.2 Nanowires of ternary (In/Ga/Sn)ZnO oxides

Recently, studies on nanostructures of ZnO-based ternary compounds are rapidly increasing because they are technologically very important, especially for the production of nanostructured transparent oxides for multi-color light-emitting device, sensors, transparent electrodes, or catalysis [61,62].

Undoped zinc oxide shows typically n-type conductivity, generally ascribed to stoichiometric defects (e.g. oxygen vacancies or zinc interstitials) or due to unavoidable contamination of hydrogen that acts as interstitial donor [63-65]. Most of the applications actually require a good control of electrical conductivity that can be achieved by doping or alloying ZnO. In particular, high n-type conductivity can be achieved by alloying zinc oxide with group III, IV, V elements (such as Al, In, Ga, Sn or Sb) in ternary or even quaternary oxide compounds [66-80]. On the other side, it has been observed that the introduction of a third element (In, Ga, etc.) in to the ZnO nanostructures can give rise to dramatic changes in the morphologies of nanostructures [81-83].

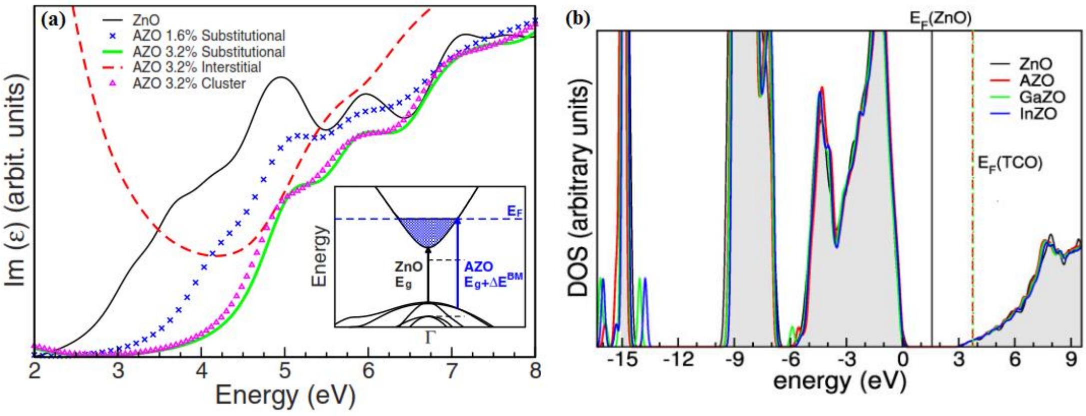

Figure 17. Influence of dopant in ZnO to change electrical properties (a) Imaginary part of the dielectric function at varying Al content. Inset: schematic band structure representation of the BM effect and the optical gap enhancement [84] (b) DOS for ZnO derived TCOs, as obtained via Al (AZO), Ga (GaZO), and In (InZO) incorporation in substitutional Zn sites, with respect to bulk ZnO, which is also represented to enhance comparison in grey background [85].

The Al doping increases the conductivity without damaging the optical transmission and is regarded as a potential alternative cheaper candidate for indium-tin-oxide (ITO) materials [10, 11]. Indeed, numerical calculations recently showed that 1-3% concentration of an element such as Al in a ZnO matrix, pushes Fermi level to penetrate into the conduction band, thus giving rise to a metallic behavior [84]. These effects are shown in Figure 17a.

In and Ga are other excellent dopants for increasing the conductivity, and this kind of source is less reactive and more resistant to surface oxidation [68,69]. In-doped ZnO films show similar electrical conductivity and better transparency, in both the visible and the infrared regions, than ITO. Also when Ga is introduced into ZnO nanorods a resistivity of about 10^{-3} Ω cm could be achieved. Comparable results are obtained from numerical calculations in the case of doping with Ga or with In [85]. These results were shown in Figure 17b. The reported resistivity values for this kind of alloying (1-3% in content cannot be simply considered a “doping”) are as low as values reached for transparent conductive oxide (TCO) materials [70-72], making them suitable for a large number of possible applications, as in the case of TCOs in solar cells.

Moreover, for higher In content in InZnO ternary compounds may give rise to self-assembled micro-superlattices in a one-dimensional structure, with the formation of In–O and In/Zn–O layers, which appears to favor the formation of nanorings and is expected to have novel properties, like a quantum confinement of carriers and excitons, and to have potential application in nano-optoelectronics or thermoelectricity [86-89].

Presence of a second metal in ZnO may also produce surface plasmonic effects. Researchers found that Al-doped zinc oxide may be considered as a new plasmonic material and they experimentally demonstrated negative refraction in an Al:ZnO/ZnO metamaterial in the near-infrared range [90].

On the other hand, it was reported that a Sn-doping increases the resistivity of ZnO films and induces an emission at blue wavelength region [75,76]. The grain size and resistivity of ZnO were controlled by the doping levels of Sb [77,78].

4.2.1 Synthesis

In the previous chapter a good way to grow vertically aligned ZnO nanorods by vapor-phase technique over a ZnO or Al:ZnO (AZO) film has been described. The main result of that growth technique is that, even if Zn vapors are used for the growth, the required temperature is low enough (450-480 °C) to allow the use of low-cost glass substrates, as the ones typically adopted for solar cell technology. By growing such nanostructures starting from a metallic Zn source, without the use of any catalyst or metal-organic precursor, contaminations from reaction environment (often intrinsic and noteworthy in wet chemical methods) has been drastically reduced allowing to grow ZnO nanorods with high crystalline quality and controlled physical properties.

It is important to note that in the described technique a layer of liquid metal droplets is formed on the substrate during the first growth stage and that only afterwards, when oxygen is introduced, a corrugated oxide wetting layer is formed and nanostructures start to grow. This two-step process was successfully used in the past at IMEM-CNR also for growing SnO_2 [91], In_2O_3 [92], and ZnO nanowires [93]. It mainly differs from standard VLS (vapor-liquid-solid) growth technique because in this case the liquid phase is not used as an inert solvent through which the solid phase of different materials precipitate but to induce a localized preferential fast nucleation point that also provides high metal vapor supersaturation for a self-catalyzed vapor-solid growth.

Unfortunately, the growth of ternary oxides by a similar vapor deposition technique, starting directly from the co-evaporation of two different metals, is much more difficult because vapor pressure of the two metals may differ by several orders of magnitude and their transport and deposition in the correct ratio could be not possible. This is the case, for example, of zinc and the mentioned group III elements, whose boiling point are generally over 2000°C and, hence, have insufficient vapor pressure around 500°C. For this reason, growth of InZnO nanowires was achieved up to know at temperatures well above 500°C (typically on the range 700-1400 °C) [94-97], and thus not compatible with the use of low-cost glass substrates.

Other authors proposed to use an indium drop as a nucleation site for the growth of ZnO nanorods [98]: in this way they achieved effective indium doping with a decrease of resistivity of one order of magnitude. Unfortunately, the growth temperature they used was still too high (750 °C) to be compatible with the use of a glass substrate [99].

In this thesis work a similar approach has been exploited to grow indium zinc oxide nanorods (IZO-NRs hereafter in the text) in a conventional CVD system with an indium concentration larger than 1% (that is the concentration required to get metallic behavior) at temperatures lower than 500°C. The possibility to use the same technique to growth nanowires of a wider family of ternary oxides such as GaZnO, SnZnO were discussed.

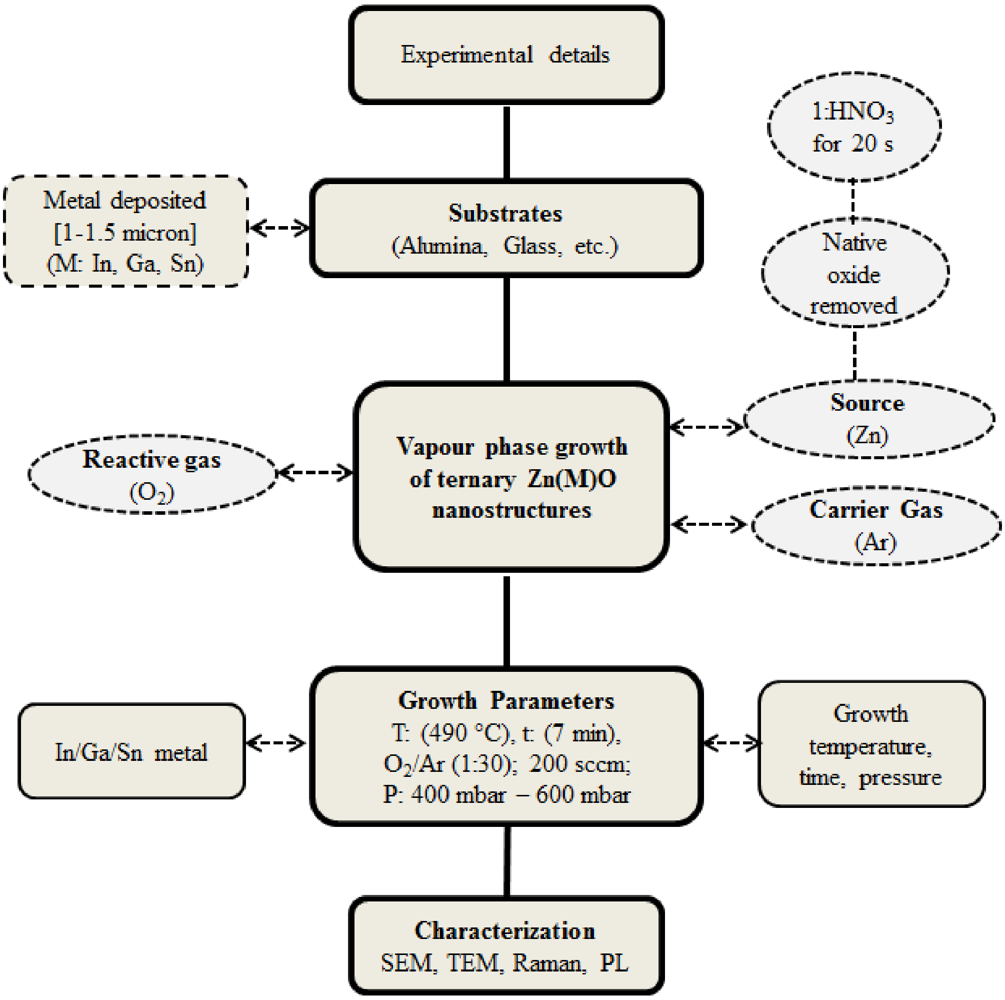

Figure 18. Flowchart of experimental scheme

Ternary compound of ZnO nanostructures have been grown using home-made thermal chemical vapor deposition (CVD) reactor. The experimental details are shown in the flowchart given in Figure 18. Indium was deposited in form of a 1-5 μm layer on different substrates, as glass, alumina and silicon. Part of the substrate was masked during the deposition in order to have an In-free zone on the substrate. This was done to monitor directly the effect of the seed layer on the growth and the patterning capabilities for the grown nanostructures by a simple comparison of the growth results on the two zones.

The following procedure is derived from the one previously described for pure ZnO nanorods. A laboratory scale reactor (a tubular furnace) equipped with a flow control system, by means of which it is possible to flow different gasses during the growth, has been used. Schematic diagram of the reactor as shown in Figure 19. Pure metallic Zn powders (5N purity) were chosen as source materials and placed in an alumina container with a small window on the top. The used powders were softly etched before use in order to have a better reproducibility during the Zn evaporation process. Different amount of native oxide, indeed, may rather affect the evaporation rate in the used temperature range (slightly higher than the melting point). Substrate with a 1-1.5 micron layer of metallic In, Ga or Sn were then placed close to the source, few mm downstream near the center of the furnace. In this part of the reactor no temperature gradient is present in static conditions.

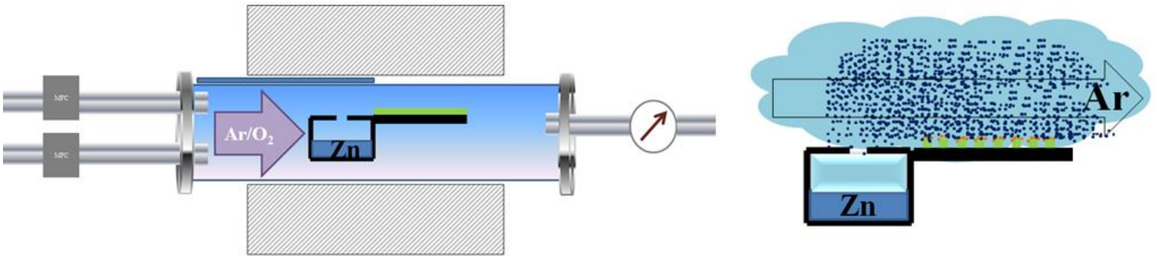

Figure 19. Schematic diagram of thermal CVD reactor

Nanostructures were obtained as a result of three subsequent steps (Figure 20). At the beginning temperature was increased up to 490°C. Then, once the maximum temperature was reached, furnace heating was maintained for about 8 minutes in a flow of Ar/O_2 mixture (20:1 ratio, 50 sccm). Finally the gas mixture was substituted by a larger Ar flow (250 sccm) and furnace cooling started.

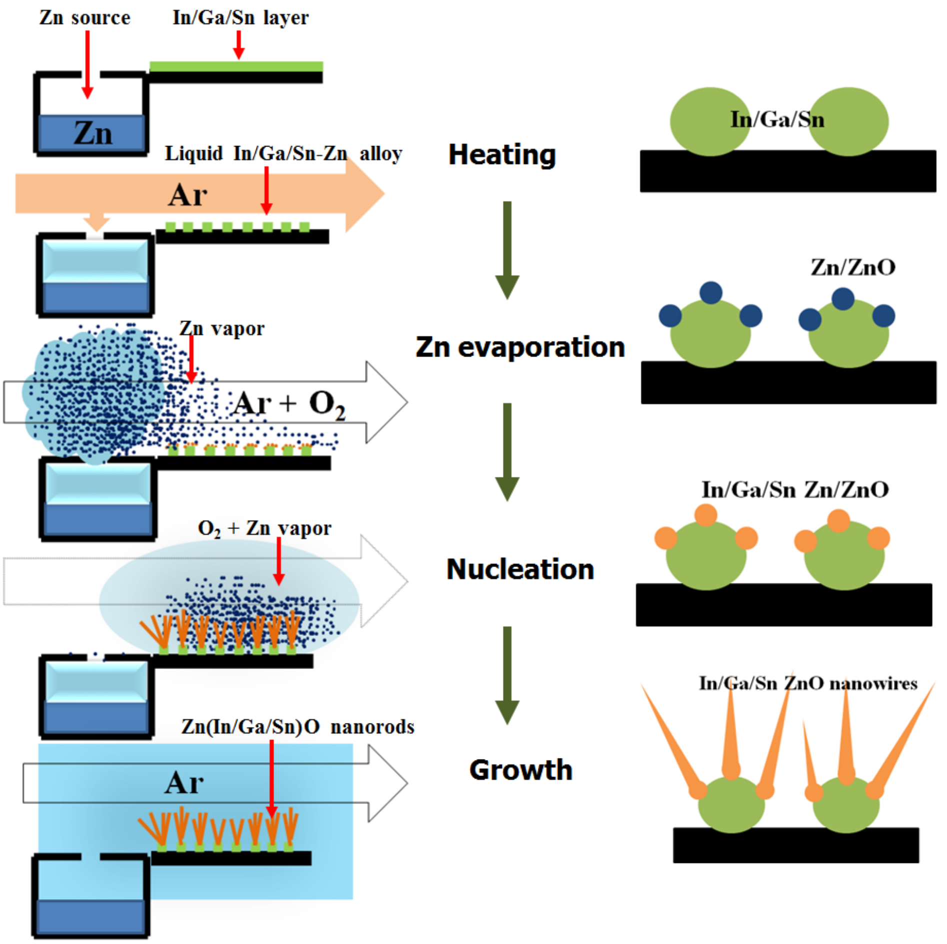

Figure 20. Scheme of the main growth steps that lead to the formation of ternary compound of InZnO, GaZnO and SnZnO nanostructures.

Substrates were collected once room temperature is reached and then they were characterized by different techniques. The general morphology of obtained samples was analyzed by means of Scanning Electron Microscope (Philips 515 SEM), while shape, crystal structure and orientation of single nanostructures were studied by high resolution and analytical investigations of a Transmission Electron Microscope (JEOL 2200FS field emission) equipped with in-column Ω filter, two High Angle Annular Dark Field (HAADF) detectors and X-ray microanalysis (EDS). Photoluminescence (PL) measurements were instead performed using a laser excitation at 325 nm (He-Cd, 20 mW) both at room temperature and low temperature (7K). The Raman spectra were excited using 488 nm of Ar-ion laser in the backscattering geometry. The incident power was 180 mW through a 100x objective and the collection time of 10 s. The 1800 grating were used as filter to avoid some emission from the back substrate. Prior to the measurements, the monochromator was calibrated using 520 and 1332 cm^{-1} peaks of Si and diamond, respectively.

4.2.1.1 Growth mechanism

In, Ga and Sn have all low melting points and a very high boiling point. A similar discussion can be made in the case of all these three elements, but here the case of In is reported more in detail as it gave the best growth results.

Indium vapor pressure is about 8 orders of magnitude lower than Zn vapor pressure in the exploited temperature range (Figure 21).

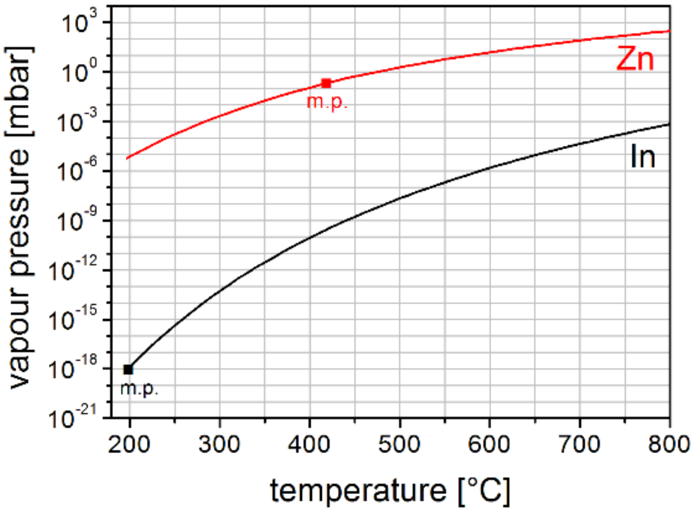

Figure 21. Equilibrium vapor pressures for In and Zn in the 200-800°C temperature range (data from Ref. [100]).

So, even in the approximation of kinetically not limited evaporation processes, a co-evaporation of the two metal sources in order to obtain an In-Zn oxide with at least a 1-3% indium content (i.e. typical values for an InZnO-based TCO application [101]) has to be considered almost impossible. On the other hand In-Zn phase diagram is characterized by an eutectic point assessed at $T \approx 145°C$, but it is characterized by a $0.03 < x < 0.05$ Zn molar fraction [102] and at this temperature oxidation processes are not sufficiently favored. At higher temperature, i.e. above Zn melting point at 419.5°C, the two metals can form liquid alloys in any ratio.

In the described growth procedure Zn evaporates and condenses on the substrate where In layer is placed. At the growth temperature (490°C) In is liquid and a liquid In-Zn alloy is expected to form. Then, during the last stage of the growth, oxygen can form solid oxide nuclei that, thanks to the presence of Zn vapors and residual oxygen, can give rise to the obtained IZO-NRs.

In principle In could enter the nanorod in different ways, i.e. by diffusion through the solid, by a VLS growth from an In (or In-rich In-Zn alloy) droplet or by the $In+Zn+O_2$ vapor phase reaction. The first hypothesis is in contrast with the homogeneity of In concentration along the IZO-NRs, as a decreasing concentration towards the tip of the rod is generally obtained with such a mechanism. The second hypothesis, on the other hand, should be confirmed by the presence of some residual drop on the tip. But no droplet was generally observed on the growth tip of the IZO-NRs and TEM-EDS mapping also excludes that any In rich zone is present in the last part of the rods. So, the third hypothesis could be suggested as the most probable mechanism for this kind of growth, as previously reported for Sn in the growth of SnO_2 nanowires [103].

Although temperature and In vapor pressure are low, within a micrometric distance from the liquid surface In atoms can move very fast as this distance is comparable with the mean free path in the described growth conditions. So, in this configuration In vapor feeding rate from the neighboring In-Zn alloy to the growth tip can be sufficient during all the NRs growth.

The described approach to the growth of such ZnO-based ternary oxides could be in principle extended to other metals that are molten at the growth temperature (i.e. with a melting point below 500°C) but limited in the evaporation because of a much higher boiling point. This is for example the case of Ga and Sn, that have been also investigated for this thesis work.

4.2.2 Characterization

4.2.2.1 InZnO nanorods

A general overview of the grown InZnO nanorods distribution is show in Figure 22a.

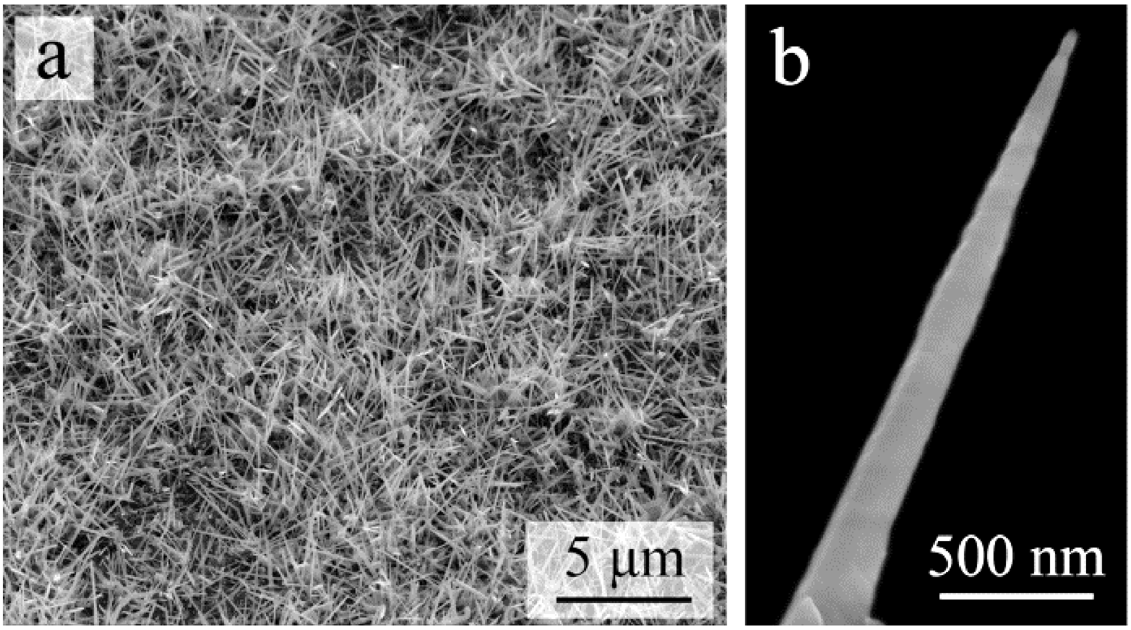

Figure 22. SEM images of the collected samples: (a) general overview at lower magnification of the growth over the In layer (b) detail of a tapered nanorod

Nanorods grew on the substrate wherever the In film was present while, on the contrary, any nanostructure growth was strongly inhibited in the In-free zones of the substrate. In the used growth system and temperature range (i.e. below 500°C) substrate wettability, indeed, plays a fundamental role into determine on which surface Zn condensation can occur. In fact, when wettability is low, the formation of larger “liquid nuclei” (i.e. condensation droplets) is favored and if vapor supersaturation is not high enough to feed and increase the size of the nuclei above this large critical size, nuclei are unstable and tend to re-evaporate. A similar behavior was observed in Ref. [104], where ZnO nanorods were reported to grow selectively only on the seed layer. This is clearly the case of Zn vapors on glass, alumina and silicon (with native oxide) substrates in the described growth system. Nevertheless any clean imperfection or local excessive roughness (e.g. the presence of sharp tips) can act as a preferential nucleation site, especially when commercial and low cost substrate are used, and in such case the growth of some ZnO nanostructure can be occasionally observed also in the In-free zones. If necessary, better masking/patterning results can be obtained by adding mechanical masks on these areas during the growth.

SEM images of these nanostructures grown on the top of the In layer are however not sufficient to state that they are IZO-NRs, i.e. they really have both In and Zn in their structure. So some of them were removed from the substrate and put on a TEM grid for a structural and compositional analysis.

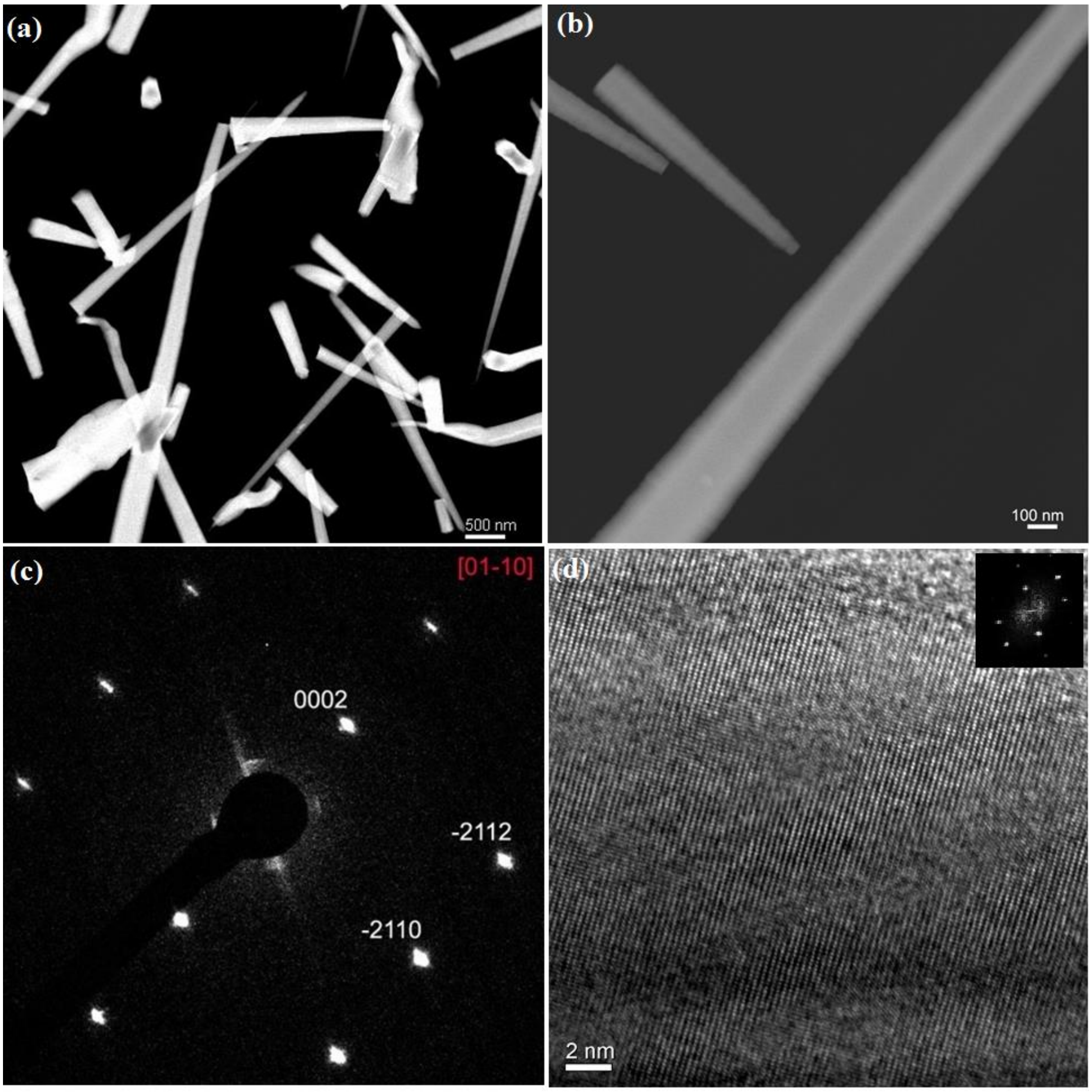

Figure 23. (a),(b) TEM HAADF image of IZO-NRs; (c) diffraction pattern of the largest nanorod in the picture; (d) HREM image with related FFT in the inset.

In Figure 23a and 23b TEM HAADF image is reported, where the typical tapered shape and the growth tip of analyzed NRs can be clearly observed. The diffraction patterns (Figure 23c) confirmed that also these NRs are single-crystals grown along the [001] direction of the hexagonal wurtzite structure typical of ZnO and no measurable difference has been found in the lattice parameters, within the error related with ED pattern blur, when compared with those of a pure ZnO nanocrystal. HREM investigations on several wires showed that, more than being single crystal, the nanorods usually don't present extended crystal defects such as stacking faults or dislocations. Figure 23d shows a typical HREM image taken on a nanorod laying in the same projection as in Figure 23c, as testified by its diffractogram reported as inset.

TEM-EDS analysis (Figure 24) then finally confirmed that In is really inside the nanostructures and that it is homogeneously distributed along the length and radius of the NRs. Moreover, by semi-quantitative analysis of the collected EDS spectra the In content has been assessed around 1-2%. This value is in the typical range of doping (or alloying) level that is desired for a TCO material with good electrical conductivity.

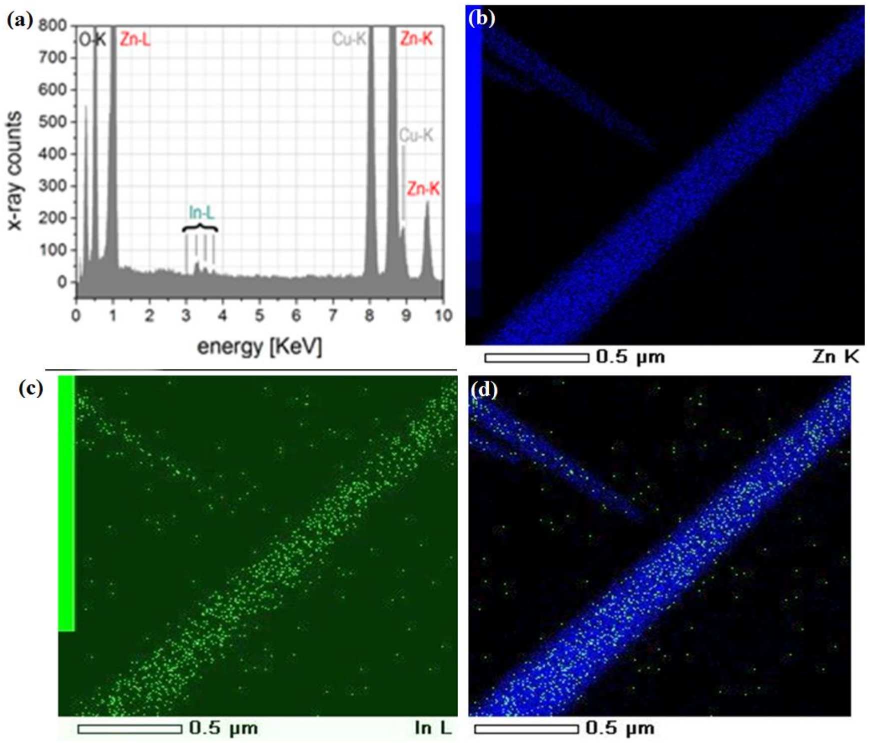

Figure 24. (a) TEM-EDS spectrum of the IZO-NRs sample shown in Figure 6a; (b-d) TEM-EDS elemental mapping of the same sample for Zn and In respectively. Cu peaks are present because of TEM grid support.

Raman spectra of both ZnO and InZnO nanorods are shown in Figure 25 for the range between 100 cm^{-1} an 800 cm^{-1}. The Raman spectra have been measured on as-grown samples as shown in Figure 25a, which are ensembles of nanorods. There were clear differences witnessed between ZnO and InZnO nanorods. It showed that the best crystalline quality was observed on the ZnO nanorods. There were sharp E_{2h} peak and intense broad quasi-LO band observed on ZnO nanorods. Crystal quality in Raman spectra changes due to the defects and other factors [94]. They are:

1) the E_{2h} mode broadens and reduces its intensity with increasing density of defects

2) the LO to E_{2h} intensity ratio also correlates with the density of defects (probably oxygen vacancies)

3) the distance between neighbor defects (L_0) decreases

4) optical phonons confined at the surface (SOP) appear at frequencies between LO and TO modes

The intensity of SOP also increases for more disordered samples. From these explanations, it can be understand that presence of Indium in ZnO changes the crystal quality. From the Raman spectra observations of InZnO nanorods, the signal from E_{2h} is found to be weaker and broader. The shape of the spectra is consistent with defect-mediated Raman scattering. More disordered structure in In-doped ZnO is expected due to the large difference in atomic radius between In and Zn.

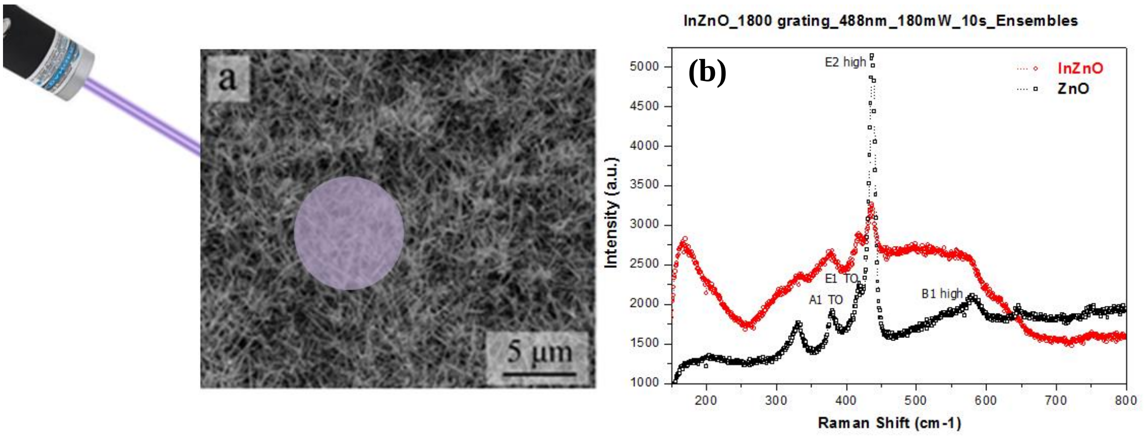

Figure 25. Raman spectra comparison of IZO-NRs and ZnO-NRs ensembles at room temperature.

PL measurements were also performed on the as-grown IZO NRs. The optical emission of the obtained nanostructures was compared with that of ZnO-NRs like those previously reported in Ref. [88], with similar size and grown in similar conditions. As shown in Figure 26a, the presence of In atoms induces only a small shift in the near band edge (NBE) emission peak at room temperature.

However, a similar shift was observed in the past in the case of different samples of pure ZnO nanorods grown by our group in slightly different conditions, thus we do not think that it can be ascribed to the presence of indium. We rather ascribe this small shift measured at room temperature (Figure 26a) to the different weight of the NBE peak components, also taking into account 20 that in the low temperature measurement (Figure 26b) it is not observed (only the expected blue-shift at low temperature is visible for both spectra according to Varshni equation). This can be explained in the frame of the model recently proposed to account for the metallic behavior of AlZnO, InZnO, and GaZnO ternary compounds [84,85].

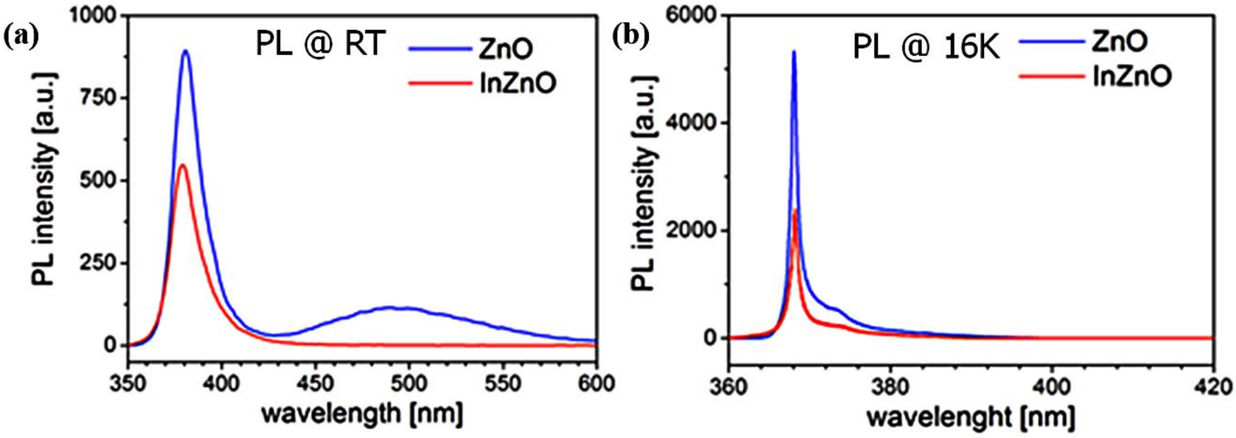

Figure 26. PL spectra comparison of IZO-NRs and ZnO-NRs: (a) at room temperature; (b) at 16K.

In fact, according to calculations, the introduction of group III elements in little percentage range does not increase the band gap energy, but rather pushes the Fermi level into the conduction band. The consequence is that the band gap PL emission does not change.

On the other hand, the typical band in the visible region, generally present in the emission of ZnO nanostructures and recently ascribed to Zn vacancies, [104,105] is not observed in the PL spectrum of IZO-NRs. This result seems to suggest that indium (In) atoms could passivate these typical point defects that are generally associated with the rise of the “green” band. No comment can be done about the intensity of PL spectra, as the reported measurements cannot be quantitative; however the order of magnitude of the two intensities is almost comparable.

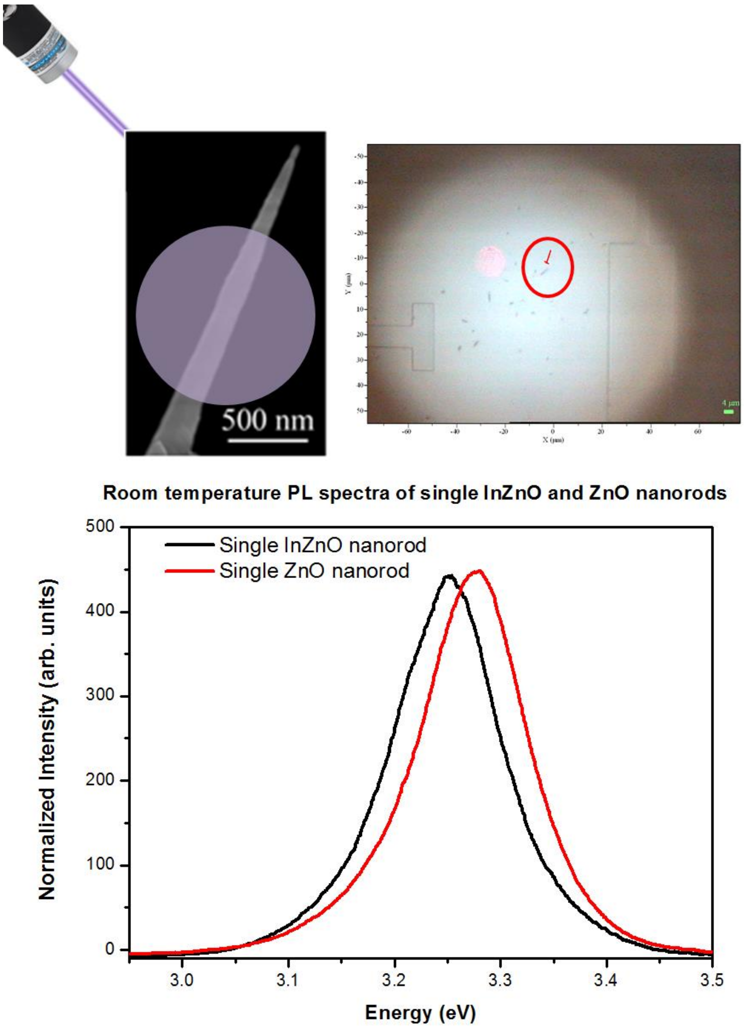

Figure 27. PL spectra comparison of single IZO-NRs and ZnO-NRs: at room temperature

In order to confirm these data come from InZnO nanorods and that they are not affected by artifacts originating from the bottom seeding film, PL on single nanowires at room temperature was also measured, as shown in Figure 27. The near band edge peak of In-doped single NWs is centered at 3.25 ± 0.01 eV and presents a FWHM of ~ 130 meV. The small red-shift of ~ 30 meV with respect to the undoped ZnO NWs have been observed. A blue-shift of the emission of In doped ZnO due to the filling of bands (Burstein-Moss effect) has also not been observed in single nanorod. Because, only at high doping levels, electron-electron interaction (band-gap renormalization) reduces the band-gap energy. While, at low doping levels, localization effects for electrons and holes due to the states introduced by the dopants could also induce the red-shift of the emission [94]. This PL measurement on single nanorods also suggests that there is small percentage of In in the obtained InZnO nanorods.

4.2.2.2 GaZnO and SnZnO nanorods

In a preliminary study, also GaZnO and SnZnO nanorods were synthesized using the above described growth mechanism in which the metal with lower vapor pressure acts as liquid metal source. In this case, Ga or Sn metal forms metal liquid droplets at the growth temperature and acts as Ga or Sn source respectively.

A SEM image of as-grown sample of GaZnO is shown in Figure 28a. Bunches of wire-like nanostructures were observed to originate from the Ga-Zn alloy. The observed nanowires were 50-100 nm in thickness and 5-10 microns in length. The density of grown GaZnO nanorods was definitely lower when compared to that of InZnO nanorods.

Photoluminescence spectra of as-grown GaZnO nanorods and ZnO nanorods are shown in Figure 28b. As in the case of InZnO nanorods, also GaZnO nanorods seemed to be not affected by significant near band edge shift, while the typical green defect band is in this case not completely quenched.

Raman spectra of GaZnO and ZnO nanorods is shown in Figure 28c. A sharp E_{2h} peak points and a strong quasi-LO mode peaks at an intermediate frequency between the A1 and the E1 modes were observed on ZnO nanorods and it points out a good crystalline quality and a typical effect of nanowire-like morphology. A surface optical phonon (SOP) is also observed in the undoped nanorods. On the contrary, a very weak E_{2h} peak and an increased SOP was observed on GaZnO nanorods. These results might be correlated with the presence of Ga in ZnO nanorods.

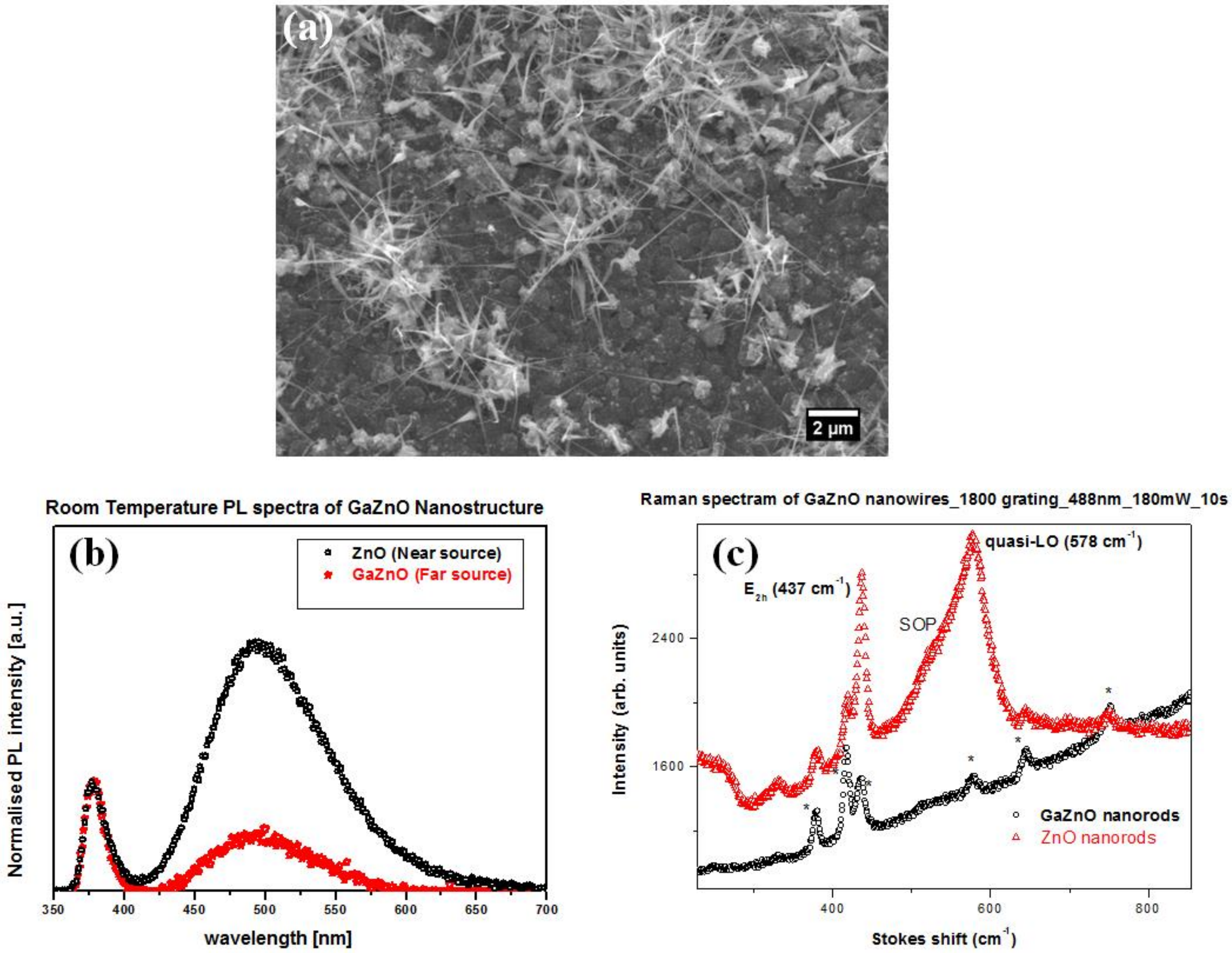

Figure 28. Growth GaZnO nanorods using Ga metal liquid seeded on alumina substrate. (a) SEM image of as grown GaZnO nanorods, (b) comparison of PL spectra of ZnO and GaZnO nanorods and (c) comparison of Raman spectra of ZnO and GaZnO nanorods.

A SEM image of as-grown sample of SnZnO is shown in Figure 29a. As for the case of GaZnO nanorods, also here bunches of nanorods were observed. The observed nanowires were 30-50 nm in thickness and 5-10 microns in length. The density of grown SnZnO nanorods, also in this case, was much lower than that of InZnO nanorods.

PL spectra of as-grown SnZnO nanorods and ZnO nanorods are shown in Figure 29b. As in the case of GaZnO nanorods, also here there is no significant near band edge shift and a partial quench of the visible-range green band typically ascribed to surface defects.

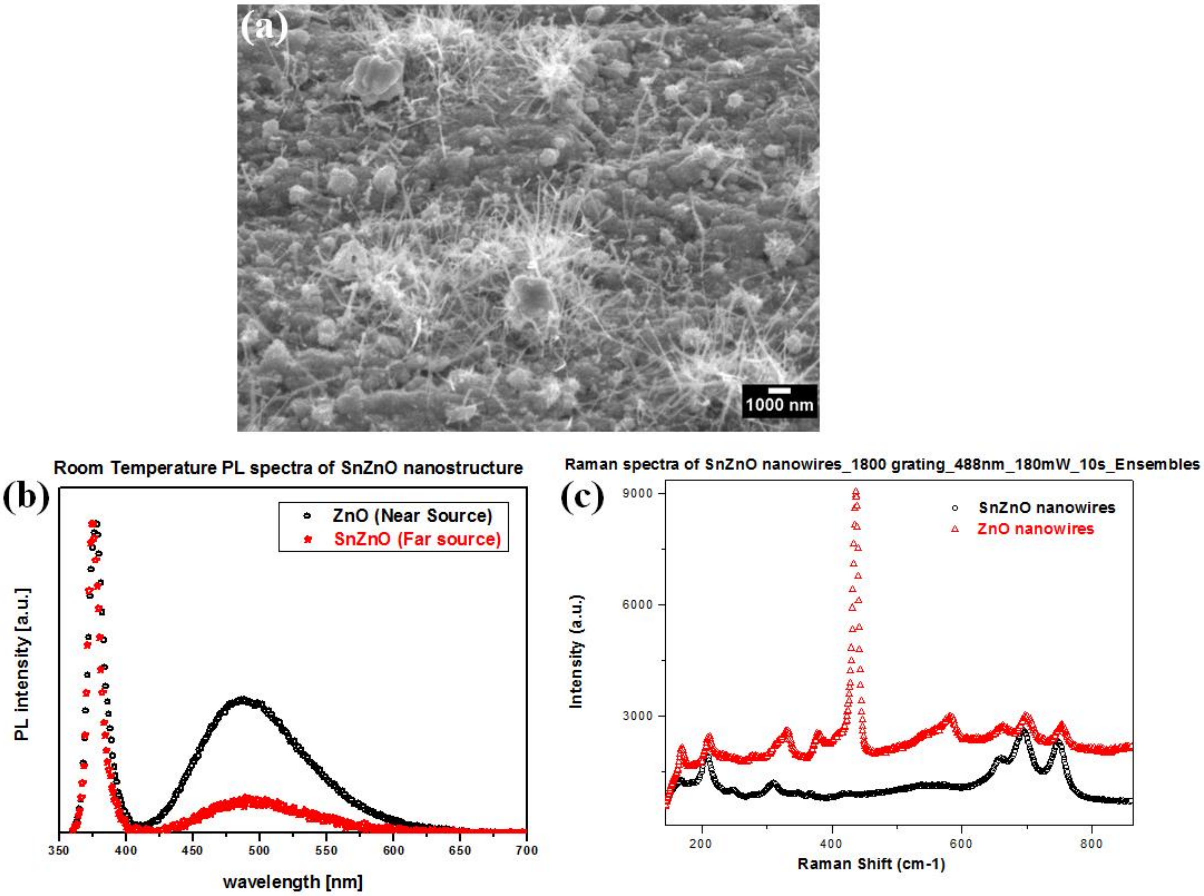

Figure 29. Growth SnZnO nanorods using Sn metal liquid seeded on alumina substrate. (a) SEM image of as grown SnZnO nanorods, (b) comparison of PL spectra of ZnO and SnZnO nanorods and (c) comparison of Raman spectra of ZnO and SnZnO nanorods.

Raman spectra of SnZnO and ZnO nanorods are instead shown in Figure 29c. E_{2h} peak observed on SnZnO nanorods is very weak. There are also three peaks that indicates the formation of a second phase, which is however not SnO_2 because modes are not corresponding.

Further studies have to be performed on both GaZnO and SnZnO and the presented results are just preliminary. Although incomplete, they have been shown to demonstrate that, in principle, the same technique used to produce InZnO nanorods from vapor phase below 500°C can be extended also to different ZnO-based ternary compounds with other metals that are molten at this temperature but limited in the evaporation because of a much higher boiling point.

4.3 3C-SiC nanowires

Silicon carbide (SiC) is very interesting and widely investigated semiconducting materials [107] due to its physical properties such as the wide bandgap, high thermal conductivity, high breakdown electric field, high electron drift velocity, high Young's modulus and hardness, high melting temperature, excellent oxidation and corrosion durability, high strength at elevated temperatures, good thermal shock resistance and excellent chemical and physical stability. Owing to these numerous major advantages combined with the above properties, one dimensional (1D) SiC nanostructures plays an important role in device fabrication than SiC bulk and thin films. SiC nanowires have attracted many researchers after the discovery of carbon nanotubes because of their unique electronic [108, 109], field-emitting [110], hydrophobic [111] and mechanical properties [112] and their potential applications in areas such as electronic and optoelectronic nanodevices, nanocomposites and hydrophobic devices.

SiC crystallizes in various forms known as polytypes which can be the cubic form (3C or β), the two hexagonal ones (4H and 6H) and some rhombohedral forms (9R, 15R and 21R) are most common ones. Notably, cubic polytype is the most stable at low growth temperatures even though 6H-polytype is the most stable from thermodynamic equilibrium aspect [113]. Among the over 200 known polytypes of SiC, 3C–SiC NWs synthesized in the vast majority of literatures due to their high strength, high stiffness, high temperature stability and low density compared to other polytypes [114, 115]. It was reported that single crystalline 3C–SiC nanowires on a Si substrate have been shown to possess visible photoluminescence (PL) at room temperature and blueshift effect depending on the diameter of nanowires [116]. Furthermore, 3C-SiC nanostructures are favorable candidate in biology and medicine as well, due to their excellent biocompatibility, especially blood compatibility, low density and high rigidity [117].

4.3.1 Synthesis

To achieve the technological applications, significant progress in 3C-SiC nanowires synthesis was attained by various growth techniques. The growth of 3C-SiC whiskers/nanowires/nanorods were reported in literature using different approaches. The synthesis methods that have been used to synthesize SiC nanowires can be broadly classified into following categories: (i) carbothermal reduction of silica [118, 119]; (ii) decomposition of organic silicon compounds/polymers [120]; (iii) reaction between silicon halides and CCl_4 [121] (iv) reacting carbon nanoclusters with SiO at elevated temperature [122, 123]; (v) metal catalyst reduction of silicon powder [124, 125]; (vi) High temperature catalytical reaction of SiC powder [126]; (vii) chemical vapor deposition (CVD) with the aid of catalysts through the vapor–liquid–solid (VLS) mechanism [127, 128]; (viii) CVD process hydrogen reduction of methyltrichlorosilane (CH_3SiCl_3) [129, 130]. Table 1 summarizes the growth of 3C-SiC nanostructures using different methods reported in literatures.

Method	**Experimental conditions**	**Grown SiC nanostructures: Highlights of work**	**Ref.**
CVD	Single crystal Si wafers (n-type), detonation soot precursor	β-SiC (1D) nanostructures VLS: Morphology can be tuned during 2h reaction time from NWs (1250°C), hexagonal columns (1300°C), nanopyramids (1350°C)	Sun et al 2010 [131]
Chemical Vapour Reaction (CVR)	Si+ SiO_2 powder with Si and graphite substrates, Ni catalyst (few), CH_4 flow, Ar, 1250°C kept at 10-20 min	Felted, curly and straight β-SiC NWs: FE properties strongly depend on their morphologies was elucidated.	Li ZJ et al 2010 [132]
Chemical Vapour Reaction (CVR)	anodic nanoporous anodic aluminium oxide template, graphite reaction cell,Si,SiO_2 powder ball milled 48h,C_3H_6 flow 3-5 min at 1230°C	β-SiC NWs highly oriented solid-solid reaction: uniformly distributed, highly oriented NWs are in agreement with nanopore diameter of employed AAO template.	Li ZJ et al 2006 [133]
CVD	catalyst nanoparticles (Fe–Ni/Si–SiO_2) Template: carbon nanotube (CNT)/Si–SiO_2 (CNT on Si–SiO_2 core–shell substrates), 1300°C, 15 min, Ar	SiC NWs VLS: The growth mechanism of the SiC NWs is proposed to be the combination of the chemical vapor deposition (CVD) method and the CNTs confined reaction method. Both CNT and SiC NWs synthesized together.	Chiu and Li 2009 [134]
Hot filament CVD	Solid carbon, Si source on Si (100) substrate, metal catalyst, H_2, metallic catalyst particles.	β-SiC nanorods VLS: Hydrogen in reaction chamber react with solid plate to produce hydrocarbon and hydrosilicon radicals form nanorods with crystalline β -SiC core and amorphous silicon oxide shell layer.	Zhou et al 1999 [135]
CVD	graphite coated with C fiber thermo-insulating layer, SiO,	β-SiC nanoarchitectures: FE showed turn-on field of ~12 V/µm,. Two growth mechanisms proposed, (1) formation of inner 1D core	Shen et al 2007 [136]

	Ga_2O_3, graphite powder, Ar, 1350°C,1h	structures and then epitaxial growth secondary branches, (2) self-assembly of nano building blocks, such as platelets, into hierarchical structures.	
CVD	Si, SiO_2 powder, CH_4,1350°C, 30min, Ar	β-SiC NWs with fins: diameter of fins ~100–120 nm, inner core stems ~60–70 nm, two-step epitaxial growth process through CVR was proposed, (1)fast formation of inner 1D core stem owing to high temp(1350°C),(2)epitaxial growth of fins under lower temp(800–1350°C) during cooling process.	Guo JZ et al 2007 [137]
CVD	carbon tetrachloride, Si substrate, nickel catalyst, N_2, 1273K, 30 min	3C-SiC NWs: NWs diameter of about 50 nm and length of 10 μm, CL-broad optical emission centred at about 2 eV	Attolini et al 2009 [138]
Thermal CVD	Si(111) nanoporous pillar array substrate, Ni catalyst, 1100°C	3C-SiC NWs,SiC-SiO_2 core-shell fibers: Two broad photoluminescence peaks located at 409 and 494 nm	Wang HY et al 2013 [139]
Thermal evaporation	ZnS powders covered with pieces of silicon wafers in a ceramic boat, Ar, 1100°C, 2h	SiC NWs aligned arrays- vapor-solid: vapor-solid reaction of carbon oxide and silicon powders, solid carbon materials were stuck on the surface of tube by sintering at a high temperature	Niu and Wang 2009, Niu and Wang 2007 [140, 141]
Thermal evaporation	SiO+C+GaN powders, Ar, 1350°C, 1h	β-SiC bamboo-like NWs- VLS: SiC NWs composed of hexagonal stems decorated with larger diameter knots along their whole length with <111> growth direction, stems are defect-free while knot-part has high-density stacking faults, FE-turn-on field of about 10.1 Vμm^{-1}	Shen et al 2006 [142]
Thermal evaporation	SiC powder, iron powder (as catalyst), 1700°C, 1h, Ar	3C-SiC NWs needle shaped-VLS: A strong broad photoluminescence peak located around 450 nm was observed at RT ascribed to quantum size effects of nanomaterials	Feng et al 2003 [143]
Thermal evaporation	Polyacrylonitrile (PAN) carbon fibers, Si, 1200°C, 60 min	3C-SiC NWs needle shaped vapor-solid: SiC nanoneedles have tapered and smooth surface, dia ranges from 30 to 70 nm and root dia ranges from 150 to 200 nm, A strong photoluminescence peak located around 468 nm was observed at RT	Chen et al 2008 [144]
Sol-gel carbothermal reduction	C/SiO_2 xerogel, carbon black, 5h, Ar	β-SiC-vapor-solid: Smooth NWs (1500°C), hierarchial nanodihes (1550°C), short nanorods (1600°C)	Xin et al 2012 [145]
Sol-gel carbothermal reduction	sol-gel derived silica (xerogel) containing carbon nanoparticles,	β-SiC NWs with SiO_2 wrappers, dia 10-25 nm: Large quantities of Sic nuclei and nanometer-sized Sic nucleus sites on carbon	Meng et al 1999 [146]

	Ar, 1650°C, 1.5h, 1800°C, 30 min	nanoparticles result in nanometer-diameter β-SiC wires.	
Bamboo-based carbothermal	bamboo powders, amorphous SiO_2, 1000-1350°C, 1-3h, Ar	SiC and other carbide NWs, VLS: natural nanoporous bamboo as carbon source and template for formation of catalyst particles, Synthesis process is nontoxic without producing hazardous waste, cost-effective	Tao et al 2011 [147]
Sol-gel carbothermal reduction	carbonaceous erogel,1300°C, Ar, 5h, CTAB and lanthanum nitrates as additives	SiC beaded nanochains: Nanochains have an unusual reinforcing effect due to the mechanical interlocking between beads, which can enhance interfacial adhesion between filler and matrix	Hao et al 2006 [148]
Carbothermal reduction	carbanaceous silica xerogel, Pd/SiC catalyst	Nanoditches from twinned SiC NWs for Pd NPs: produced different-size nanoditches on SiC NW surface by adjusting etching conditions, assembled Pd NPs into nanoditches to obtain nanostructured Pd/SiC catalyst	Guo XN et al 2010 [149]
Combustion synthesis	Si-containing compounds, halocarbons	β-SiC nanostructures, nanofibers, nanotubes: Advantages of combustion synthesis include simple, fast and unique one-pot process without need for catalyst or template, is low-cost, and has high yield, and starting reactants.	Huczko et al 2005 [150]
Catalyst assisted pyrolysis	Polyaluminasilazane precursor, graphic papers as substrates over alumina crucible, pyrolysis at 1400 °C for 30 min, Ar	3C- SiC nanoneedles: polyureamethylvinylsilazane and aluminuim isopropoxide with weight ratio 16:1 mixed by ball milling for 12h,obtained polyaluminasilazane solidified at 260°C for 30 min under Ar and then ball-milled to powders	Wei G et al 2011 [151]
Catalyst-assisted pyrolysis	polymeric precursors polyaluminasilazane with $FeCl_2$ catalyst, 1450 °C, 2h	Al-doped 6H-SiC NWs, SLS mechanism: precursors were obtained by reaction of polyureamethylvinylsilazane and aluminum isopropoxide. Al dopants caused red-shifts of the PL bands.	Gao et al 2008 [152]
Catalyst-assisted pyrolysis	polysilazane polymeric precursor, with/without $FeCl_2$ catalyst, 1700°C, 2h	β -SiC nanorods SLS mechanism: solution–precipitation interaction with Si–Fe–C liquid alloy and SLS mechanism	Yang et al 2004 [153]
Polymer Pyrolysis	SiC substrate polysilazane source, $Fe(NO_3)_3$, 1550°C, Ar	SiC NWs Eiffel tower, spindle shaped, VLS growth: New technique to manipulate and control the morphology of VLS grown SiC NWs by varying pressure of source species. Eiffeltower, spindle and modulated nanowires have been synthesized	Wang HT et al 2008 [154]
Polymer Pyrolysis	6H-SiC (0001), (1010),(1120) substrates, polysilazane, $Fe(NO_3)_3$, 1350°C, 0.5-2h, Ar	SiC NWs: Impacts of substrate orientation on growth habits of NWs investigated,	Wang HT et al 2010 [155]

High-frequency induction heating	SiO, activated carbon without metal catalyst, 1450 °C, 15min, Ar, 50-100 Torr	β-SiC NWs-V-S growth: 2 g of commercial SiO powder was put into graphite crucible, light blue product was successfully deposited on large-scale on the activated carbon fibers surfaces. The 1-D nano-coaxial-cable and in situ formed 2-D novel nano-network display huge potential applications as reinforcements in next generation tough ceramic matrix composites and as building blocks in nanodevices.	Zhou et al 2006 [156]
Microwave method	Xerogel, 0 to 800 W power, Nano Al powders, 30 min, Ar	Al doped6H-SiC NWs VLS: because of strain existing in the growth process of the nanowires, the nanowires could form twinning structures and periodical stacking faults, which made the nanowires exhibit different Raman properties, PL and chemical stability	Wei GD et al 2008 [157]
Arc-discharge	SiO powder, CNT, Ar, 1400°C, 2 h	Aligned SiC NWs: The reaction was carried out in a conventional furnace with a horizontal alumina tube. Solid SiO powder placed in a graphite crucible was covered with a molybdenum grid. Carbon nanotube arrays that had been stripped off the substrates were placed on the molybdenum grid. The crucible was covered with a graphite lid, placed in the hot zone inside the alumina tube, Ar atmosphere at 1400°C for 2 h. It was expected that SiO gas evaporating from the solid SiO powder would flow towards the region of carbon nanotubes and react with the aligned nanotubes.	Pan et al 2000 [158]
Arc-discharge	Silicon carbide rod (anode), graphite plate (cathode), He	6H-SiC cone shaped, hexagonal nanorods, VLS: Formation of gradually enlarged Fe–Al–Si–C droplets and their high enthalpy have led to the growth of cone-shaped hexagonal structure SiC nanorods by a VLS mechanism	Li YB et al 2002 [159]
Arc-discharge	SiO_2 or silicon powder as silicon source, graphite powder as carbon source, He	β-SiC NWs-Catalyst free, V-S growth: oxygen plays a key role in the growth process and suggest that growth mechanism of SiC nanowires is a catalyst-free vapor-solid (VS) mechanism. PL measurements-material emits blue-green light with a peak wavelength of 472 nm	Chiu et al 2007 [160]
Reactive laser ablation	compressed powder of BN, C, SiO, and Li_3N	Multi element nanotubes B-C-N nanotube: β -phase silicon carbide core, an amorphous silicon oxide intermediate layer, and graphitic outer shells made of boron nitride and carbon layers separated in the radial direction. coaxial nanocable suggests applications in nanoscale electronic devices	Zhang et al 1998 [161]

Laser ablation	SiC target, graphite substrate, iron nitrate, Ar, 2h 900°C	SiC NWs VLS: wires contained a high density of stacking faults and were wrapped by thin silicon oxide layers (~17 nm) Growth mechanism was VLS as nanosized iron particles acted as catalysts at the tip of each SiC NW	Shi et al 2000 [162]
Low-temp Solvothermal route	$SiCl_4$, CaC_2, 180°C, 36h, Ar, autoclave	2H-SiC nanoflakes, VS: nanoflakes dia of 200–500 nm, thickness of 15 nm, grow along [001] direction exhibit new PL peak at 314 nm, ascribed to defects in SiO_x	Zou et al 2006 [163]
Autoclave route	$SiCl_4$, $(C_5H_5)_2Fe$, metallic Na, 500°C, 10h	3C-SiC NWs-may be VLS: Electron microscopy show that NWs diameters of 15–50 nm, lengths up to several tens of micrometers and grow along [111] direction.	Ju et al 2007 [164]
Lithium assisted synthesis autoclave	CH_3CH_2OH, $SiCl_4$, Li, autoclave, 600°C, 10 h	3C-SiC nanobelts: Electron microscopy-nanobelts are 50-200 nm wide, 20-60 nm thick, and up to tens of micrometers long	Xi et al 2004 [165]
Autoclave	poly(ethylene terephthalate) PET waste with carbon, SiO_2 microspheres in CO_2, 650°C, 3h	3C-SiC NWs: NWs are tens of microns in length and 30–150 nm in diameter, reaction forming NWs take place in inner of carbon microspheres generated from PET	Gao et al 2013 [166]
Direct synthesis without catalyst	silicon monoxide, methane, Ar, 1300°C, 4 h	2H-SiC nanowhiskers-oxide assisted growth: Diameter range from several ten to several hundred nanometers. 2H–SiC nanowhiskers had 3C polytype tip. Lots of stacking faults and micro-twins present.	Yao et al 2003 [167]
Electrochemical etching	bulk 3C-SiC substrates	3C-SiC nanoparticles (NPs): Influence of different interfacial chemical environments-surface chemistry, solvent nature, and surface charges on photo induced absorption and luminescence of NPs at RT is described	Zakharko et al 2010 [168]

Table 1. Growth of 3C-SiC nanostructures using different methods

From the knowledge of the methods already reported in the literature as tabulated above, one can know that chemical vapor deposition (CVD) process is a widely used technique and has a potential to produce SiC nanostructures. The CVD with the aid of catalysts through the VLS growth mechanism offer the advantages of a precise control over morphology and deposition chemistry of reaction and it can deal with most of the problems associated with SiC nanowires growth. Let us discuss in brief the role of VLS mechanism during the growth of SiC nanowires.

The significance of 3C–SiC NW growth based on the vapour–liquid–solid (VLS) mechanism was well explained by Zekentes and Rogdakis [172] and the highlights are detailed in this section. The growth of SiC NWs having small-diameter which followed the VLS mechanism was first reported by means of hot filament chemical vapour deposition (HFCVD) reaction in the presence of ambient atomic hydrogen. The studies of Zhou et al [135] showed the VLS growth of SiC NWs with Si and C as solid sources by HFCVD system. Briefly, metallic particles of impurities from the solid source were used as catalyst. The resultant gaseous hydrocarbon radicals, hydrosilicon radicals or organosilicon molecules were formed by the atomic hydrogen resulting from etching of solid plate source. The dissociation process of Si and C atoms occurs at the time of arrival of these vapour molecules to attain vapour–liquid surface. Further, the liquid catalyst was produced when these atoms were dissolved and solid SiC precipitation onto the Si substrate was induced during supersaturation. The growth of NW happens together with the lifting of catalyst particle from substrate as precipitation continued. The NWs grown [135] were 10–30 nm in diameter and less than 1 µm in length having a crystalline 3C–SiC core with an amorphous silicon oxide shell layer. It was confirmed from high resolution transmission electron microscopy (HRTEM) measurements that the reported NWs grew along [1 0 0] direction.

According to previous studies, the [1 0 0] oriented SiC NWs formation could be better understood from the relatively low diameter of NWs. In the case of SiC, larger diameter results in [1 1 1] oriented NWs and the smaller diameter will leads to the growth of [1 0 0] oriented NWs as reported in the literature for Si [169]. It is well known that the growth of NWs is most favorable in the crystal direction which minimizes the total free energy. Generally, the surface free energy of the interface between the semiconductor and the metal catalyst dominated the growth. As reported in diamond and zinc-blende crystals [170], at the lowest-energy (1 1 1) plane, interface between semiconductor and catalyst frequently forms a single surface. Hence, in major growth conditions the growth of NWs will be in [1 1 1] direction. There are few reports related to the other low-index growth directions which includes [0 0 1], [1 1 0] and [1 1 2] influenced by the NW diameter. An excellent review on the control of NW orientation is given in [169]. Additionally, VLS was the mechanism used for the preparation of large areas of centimeter-long SiC nanowires by means of pyrolysis of polymer precursor using ferrocene catalyst [171]. Although VLS growth offers high NW growth rate, there are many factors which play significant role in the properties of NWs such as crystalline, phase, density, composition, presence of planar defects and occurrence of dislocations along NW direction. Those factors include the control in diameter and length of NWs, growth location of NWs, possibility of in-situ doping, presence of catalyst. There is almost no experimental study reported in the literature based on defect free i.e. without any planar defects or at least with a very low density in synthesis of single crystalline 3C–SiC NWs. Therefore it is essential to concentrate the growth of 3C-SiC nanowires for device fabrications.

In the present work, 3C-SiC nanowires were successfully grown using home-made induction heated Vapor Phase Epitaxy (VPE) reactor using silane and propane as precursor through VLS growth mechanism on Si (100) and Si (111) substrate using nickel (Ni) and iron (Fe) as a catalysts. The main aim of this work is to optimize the condition to grow SiC nanowires with Ni and Fe catalyst. The size and shape of the nanowires has been controlled using temperature and gas flow rate. The as grown samples were subjected to morphology and structural characterization.

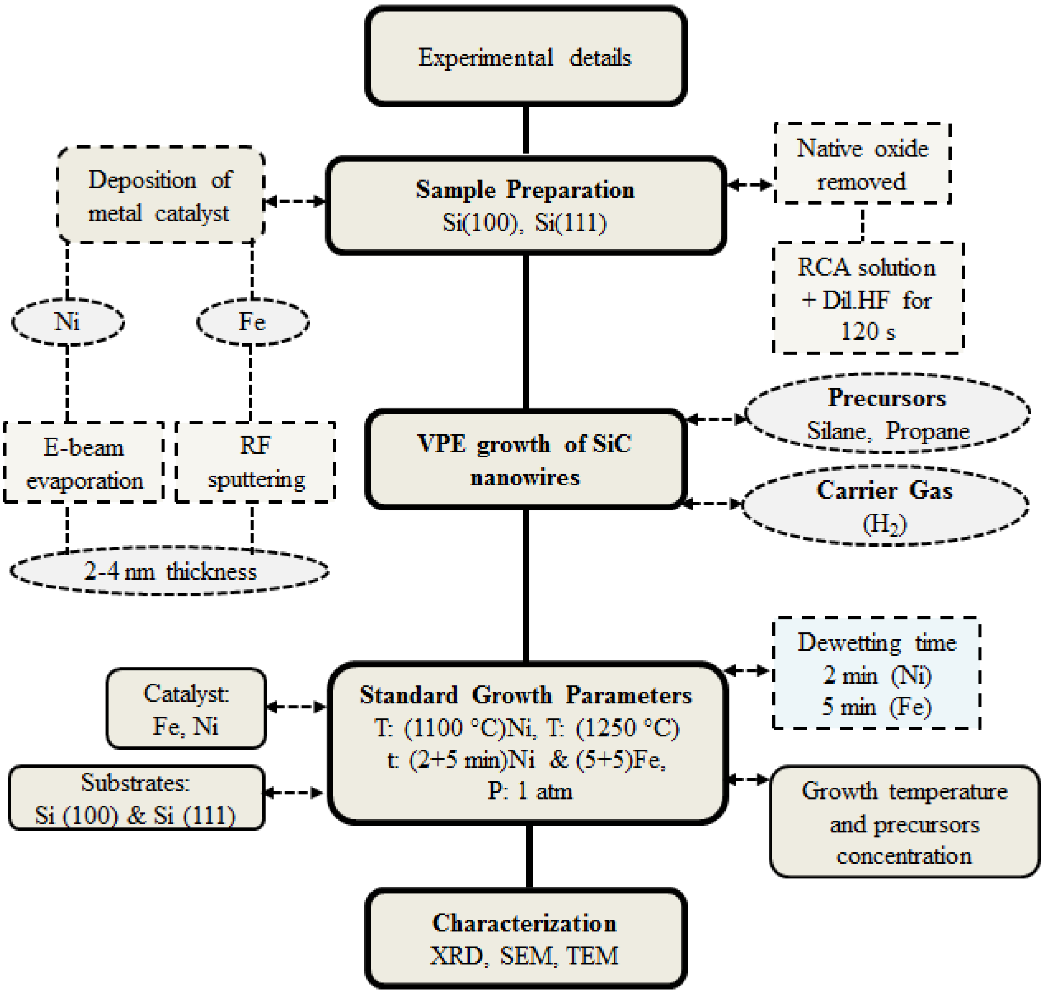

Figure 30. Flowchart of experimental scheme.

3C-SiC nanowires have been grown using home-made laboratory scale VPE reactor. The experimental details are shown in the flowchart given in Figure 30.

The substrates used for growth were Si (100) and Si (111) with Ni and Fe catalysts. The native oxide and some other metal contaminant presents on the silicon substrates were removed using standard RCA cleaning [188, 189] prior to deposition of metal catalyst such as Ni and Fe.

Sample	**Growth temperature (°C)**	**Dewetting temperature (°C)**	**Dewetting time (min)**	**Growth time (min)**
Si(100) substrate; Ni catalyst; Precursors and carrier gas (flow rate in ml/min): Silane (20), Propane (12) and Hydrogen (1000); Pressure: 1bar				
SiC-1	1000	1100	2	5
SiC-2	1050	1100	2	5
SiC-3	**1100**	**1100**	**2**	**5**
SiC-4	1150	1100	2	5
SiC-5	1200	1100	2	5
Si(111) substrate; Ni catalyst; Precursors and carrier gas (flow rate in ml/min): Silane (20), Propane (12) and Hydrogen (1000); Pressure: 1bar				
SiC-6	1100	1100	2	5
Si(100) substrate; Fe catalyst; Precursors and carrier gas (flow rate in ml/min): Silane (**20**), Propane (**12**) and Hydrogen (1000); Pressure: 1bar				
SiC-7	**1250**	**1250**	**5**	**5**
Si(100) substrate; Fe catalyst; Precursors and carrier gas (flow rate in ml/min): Silane (**30**), Propane (**18**) and Hydrogen (1000); Pressure: 1bar				
SiC-8	1250	1250	5	5
Si(100) substrate; Fe catalyst; Precursors and carrier gas (flow rate in ml/min): Silane (**40**), Propane (**24**) and Hydrogen (1000); Pressure: 1bar				
SiC-9	1250	1250	5	5
Si(**111**) substrate; Fe catalyst; Precursors and carrier gas (flow rate in ml/min): Silane (20), Propane (12) and Hydrogen (1000); Pressure: 1bar				
SiC-10	1250	1250	5	5

Table 2. Experimental conditions for growth of 3C-SiC nanowires using VPE.

There were generally three main steps in RCA cleaning, a Standard Clean 1 bath (SC1), a Hydrofluoric Acid (HF) dip, and a Standard Clean II bath (SC2). The first step called SC-1, Standard Clean is performed with a 1:1:5 solution of NH_4OH (ammonium hydroxide) + H_2O_2 (hydrogen peroxide) + H_2O (water) at 75 or 80 °C [107] typically for 10 minutes.

This treatment results in the formation of a thin solid dioxide layer (about 10 Å) on the silicon surface, along with a certain degree of metallic contamination (Iron) that shall be removed in subsequent steps. This was followed by transferring the wafers into a DI water bath. The second step was a short immersion in a solution of 1:50 HF + H_2O at 25 °C in order to remove thin silicon dioxide layer and some fraction of ionic contamination. The third and last step was performed with a solution of 1:1:6 solution of $HCl+H_2O_2+H_2O$ at 75 to 80 °C. This treatment effectively remove the remaining traces of metallic (ionic) contaminants. The substrates were etched with diluted HF solution for 2 min after the RCA cleaning prior to metal catalyst deposition. The Ni and Fe catalyst were deposited using E-beam evaporation and RF-sputtering technique. The thickness of the Ni and Fe catalyst deposition was 4 nm and 2 nm respectively and was kept in the vacuum chamber till used in the VPE reactor for the nanostructure growth in order to prevent surface oxidation.

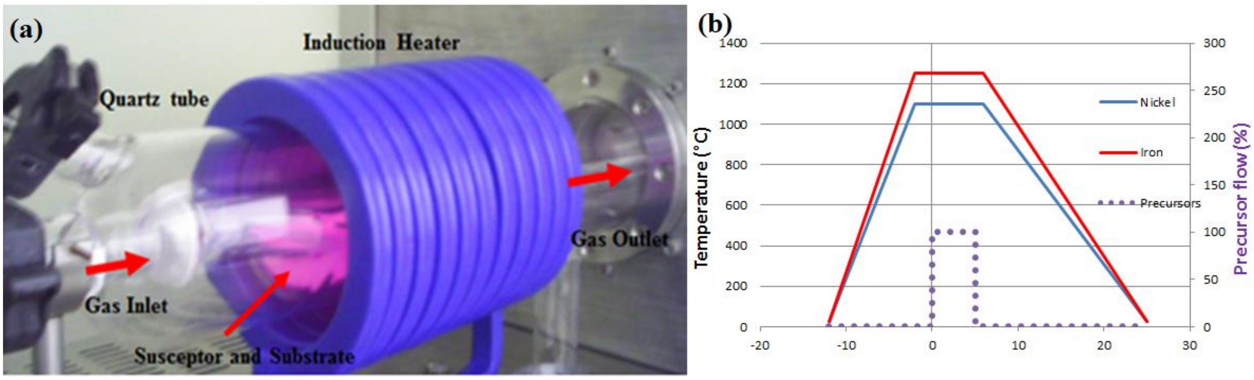

Figure 31. Experimental apparatus and experiment details for the growth of SiC nanowires.

The metal deposited substrates were loaded in the VPE reactor for growth of SiC nanowires. The experimental setup of reactor is composed of (i) quartz tube which allows graphite susceptor insertion to support the substrates, (ii) inlet and outlet for carrier and precursor gases, (iii) the inductive type heating system can stabilize the temperature constantly at maximum of

1400 °C as shown in Figure 31. In other words, the substrate was loaded on graphite susceptor heated with an induction system and placed in the horizontal quartz tube of the epitaxial system.

Silane and propane were used as precursors to obtain SiC nanowires and both precursor (3%) were diluted in hydrogen which acts as carrier gas. The growth processes follow two major steps: formation of catalytic droplet clusters on silicon substrate in hydrogen atmosphere also called “dewetting”, followed by the growth of SiC nanowires with regulated flows of precursors. All the growths were performed at atmospheric pressure with optimized C/Si ratio used as 1.6. The detailed growth conditions of the samples were given in Table 2. After the growth was completed, the precursor flow was stopped and the sample was allowed to cool down in hydrogen atmosphere. The as-grown samples were collected for further characterization.

The morphology of the as-grown SiC nanowires was characterized by Field Emission Gun Scanning Electron Microscopy (FEG-SEM). The structural analysis of single nanowires was performed using Transmission Electron Microscopy (TEM) (Jeol – JEM 2200 FS) for High – Resolution (HR-TEM) studies. High Angle Dark Field imaging in Scanning mode (HAADF-STEM) and the SAD patterns were proved to be useful for detailing the nanowires structure.

4.3.2 Characterization

Silicon carbide (SiC) nanowires have been grown using Vapor phase epitaxy (VPE) reactor that was previously used by our group [173] to obtain SiC layers at atmospheric pressure using silane and propane precursors mixed with hydrogen gas. Almost, the same procedure have been followed to grow the SiC nanowires. The precursors were flowed on the heated susceptor in which the chemical pyrolysis takes place. Subsequently, (i) in the presence of hydrogen, decomposition of propane occurs to yield methane (CH_4) and (ii) silane decomposes to give SiH_2 and Si_2H_2 species. These chemical species were responsible of the growth of the final product of SiC [174]. Two different catalyst such as nickel and iron were used to assist the growth and can be discussed below in detail.

4.3.2.1 Nickel assisted 3C-SiC nanowires

The growth procedure for SiC nanowires followed in the present study consists of three major steps which are almost similar argument of classical VLS mechanism as described in the Figure 32.

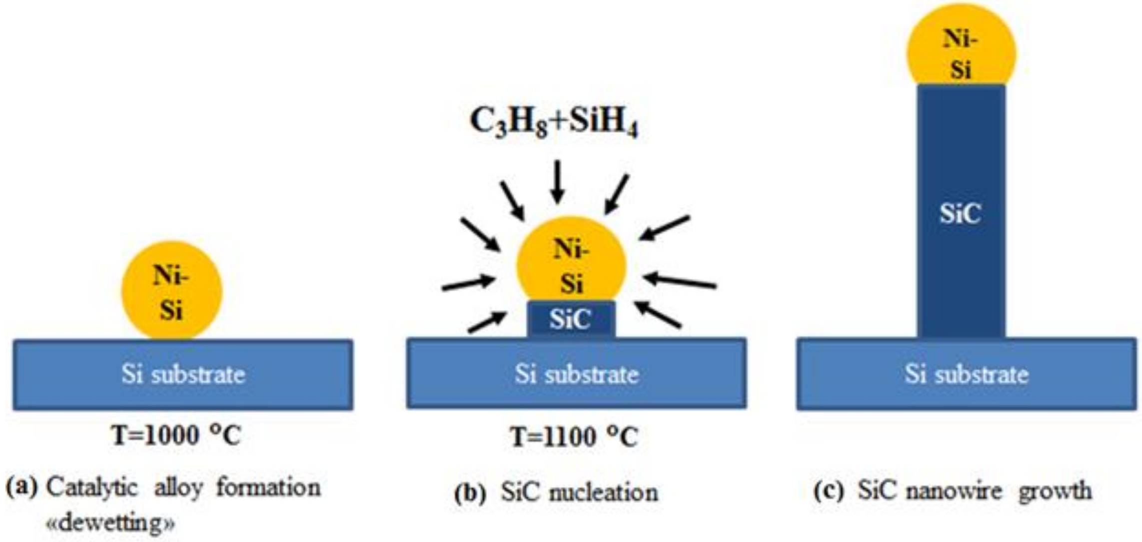

Figure 32. Illustration of growth mechanism of SiC nanowires.

1. Formation Ni-Si alloy droplets: This step can also be called as dewetting. The nickel coated Si substrate have been rapidly heated to 1100 °C in hydrogen atmosphere leads to the formation of Ni-Si alloy droplets. This is due to the eutectic phase of Ni-Si system (966 °C) as given in Figure 33(a) [175]. Thus, we suppose that during the dewetting the thin Ni layer produces a Ni-Si alloy with a composition of about 50 % at the Si substrate surface. The catalytic alloy droplets were formed uniformly on the substrate as shown in the Figure 33(b). The size of the Ni-Si alloy droplets were found to be in the range of 50 to 500 nm.

2. SiC nucleation: In this step, growth temperature was increased following the dewetting. Once the desired growth temperature was reached, the precursors were introduced. The precursors decompose to give gaseous chemical species of CH_4, SiH_2/Si_2H_2 as described above and it gets adsorbed and dissolved in the Ni-Si alloy liquid droplets. SiC nucleation occurs and it precipitates at bottom of the liquid alloy droplets due to the supersaturation of gaseous species into it.

3. SiC nanowire growth: After the SiC nucleation, again the liquid droplet start to adsorb gaseous species from the vapor and it supersaturate to form solid SiC and it continues to grow along one direction.

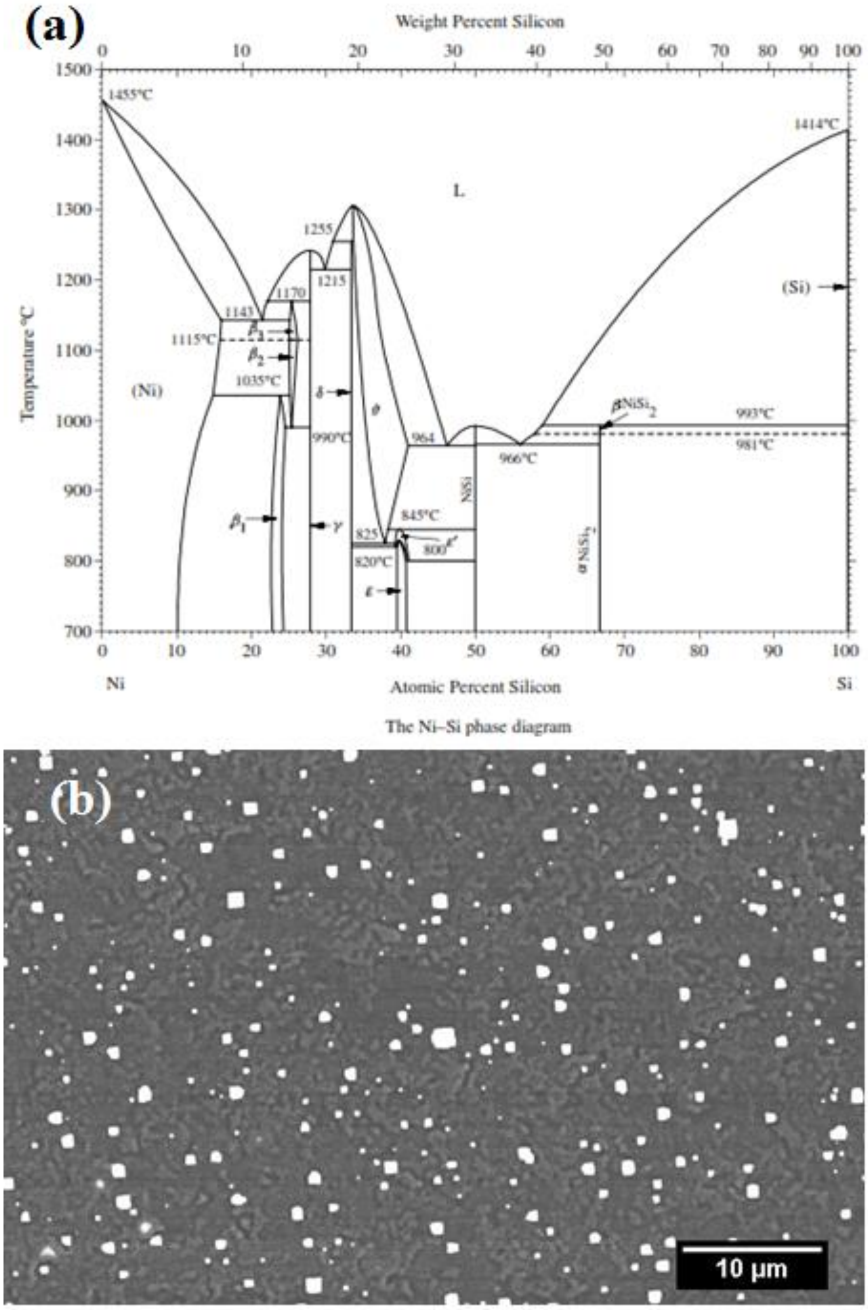

Figure 33. (a) Phase diagram of Ni-Si system [175]; (b) SEM image of Ni-Si dewetting at 1000 °C.

Several experiments have been done by varying the different growth parameters to optimize the standard condition for better SiC nanowires having smooth surface, high aspect ratio, less defects along nanowires, etc. The optimized condition for the growth of SiC nanowires using Ni as catalyst are given as follows (sample SiC-3):

Substrate: Si (100),

Precursors and carrier gas flow rate:

  Silane: 20 ml/min,

  Propane 12 ml/min and

  Hydrogen 1000 ml/min,

Growth Pressure: 1 bar,

Dewetting time: 2 min.,

Growth time: 5 min and

Growth temperature: 1100 ° C.

The crystalline structure of samples grown with optimized condition was analyzed by X-ray diffraction as shown in Figure 34(a). All the strong diffraction peaks can be indexed in the 3C-SiC structure. 3C-SiC characteristic peaks at $2\theta = 35.6°$ (111), 41.4° (200), 59.9° (220), and 89.9° (004) were detected. These results point out that the 1D growth occurs in the zinc-blende phase, with no evidence of extended hexagonal phases.

Figure 34(b) shows a SEM image of the as-grown silicon carbide nanowires (sample SiC-3) at optimized conditions. It confirm the growth of nanowires over the nickel covered area and revealing high-yield nanowire growth with high density of nanowires over large area. The morphology revealed that surface was covered by a number of wires of tapered shape and tends to be straight or curved gradually. The observed wires had circular section with a conical shape. The length of the nanowires were of the order of tens of microns with their base diameter of about 60-130 nm, and the diameter was smaller at the tip over which a small sphere was observed. The average diameter of the nanowires were 70 nm.

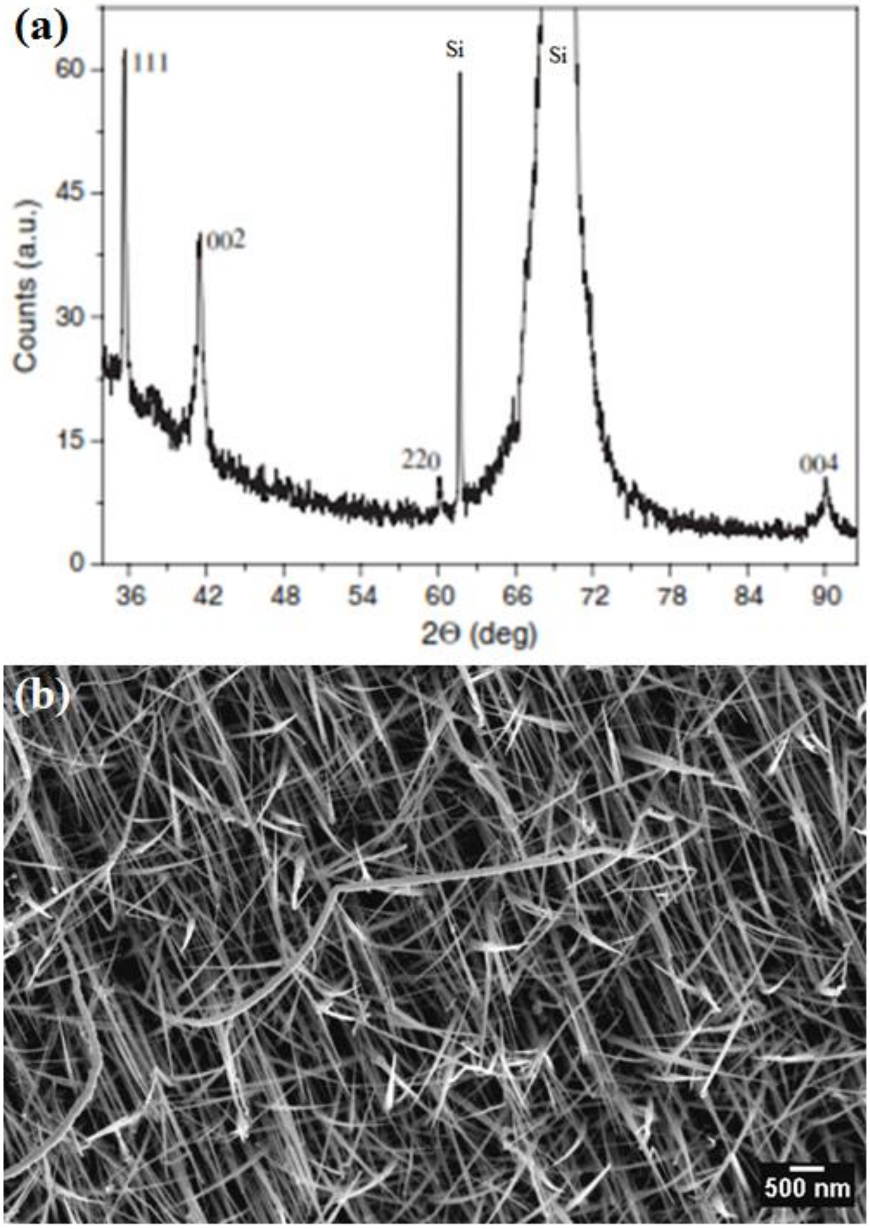

Figure 34. (a) XRD and (b) SEM image of SiC nanowires with Ni catalyst (sample SiC-3).

Figure 35 shows the TEM analysis of the single SiC nanowire grown at optimized condition. It is clearly seen that the surface of SiC nanowires were smooth and clear. Figure 35 (b), (c) shows the HRTEM images of different segment along the nanowires in [110] zone axis. The smooth part of the nanowire (Figure 35 (b)) shows small defect density and some parts with rough surface indicates the presence of planar defects along the growth direction and perpendicular to nanowire axis.

Fast Fourier Transform (FFT) image as shown in Figure 35(d), the clear diffraction spots indicates that the nanowires are single 3C-SiC crystal with <111> growth direction. Certainly, planar defects mainly stacking faults (SFs) and twins were visible in some segments along the nanowires which are common in bulk SiC due to the polymorphism of this material and they can be viewed as nanoscale polytype inclusions within the pure 3C–SiC phase. Note that the 3C– SiC has a negative SF energy (the only material with ZnS presenting negative SF energy) and it is very easy to generate SFs in 3C–SiC even under the thermal stress created by the electron beam in the TEM. The diameter of the defect zone in nanowire is quite larger than that of the defect free zones and it is giving a faceted shape in the NW surface with each facet belonging to a SF section. The large diameter of the defected zones is quite probably due to the strain relaxation in these SFs areas [176, 177]. In the extreme case the defected zones are looking like periodic along the NW axis giving a bamboo-like shape to the SiC NWs.

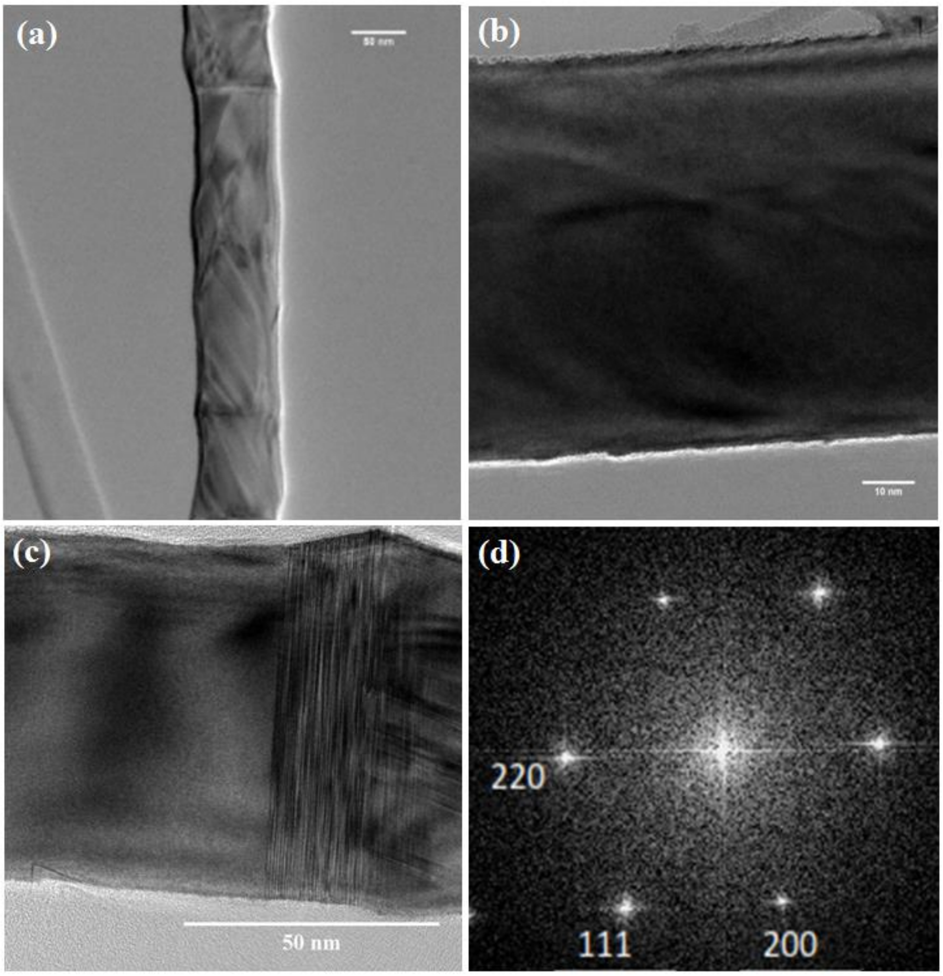

Figure 35. TEM images of Ni catalyst assisted SiC nanowires at optimized condition.

The experiment have been continued on Ni catalytic assisted Si (100) substrates at different temperatures above and below the optimized growth temperature of 1100 °C by maintaining all other growth parameters as before. The as-grown samples at different temperatures were studied and discussed below. The SEM image of the sample grown at the temperature of 1000 °C is shown in Figure 36(a). It was observed that there was no nucleation leading to the absence of the growth of SiC nanowires and this temperature did not favor the VLS growth.

The sample grown at 1050 °C exhibited a considerable growth of SiC nanowires (Figure 36(b)), comparably lesser in density than that obtained in the optimized growth conditions. The diameter of the nanowires widely varied from 30 to 100 nm and these values were lower than the optimized growth. From the TEM image given in Figure 36(c), the surface of the nanowires was seemed to be very rough and notably planar defects have been observed along every segments of the nanowires. Fast Fourier Transform (FFT) image is shown in Figure 36(c) (inserted right corner). However, the SiC NWs contain a large number of SFs and in some cases their density is enough to result in streaked diffraction spots [177]. Frequent observations of SFs along the SiC nanowires can be ascribed by two factors: the low energy of SF formation (34 erg cm^{-2} [178]) and the lower energy of the SF SiC 3C-polytype lattice as compared to that of the SF-free lattice [179, 180]. The presence of twins in the NWs can be accounted for by the polarity of the SiC structure [181]. The energy of the Si (111) facet differs from that of the C (111) facet. Although the energy difference is assumed to be small, it will produce stress and bending in the nanorods resulting from the surface tension. Introduction of twins compensates the difference in the surface energy caused by {111} surface polarity [182].

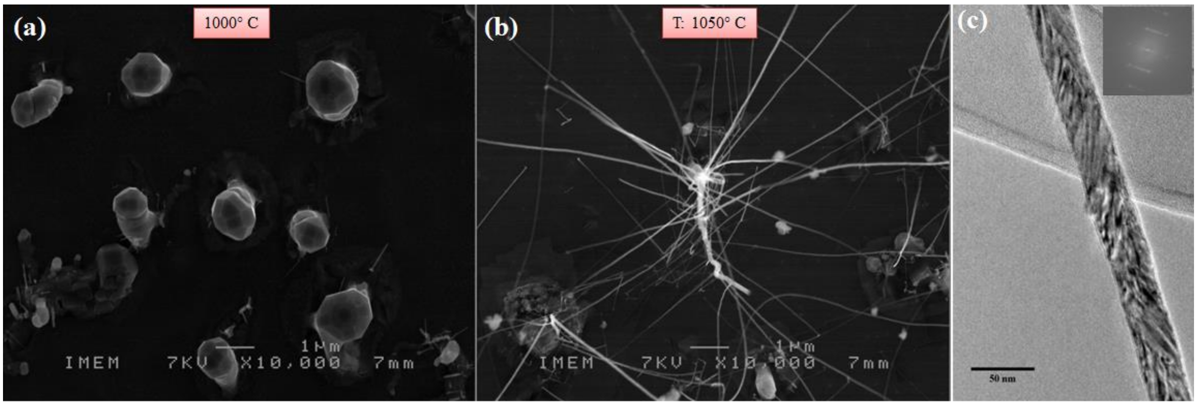

Figure 36. (a) SEM image of the sample prepared at 1000 °C (sample SiC-1), (b) & (c) SEM and TEM image of the sample prepared at 1050 °C (sample SiC-2).

Rod-like hexagonal shaped, cubic SiC nanostructures were observed at higher temperatures. Figure 37(a) shows the SEM image of the sample grown at 1150 °C. The observed nanoorods were thinner (50 nm) than standard sample (70 nm), rectilinear shape with the catalyst present on the head of the nanowire. Their density was similar to the optimized growth sample. From TEM images it could be observed the presence of planar defects perpendicular to the axis of the wire and some minority regions with different stacking fault oriented included in the more regular and the wire is much shorter and tapered at the base have an average diameter of 126 nm and length of a few microns. Same-like SiC nanostructure also have been observed for the sample grown at further higher temperatures. Figure 37(c) shows the SiC nanorods grown at 1200 °C. The side facets of hexagonal shape of SiC nanorods were very clear with increase in diameter compare to the sample grown at 1150 °C.

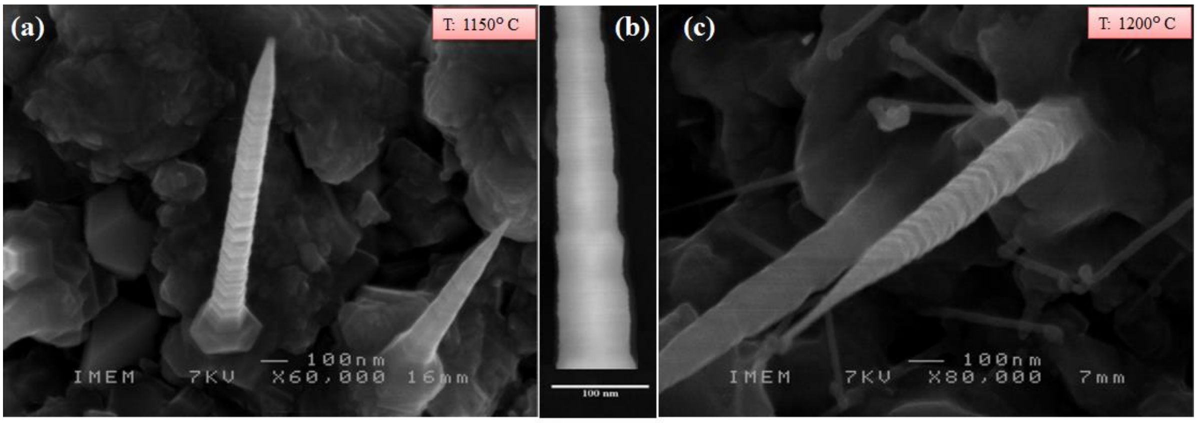

Figure 37. (a), (b) SEM and TEM image of the sample prepared at 1150 °C (sample SiC-4) and (c) SEM and TEM image of the sample prepared at 1200 °C (sample SiC-5).

At low temperature, (1050 °C, 1100 °C), the nuclei formation of SiC were a round disc shaped. At high temperature, however, (1150 °C, 1200 °C), because the kinetic condition for atom rearrangements was better satisfied, it became hexagonal, a shape with lower specific line energy. Also the density of SFs and twins throughout the nanowire length depends on the kinetic growth conditions. The most common morphological type of cubic SiC nanowire was a hexagonal shape with the [111] growth axis. Figure 38 shows atomic configurations of the unsaturated twinned SiC nanowires in a cubic crystal structure with nonparallel {111} side facets viewed from <110>, <112>, and <111> direction [183]. The wide surface of the hexagonal nuclei is a (111) plane, and the six peripheral planes are {110} since they have the lowest specific surface energy and the lowest specific line tension, respectively. The initial nuclear shape was determined the final nanowire morphology such as cylindrical shape and hexagonal shape respectively. It is well known that surface energy associated with different crystallographic planes is usually different as tabulated Table 3. For 3C-SiC, γ {111} < γ {200} < γ {211}. The final shape, the so-called equilibrium shape of the nanowires, should be determined by the lowest surface energy principle.

As was mentioned above, the hexagonal prisms nucleate and grow on the SiC crystallites with the [111] preferential growth direction and a high density of SFs and micro twins. The cross section of the crystallites gradually reduces and at some critical size the SiC nanowire starts to grow further [184].

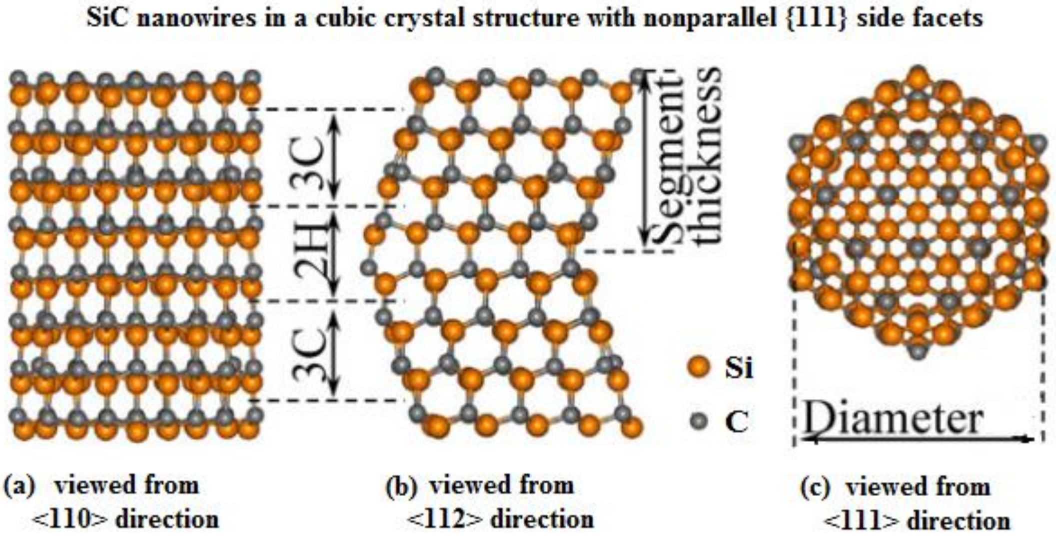

Figure 38. Atomic configurations of the unsaturated twinned SiC nanowires in a cubic crystal structure with nonparallel {111} side facets [183].

Crystallographic plane	**Surface energy (γ) at T=1373 K (= 1100° C) (erg · m^2)**
(111)	0,28
(220)	0,35
(211)	0,40

Table 4. Surface energy values of different SiC crystallographic planes [184, 187].

However, kinetic conditions may not be always satisfied so that metastable shape was often found. In this sense, the SiC nanowires obtained at low temperature of 1050 °C and 1100 °C can be regarded as two metastable phases, but the latter was more stable. From crystallography point of view, the rounded surface of the nanowires (Figure 35 and Figure 38) cannot be defined by crystallography, and it must have some atomic disorder over the rounded surface. However, it gives relatively low specific surface area, and is hence the first metastable shape of the nanowires.

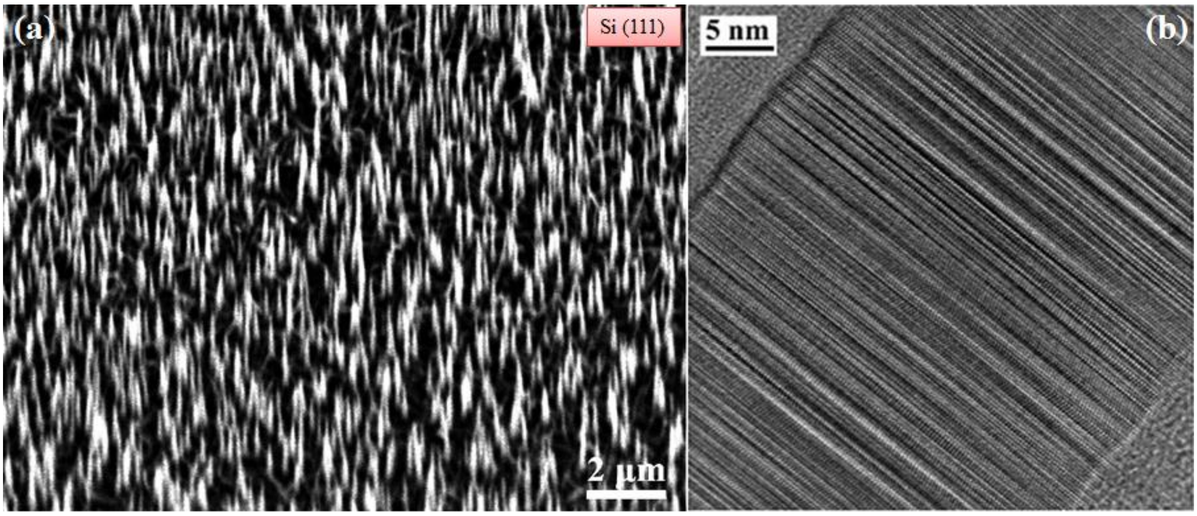

Figure 39. Ni-assisted SiC nanowires grown on Si (111) at optimized growth condition (sample SiC-6).

The use of Si (100) oriented substrates proved to be ineffective to achieve a selective alignment of the SiC nanowires. Consistently with the preferred <111> nanowire growth direction, this issue was addressed by performing growth runs on Si (111) oriented substrates. Vertically aligned, out-of-plane nanowire growth along the surface normal was demonstrated, as shown in the wide-scale side-view SEM image of Figure 39(a). Needle like oriented nanowires were observed over the substrate where the Ni catalysts presents. Also, it was observed the larger diameter of basal-central regions compared to the near-tip region. Figure 39(b) shows HRTEM images of oriented SiC nanowires, it can be observed that the occurrence of (111) stacking defects along the nanowire direction of <111> axis.

4.3.2.1 Iron assisted 3C-SiC nanowires

The growth conditions were stabilized for Ni assisted SiC nanowires. Our intention was to use these nanowires towards biomedical applications as SiC is biocompatible and hemocompatible [190]. The Ni catalyst creates some adverse effect in biocompatibility due to its carcinogenic nature. Hence it is better to avoid Ni catalyst and to use Iron (Fe) catalyst which could be a better option for biocompatibility [186]. In order to obtain Fe assisted SiC nanowires, it is necessary to optimize the growth conditions.

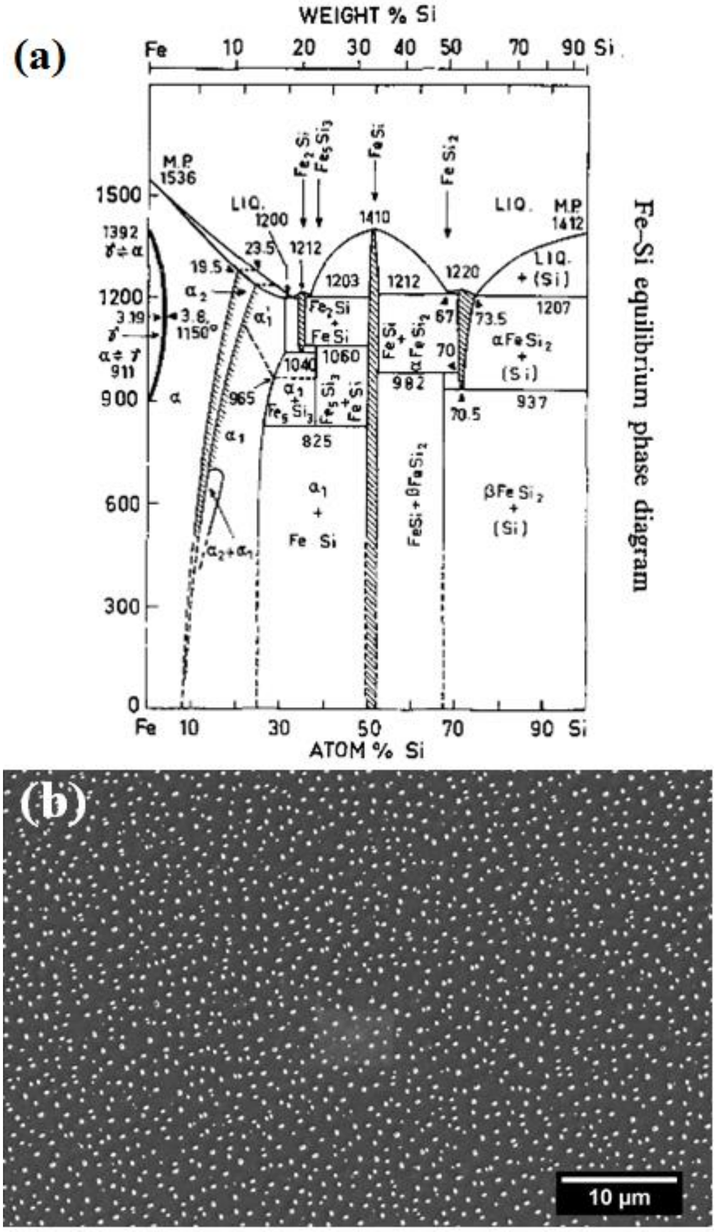

Figure 40. (a) Phase diagram of Fe-Si system [185] (b) SEM image of Fe-Si dewetting at 1250 °C.

During dewetting of the Fe assisted sample was quickly heated up to 1250 °C in presence of hydrogen to obtain many droplets uniformly distributed on the silicon surface, as shown in Figure 40(b). The droplets have a diameter approximately ranging from 100 to 300 nm and height of approximately 30 nm. The Fe-Si system has a eutectic phase at a temperature of 1203 °C [185]. Thus, we suppose that during the dewetting the thin Fe layer produces a Fe-Si alloy with a composition of about 20 % at the Si substrate surface.

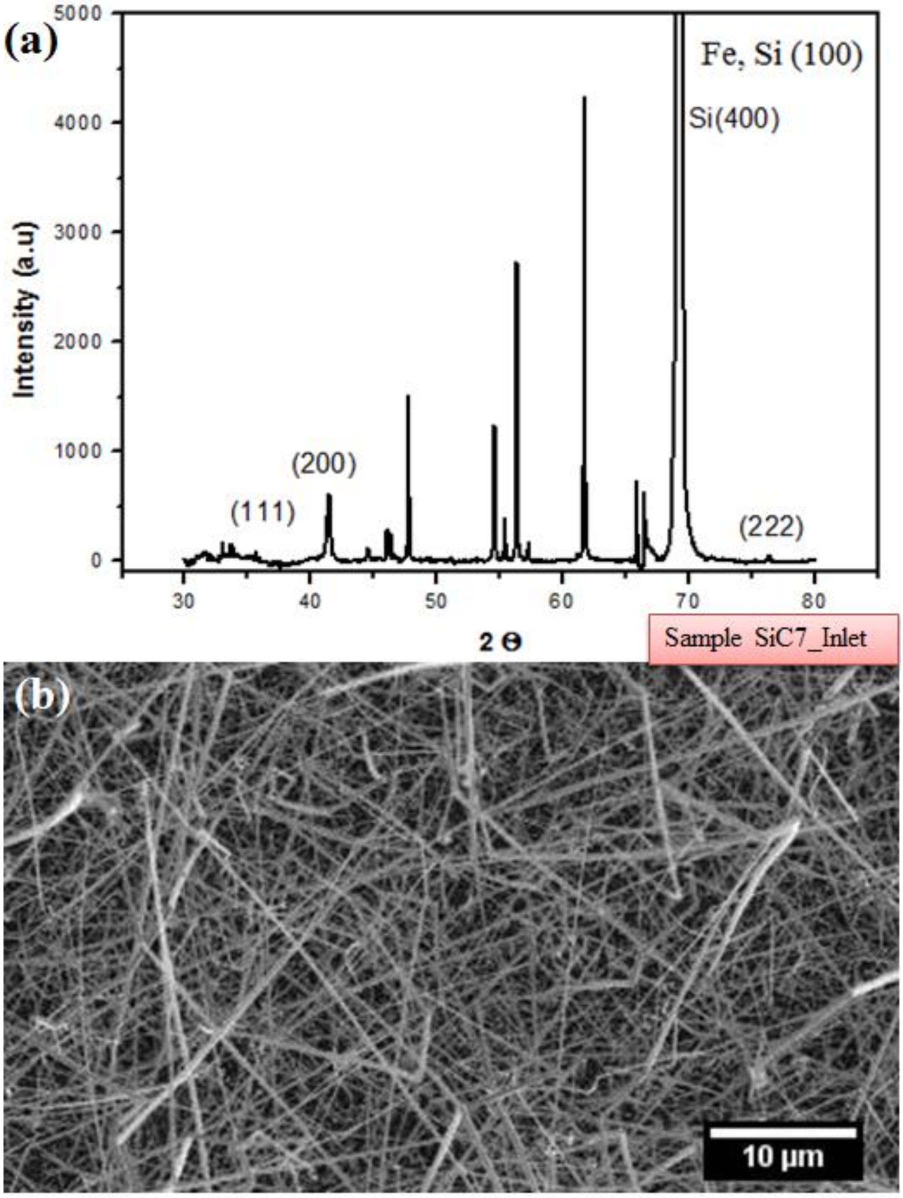

Figure 41. (a) XRD and (b) SEM image of SiC nanowires with Fe catalyst (sample SiC-7).

Given the presence of a eutectic, the growth occurs with a classical VLS mechanism: the gaseous species generated from decomposition of precursors dissolve into the droplets and when supersaturation is reached within the catalyst droplets the silicon carbide precipitates at the interface as wires continues to elongate. Nevertheless, it couldn't be observed that the presence of a metallic Si-Fe tip from the TEM analysis. This could be either due to the fact that these particles can be consumed during the growth or detached, because of the interfacial dewetting and thermal strain, during the cooling step. Another possibility could be that the growth mechanism is actually different from the standard VLS but, to have more insight about this problematic, more investigations would be needed.

The X-ray pattern in Figure 41(a) clearly shows the presence of a cubic SiC structure, confirmed by the presence of the characteristic peak at 35.6° (111), 41.4° (200), 75.5° (222). In particular the most intense (200) diffraction is at $2\theta = 41,4°$. Considering that the NWs show a <111> growth direction, as indicated by TEM images, the presence of the XRD at 41,5° could be due to the presence of a thin SiC film deposited on silicon substrate, in the regions free of iron islands droplets. Figure 41(b) shows a SEM image of the as-grown silicon carbide nanowires on (100) Si substrate, revealing high-yield nanowire growth. The NWs have diameter ranging from 30 nm to 100 nm and are up to tens of micrometers in length.

Figure 42 shows TEM analysis of the grown nanowires. Figure 42(a), Figure 42(b) and Figure 42(c) representative HRTEM images of nanowire are shown, in [110] zone axis. They are single 3C-SiC crystal with <111> growth direction; Fast Fourier Transform, shown in Figure 42(d), was obtained from a squared region in the bottom part of the wire in figure 3b. The analysis of the TEM images show that there are areas with a high density of stacking faults, but also region showing the unperturbed and defect-free 3C-SiC lattice.

Figure 43 shows that SEM images of the Fe assisted SiC nanowires sample on different part of the sample and it could be observed that different density of the nanowires grown on the surface depending on the position on the substrate respect to the flow direction (inlet, outlet) which is a function of the carrier gas flow, corresponding to different speed of the gases. Figure 43(a) shows the growth of nanowires at front corner edge of the sample. Figure 43(b-d) shows the growth of nanowires at inlet, center and outlet of the sample. From this, it can be seen that the density of nanowires were decreased from the inlet to the outlet as shown in Figure 43 b-d.

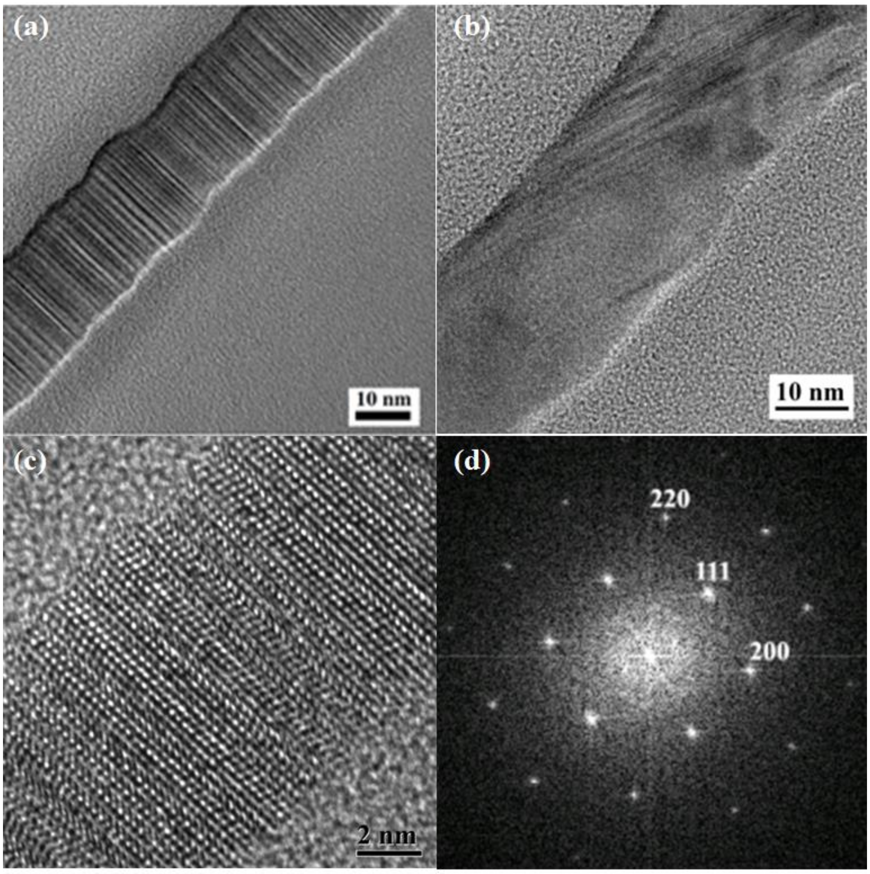

Figure 42. TEM images of Fe catalyst assisted SiC nanowires at optimized condition.

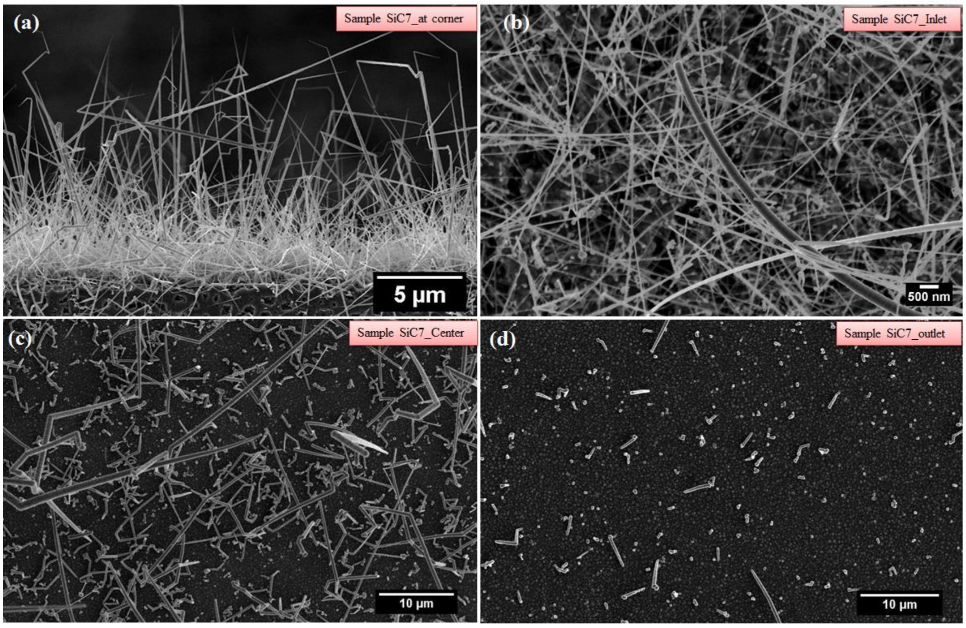

Figure 43. SEM images of Fe assisted growth of SiC nanowires on different parts of the substrates (sample SiC-7); (a) front corner edge of the sample (b) Inlet (c) Center and (d) Outlet

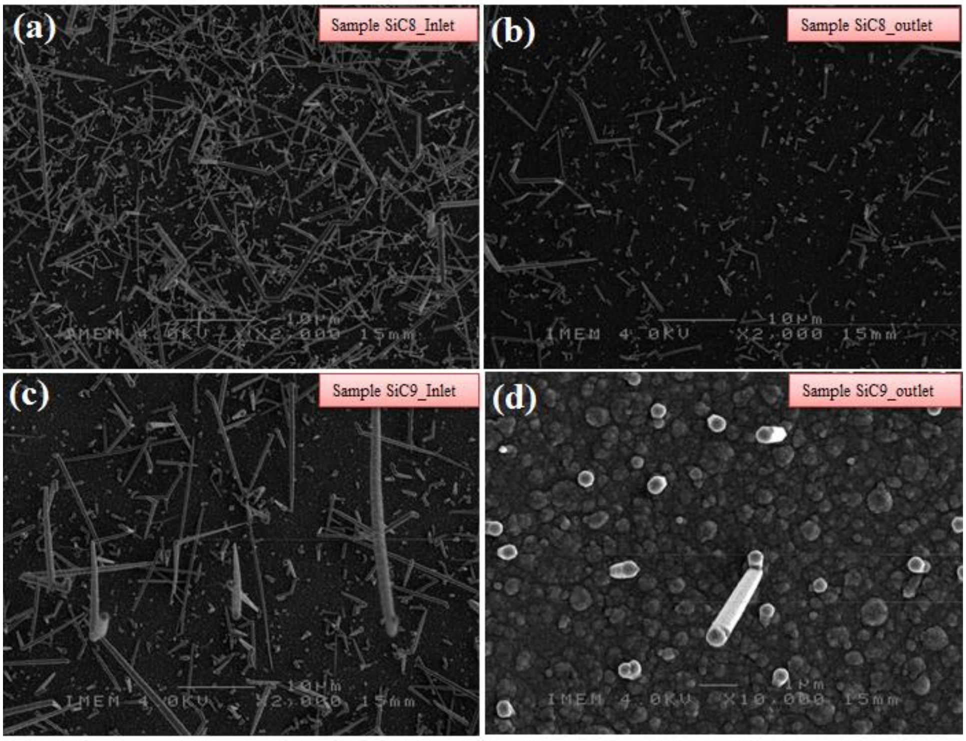

Figure 44. SEM images of Fe assisted growth of SiC nanowires using different precursor's concentration (a)-(b) inlet and outlet using Silane: 30, Propane:18 (sample SiC-8); (c)-(d) inlet and outlet using Silane:30, Propane:18 (sample SiC-9)

The experiment have been continued on Fe catalytic assisted Si (100) substrates using different precursors concentration at optimized growth temperature of 1250 °C by maintaining all other growth parameters as before. The as-grown samples using different precursor's concentration were studied and discussed below. Figure 44 shows the SEM images of Fe assisted growth of SiC nanowires using different precursor's concentration on inlet and outlet of the samples. It can be observed that a higher density in the inlet part was related to a total flow (H_2 + precursors) of 2047 sccm, with a gas velocity of 0.023 m/s as shown in Figure 43b, but the density of the nanowires decreases with the total gas flow (H_2 + precursors) was 3046 sccm, corresponding to a gas velocity of 0.034 m/s as shown in Figure 44c. The density of the nanowires further decreases with increasing the concentration and flow rate as shown in Figure 44c. Also, the diameter of the nanowire increases with increasing the concentration of precursors. It could be concluded that when the gas velocity is too high the resident time on the substrate surface is not long enough to have the optimal conditions for nanowires crystallization.

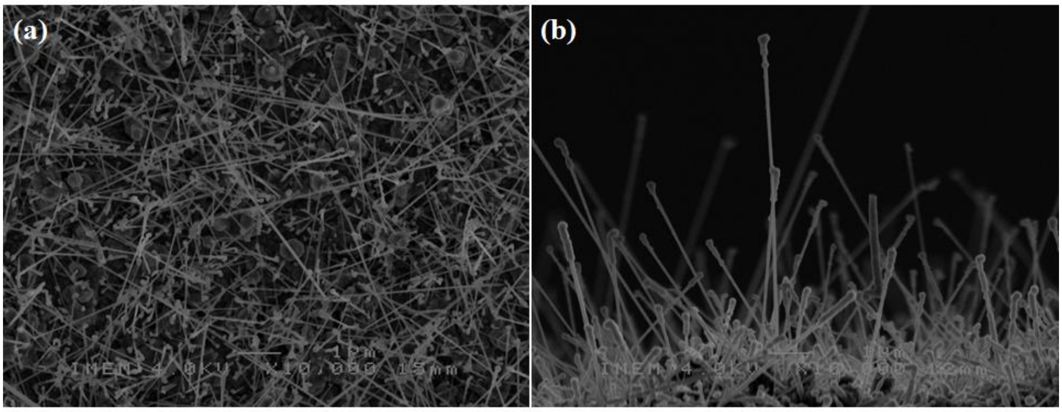

Figure 45. Fe-assisted SiC nanowires grown on Si (111) at optimized growth condition (sample SiC-10).

Figure 45 shows the SiC nanowires grown on Si (111) substrate with Fe as catalyst at optimized growth condition. It could be observed that there was no alignment of SiC nanowires on Si (111) substrate as expected with Ni assisted growth of SiC nanowires on Si (111) substrate.

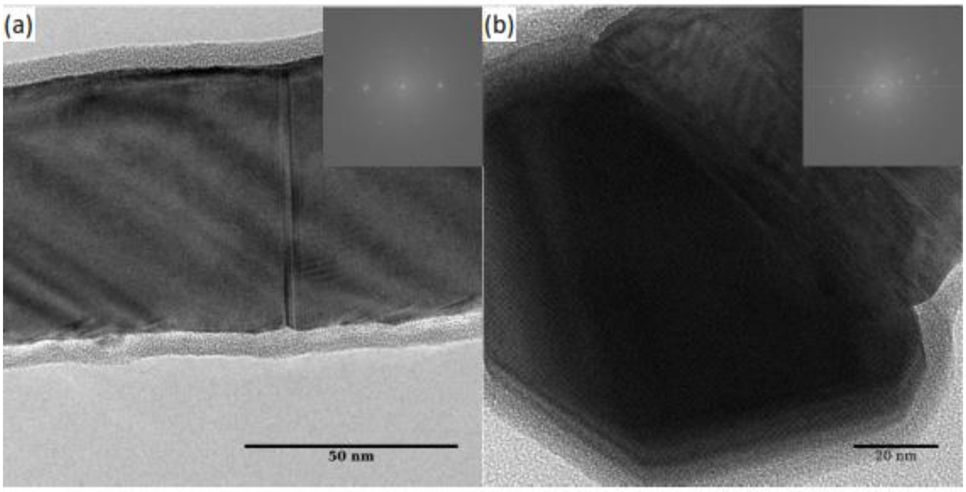

Figure 46. TEM images of the SiC Nanowires grown using magnetite nanoparticles a) regular zone of nanowires with some stacking fault b) crystalline particle observed at tip of a nanowire

Figure 46 shows TEM images of the SiC Nanowires grown using magnetite nanoparticles as catalyst. Interestingly, it was observed that the particle presented on tip of a nanowire was crystalline can be very useful in nano-medical applications.

4.4 SiC/SiO_2 core/shell nanostructures:

Surface layers of semiconductors are of much important for their properties and applications. A well-known example is the silicon oxide layer on silicon, which is the most popular surface dielectric layer in silicon-based semiconductor technology. For one-dimensional semiconducting nanomaterials, such as nanowires and nanorods, surface layers play a more special role in affecting the properties due to the large ratio of surface to volume in the small size system. Core-shell heterostructures in radial direction offer to change the physical and chemical properties of the core due to the presence of the shell [191]. In particular, semiconductor nanowires coated with dielectric layers form cable-like nanostructures that have potential applications in nano-electronics. Nowadays, many reports have shown that the as-grown no-oxide semiconductor nanowire surfaces are often covered by amorphous oxide layers because of the residual oxygen from the growth system or oxide species involved in the synthesis [192]. The typical examples include GaN nanowires coated with gallium oxide layers, [193] Si nanowires with silicon oxide shells [194–196] as well as SiC nanowires with silicon oxide outer layers [197–200].

As described in the previous section, SiC nanowires have specific and unique properties which include: wide bandgap, high thermal conductivity, high breakdown electric field, high electron drift velocity, high Young’s modulus and hardness, high melting temperature, excellent oxidation and corrosion durability and high strength at elevated temperatures. The excellent chemical and physical stability makes it very suitable for large power, high frequency electronic devices and field emitting devices.

SiC/SiO_2 core/shell cable like nanowires that is crystalline SiC core covered with amorphous silicon oxide shell, are typical semiconductor–insulator heterostructures along the radial direction which offers to enhance the properties of SiC core for device fabrications. Silicon dioxide layer presence on the SiC core allow an energy transfer from shell to the core and it helps to increase the optical emission efficiency [201, 202] without any modification of the emission energy. As SiC is an indirect wide bandgap semiconducting material, it has inherently low emission intensity. A model was proposed to explain the increase in radiative recombination of silicon carbide core due to the presence of silicon dioxide shell [202] as shown in Figure 47.

The conduction and valence band offsets have been experimentally found in [203] in the case of bulk material and they are equal to $\Delta E_C = 3.6$ eV and $\Delta E_V = 2.9$ eV, respectively. In this framework, the carriers generated by the electron beam in the shell diffuse into the core, and thereby recombine according to the allowed transitions in 3C-SiC. In this system, the amorphous shell results in being beneficial in enhancing the luminescence intensity of the crystalline core, preferentially the SiC near band edge radiative recombination.

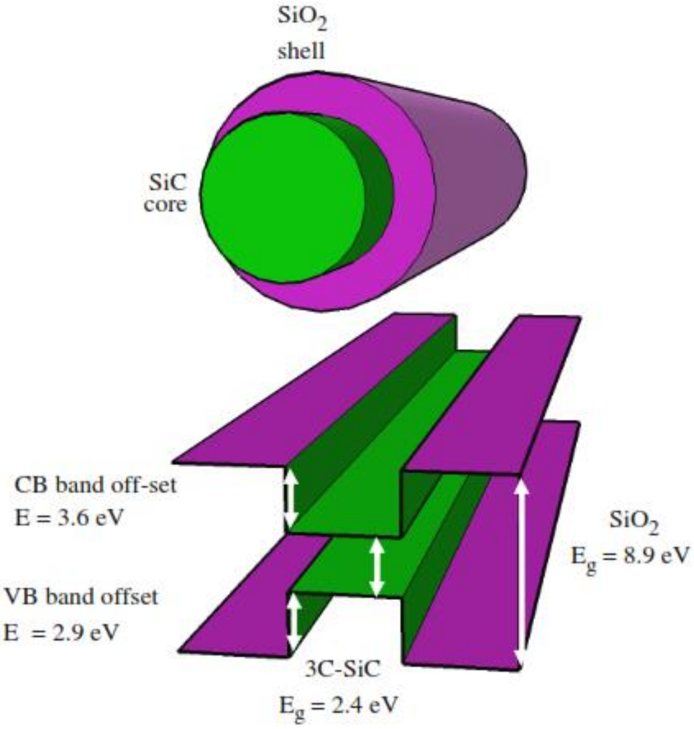

Figure 47. Sketch of the type I band alignment between 3C-SiC and SiO_2. The valence and conduction band offsets are indicated [202].

3C-SiC is also a promising material for biomedical applications [204-206] due to its high biocompatibility [207, 208]. SiC/SiO_2 core/shell system functionalize with organic molecules by well-known chemical methods [209] can be intriguing to design an innovative multifunctional hybrid material which exploits an efficient inorganic/organic energy transfer for nanomedical applications. It is very difficult to functionalize with different organic molecules directly on the surface of SiC nanowires for bio-medical applications. But, the presence of SiO_2 shell allows with different organic, magnetic particles for surface functionalization and it helps to enhance/ change the chemical and physical properties of SiC.

A suitable inorganic/organic interface could be created with an aromatic macrocycle, considering the good match between SiO_2 and/or SiC related optical emissions and the aromatic macrocycle absorption bands. As an example, a radiative energy transfer between the inorganic donor and the organic acceptor could be possible in the case of a 3C-SiC/SiO_2 system functionalized with porphirins. The room temperature donor emission covers the visible range between 2 and 3 eV, where the acceptor absorbs according to the Q bands and in the tail of the Soret band. This is intriguing in view of designing a system based on an efficient inorganic/organic energy transfer to realize electro-optical sensing devices [210]. SiC/SiO_2 core/shell system can also be used for cancer treatment. The 3C-SiC green emission can be used to activate by porphyrins for the production of the singlet oxygen, the dominant cytotoxic agent produced during photodynamic therapy [211-213]. The emission energy can be tuned in SiC/SiO_2 core/shell nanosystem by varying the size of SiC core or functionalizing with specific organic molecules on the SiO_2 layer [214]. For instance Liu and Yao [215] have evidenced a blue-shift of about 200 meV by changing the core diameter from 10 to 20 nm in SiC/SiO_2 core/shell nanocables. Further, Wu et al [216] have obtained a photoluminescence emission in the range of 440 to 560 nm by changing the nanoparticle size from 1 nm to 6 nm.

SiC-SiO_2 nanowire surfaces also exhibit superhydrophobic nature when functionalized conveniently [217-221]. Kwak et al [217] reported facile method for fabricating superhydrophobic SiC-SiO_2 nanowire surfaces with a static water contact angle of 164°. The high roughness and low surface energy provided by the particular geometry of nanostructure and alkyltrichlorosilane coating contributed to the superhydrophobicity. The surface energy of the nanowire substrates, which determined the wetting state of the water droplet, could be systematically modified through chemisorption of alkyltrichlorosilanes with varying carbon chain lengths and by UV-assisted photodecomposition of SAM molecules on the nanowire surfaces. This stable nanostructured surfaces that were acted as antiwetting with respect to water and were self-cleaning.

Moreover, SiC/SiO_2 core-shell nanowires are expected to substitute large-sized SiO_2 that act as the reinforcing phase in the rubber which would improve the interface bonding intensity of the rubber and make full use of the role of SiC. The mechanical strength of the rubber that was added to SiC/SiO core/shell nanowires will be greatly improved [222].

One has to considerably concentrate to synthesis of SiC/SiO_2 core/shell nanowires, meanwhile, it is very difficult to control the amorphous oxide layers in order to obtain desired core/shell cable like nanowire structures and the related growth mechanism has not been well investigated.

4.4.1 Synthesis

Crystalline SiC core covered by amorphous silicon oxide shell were first synthesized through laser ablation in 1998, and they were expected to be an ideal semiconductor-insulator heterojunctions in the radial direction [223]. After that, SiC/SiO_2 core/shell nanowires have been synthesized by several methods, such as laser ablation [223, 224], chemical vapor deposition (CVD), [197-200, 225-235] physical vapor deposition (PVD) [236], and arc discharge process [237, 238]. Among them, CVD is a widely used technique to fabricate SiC nanowires and SiC/SiO_2 core/shell nanowires using carbon nanotubes as the templates to react with SiO or Si, [225-227] and using $SiCl_4$ and CCl_4 as the reactants and metal Na as the coreluctant [228]. This process utilizes the vapor liquid-solid (VLS) growth mechanism to synthesize the SiC nanowires [229-231], and one-dimensional SiC nanostructure without any catalysts [232-235]. However, the above-mentioned methods need to be operated at higher temperature and the synthesis processes are complex. Among the different growth method and fabrication methods to synthesize, the VLS assisted chemical vapor deposition (CVD) process in a horizontal tube furnace is particularly interesting for SiC/SiO_2 core/shell nanowires due to the low cost of the process and the equipment does not require complicated apparatus and generally can be adapted to many process and chemical system. Its flexibility is such that it allows many changes in deposition parameters. However, synthesis of large scale, high yield SiC nanowires, controlled over growth of core and shell thickness and SiC/ SiO_2 core/shell nanowires remains still difficult, which limits further studies and applications in many fields.

In the present work, the main focus is to synthetize self-assembled SiC core with SiO_2 shell coaxial nanowires by Ni and Fe catalyst assisted VLS growth using conventional CVD system. The growth conditions were optimized for both catalyst varying growth temperature, gas flow rate, substrates etc. in order to understand the growth mechanism. SiC/SiO_2 core/shell nanowires have been grown using home-made thermal chemical vapor deposition (CVD) reactor. The experimental details are shown in the flowchart given in Figure 48.

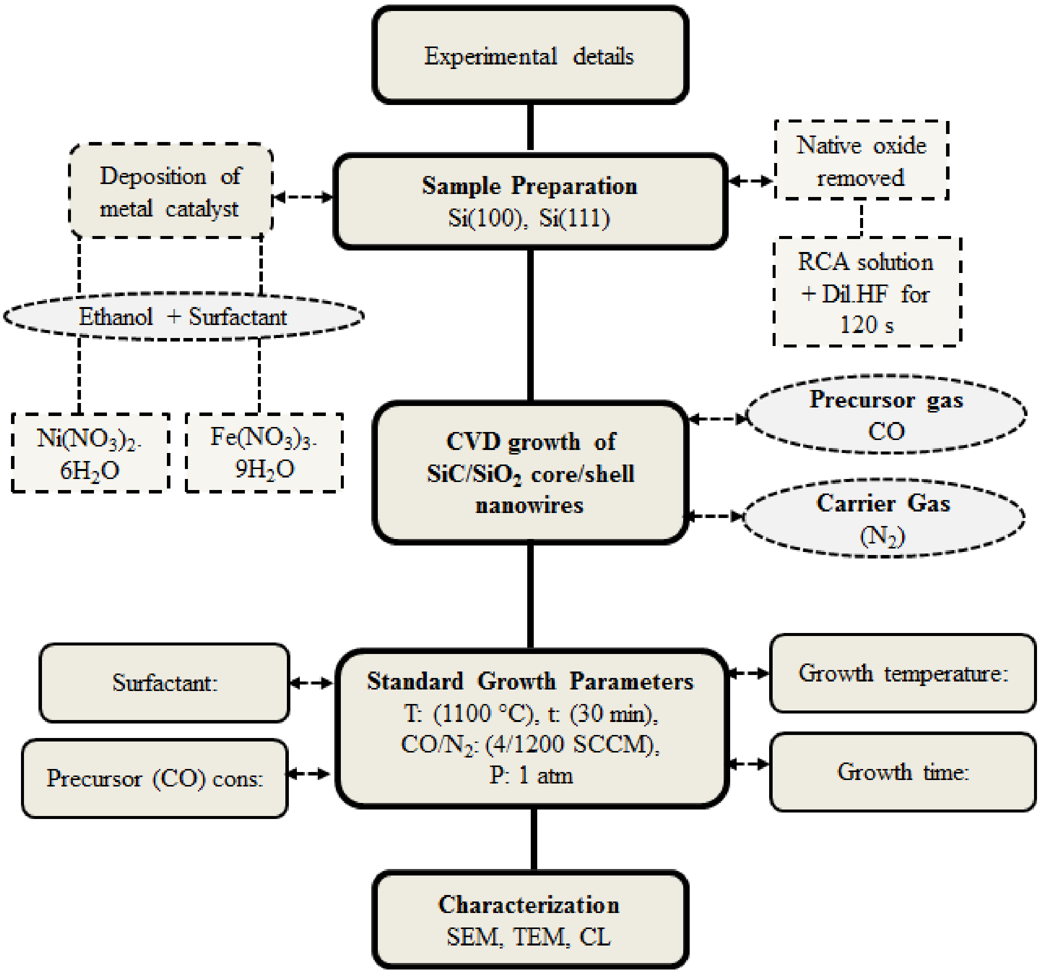

Figure 48. Flowchart of experimental scheme.

The substrates used were Si (100) and Si (111) for the growth of core/shell nanowires. The native oxide and some other metal contaminant presents on the silicon substrates were removed using standard RCA cleaning [188, 189] as described in the previous section of this chapter 4.3. RCA cleaning process was performed before the deposition of metal catalyst such as nickel nitrate ($Ni(NO_3)_2\ 6H_2O$) for nickel (Ni) and iron nitrate ($Fe(NO_3)_3\ 9H_2O$) for Iron (Fe).

The preparation of metal catalyst using metal nitrate solutions ($Ni(NO_3)_2\ 6H_2O$) is clearly explained in the Figure 49. In order to prepare the Ni catalyst, nickel nitrate salt was dissolved in ethanol solvent with the concentration of 0.05 M. Following this, few drops (~ 3 drops) of

Oleylamine surfactant were added to the above prepared solution. The role of the surfactant here was to avoid the aggregation of nickel nitrate salt during the drying process and it also helped the uniform distribution.

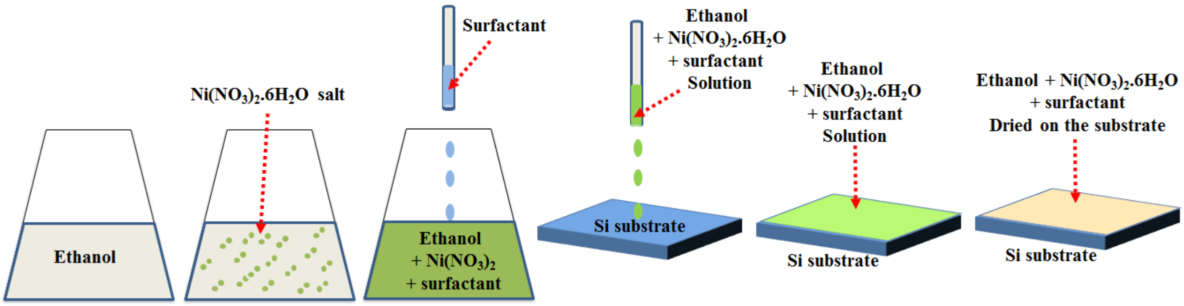

Figure 49. Preparation of catalytic solution for the growth of catalyst assisted growth of SiC/SiO_2 core/shell nanowires.

The prepared solution was added drop by drop (~ 25 drops) on the cm^2 area of Si substrate which were etched with hydrofluoric acid (HF) for 120s to remove the native oxide present on the substrate. Then, the substrate coated with catalytic solution was dried in the oven for 15 minutes. The important thing here is that there should not be any delay to transfer the catalyst solution to the substrates after HF etching and the drying time. The delay in the above process will lead to the formation of oxide layer which could be a hindrance in the core/shell growth and it also plays an important role in the growth mechanism. There is also a possibility of formation of very thin oxide layer on Si substrate while drying the sample which determines the SiC/SiO_2 core/shell growth. The preparation and deposition of $Fe(NO_3)_3$ $9H_2O$ catalyst on Si substrate was also carried out in the above described process. The dried samples were immediately loaded in the center of open tube furnace in which quartz tube was inserted as shown in the Figure 50.

The oxygen present inside the chamber was removed by sucking the air inside with the help of vacuum pump. The chamber was kept in nitrogen atmosphere at constant nitrogen flow in order to remove some of the residual oxygen in the chamber for minimum two hours. The growth procedure is described as follows: The furnace was switched on to increase the temperature with normal gradient. But, the sample was kept at room temperature with the continuation of N_2 flow. Once the required temperature was reached, the samples were introduced into the hot zone of the furnace in order to avoid some other thermal reactions. After stabilizing the temperature (~ 5 minutes), the CO was introduced for the required growth time. After the growth was completed, the samples were cooled down immediately. The as-grown samples were collected for further characterization.

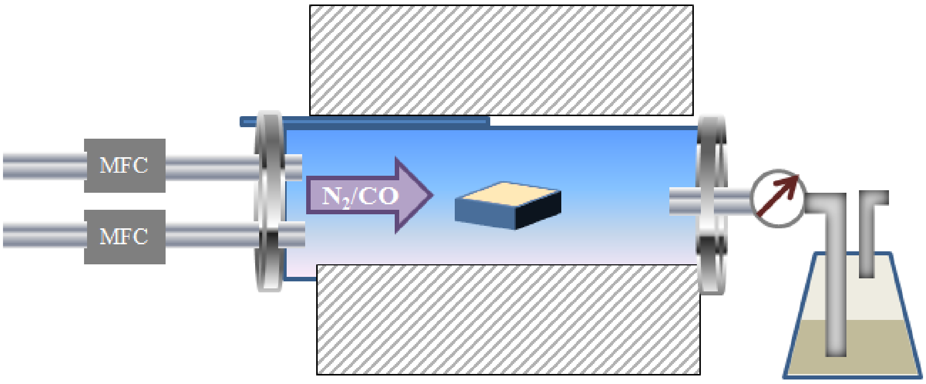

Figure 50. Schematic diagram of the experimental apparatus of the growth of SiC/SiO_2 core/shell nanowires.

The morphology of the as-grown SiC nanowires was characterized by Field Emission Gun Scanning Electron Microscopy (FEG-SEM). The structural analysis of single nanowires was performed using Transmission Electron Microscopy (TEM) (Jeol – JEM 2200 FS) for High – Resolution (HR-TEM) studies. High Angle Dark Field imaging in Scanning mode (HAADF-STEM) and the SAD patterns were proved to be useful for detailing the nanowires structure. Cathodoluminescence (CL) measurements were studied for optical properties.

Several experiments have been done by varying the different growth parameters such catalyst (nickel nitrate and iron nitrate), catalyst concentration (0.001 M, 0.01 M, 0.05 M and 0.1 M), surfactant (oleylamine, sodium dodecyl sulfate), temperature (1050 °C – 1150 °C), CO concentration, growth time (5, 15, 30, 45, 60 min.) and so on. The main aim was to understand the growth mechanism and to optimize the standard condition to obtain good quality SiC/SiO_2 core/shell nanowires.

4.4.2 Growth mechanism

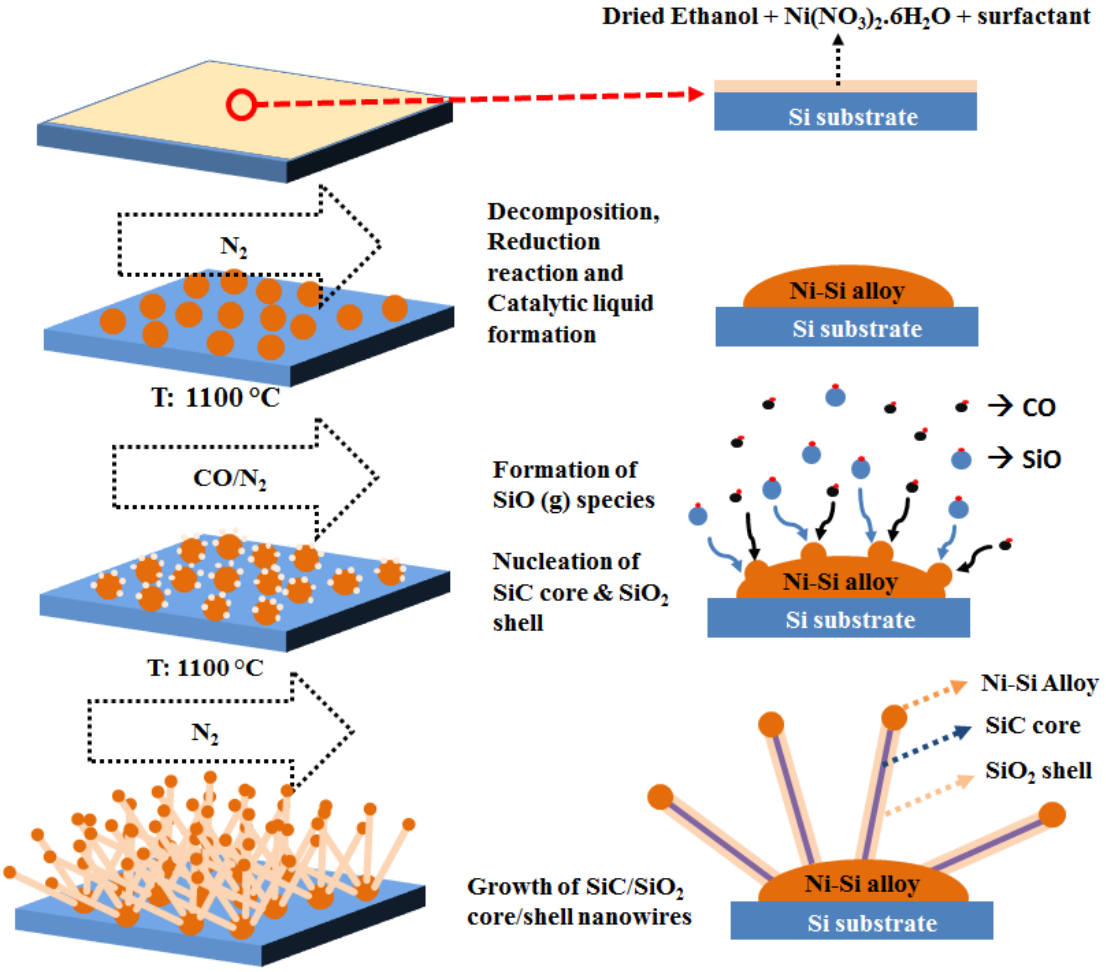

Figure 51. Schematic diagram of the growth mechanism of SiC/SiO$_2$ core/shell nanowires.

The growth mechanism of SiC/SiO$_2$ core/shell nanowires on Si substrates using the nickel nitrate and iron nitrate were found to be almost similar. Subsequently, the mechanism followed by nickel nitrate will be discussed in detail. The growth of SiC/SiO$_2$ core/shell nanowires is compared on the basis of the well-known classical VLS process. The VLS mechanism states that gaseous species are adsorbed by the liquid particle. The liquid droplet got supersaturated and then SiC and SiO$_2$ precipitate. The liquid pushes up with the same repeated process elongate the material in one dimension. Interestingly, the interplay in the self-assembled growth process of SiC core together with SiO$_2$ shell with different steps can be described below.

1. Decomposition of chemical species:

Once the substrate is introduced in the hot zone the chemicals which were presented on the substrate (ethanol, surfactant, and nickel nitrate) starts to decompose. Ethanol was thermally decomposed into several species, such as CO, CO_2, CH_4, C_2H_4, C_2H_2, H_2O and H_2 at the temperature higher than 700 °C [239]. Literature reported that the temperature goes above 1000 °C, the hydrocarbon species were decomposed into H_2 and C [240], in these experiments of oleylamine ($C_{18}H_{37}N$) surfactant. Among the several species produced by ethanol pyrolysis, H_2 and CO were main gaseous products [239]. Nickel nitrate salt ($Ni(NO_3)_2$ $6H_2O$) was thermally decomposed and gives NiO product [241] at the temperature higher than 400 °C with the following decomposition reaction.

$$Ni(NO_3)_2.6H_2O \rightarrow NiO + 2\ NO_2 + \frac{1}{2}\ O_2 + 6\ H_2O \qquad (1)$$

2. Reduction reaction:

After the decomposition of nickel nitrate, Ni particles have been formed between NiO and hydrogen (which is decomposed species from ethanol and surfactant) by the reduction reaction. Also NiO became Ni particle with reacting with CO when introduced in the reactor.

3. Catalytic liquid formation:

After the reduction reaction, the Ni particle reacted with the Si substrate to form of Ni-Si liquid alloy droplets. This is due to the eutectic phase of Ni-Si system (966 °C) as like explained in the previous section 4.3. The liquid droplets diffuse and agglomerate to form large number of micron sized catalytic droplets. The micron sized droplets were distributed uniformly with the help of surfactant as shown in Figure 51. That is the reason, why the surfactant was used in the catalytic solution. If there was no surfactant, the droplets were agglomerated to form a lower number of milli-meter size droplet. Last three steps happened during the stabilization of the growth temperature from the sample introduced in to the chamber.

4. Gaseous SiO species formation:

Once the temperature stabilized at growth temperature CO gases were introduced in to the chamber. At growth temperature, the carbon monoxide was decomposed into carbon (it may be absorbed onto the chamber wall or incorporated in the catalytic alloy) and carbon dioxide [242]:

$$2CO\ (g) \leftrightarrow C\ (s) + CO_2\ (g) \qquad (2)$$

Then the resultant carbon dioxide etched the silicon substrates:

$$CO_2\ (g) + Si\ (s) \rightarrow SiO\ (g) + CO\ (g) \qquad (3)$$

Gaseous SiO species formation in the reactor played a major role in the growth of SiC/SiO_2 core/shell nanowires. There was another possibility of the formation of gaseous SiO species which was a solid–solid reaction between the Si (substrate) and SiO_2 (very thin oxide layer on Si substrate when drying the sample) [243].

$$Si\ (s) + SiO_2\ (s) \rightarrow 2SiO\ (v) \qquad (4)$$

5. Nucleation of SiC core and SiO_2 shell:

Subsequently, the gases of CO, SiO, and CO_2 adsorbed and diffused into the catalytic liquid alloy droplets. Because of the supersaturation of carbon, silicon and oxygen, the silicon carbide and silicon oxide concurrently segregated from the alloy droplet by the reactions [242]:

$$3SiO + CO \rightarrow SiC + 2SiO_2 \text{ (most preferable)} \qquad (5)$$

$$4SiO + CO_2 \rightarrow SiC + 3SiO_2 \qquad (6)$$

$$2SiO + C \rightarrow SiC + SiO_2 \qquad (7)$$

$$6Si + 4\ CO \rightarrow 4SiC + 2SiO_2 \qquad (8)$$

In general, classical VLS growth mechanism, size of the catalytic alloy droplet was a major issue and apparently limits the number of possible nucleation events. In contrast, literature reported that the micron-sized alloy droplet systems where tens or hundreds of nanowires can be observed, a large amount of nucleation events on a single droplet were possible [244]. Here also there were lot of nucleation events on single micron sized liquid droplet as shown in Figure 51.

6. Growth of SiC/SiO_2 core/shell nanowires:

As a result of about 1000 °C higher melting point of SiC than that of SiO_2, SiC is earlier solidified and drags out the viscous SiO_2. Thus the nanowires was formed and pushed upwards the liquid alloy droplet, with SiC core covered by SiO_2 shell.

In this growth mechanism, SiO vapour was an important species. If the formation of SiO vapour was higher by the solid state reaction between Si and oxide layer, more number of SiO species with small number of CO adsorbed and diffused in to the catalytic liquid alloy droplet to hindrance the SiC nucleation and it favors the growth of silica nanowires incorporated with carbon molecules ($SiCO_x$ nanowires). Due to this reason, one has to be considerably concentrate in the sample preparation to control the oxide layer formation on the Si substrate and the growth parameters such as growth temperature, growth time, choosing the surfactant (without oxygen), concentration of the catalytic solution, carrier gas/precursor gas ratio, flow rate of carrier gas, substrate drying time, substrate etching time and so on.

4.4.3 Characterization

Several experiments have been done to optimize the condition for the growth of SiC/SiO_2 core/shell nanowires varying with different growth parameters for both nickel nitrate and iron nitrate catalytic solutions. The standard optimized condition for the high yield and better quality SiC/SiO_2 core/shell nanowires for both catalyst were found to be:

Substrate: (100) (111) oriented silicon,

Substrate preparation: Si etching time with HF acid: 120 s,

Catalytic solution drying time: 15 minutes,

Drying oven temperature: 40 °C,

Surfactant: Oleylamine,

Concentration of catalytic solution: 0.05 M,

Carrier gas (N_2) flow rate: 1200 standard cubic centimeter (SCCM),

Concentration ratio of CO/N_2: 0.4 %,

Growth temperature (T): 1100 °C,

Growth time (t): 30 minutes.

Figure 52 shows SEM image of the as-grown sample of SiC/SiO_2 core/shell nanowires at standard condition using nickel nitrate as catalyst. The morphology of the as-grown sample showed that the wires like shape have been observed (Figure 52(a)) and composed of large quantities of randomly distributed nanowires with higher density over large area on the substrate. The length and diameter of the nanowires range from 0.1 mm to tens of microns and 40 to 80 nm, respectively and average diameter of the nanowire were measures to be 60 nm. It can be obviously observed that there are sphere- like catalyst particles adhered on tip of the nanowires, which is Ni-Si catalytic alloy and it suggests a catalyst-assisted vapor–liquid–solid (VLS) mechanism leading the growth of the nanowires. Figure 52 (b) is a high-magnification SEM image showing straight and smooth surface morphological details of the nanowires and the presence of catalytic particle on the nanowire tip. Each observed nanowire has uniform diameter along its length direction and no recognizable tapered shape was observed.

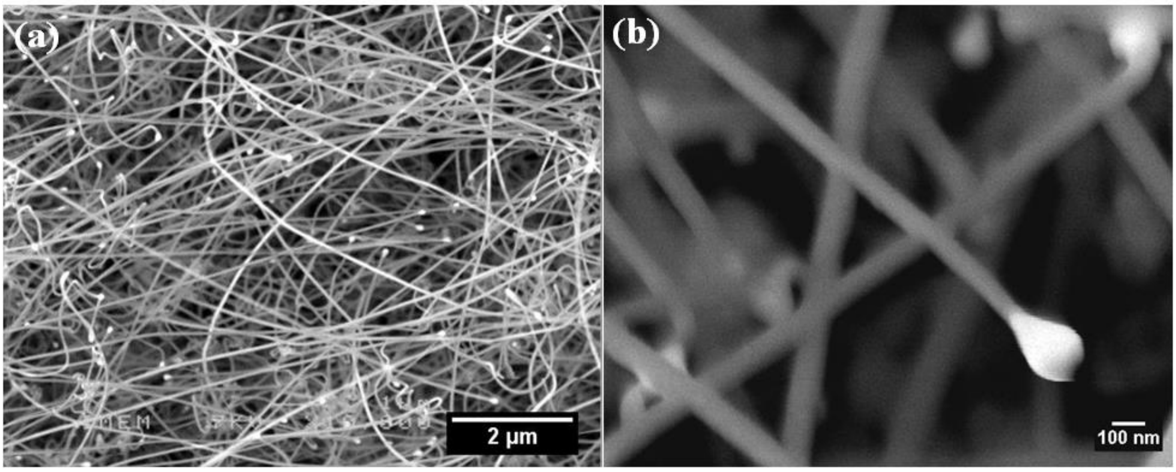

Figure 52. SEM image Ni catalyst assisted of SiC/SiO_2 core/shell nanowires grown at standard condition (a) low-magnification SEM image of dense nanowires (b) high-magnification view with Ni catalytic particle present on the tip of nanowires.

Figure 53 shows TEM image of the single nanowires grown at standard condition using nickel nitrate as catalyst. Core and shell like structures were observed in the TEM image as shown in Figure 53(a). From the Fast Fourier Transform (FFT) image (Figure 53(b)) the symmetry of the crystal and the lattice spacing can be identify. The identified crystal structure of the core was 3C-SiC, with <111> growth axis. The circle like structure was observed at center in the FFT image due to the diffraction of amorphous silica shell.

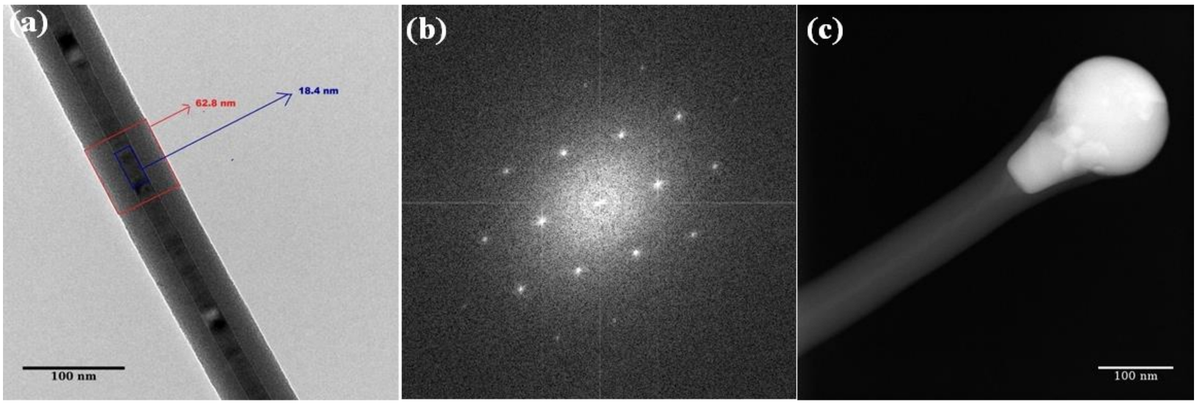

Figure 53. TEM analysis of Ni catalyst assisted SiC/SiO_2 core/shell nanowires grown at standard condition (a) TEM image of crystalline SiC core and amorphous SiO_2 shell (b) corresponding FFT image (c) HAADF image of the Ni-Si alloy on tip of the nanowire.

Remarkably, the nanowire is almost free from planar defects in long segments as shown in Figure 53a. However, occasionally some stacking faults have been observed in the 3C-SiC crystalline core mainly on (111) planes perpendicular to the growth axis. The SiC core is surrounded by a coaxial amorphous layer, whose chemical composition has been assessed by TEM-EDX measurements (not shown here) allowing to identify the shell as SiOx with $1.9 \leq x \leq 2$. Figure 53c shows an high angle annular dark field (HAADF) image based on the atomic number contrast that shows the crystalline core (whiter) wrapped by the amorphous shell (darker) with the catalytic particle at the nanowire tip. This particle contains Ni and Si elements as confirmed by TEM-EDX measurements (not shown here).

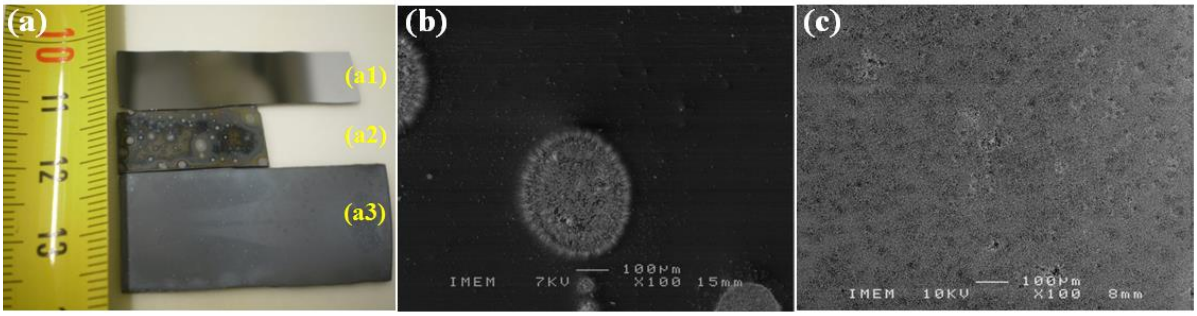

Figure 54. Surfactant effect in the growth of SiC/SiO_2 core/shell nanowires (a) photographical image the samples (a1) silicon substrate (a2) as-grown sample of SiC/SiO_2 core shell nanowires without surfactant (nanowire growth at only white spots) (a3) as-grown sample of SiC/SiO_2 core shell nanowires using oleylamine surfactant (all regions covered by nanowires) (b) SEM image of the sample a2 (c) SEM image of the sample a3.

High yield and large area over growth of SiC/SiO_2 core/shell nanowires have been achieved using surfactant in the catalytic solution. Adding surfactant in the solution helped to distribute and perform uniform coating of catalytic solution on silicon substrates. Figure 54(a) shows a macroscopic optical image of silicon (Figure a1) and as-grown samples of SiC/SiO_2 core/shell nanowires without surfactant (Figure a2) and with surfactant (Figure a3). It could be clearly observed that there are few white circled dots on the sample without surfactant (a2). A white deposited layer was observed on the as-grown sample using surfactant (a3). This white region contains full of SiC/SiO_2 core/shell nanowires, as confirmed by SEM imaging (Figure 54 b, c). Higher magnification SEM images have already been shown in the Figure 52.

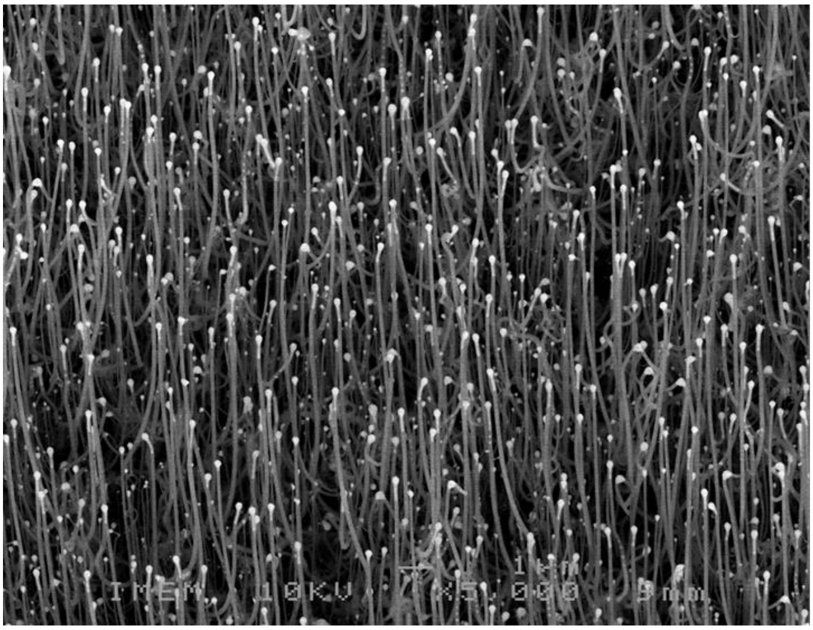

Figure 55. SEM image of aligned nanowires obtained using surfactant

A careful choice of the surfactant for the growth of SiC/SiO_2 core/shell nanowires is necessary. Oleylamine surfactant have been used in the growth of SiC/SiO_2 core/shell nanowires since oleylamine contains no oxygen. If the surfactant contained oxygen in its molecular unit, it helped to distribute the catalyst for uniform coating, but it also helped to increase the oxidization of silicon substrate while drying the sample. If the oxide layer considerable increased, the formation of gaseous SiO increased by the solid-state reaction between Si substrate and oxide layer. If the formation of SiO vapour was higher, more number of SiO species with small number of CO adsorbed and diffused in to the catalytic liquid alloy droplet to hindrance the SiC nucleation and it favors the growth of silica nanowires incorporated with carbon molecules ($SiCO_x$ nanowires). However, if the surfactant contained oxygen in its molecular unit, that helped to grow good and smooth silica nanowires. Also, it helped to the growth of aligned nanowires as shown in Figure 55, when the catalytic particles distributed very evenly on the substrate and then the smaller liquid droplet size less than micron formation.

The effect of growth temperatures on the growth of nanowires and as-grown samples was investigated by SEM and TEM imaging. Figure 56 shows the SEM and TEM images of the samples grown at 1070 °C, 1100°C and 1150°C, respectively using nickel catalyst keeping all other standard growth parameters fixed. Figure 56 shows that the samples grown at lower and higher temperature do not present the SiC core and that therefore only silica nanowires are observed. The silica nanowires were bended and not straight nanowires were observed in comparison with the nanowires grown at standard condition. The same behavior has been observed in the growth of Fe assisted SiC/SiO_2 core/shell nanowires. There was no growth observed below 1050 °C for nickel nitrate and 1070 °C for iron nitrate catalyst.

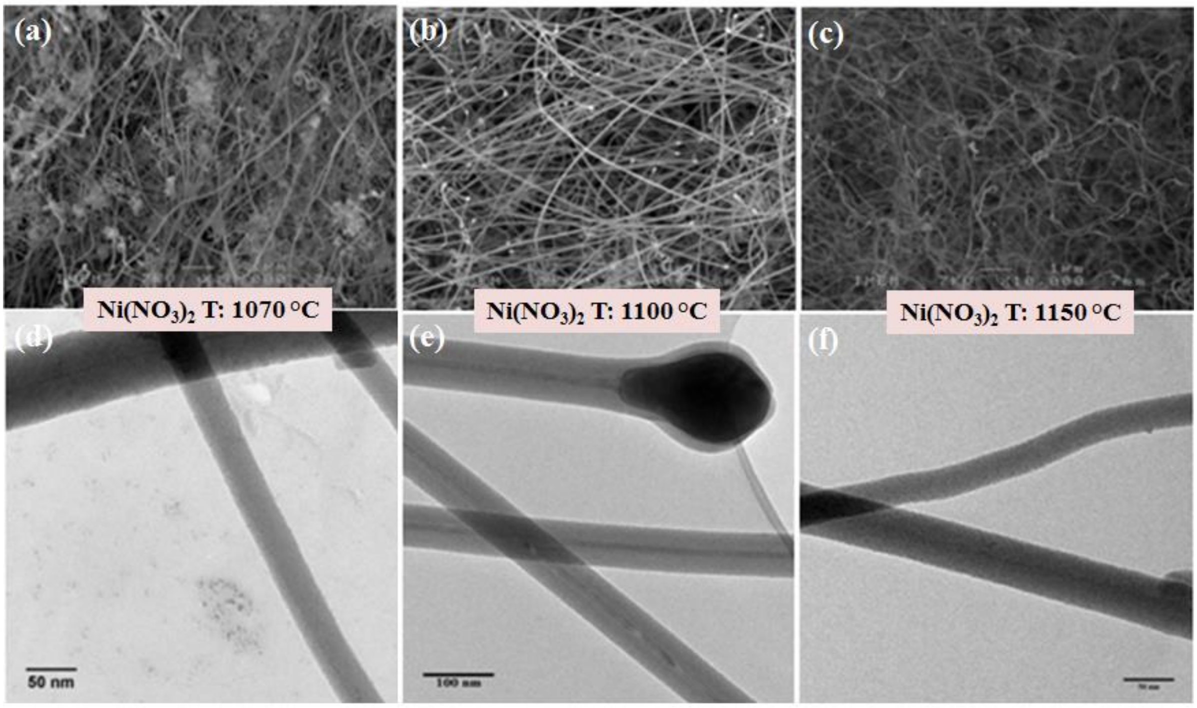

Figure 56. Temperature effect of SiC/SiO_2 core/shell nanowires (a, b, c) SEM images of nanowires grown at 1070 °C, 1100 °C and 1150 °C using nickel nitrate catalyst (d, e, f) corresponding TEM images

Since SiC is biocompatible and hemocompatible [190] our purpose was to use the properly functionalized SiC/SiO_2 core/shell nanowires in the of different nano-medical applications, such as targeted therapy, against deep solid tumors. Nickel catalyst assisted growth of SiC/SiO_2 core/shell nanowires is not applicable in bio-applications due to its known carcinogenicity, mutagenicity and teratogenicity, [186] and it has been therefore replaced by iron catalyst. The growth conditions were optimized for the iron nitrate catalyst. The growth mechanism is similar to the nanowires grown using nickel nitrate as catalyst.

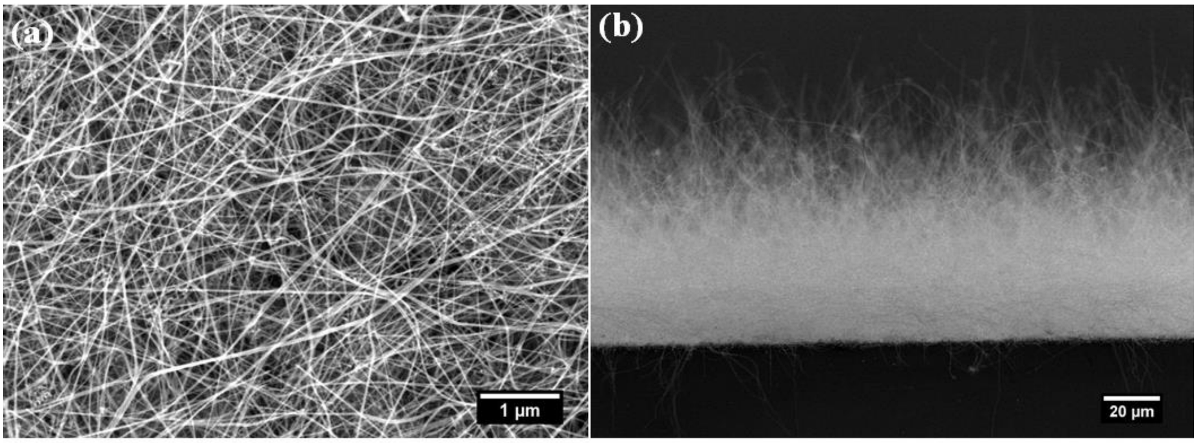

Figure 57. SEM image Fe catalyst assisted of SiC/SiO_2 core/shell nanowires grown at standard condition (a) at lower magnification view of dense nanowires (b) cross section view of the as-grown nanowires sample

Figure 57 shows SEM image of the as-grown sample of SiC/SiO_2 core/shell nanowires at standard condition using iron nitrate as catalyst. The morphology of the as-grown sample showed a wire-like shape (Figure 57a) composed of large quantities of randomly distributed nanowires with higher density over a large area on the substrate. The length and diameter of the nanowires range from 0.1 mm to tens of microns and from 40 to 80 nm, respectively. Also in this case the average diameter of the nanowires was measured to be 60 nm. An SEM image of cross sectional view of as-grown sample was shown in Figure 57b.

Figure 58 shows TEM image of the single nanowires grown at standard condition using iron nitrate as catalyst. Core and shell like structures was observed in the TEM image as shown in Figure 58a. From the Fast Fourier Transform (FFT) image (Figure 58b) the symmetry of the crystal and the lattice spacing can be identify. The identified crystal structure of the core was

3C-SiC, with <111> growth axis. The circle like structure was observed at center in the FFT image due to the diffraction of amorphous silica shell. Some stacking faults have been observe in the 3C-SiC crystalline core mainly on (111) planes perpendicular to the growth axis as shown in Figure 58a.

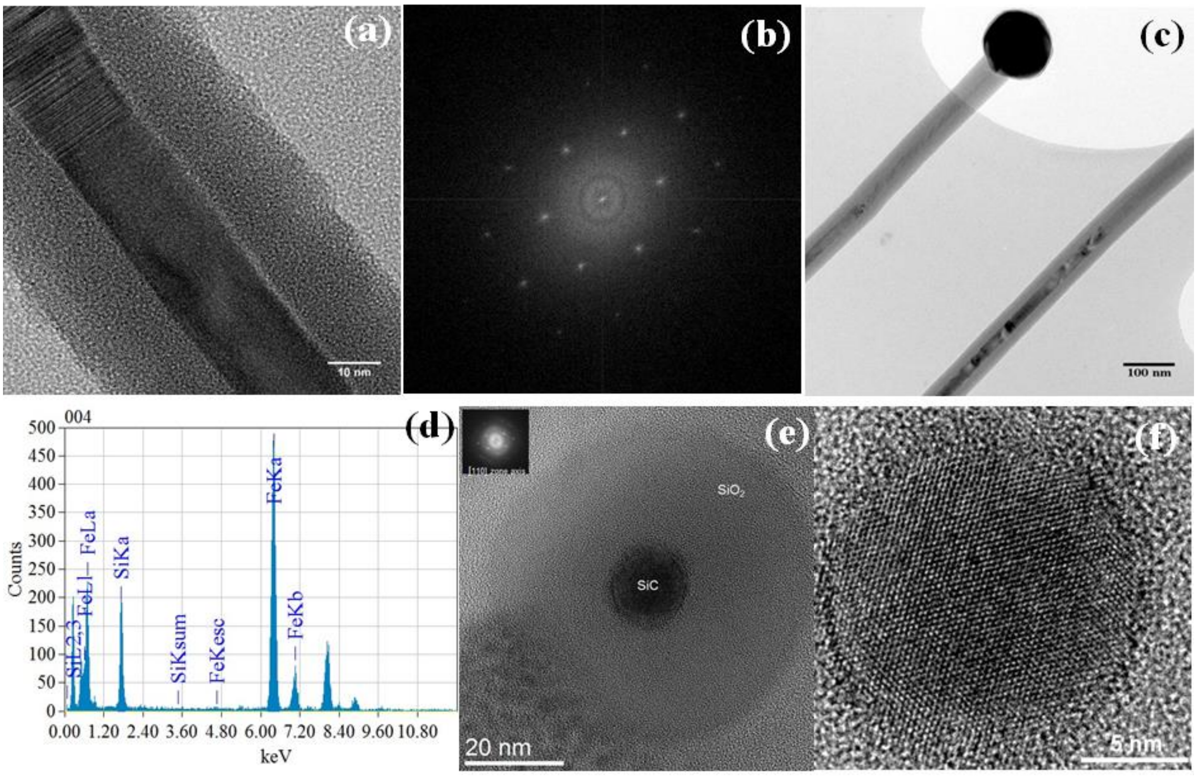

Figure 58. TEM analysis of Fe catalyst assisted of SiC/SiO_2 core/shell nanowires grown at standard condition (a) TEM image of crystalline SiC core and amorphous SiO_2 shell (b) corresponding FFT image (c) TEM image of the Fe-Si alloy on tip of the nanowire (d) EDX analysis shows the presence of silicon and iron on tip of the nanowire (and copper from TEM grid) (e) TEM image of a single nanowire in cross-section view and (f)The core lattice is seen in atomic resolution.

Figure 58c shows that TEM image of the catalytic particle presence on tip of the nanowires and it confirm the growth was attributed by the VLS mechanism. The catalytic particle contains Fe and Si elements which were confirmed by TEM-EDX measurements as shown in Figure 58d. TEM image for a single nanowire in cross-section view as shown in Figure 58e. The SiC core was at center covered by SiO_2 shell. The atomic resolution of SiC core was shown in Figure 58f.

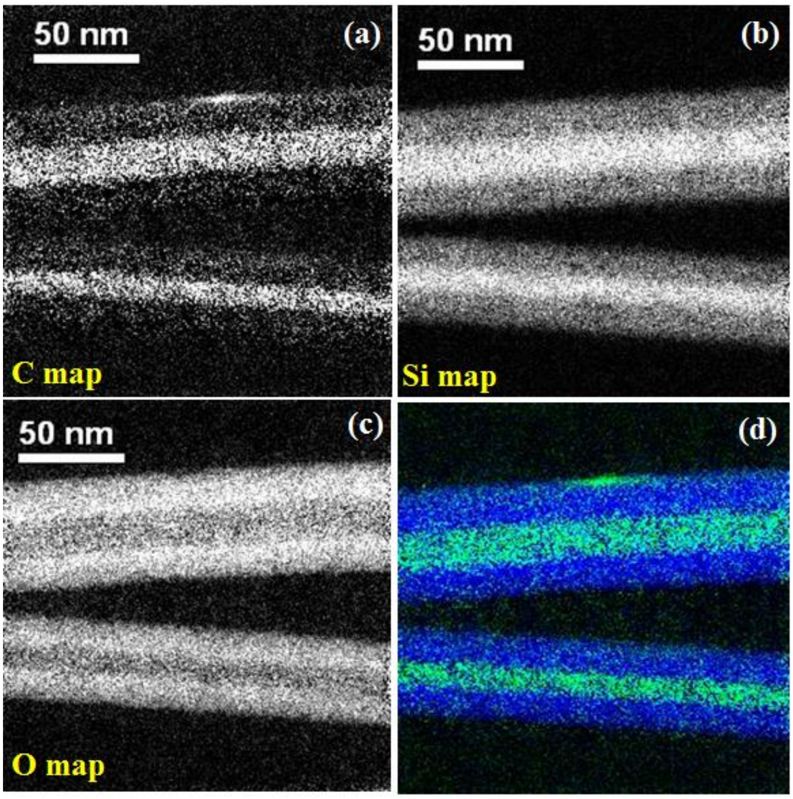

Figure 59. Elemental mapping analysis acquired by TEM energy filtering on Fe catalyst assisted of SiC/SiO_2 core/shell nanowires (a) C map obtained on the K edge at 284 eV (b) Si map obtained on the L edge at 99 eV (c) O map obtained on the K edge at 532 eV (d) total color-coded map (C in green, O in blue).

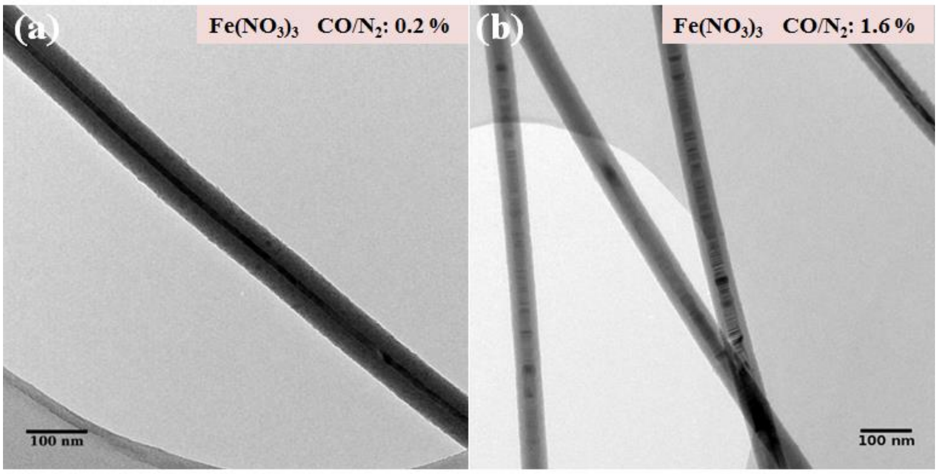

Figure 60. CO concentration effect in the SiC/SiO_2 core/shell nanowires (a) TEM image of SiC/SiO_2 core/shell nanowires using CO concentration of 0.2 % (b) TEM image of SiC/SiO_2 core/shell nanowires using CO concentration of 1.6 %.

The elemental mapping analysis acquired by TEM energy filtering on Fe catalyst assisted of SiC/SiO$_2$ core/shell nanowires is shown in Figure 59. It confirmed the complementary distribution of carbon and oxygen, in the SiC core and in the oxide shell, respectively. The oxygen to silicon ratio in the shell, as estimated by EDX point spectra, is very close to 2, allowing us to identify the shell as silicon dioxide.

The thickness of SiC core can be tuned using the dilution of CO concentration in the carrier gas of nitrogen. Figure 60 and Figure 61 shows that effect of CO concentration in the growth of SiC/SiO$_2$ core/shell nanowires. The diameter of the SiC core increases with increasing the CO concentration in the N$_2$ gas. It could be observed that the thickness of the wire remains almost constant with increasing the CO concentration. Also, the diameter of the SiC core saturated with increasing the CO concentration. The core shell diameter can be tuned by controlling the relative amounts of CO and SiO vapour during the growth.

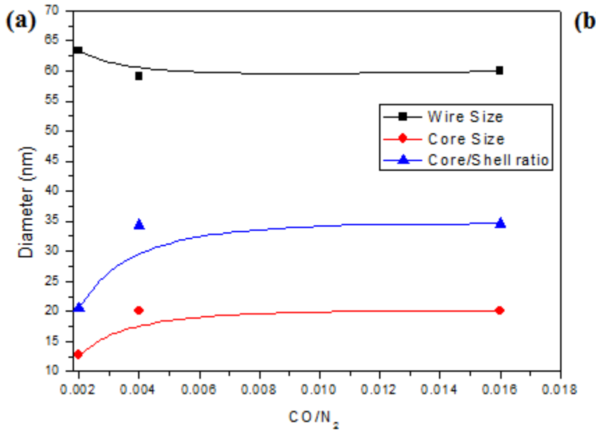

(b)

CO/N$_2$	Average wire diameter [nm]	Average SiC core diameter [nm]	Average core/wire ratio
0.2 %	63.3	12.7	20%
0.4 %	59.0	20.1	34%
1.6 %	60.0	19.9	35%

Figure 61. Variation of SiC core and SiO$_2$ shell diameter versus CO concentration (a) Graph of CO/N$_2$ Vs nanowire thickness (x axis in logarithmic scale) (b) Tabulation of the measurement

The optical properties of the SiC/SiO$_2$ core/shell nanowires have been studied by SEM-Cathodoluminescence at room temperature. Two sets of samples have been considered for the CL measurements (Table 5): (i) as-grown Fe assisted SiC/SiO$_2$ core/shell nanowires and (ii) annealed NWs at 800 °C for 1 hr. in oxygen atmosphere. The CL spectrum acquired on both the samples is shown in Figure 62.

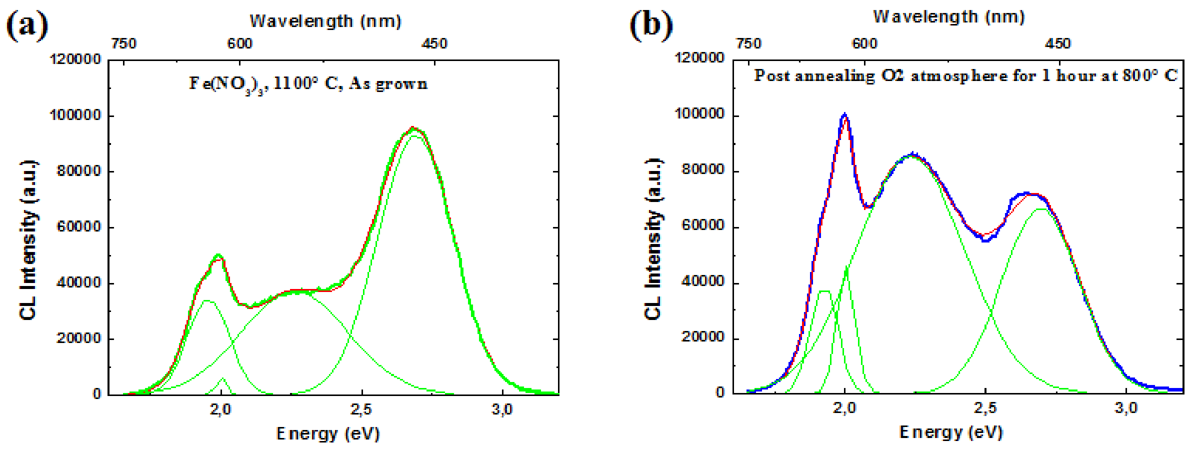

Figure 62. CL studies of SiC/SiO$_2$ core/shell nanowires (a) CL spectra of an as-grown sample of SiC/SiO$_2$ core/shell nanowires (b) CL spectra of the same SiC/SiO$_2$ core/shell sample as in (a) after annealing in oxygen atmosphere.

Energy (eV)	**As-grown Integrated Intensity (a.u)**	**Post-Annealing Integrated Intensity (a.u)**	**Peak attribution**
2.7	31436	23125	ODC II, center on the lack of an oxygen [246]
2.26	17761	41402	the β−SiC near band edge emission [245]
1.99	302	3825	relative to excess oxygen center [247, 248]

Table 5. Resume of the integrated intensities of the CL bands of SiC/SiO$_2$ core/shell nanowires

As obtained by Gaussian deconvolution, the spectrum has three different components peaked at 2.7 eV, 2.26 eV and 1.99 eV. The 2.7 eV emission is related to the triplet state of the oxygen-deficiency ODC(II) center, and the 2.26 eV is related to the β−SiC near band edge emission and 1.99 eV is related to the excess oxygen in the nanowires. The CL emission enhancement has been observed in the post-annealed samples due to the incorporation of oxygen in the SiO$_2$ shell.

References

1. J. Fan, C. Fábrega, R. Zamani, A. Shavel, F. Güell, A. Carrete, T. Andreu, A. M. López, J. R. Morante, J. Arbiol, A. Cabot, Journal of Alloys and Compounds 555, 213 (2013)

2. C. K. Xu, P. Shin, L. L Cao, D. Gao, J. Phys. Chem. C, 114, 125 (2010)

3. M. Law, L. E. Greene, A. Radenovic, T. Kuykendall, J. Liphardt, P. D. Yang, J. Phys. Chem. B, 110, 22652 (2006)

4. Y. Qin, X.Wang, Z. L Wang, Nature, 451, 809 (2008)

5. Z. L. Wang, J. H. Song, Science, 312, 242 (2006)

6. R. Könenkamp, R. C. Word, M. Godinez, Nano Lett., 5, 2005 (2005)

7. Q. Yang, Y. Liu, C. F. Pan, J. Chen, X. N. Wen, Z. L. Wang, Nano Lett., 13, 607 (2013)

8. P. Yang, H. yan, S. Mao, R. Russo, J. Johnson, R. Saykally, N. Morris, J. Pham, R. He and H. J. Chio, Adv. Funct. Mater. 12, 323 (2002)

9. Y. Li, J. Z. Zhang, Laser Photonics Rev. 4, 517 (2010),

10. J. D. Fan, F. Guell, C. Fábrega, A. Shavel, A. Carrete, T. Andreu, J. R. Morante, A. Cabot, Appl. Phys. Lett., 99, 262102 (2011)

11. J. D. Fan, C. Fábrega, R. Zamani, A. Shavel, F. Güell, A. Carrete, T. Andreu, A. M. López, J. R. Morante, J. Arbiol, A. Cabot, J. Alloys Compd, 555, 213 (2013)

12. H. T. Ng, J. Han, T. Yamada, P. Nguyen, Y. P. Chen and M. Meyyappan, Nano Lett. 4 1247 (2004)

13. J. Singh, A. P. Bhondekar, M. L. Singla, and A. Sharma, ACS Appl. Mater. Interfaces 5, 5346 (2013)

14. G. Wang, W. Lu, J. Li, J. Choi, Y. Jeong, S. Y. Choi, J. B. Park, M. K. Ryu, K. Lee, Small, 2, 1436 (2006)

15. G. Wang, Q. Wang, W. Lu, J. J. Li, Phys. Chem. B, 110, 22029 (2006)

16. S. R. Hejazi and H. R. M. Hosseini, J. Cryst. Growth, 309, 70 (2007)

17. C. W. Blackledge, J. M. Szarko, A. Dupont, G. H. Chan, E. L. Read and S. R. Leone, J. Nanosci. Nanotechnol. 7, 3336 (2007)

18. D. Ito, M. L. Jespersen and J. E. Hutchison, ACS Nano, 2(10), 2001 (2008)

19. P. D. Yang, H. Q. Yan, S. Mao, R. Russo, J. Johnson, R. Saykally, N. Morris, J. Pham, R. R. He and H. J. Choi, Adv. Funct. Mater., 12, 323 (2002)

20. H. Huang, S. Mao, H. Feick, H. Yan, Y. Wu, H. Kind, E. Weber, R. Russo and P. Yang, Science, 292, 1897 (2001)

21. W. I. Park, D. H. Kim, S. W. Jung and G. C. Yi, Appl. Phys. Lett., 80, 4232 (2002)

22. H. T. Yuan and Y. Zhang, J. Cryst. Growth, 263, 119– (2004)

23. D. J. Park, D. C. Kim, J. Y. Lee and H. K. Cho, Nanotechnology, 18, 395605 (2007)

24. L. E. Greene, M. Law, J. Goldberger, F. Kim, J. C. Johnson, Y. F. Zhang, R. J. Saykally and P. D. Yang, Angew. Chem., Int. Ed., 42, 3031 (2003)

25. L. E. Greene, B. D. Yuhas, M. Law, D. Zitoun and P. D. Yang, Inorg. Chem., 45, 7535 (2006)

26. L. Shi, K. Y. Bao, J. Cao and Y. T. Qian, CrystEngComm, 11, 2009 (2009)

27. L. E. Greene, M. Law, D. H. Tan, M. Montano, J. Goldberger, G. Somorjai and P. D. Yang, Nano Lett., 5, 1231 (2005)

28. D. W. Wu, Z. B. Huang, G. F. Yin, Y. D. Yao, X. M. Liao, D. Han, X. Huang and J. W. Gu, CrystEngComm, 12, 192 (2010)

29. C. Y. Geng, Y. Jiang, Y. Yao, X. M. Meng, J. A. Zapien, C. S. Lee, Y. Lifshitz and S. T. Lee, Adv. Funct. Mater., 14, 589 (2004)

30. C. Li, G. J. Fang, Q. Fu, F. H. Su, G. H. Li, X. G. Wu and X. Z. Zhao, J. Cryst. Growth, 292, 19 (2006)

31. J. H. He, C. H. Ho, C. W. Wang, Y. Ding, L. J. Chen and Z. L. Wang, Cryst. Growth Des. 9, 17 (2009)

32. Y. Sun, G. M. Fuge and M. N. R. Ashfold, Chem. Phys. Lett., 396, 21 (2004)

33. D. Q. Yu, L. Z. Hu, J. Li, H. Hu, H. Q. Zhang, Z. W. Zhao and Q. Fu, Mater. Lett., 62, 4063 (2008)

34. B. Q. Cao, J. Zuniga–Perez, C. Czekalla, H. Hilmer, J. Lenzner, N. Boukos, A. Travlos, M. Lorenz and M. Grundmann, J. Mater. Chem., 20, 3848 (2010)

35. H. Q. Yang, Y. Z. Song, L. Li, J. H. Ma, D. C. Chen D C, S. L. Mai and H. Zhao, Cryst. Growth Des. 8, 1039 (2008)

36. S. S. Warule, N. S. Chaudhari, B. B. Kale and M. A. More, CrystEngComm, 11, 2776 (2009)

37. B. Q. Cao, Y. Li, G. T. Duan and W. P. Cai, Cryst. Growth Des. 6, 1091 (2006)

38. C. J. Yang, S. M. Wang, S. W. Liang, Y. H. Chang, C. Chen and J. M. Shieh, Appl. Phys. Lett. 90, 033104 (2007)

39. J. F. Yu, F. Wanf, Y. Wang, H. Gao, J. L. Li and K. Wu, Chem. Soc. Rev. 39, 1513 (2010)

40. T. L. Chou and J. M. Ting, Thin Solid Films, 494, 291 (2006)

41. S. W. Kan, S. K. Mohanta, Y. Y. Kim and H. K. Cho, Cryst. Growth Des. 8, 1458 (2008)

42. H. Wang, Z. P. Zhang, X. N. Wang, Q. Mo, Y. Wang, J. H. Zhu, H. B. Wang, F. J. Yang and Y. Jiang, Nanoscale Res. Lett., 3, 309 (2008)

43. S. Li, X. Z. Zhang, B. Yan and T. Yu, Nanotechnology, 20, 495604 (2009)

44. J. I. Hong, J. Bae, Z. L. Wang and R. L. Snyder, Nanotechnology, 20, 085609 (2009)

45. M. Breedon, M. B. Rahmani, S. H. Keshmiri, W. Wlodarski, K. Kalantar-zadeh, Mater. Lett., 64, 291 (2010)

46. D. Charu, V. Dutta, Adv. Nat. Sci.: Nanosci. Nanotechnol. 3, 015011 (2012)

47. Z. Yang, T. Xu, Y. Ito, U. Welp, W. K. Kwok, J. Phys. Chem. C., 113, 20521 (2009)

48. M. Law, L. E. Greene, J. C. Johnson, R. Saykally, P. D. Yang, Nat. Mater., 4, 455 (2005)

49. L. E. Greene, B. D. Yuhas, M. Law, D. Zitoun, P. D. Yang, Inorg. Chem., 45, 7535 (2006)

50. Q. Zhang, C. S. Dandeneau, X. Zhou and G. Cao, Review: Adv. Mater., 21, 1 (2009)

51. S. H. Ko, D. Lee, H. W. Kang, K. H. Nam, J. Y. Yeo, S. J. Hong, C. P. Grigoropoulos, and H. J. Sung, Nano Lett., 11, 666 (2011)

52. M. Guo, P. Diao, S. M. Cai, Appl. Surf. Sci., 249, 71 (2005)

53. J. B. Baxter, A. M. Walker, K. van Ommering, E. S. Aydil, Nanotechnology, 17, S304 (2006)

54. M. Guo, P. Diao, X. D. Wang, S. M. Cai, J. Solid State Chem., 178, 3210 (2005)

55. R. Zhang, S. Kumar, S. Zou, L. L. Kerr, Cryst. Growth Des. 8, 381 (2008)

56. Z. L. Wang and J. Song, Science, 312, 242 (2006)

57. D. Calestani, F. Pattini, F. Bissoli, E. Gilioli, M. Villani and A. Zappettini, Nanotechnology 23 194008 (2012)

58. D. Calestani, M. Z. Zha, L. Zanotti, M. Villani and A. Zappettini, CrystEngComm, 13, 1707 (2011)

59. J. C. Monier and R. Kern, C. R. Hebd. Acad. Sci., 240, 2338 (1955)

60. H. Iwanaga, M. Fujii and S. Takeuchi, Phase Transitions, 66, 147 (1998)

61. W. I. Park, J. S. Kim, G. C. Yi, M. H. Bae and H. Lee, J. Appl. Phys. Lett., 85, 5052-5054 (2004)

62. H. J. Fan, Y. Yang and M. Zacharias, J. Mater. Chem., 19, 885–900, (2009)

63. C. G. Van de Walle, Phys. Rev. Lett., 85, 1012-1015 (2000)

64. H. Qiu, B. Meyer, Y. Wang and C. Wöll, C. Phys. Rev. Lett., 101, 236401 (2008)

65. F. Gallino, G. Pacchioni and C. Di Valentin, J. Chem. Phys., 133, 144512 (2011)

66. H. Mondragón-Suárez, A. Maldonado, M. De la L. Olvera, A. Reyes, R. Castanedo-Pérez, G. Torres-Delgado and R. Asomoza, Appl. Surf. Sci., 193, 52 (2002)

67. H. Von Wenckstern, H. Schmidt, M. Brandt, A. Lajn, R. Pickenhain, M. Lorenz, M. Grundmann, D. M. Hofmann, A. Polity, B. K. Meyer, H. Saal, M. Binnewies, A. Börger, K. D. Becker, V. A. Tikhomirov and K. Jug, Prog. Solid State Ch., 37,153-172 (2009)

68. R. Cebulla, R. Wendt and K. Ellmer, J. Appl. Phys., 83, 1087 (1998)

69. J. Ma, F. Ji, D. H. Zhang, H. L. Ma and S. Y. Li, Thin Solid Films, 357, 98. (1999)

70. J. Hu and R. G. Gordon, J. Appl. Phys., 72, 5381 (1992)

71. R. Wang, A. W. Sleight, and D. Cleary, Chem. Mater., 8, 433 (1996)

72. H. Go´mez, A. Maldonado, R. Asomoza, E. P. Zironi, J. Can_etasOrtega and J. Palacios-Go´mez, Thin Solid Films, 293, 117 (1997)

73. A. Wang, J. Dai, J. Cheng, M. P. Chudzik, T. J. Marks, R. P. H. Chang and C. R. Kannewurf, Appl. Phys. Lett., 73, 327 (1998)

74. J. Zhong, S. Muthukumar, Y. Chen, Y. Lu, H. M. Ng, W. Jiang, and E. L. Garfunkel, Appl. Phys. Lett. 83, 3401 (2003)

75. H. Sato, T. Minami and S. Takata, J. Vac. Sci. Technol., A, 11, 2975 (1993)

76. A. Bougrine, A. El Hichou, M. Addou, J. Ebothe´, A. Kachouane, and M. Troyon, Mater. Chem. Phys., 80, 438 (2003)

77. N. J. Dayan, R. N. Karekar, R. C. Aiyer and S. R. Sainkar, J. Mater. Sci.: Mater. Electron, 8, 277 (1997)

78. A. Gulino and I. Fragala, I. Chem. Mater. 2002, 14, 116.

79. D. C. Reynolds, D. C. Look, B. Jogai, C. W. Litton, G. Cantwell and W. C. Harsch, Phys. Rev. B 60, 2340 (1999)

80. M. X. Jung, E. S. Lee, E. I. Jeon, K. S. Gil, J. J. Kim, Y. Murakami, S. H. Lee, H. J. Lee, T. Yao, H. Makino and J. H. Chang, J. Alloys Compd. 481, 649 (2009)

81. H. J. Fan, A. S. Barnard and M. Zacharias, Appl. Phys. Lett. 90, 143116 (2007)

82. J. Y. Lao, J. Y. Huang, D. Z. Wang, Z. F. Ren, Nano Lett. 3, 235 (2003)

83. Y. Ding, X. Y. Kong and Z. L. Wang, Phys. Rev. B 70, 235408 (2004)

84. M. Bazzani, A. Neroni, A. Calzolari, A. Catellani, Appl. Phys. Lett., 98, 121907 (2011)

85. A. Catellani, A. Ruini, G. Cicero, A. Calzolari, Phys. Status Solidi, in press.

86. J. Jie, G. Wang, X. Han, and J. G. Hou, J. Phys. Chem. B 108, 17027 (2004)

87. L. Wu, X. Zhang, Z. Wang, Y. Liang, and H. Xu, J. Phys. D: Appl. Phys. 41, 195406 (2008)

88. C. W. Na, S. Y. Bae, and J. Park, J. Phys. Chem. B 109, 12785 (2005)

89. B. Alemán, P. Fernández, and J Piqueras, Appl. Phys. Lett. 95, 013111 (2009)

90. G. V. Naik, J. Liu, A. V. Kildishev, V. M. Shalaev and A. Boltasseva, PNAS, 109, 23, 8835, 2012

91. D. Calestani, M. Zha, G. Salviati, L. Lazzarini, L. Zanotti, E. Comini and G. Sberveglieri, J. Cryst. Growth, 275, e2083 (2005)

92. D. Calestani, M. Zha, A. Zappettini, L. Lazzarini and L. Zanotti, Chem. Phys. Lett., 445, 251 (2007)

93. M. Zha, D. Calestani, A. Zappettini, R. Mosca, M. Mazzera, L. Lazzarini and L. Zanotti, Nanotechnology, 19, 325603 (2008)

94. S. Y. Bae, C. W. Na, J. H. Kang, and J. Park, J. Phys. Chem. B, 109, 2526-2531 (2005)

95. H. Gao, H. Ji, X. Zhang, H. Lu and Y. Liang, J. Vac. Sci. Technol. B, 26, 585 (2008)

96. S. Lin, Z. Ye, H. He, Y. Zeng, H. Tang, B. Zhao and L. Zhu, J. Cryst. Growth, 306, 339 (2007)

97. K. W. Liu, M. Sakurai and M. Aono, J. Appl. Phys., 108, 053516 (2010)

98. H. Zhou, J. Fallert, J. Sartor, R. J. Dietz, C. Klingshirn, H. Kalt, D. Weissenberger, D. Gerthsen, H. Zeng and W. Cai, Appl. Phys. Lett., 92, 132112 (2008)

99. H. Zhou, M. Wissinger, J. Fallert, R. Hauschild, F. Stelzl, C. Klingshirn and H. Kalt, Appl. Phys. Lett., 91, 181112 (2007)

100. O. Kubaschewsky, E. L. L. Evans and C. Alcock, B. Metallurgical Thermochemistry, Pergamon Press: Oxford U.K. (1967)

101. C. Hong, H. Kim, H. W. Kim, N. Cho, I. Lee and C. Lee, J. Ceram. Soc. Jpn., 117, 566 (2009)

102. J. Dutkiewicz and W. Zabulski, Bull. Alloy Phase Diagr., 5, 284 (1984)

103. L. Zanotti, M. Zha, D. Calestani, E. Comini and G. Sberveglieri, Cryst. Res. Technol., , 40, 932 (2005)

104. D. Calestani, M. Zha, L. Zanotti, M. Villani and A. Zappettini, CrystEngComm, 13, 1707 (2011)

105. A. Janotti and C. G. Van de Walle, Phys. Rev. B, 76, 165202 (2007)

106. A. Janotti and C. G. Van de Walle, Appl. Phys. Lett., 87, 122102 (2005)

107. Special issue on silicon carbide devices and technology, IEEE Trans. Electron Dev. **55** 1795–2065 (2008)

108. H. K. Seong, H. J. Choi, S. K. Lee, J. I. Lee and D. J. Choi, Appl. Phys. Lett. 85 1256 (2004)

109. H. K. Seong, H. J. Choi, S. K. Lee, J. I. Lee and D. J. Choi, Mater. Sci. Forum 527–529 771–5 (2006)

110. Z. W. Pan, H. L. Lai, C. K. Frederick, X. F. Duan, W. Y. Zhou, W. S. Shi, N. Wang, C. S. Lee, N. B. Wong, S. T. Lee and S. S. Xie, Adv. Mater. 12 1186 (2000)

111. J. J. Niu, J. N. Wang and Q. F. Xu, Langmuir 24 6918 (2008)

112. E. W. Wong, P. E. Sheehan and C. M. Lieber, Science 277 1971 (1997)

113. T. Kimoto, A. Itoh and H. Matsunami, Phys. Status Solidi b 202 247–62 (1997)

114. P.F. Becher, G.C. Wei, J. Am. Ceram. Soc. 67, C-267 (1984)

115. P. Kim, C.M. Lieber, Science 286, 2148 (1999)

116. Y. Zhang, M. Nishitani-Gamo, C. Xiao and T. Ando, J. Appl. Phys. 91, 6066 (2002)

117. L. Nordsletten L, A. K. M. Høgåsen, Y. T. Konttinen, S. Santavirta, P. Aspenberg and A. O. Aasen, Biomaterials 17 1521 (1996)

118. Choi, H.-J.: Continuous synthesis of silicon carbide whiskers. J. Mater. Sci. 30, 1982 (1995)

119. G. W. Meng, L. D. Zhang, C. M. Mo, S. Y. Zhang, Y. Qin, S. P. Feng and H. J. Li, J. Mater. Res. 13, 2533 (1998)

120. W. Yang, H. Miao, Z. Xie, L. Zhang and L. An, Chem. Phys. Lett. 383, 441 (2004)

121. G. Shen, D. Chen, K. Tang, Y. Qian and S. Zhang, Chem. Phys. Lett. 375, 177–184 (2003)

122. S. C. Chiu and Y. Y. Li, J. Cryst. Growth 311, 1036 (2009)

123. J. Zhu and S. Fan, J. Mater. Res. 14, 1175 (1999)

124. B Park, Y Ryu and K Yong, Surf. Rev. Lett. 11, 373 (2004)

125. Y. Ryu, Y. Tak and K. Yong, Nanotechnology 16, S370 (2005)

126. D.F. Liu, S.S. Xie, X.Q. Yan, L.J. Ci, F. Shen, J.X. Wang, Z.P. Zhou, H.J. Yuan, Y. Gao, L. Song, L.F. Liu, W.Y. Zhou and G. Wang, Chem. Phys. Lett. 375, 269–272 (2003)

127. H. J. Choi, H. K. Seong, J. C. Lee and Y. M. Sung, J. Cryst. Growth 269, 472 (2004)

128. X. T. Zhou, H. L. Lai, H. Y. Peng, Frederick C. K. Au, L. S. Liao, N. Wang, I. Bello, C. S. Lee and S. T. Lee, Chem. Phys. Lett. 318, 58 (2000)

129. W. J. Kim, S. M. Kang, C. H. J., J. Y. Park and W. S. Ryu, J. Cryst. Growth 300, 503–508 (2007)

130. W. Yang, H. Araki, Q. Hu, N. Ishikawa, H. Suzuki and T. Noda, J. Cryst. Growth 264, 278–283 (2004)

131. Y. Sun, H. Cui, G.Z. Yang, H. Huang, D. Jiang and C.X. Wang, Cryst. Eng. Comm., 12, 1134-1138 (2010)

132. Z. J. Li, W. P. Ren and A. L. Meng, Appl. Phys. Lett., 97, 263117 (2010)

133. Z. J. Li, J. L. Zhang, A. L. Meng and J. Z. Guo, J. Phys. Chem. B, 110, (2006) 22382–22386

134. S. C. Chiu and Y. Y. Li, J. Cryst. Growth, 311, 1036–1041 (2009)

135. X. T. Zhou, N. Wang, H. L. Lai, H. Y. Peng, I. Bello, N. B. Wong, C. S. Lee and S. T. Lee, Appl. Phys. Lett., 74, 3942 (1999)

136. G. Z. Shen, Y. Bando and D. Golberg, Cryst. Growth Des., 7, 35–38 (2007)

137. J. Z. Guo, Y. Zuo, Z. J. Li, W. D. Gao and J. L. Zhang, Physica E, 39, 262–266 (2007)

138. G. Attolini, F. Rossi, F. Fabbri, M. Bosi, B. E. Watts and G. Salviati, Materials Letters, 63, 2581–2583 (2009)

139. H. Y. Wang, W. F. Jiang, L. P. Kang and Z. J. Li, Journal of Alloys and Compounds, 553, 125–128 (2013)

140. J. J. Niu and J. N. Wang, J. Phys. Chem. B, 113, 2909–2912 (2009)

141. J. J. Niu and J. N. Wang, J. Phys. Chem. B, 111, 4368-4373 (2007)

142. G. Z. Shen, Y. Bando, C. H. Ye, B. D. Liu and D. Golberg, Nanotechnology, 17, 3468–3472 (2006)

143. D. H. Feng, T. Q. Jia, X. X. Li, Z. Z. Xu, J. Chen, S. Z. Deng, Z. S. Wu and N. S. Xu, Solid State Communications, 128, 295–297 (2003)

144. J. J. Chen, R. B. Wu, G. Y. Yang, Y. Pan, J. Lin, L. L. Wu and R. Zhai, Journal of Alloys and Compounds., 456, 320–323 (2008)

145. L. P. Xin, Q. Shi, J. J. Chen, W. H. Tang, N. Y. Wang, Y. Liu and Y. X. Lin, Materials Characterization, 65, 55-61 (2012)

146. G. W. Meng, L. D. Zhang, Y. Qin, C. M. Mo and F. Phillipp, Nanostruct. Mater., 12, 1003–1006 (1999)

147. X. Tao, Y. Li, J. Du, Y. Xia, Y. Yang, H. Huang, Y. Gan, W. Zhang and X. Li, Journal of Materials Chemistry, Vol. 21, 9095-9102 (2011)

148. Y. J. Hao, J. B. Wagner, D. S. Su, G. Q. Jin and X. Y. Guo, Nanotechnology, 17, 2870–2874 (2006)

149. X. N. Guo , R. J. Shang, D. H. Wang, G. Q. Jin, X. Y. Guo and K. N. Tu, Nanoscale Res. Lett., 5, 332–337 (2010)

150. A. Huczko, M. Bystrzejewski, H. Lange, A. Fabianowska, S. Cudziło, A. Panas and M. Szala, J. Phys. Chem. B, 109, 16244-16251 (2005)

151. G. Wei, H. Y. Liu, C. K. Shi, F. M. Gao, J. J. Zheng, G. D. Wei and W. Y. Yang, J. Phys. Chem. C, 115, 13063–13068 (2011)

152. F. M. Gao, W. Y. Yang, H. T. Wang, Y. Fan, Z. P. Xie and L. N. An, Cryst. Growth Des., 8, 1461–1464 (2008)

153. W. Y. Yang, H. Z. Miao, Z. P. Xie, L. G. Zhang and L. N. An, Chem. Phys. Lett., 383, 441–444 (2004)

154. H. T. Wang, Z. P. Xie, W. Y. Yang, J. Y. Fang, L. N. An, Cryst. Growth Des., 8, 3893–3896 (2008)

155. H. T. Wang, L. Lin, W. Y. Yang, Z. P. Xie and L. N. An, J. Phys. Chem. C, 114, 2591–2594 (2010)

156. W. M. Zhou, B. Yang, Z. X. Yang, F. Zhu, L. J. Yan and Y. F. Zhang, Applied Surface Science, 252, 5143-5148 (2006)

157. G. D. Wei, W. P. Qin, G. F. Wang, J. B. Sun, J. J. Lin, R. J. Kim, D. S. Zhang and K. Zheng, J. Phys. D: Appl. Phys. 41, 235102 (2008)

158. Z. W. Pan, H. L. Lai, F. C. K. Au, X. F. Duan, W. Zhou, W. S. Shi, N. Wang, C. S. Lee, N. B. Wong, S. T. Lee and S. Xie, Adv. Mater., 12, 1186-1190 (2000)

159. Y. B. Li, S. S. Xie, W. Y. Zhou, L. J. Ci and Y. S. Bando, Chem. Phys. Lett., 356, 325–330 (2002)

160. S. C. Chiu, C. W. Huang and Y. Y. Li, J. Phys. Chem. C, 111, 10294-10297 (2007)

161. Y. Zhang, K. Suenaga, C. Colliex and S. lijima, Science, 281, 973-975 (1998)

162. W. S. Shi, Y. F. Zheng, H. Y. Peng, N. Wang, C. S. Lee and S. T. Lee, J. Am. Ceram. Soc., 83, 3228–3230 (2000)

163. G. Zou, C. Dong, K. Xiong, H. Li, C. L. Jiang and Y. Qian, Applied Physics Letters, 88, 071913 (2006)

164. Z. C. Ju, X. C. Ma, N. Fan, P. Li, L. Q. Xu and Y. Qian, Materials Letters, 61, 3913–3915 (2007)

165. G. C. Xi, Y. Peng, S. M. Wan, T. W. Li, W. C. Yu and Y. Qian, J. Phys. Chem. B, 108, 20102-20104 (2004)

166. L. Gao, H. Zhong and Q. W. Chen, Journal of Alloys and Compounds, 566, 212-216 (2013)

167. Y. Yao, S. T. Lee and F. H. Li, Chemical Physics Letters, 381, 628–633 (2003)

168. Y. Zakharko, J. Botsoa, S. Alekseev, V. Lysenko, J. M. Bluet, O. Marty, V. A. Skryshevsky and G. Guillot, Journal of Applied Physics, 107, 013503 (2010)

169. S. A. Fortuna and X. Li, Semicond. Sci. Technol., 25, 024005 (2010)

170. R. S. Wagner and W. C. Ellis, Appl. Phys. Lett., 4, 89–90 (1964)

171. G. Y. Li, X. D. Li, Z. D. Chen, J. Wang, H. Wang and R. C. Che, J. Phys. Chem. C, 113, 17655–60 (2009)

172. K. Zekentes and K. Rogdakis, J. Phys. D: Appl. Phys., 44, 133001 (2011)

173. M. Bosi, B. E. Watts, G. Attolini, C. Ferrari, C. Frigeri, G. Salviati, A. Poggi, F. Mancarella, A. Roncaglia, O. Martnez and V. Hortelano, Crystal Growth and Design, 9, 11, 4852-4859 (2009)

174. C. D. Strinespring and J. C. Wormmhoudt, J. of Crystal Growth, 87, 481-493 (1987)

175. T.B. Massalski, P.R. Subramanian, H. Okamoto, L. Kacprzak, Binary Alloy Phase Diagrams, second ed., ASM International, Materials Park, OH, 1990.

176. R. Wu, B. Li, M. X. Gao, J. J. Chen, Q. M. Zhu and Y. Pan, Nanotechnology, 19, 335602 (2008)

177. Z. J. Li, X. J. Li, X. L. Chen, A. L. Meng, K. L. Li, Y. P. Xu and L. Dai, Appl. Phys. A, 76, 637–40 (2003)

178. X. G. Ning and H. Q. Ye, J. Phys.: Condens. Matter, 2, 10223 (1990)

179. L. Wang, H. Wada and L. F. Allard, J. Mater. Res., 7, 148–62 (1992)

180. C. Cheng, R. J. Needs and V. Heine, J. Phys. C: Solid State Phys., 21, 1049 (1988)

181. D. H. Wang, D. Xu, Q. Wang, Y. J. Hao, G. Q. Jin, X. Y. Guo and K. N. Tu, Nanotechnology, 19, 215602 (2008)

182. E. Kudrenko, V. Roddatis, A. Zhokhov, I. Zverkova, I. Khodosc and G. Emelchenko, RSC Adv., 2, 4913–4919 (2012)

183. Z. Wang, S. Wang, C. Zhang and J. Li, J. Nanopart. Res., 13, 185–191 (2011)

184. J. Chen, Y. Pan and R. Wu, Phys. E., 42, 2335–2340 (2010)

185. W. G. Moffatt, The Handbook of Binary Phase Diagrams, Vol. 3, Genium, New York, (1984)

186. E. Denkhaus, and K. Salnikow, Reviews in oncology/hematology, 42, 35–56 (2002)

187. E.I. Givargizov, Growth of Crystals, in: A.A. Chernov (Ed.), Translated by J.E.S. Bradley, Consultants Bureau, New York; 11, 136 (1979)

188. W. Kern, J. Electrochem. Soc., 137, 6, (1990)

189. M. Itano, F. W. Kern Jr., M. Miyashita, and T. Ohmi, IEEE TRANSACTIONS ON SEMICONDUCTOR MANUFACTURING. 6, 3, 258, (1993)

190. S. E. Saddow, Editor Silicon Carbide Biotechnology: A Biocompatible Semiconductor for Advanced Biomedical Devices and Applications, Elsevier LTD, UK, (2011)

191. L. J. Lauhon, M. S. Gudiksen, D. Wang and C. M. Lieber, Nature, 420, 57 (2002)

192. Z. L. Cai, G. Wang, B. Song, R. Wu, J. Li and J. K. Jian, CrystEngComm, 15, 5082–5086 (2013)

193. J. K. Jian, C. Wang, M. Lei, Z. H. Zhang, T. M. Wang and X. L. Chen, Appl. Surf. Sci., 254, 6637 (2008)

194. A. M. Morales and C. M. Lieber, Science, 279, 208 (1998)

195. R. Q. Zhang, Y. Lifshitz and S. T. Lee, Adv. Mater., 15, 635 (2003)

196. H. Y. Peng, Z. W. Pan, L. Xu, X. H. Fan, N. Wang, C. S. Lee and S. T. Lee, Adv. Mater., 13, 317 (2001)

197. A. L. Meng, M. Zhang, W. D. Gao, S. B. Sun and Z. J. Li, Nanoscale Res. Lett., 6, 34 (2011)

198. Z. J. Li, W. D. Gao, A. L. Meng, Z. D. Geng and L. Gao, J. Phys. Chem. C, 113, 91 (2009)

199. C. S. Wang, J. L. Zhang, A. L. Meng, M. Zhang and Z. J. Li, Phys. E., 9, 128 (2007)

200. A. L. Meng, Z. J. Li, J. L. Zhang, L. Gao and H. J. Li, J. Cryst. Growth, 308, 263 (2007)

201. F. Fabbri, F. Rossi, G. Attolini, G. Salviati, B. Dierre, T. Sekiguchi, N. Fukata, Materials Letters, 71, 137–140 (2012)

202. F. Fabbri, F. Rossi, G. Attolini, G. Salviati, S. Iannotta, L. Aversa,R. Verucchi, M. Nardi, N. Fukata,B. Dierre and T. Sekiguchi, Nanotechnology, 21, 345702 (2010)

203. V. V. Afanas’ev, M. Bassler, G. Pensl and M. J. Schulz, J. Appl. Phys., 79, 3108 (1996)

204. R. Yakimova, R. M. Jr. Petoral, G. R. Yazdi, C. Vahlberg, A. L. Spetz and K. Uvdal, J. Phys. D: Appl. Phys., 40, 6435 (2007)

205. C. L. Frewin, M. Jaroszeski, E. Weeber, K. E. Muffly, A. Kumar, M. Peters, A. Oliveros and S. E. Saddow, J. Mol. Recognit., 22 380–8 (2009)

206. J. Fan, H. Li, J. Jiang, L. K. Y. So, Y. Wah Lam and P. K. Chu, Small, 4, 1058–62 (2008)

207. C. Coletti, M. J. Jaroszeski, A. Pallaoro, A. M. Hoff, S. Iannotta and S. E. Saddow, Proc. 29th Annu. Int. Conf. IEEE EMBS, 5849 (2007)

208. G. Cicero, A. Catellani and G. Galli, Phys. Rev. Lett., 93, 016102 (2004)

209. H. Mader, X. Li, S. Saleh, M. Link, P. Kele, O. S. Wolfbeis, Ann N Y Acad Sci., 1130, 218–23 (2008)

210. P. G´omez-Romero and C. Sanchez (ed) Functional Hybrid Materials (Weinheim: Wiley-VCH) (2004)

211. W. Chen and J. Zhang, J. Nanosci. Nanotech., 6, 1159-1166 (2006)

212. P. Juzenas, W. Chen, Y. P. Sun, M. A. Neto Coelho, R. Generalov, N. Generalova, I. L. Christensen, Adv. Drug Deliv. Rev. 60, 1600–1614 (2008)

213. Y. Liu, W. Chen, S. Wang, A. L. Joly, Appl. Phys. Lett. 92, 043901 (2008)

214. A. Kassiba, J. Bouclé, M. Makowska-Janusik and N. Errien, J Phys Conf Ser., 79, 012002 (2007)

215. X. M. Liu and K. F. Yao, Nanotechnology, 16, 2932–5 (2005)

216. X. L. Wu, J. Y. Fan, T. Qiu, X. Yang, G. G. Siu and P. K. Chu, Phys Rev Lett., 94, 026102 (2005)

217. G. Kwak, M. Lee, K. Senthil, and K. Yong, Langmuir, 26, 14, 12273–12277 (2010)

218. Y. Jung, and B. Bhushan, Langmuir, 24, 6262 (2008)

219. T. Deng, K. Varanasi, M. Hsu, N. Bhate, C. Keimel, J. Stein, M. Blohm, Appl. Phys. Lett., 94, 133109 (2009)

220. Y. Kwon, N. Patankar, J. Choi, J. Lee, Langmuir, 25, 6129 (2009)

221. Z. Wang, ; C. Lopez, A. Hirsa, N. Koratkara, Appl. Phys. Lett., 91, 023105 (2007)

222. A. Meng, Z. Li, J. Zhang, L. Gao and H. Li, J. Cryst. Growth, 308, 263–268 (2007)

223. Y. Zhang, K. Suenaga, C. Colliex and S. Iijima, Science, 281, 973–975 (1998)

224. W. S. Shi, Y. F. Zheng, H. Y. Peng, N. Wang, C. S. Lee and S. T. Lee, J. Am. Ceram. Soc., 83, 3228 (2000)

225. H. Dai, E. W. Wong, Y. Z. Lu, S. S. Fan, and C. M. Lieber, Nature, 375, 769 (1995)

226. W. Han, Chem. Phys. Lett., 265,374(1997)

227. Y. Zhang, T. Ichihashi, E. Landree, F. Nihey, and S. Iijima, Science, 285, 1719 (1999)

228. J. Q. Hu et al., J. Phys. Chem., B 104, 5251 (2000)

229. Z. J. Li, H. J. Li, X. L. Chen, A. L. Meng, K. Z. Li, Y. O. Xu, and L. Dai, Appl. Phys. A: Mater. Sci. Process., 76, 637 (2003)

230. H. K. Seong, H. J. Choi, S. K. Lee, J. I. Lee, and D. J. Choi, Appl. Phys. Lett., 85, 1256 (2004)

231. H. Lai et al., Appl. Phys. Lett., 76, 294 (2000)

232. G. Z. Shen, Y. Bando, C. H. Ye, B. D. Liu, and D. Golberg, Nanotechnology, 17, 3468 (2006)

233. K. W. Wong, X. T. Zhou, C. K. Frederick, H. L. Lai, C. S. Lee, and S. T. Lee, Appl. Phys. Lett., 75, 2918 (1999)

234. J. Wei, K. Z. Li, H. J. Li, Q. G. Fu, and L. Zhang, Mater. Chem. Phys., 95, 140 (2006)

235. W. M. Zhou, Z. X. Yang, F. Zhu, and Y. F. Zhang, Physica E, 31, 9, (2006)

236. J. W. Liu, D. Y. Zhong, F. Q. Xie, M. Sun, E. G. Wang and W. X. Liu, Chem. Phys. Lett., 348, 357 (2001)

237. X. M. Liu and K. F. Yao, Nanotechnology, 16, 2932 (2005)

238. T. Seeger, P. Kohler-Redlich and M. Ruhle, Adv. Mater., 12, 279 (2000)

239. M. Peg, M. P. Ruiz, A. Callejas, A. Millera, R. Bilbao and M. U. Alzueta, Pyrolysis ethanol under flow reactor conditions, in: Third European Combustion Meeting ECM 2007, published by Greek Section of the Combustion Institute.

240. M. P. Ruiz, A. Callejas, A. Millera, M. U. Alzueta and R. J. Bilbao, Anal. Appl. Pyrol., 79, 244 (2007)

241. M. A. A. Elmasry, A. Gaber and E. M. H. Khater, Journal of Thermal Analysis and Calorimetry, 52, 2, 489–495 (1998)

242. D. F. Liu, S. S. Xie, X. Q. Yan, L. J. Ci, F. Shen, J. X. Wang, Z. P. Zhou, H. J. Yuan, Y. Gao, L. Song, L. F. Liu, W.Y. Zhou and G. Wang, Chemical Physics Letters, 375, 269–272 (2003)

243. Z. J. Li, W. D. Gao, A. L. Meng, Z. D. Geng and L. Gao, J. Phys. Chem. C, 113, 91 (2009)

244. R. B. Wu, G. Y. Yang, M. X. Gao, B. S. Li, J. J. Chen, R. Zhai and Y. Pan, Cryst. Growth Des., 9, 1, 100–104 (2009)

245. G. Yu, M. E. Levinshtein and S. L. Rumyantsev, Properties of Advanced SemiconductorMaterials GaN; AlN; SiC; BN; SiC; SiGe ed M. E. Levinshtein, S. L. Rumyantsev and M. S. Shur (New York: Wiley), 93–148 (2001)

246. L. Skuja, J. Non-Cryst. Solids, 239, 16–48 (1998)

247. S. Gallis, V. Nikas, M. Huang, E. Eisenbraun and A. E. Kaloyerosb, J. Appl. Phys., 102, 024302 (2007)

248. V. V. Afanas’ev, M. Bassler, G. Pensl and M. J. Schulz, J. Appl. Phys., 79, 3108 (1996)

Chapter 5

Conclusions

This Thesis work was mainly aimed to the growth of semiconductor nanowires. More in detail, quasi-1D nanostructures (“nanowires” or “nanorods”) of zinc oxide (ZnO) and silicon carbide (SiC) were grown and characterized. The self-assembly Vapor-Solid (VS) and Vapor-Liquid-Solid (VLS) growth techniques have been used to obtain such nanostructures in conventional Chemical Vapor Deposition (CVD) and Vapor Phase Epitaxy (VPE) reactors.

A large number of systematic growth experiments were done in order to understand the mechanisms and, hence, optimize the growth conditions. The obtained nanostructures were investigated by means of morphological, structural and optical characterizations.

Four main type of nanowires were obtained:

- ***vertically aligned ZnO nanowires***
- ***nanowires of ternary (In/Ga/Sn)ZnO oxides***
- ***3C-SiC nanowires***
- ***SiC/SiO$_2$ core/shell nanostructures***

The main results obtained in this work have been already published or submitted to reference Journal, as well as presented to several international conferences. A list is reported after this Chapter.

5.1 Vertically aligned ZnO nanowires

ZnO nanowires (or “nanorods”) have been grown on glass substrates with different transparent conducting oxides (TCO) films as seeding and functional layers, using a simple vapor phase process that relies on the controlled evaporation and oxidation of a cheap metallic Zn source. On Al-doped ZnO (AZO) films deposited by pulsed electron deposition (PED) and RF-sputtering ZnO aligned nanorods were grown homogeneously over a 2 cm^2 large area. After a cross-check of the influence of the different growth parameters, a simple way to control the length of the nanorods was found: their length can be increased by increasing the ratio between Zn amount and empty volume in the source container. Nanorods diameter is instead mainly influenced by the seeding-film grain size and those obtained on sputtered AZO films were generally larger than those on PED AZO films. The vertical alignment of the nanorods is however strongly influenced by the presence of a seeding film whose grains have a common orientation of the polar axis perpendicular to the substrate. This is the case of both kind of AZO films. On the other hand, a different crystal structure with no polarization, as in the case of a commercial indium tin oxide (ITO) films, gives rise to the growth of not-aligned rods. Although a vapor phase process is exploited, all the described synthesis steps are compatible with commercial glass substrates typically used for photovoltaic applications (temperature is lower than 500°C) and make no use of expensive catalysts or metal-organic precursors.

5.2 Nanowires of ternary (In/Ga/Sn)ZnO oxides

Indium zinc oxide (IZO) nanowires (or "nanorods" – NRs) have been obtained from vapor phase at relatively low temperatures by evaporating a Zn source over the substrates, where an In layer was previously deposited, and then adding oxygen in the appropriate ratio. As resulting from the different characterizations, the liquid In–Zn alloy formed during the first stage of the growth feeds the vapor–solid growth of IZO-NRs once oxygen is introduced. This growth mechanism overcomes all the co-evaporation issues related to these two metals with very different equilibrium vapor pressures, without the use of any expensive metal–organic precursor.

The obtained IZO-NRs are single crystals elongated along the [001] direction of the hexagonal wurtzite structure typical of ZnO. Optical emission didn't show any substantial shift, while the green emission band, usually found in undoped ZnO nanorods, is in this case completely quenched. The revealed 1–2% In content does not significantly affect the crystal structure of the ZnO nanostructures and but is compatible with the typically required values to obtain highly conducting ZnO based TCOs.

In a preliminary study, also GaZnO and SnZnO nanorods were synthesized using the above described growth mechanism, in which the metal with lower vapor pressure acts as liquid metal source directly on the substrate (in this case Ga or Sn). Further studies, however, have to be performed on both GaZnO and SnZnO because the presented results are just preliminary and must be considered as a proof of concept. Indeed, although incomplete, they demonstrate that the same technique used to produce InZnO nanorods from vapor phase below 500°C can be extended also to different ZnO-based ternary compounds, with other metals that are molten at this temperature but limited in the evaporation because of a much higher boiling point.

5.3 3C-SiC nanowires

3C-SiC nanowires were successfully grown using home-made induction-heated VPE reactor, using silane and propane as precursor through VLS growth mechanism on Si (100) and Si (111) substrate, and using nickel (Ni) or iron (Fe) as catalysts. The growth conditions were independently optimized to grow SiC nanowires with Ni and Fe droplet catalysts. At optimized condition, nanowires grew over the whole area catalyzed with nickel or iron, with high-yield and high density. The size and shape of the nanowires have been controlled by means of temperature and gas flow rate. The optimized temperature for smooth and round shaped nanowires were 1100 °C for Ni catalyst and 1250 °C for Fe catalyst. TEM analysis confirmed that the nanowires were single 3C-SiC crystals with <111> growth direction. A few planar defects, mainly stacking faults (SFs) and twins, were visible in some segments along the nanowires, but these are common also in bulk SiC because of the polymorphism of this material (they may be viewed as nanoscale polytype inclusions within the pure 3C–SiC phase). The morphology of the nanowires varied for Ni catalyst as a function of temperature. The observed wires had circular section with a conical shape at lower temperature. On the other hand, rod-like hexagonal shaped, cubic SiC nanostructure were observed at higher temperatures.

5.4 SiC/SiO_2 core/shell nanostructures

SiC/SiO_2 core/shell nanowires were grown using VLS mechanism with nickel nitrate and iron nitrate catalyst by home-made thermal CVD reactor. Several experiments have been done to optimize the condition for the growth of SiC/SiO_2 core/shell nanowires. The effects of different growth parameters, for both nickel nitrate and iron nitrate catalytic solutions, have been studied as a function of growth temperature, gas flow rate or substrate orientations, in order to understand the growth mechanism. Standard optimized condition were hence defined for high-yield and good quality SiC/SiO_2 core/shell nanowires for each catalyst. In these conditions large quantities of randomly distributed nanowires, with high density over large area, were found on the substrate when non-ionic surfactant is used in the catalytic solutions. The crystal structure of the nanowires was analyzed by TEM that evidenced a cubic (3C-SiC) structure for the SiC core ,with <111> growth axis. FFT images confirmed, together with EDS analysis, the presence of an amorphous silica shell ($SiO_{1.9<x<2}$). The growth mechanisms have also been defined and discussed for these nanostructures, confirming the important role of SiO vapor during the growth..

The produced good-quality SiC/SiO_2 core/shell nanowires have been used for “BioNiMed” Project at IMEM-CNR for both photodynamic and hyperthermic potential treatments of cancer cells.

List of publications

Peer reviewed papers:

1. Davide Calestani, **Sathish Chander Dhanabalan**, Marco Villani, Laura Lazzarini, Andrea Zappettini, *"Indium Zinc Oxide Nanorods by Liquid Indium Seeded Vapor Phase Deposition"*, CrystEngComm, 2013 (published on-line - DOI:10.1039/C3CE42095G)

2. **Sathish Chander Dhanabalan**, Marco Negri, Francesca Rossi, Giovanni Attolini, Marco Campanini, Filippo Fabbri, Matteo Bosi, Giancarlo Salviati, "*Effects of growth parameters on SiC/SiO$_2$ core/shell nanowires radial structure,"* The 9th European Conference on Silicon Carbide and Related Materials, 2-6 September 2012 S. Petersburg. Materials Science Forum, 740-742, 2013, p.494.

3. Giovanni Attolini, Francesca Rossi, Marco Negri, **Sathish Chander Dhanabalan**, Matteo Bosi, Francesco Boschi, Paola Lagonegro, Pierpaolo Lupo and Giancarlo Salviati. *"Growth of SiC NWs by vapour phase technique using Fe as catalyst"*, Material Letters, 2013 (***under review***)

4. **Sathish Chander Dhanabalan**, Davide Calestani, Marco Villani, Francesco Pattini, John Paul Garcia, Stefano Rampino and Andrea Zappettini, "Controllable vapor phase growth of vertically aligned ZnO nanorods on TCO/Glass substrates", Crystal Research and Technology (***submitted***)

5. M. Negri, F. Rossi, G. Attolini, F. Fabbri, **S. C. Dhanabalan**, F. Boschi, M. Bosi, M. V. Nardi, G. Salviati, "Cubic Silicon Carbide Nanowires" book chapter whitin the volume "Exotic Properties Of Carbon Nanomatter: Advances In Physics And Chemistry", Springer Series on "Carbon Materials: Chemistry and Physics", Editors: M. V. Putz & O. ORI, (***submitted***)

Conferences presentations:

1. **Sathish Chander Dhanabalan***, Davide Calestani, Marco Villani, Laura Lazzarini, Francesco Pattini1, John Paul Garcia1, Stefano Rampino, and Andrea Zappettini, "*Nanoepitaxial vapor phase growth of vertically aligned ZnO nanowires*", Italian Crystal Growth conference (ICG-2013), IMEM, Parma, Italy, 14-15 November 2013 **(Poster)**
2. G. Attolini*, M. Negri, **S.C.Dhanabalan**, M. Bosi, F. Rossi, F. Boschi, P. Lagonegro, P.P. Lupo, T. Besagni and G. Salviati. *"SiC NWs grown on silicon substrate using Fe as catalyst" HeterSic-Wasmpe"* Nice, France, June 17-19, 2013 **(Poster)**
3. **Sathish Chander Dhanabalan** , Marco Negri*, Giovanni Attolini, Matteo Bosi, Marco Campanini, Francesca Rossi, Francesco Boschi, Paola Lagonegro, Pierpaolo Lupo, Giancarlo Salviati, *"Growth and characterization of 3C-SiC nanowires on silicon substrate using different catalysts"*. International Conference on Crystal Growth and Epitaxy 17, Warsaw, Poland, August 11-16, 2013 **(Poster)**
4. A. Zappettini*, **D. S. Chander**, M. Villani, L. Lazzarini, and D. Calestani: "Indium Zinc Oxide nanorods by liquid Indium seeded vapour phase deposition", ICCG17, Warsaw, Poland, August, 11-16, 2013. **(talk)**
5. **Sathish Chander Dhanabalan***, Davide Calestani, Marco Villani, Laura Lazzarini and Andrea Zappettini, Francesco Pattini, John Paul Garcia, Stefano Rampino, *"Low temperature vapour phase growth of Vertically aligned ZnO nanowires on PED and sputtered ZnO:Al TCO substrates"* 15th International Summer School on Crystal Growth, Gdansk, Poland, 4-10 August 2013 **(Poster)**
6. Marco Negri*, Paola Lagonegro, Giovanni Attolini, Francesco Boschi, Matteo Bosi, **Sathish C. Dhanabalan**, Filippo Fabbri, Francesca Rossi, Giancarlo Salviati, *"Influence of synthesis temperature on SiC nanowires structure and shape"*. 15th International Summer School on Crystal Growth, Gdansk, Poland, 4-10 August 2013 **(Poster)**
7. **S. C. Dhanabalan***, D. Calestani, M. Villani, L. Lazzarini, A. Zappettini, *"Ternary InZnO Nanowires by Liquid Metal Seeded Growth of ZnO Nanostructures"*, Workshop on Physics and Applications of Semiconducting Nanowires, Nanowires 12 (NW12), Berlin, Germany, September 19-21, 2012 **(poster)**
8. **S.C.Dhanabalan***, M.Negri, F.Rossi, G.Attolini, F.Fabbri, M.Campanini, M.Bosi, G.Salviati, *"Optimization of the growth parameters for SiC/SiO_2 core/shell NWs."*

Workshop on Physics and Applications of Semiconducting Nanowires, Nanowires 12 (NW12), Berlin, Germany, September 19-21, 2012 **(Poster)**

9. **S.C.Dhanabalan**, M.Negri, F.Rossi, G.Attolini, F.Fabbri, M.Campanini, M.Bosi*, G.Salviati, *"Effects of growth parameters on SiC/SiO*$_2$ *core/shell nanowires radial structure"*, The 9th European Conference on Silicon Carbide and Related Materials, St. Petersburg, Russia, 2-6 September 2012 **(Poster)**

10. **S.C.Dhanabalan**, M.Negri*, F.Rossi, G.Attolini, F.Fabbri, M.Campanini, G.Salviati, *"Early processes in SiC/SiO*$_2$ *core/shell nanowires growth via chemical vapour depostition."* The 7th International Conference on Advanced Materials, ROCAM 2012, Brasov, Romania, 28-31 August 2012 **(Poster)**

11. **S.C.Dhanabalan***, M.Negri, F.Rossi, G.Attolini, F.Fabbri, M.Campanini, M.Bosi, G.Salviati, *"Influence of surfactant and role of temperature on growth of Ni cathalized SiC/SiO*$_2$ *core/shell nanowires."* XI International Conference on Nanostructured Materials, NANO2012, Rhodes, Greece, 26-31 August 2012 **(Poster)**

12. **Sathish Chander Dhanabalan***, Marco Negri, Francesca Rossi, Giovanni Attolini, Marco Campanini, Filippo Fabbri, Giancarlo Salviati, "Synthesis and Characterization of SiC-SiO$_2$ Core-shell nanowires", Summer school on Micro- and Nano- structural characterization of materials, Thessaloniki, Greece, 11-15 July 2012 **(Talk)**

13. **D S Chander***, M.Negri, M.Campanili, F.Fabbri, F.Rossi, G.Attolini, G.Salviati, *"Impact of growth parameters on SiC/SiO*$_2$ *core/shell nanowires radial structure"*. 6th Nanowire Growth Workshop St. Petersburg, Russia. June 4-6, 2012 **(Poster)**

14. D. Calestani*, **D. S. Chander**, M. Villani, L. Lazzarini, A. Zappettini, *"Low temperature vapour phase growth of ZnO aligned nanowires on ZnO:Al TCO and glass substrate for photovoltaic applications"*, 6th Nanowire Growth Workshop 2012, St. Petersburg, 4-6 June 2012 **(poster)**

Acknowledgement

With deep sense of gratitude, I whole-heartedly express my sincere thanks to my supervisors **Prof. Andrea Zappettini** and **Prof. Giancarlo Salviati**, IMEM-CNR, Parma for their inspiring guidance, for giving the freedom in research and constant encouragement to carry out the present investigation. I would like to thank especially **Dr. Davide Calestani** from the bottom of the heart for his valuable suggestions, comments and guidance as a mentor in the growth and characterization of ZnO based nanowires, also I am gratified for his constant help throughout of my Ph.D in IMEM and in Nanowiring network. I am very much grateful to **Dr. Giovanni Attolini**, for his help, support and guidance in the growth of SiC nanowires.

I am indebted to my colleagues associated in the growth of ZnO nanowires **Dr. Marco Villani**, **Mr. Giacomo Benassi**, **Mr. Nicola Zambelli**, **Dr. Nicola Coppedè**, and in the group of SiC nanowires **Dr. Matteo Bosi**, **Mr. Marco Negri**, **Mr. Francesco Boschi**, **and Ms. Paola Lagonegro** for their timely help, friendship and constant support during my experiments in the laboratory.

I am ample thankful to the collaborators who are involved in the characterization **Dr. Francesca Rossi** (TEM), **Dr. Laura Lazzarini** (TEM), **Dr. Filippo Fabbri** (SEM & CL), **Mr. Marco Campanini** (TEM), **Dr. Tullo Besagni** (XRD) for the measurements and also for their discussions. Also, I am thanking the group of **Dr. Edmondo Gilioli** with **Dr. Stefano Rampino**, **Dr. Francesco Pattini** and **Dr. Francesco Bissoli** for providing TCO films for the ZnO nanowires experiments.

I am deeply grateful to **Prof. Nuria Garro** for her support and encouragement during the one month stay in Valencia for the Raman and micro PL measurements and my special thanks to **Dr. Albert Minj** and **Ms. Eleonora Secco** for their help during the measurement.

It is my privilege to acknowledge the financial support from "**Nanowiring"** network and Marie Curie fellowship for providing international research internship and sophisticated laboratory and analytical facilities to carry out this research. I would like to extend my gratefulness to all the fellows and mentors in the Nanowiring network for their constant encouragement. Also, I am indebted to **Prof. Alessandra Catellani** for her support and encouragement when I entered in the project.

I also wish to thank Director, all the researchers, technicians, Ph.D students, master's students of the IMEM-CNR for their support and kind co-operation during my Ph.D. Also I am very thankful to the administrative workers in the IMEM for their kindness and helpful in the all bureaucratic works.

I dedicate this whole work to my beloved parents **Mr. S. Dhanabalan**, **Mrs. D. Dhanalakshmi**, my brothers **Mr. D. Lakshmi Narayanan**, **Mr. D. Balaji,** my parent-in-law **Mr. S. Ponraj**, **Mrs. M. Vasantha** and brother-in-law **Mr. P. Stephen Selvamani**. Finally, my deepest gratitude goes to my best friend and sweet wife **Dr. P. Joice Sophia** for her solidarity, companionship and support. Without her love, support and sacrifices this work could not have been accomplished. I might miss to thank someone, but my heart thanks whenever they comes to mind.